

NASA Contractor Report 4496

A General Theory of Two- and
Three-Dimensional Rotational
Flow in Subsonic and
Transonic Turbomachines

Chung-Hua Wu
Clemson University
Clemson, South Carolina

Prepared for
Lewis Research Center
under Grant NAG3-1072



National Aeronautics and
Space Administration

Office of Management

Scientific and Technical
Information Program

1993



CONTENTS

FOREWORD	v
SYMBOLS	ix
CHAPTER 1—INTRODUCTION	1
CHAPTER 2—FUNDAMENTAL AEROTHERMODYNAMIC EQUATIONS GOVERNING THE THREE-DIMENSIONAL FLOW IN TURBOMACHINES	6
2.1 Basic Aerothermodynamic Equations Governing the Three-Dimensional Flow of a Viscous Fluid Through a Stationary Blade Row	6
2.2 Effect of Viscosity on Basic Equations	9
2.3 Basic Aerothermodynamic Equations Governing the Three-Dimensional Flow of a Viscous Fluid Through a Rotating Blade Row	21
2.4 Steady Fluid Flow Through a Stationary Blade Row and Steady Relative Flow Through a Rotating Blade Row	26
2.5 Viscous terms in the Governing Equations	28
2.6 Some Remarks on the Energy Equation and the Entropy Equation	31
CHAPTER 3—GOVERNING EQUATIONS FOR FLUID FLOW ALONG RELATIVE STREAM FILAMENTS	34
3.1 Following Fluid Flow on Relative Stream Surfaces	34
3.2 Equation Governing Fluid Flow Along S_2 Stream Surface of S_2 Stream Filament	36
3.3 Principal Equation for Fluid Flow Along S_2 Stream Filament	41
3.4 Principal Equations for Fluid Flow Along S_1 Stream Filament	50
CHAPTER 4—THREE-DIMENSIONAL FLOW EQUATIONS EXPRESSED IN TERMS OF NONORTHOGONAL CURVILINEAR COORDINATES AND CORRESPONDING NONORTHOGONAL VELOCITY COMPONENTS	53
4.1 General Curvilinear Coordinates in a Three-Dimensional Space	53
4.2 General Curvilinear Coordinates on a Surface	57
4.3 Basic Equations Governing Fluid Flow on S_1 Surface of Revolution	60
4.4 Methods of Solution for S_1	64
4.5 Equations Governing Fluid Flow on General S_2 Surface	70

4.6	Governing Equations for S_2 with Independent Variable ϕ Eliminated	78
4.7	Methods of Solution For S_2 Flow	84
4.8	Computation of F Term in Inverse Problem	89
4.9	Computation of Components of Normal and W_ϕ In Direct Problem	90
CHAPTER 5—TWO- AND THREE-DIMENSIONAL SUBSONIC FLOW IN TURBOMACHINES		92
5.1	Series Expansion on S_1 Surface of Revolution	92
5.2	Series Expansion In φ -coordinate	96
5.3	Forming Successive S_2 Surfaces by Progressing Circumferentially from $S_{2,m}$	97
5.4	Coordinate Transformation and Direct Expansion Method	99
5.5	Direct Matrix Solution of Subsonic Flow Along S_1 Filament of Revolution	102
5.6	Three-Dimensional Subsonic Flow in Turbomachine	106
5.7	Three-Dimensional Flow in a High Subsonic Compressor Stator	111
5.8	Three-Dimensional Flow in CAS Research Compressor (Subsonic Case)	113
CHAPTER 6—TRANSONIC FLOW ALONG S_1 AND S_2 STREAM FILAMENTS		121
6.1	Transonic Flow Along S_1 Stream Filament of Revolution Solved by Separate Region Computation with Shock Fitting	121
6.2	Transonic Stream-Function Principal Equation Solved with the Use of Artificial Compressibility	124
6.3	Effect of Axial-Velocity Density Ratio and Viscous Effect	129
6.4	Transonic Flow Along General S_1 Stream Filament	131
6.5	Transonic Flow on S_2 Stream Filament Solved by Separate Region Computation with Shock Fitting	133
6.6	Shock Embedding Elliptic Solution for Inverse Problem of Transonic S_2 Flow	135
6.7	Direct-Problem Solution of Transonic Flow Along S_2 Stream Filament	138
CHAPTER 7—THREE-DIMENSIONAL FLOW IN TRANSONIC TURBOMACHINES		142
7.1	Quasi-Three-Dimensional Flow Field in the DFVLR Rotor	142
7.2	Full-Three-Dimensional Transonic Flow in Cas Rotor	151
7.3	Some Remarks	164
References		166

FOREWORD

Professor Chung-hua Wu pioneered the three-dimensional flow theory for turbomachines at Lewis Flight Propulsion Laboratory, NACA in 1950. He introduced the S_1 and S_2 families of relative stream surfaces and thus reduced three-dimensional flow problems to problems of iterating two solutions of two independent variables. The relaxation or direct matrix method was used for subsonic flows and the method of characteristics for supersonic flows. Laborious but accurate results were obtained without the benefit of modern digital computers. In the sixties Professor Wu developed a body-fitted, nonorthogonal curvilinear coordinate system to improve computational accuracy. In subsequent years Professor Wu and his colleagues at the Institute of Engineering Thermal Physics, the People's Republic of China, developed shock-fitting and artificial compressibility methods for solutions in two- and three-dimensional transonic flows. Professor Wu's theories were design tools used in aircraft engines such as the J69, JT-3D, Spey, RB211, JT9D, F404, etc.

Since the early sixties Clemson University has been active in internal flow analysis. Through the support of the NASA Lewis Research Center in the early seventies, an inverse design method of the Griffith diffuser was developed. Initially the method was limited to potential flow. In subsequent years, the inverse method development at Clemson for internal flow has improved to include viscosity, compressibility and turbulence. Presently Clemson's inverse solution method is used in design modification of the GE MS-7001F gas turbine using coal gas as a fuel.

Because of mutual interests in internal flows and ties to the NASA Lewis Research Center, I became familiar with Professor Wu's work. In 1979, the year after U.S.A. and China resumed a normal relationship, I met Professor Wu in Beijing. He was the director at the Institute of Engineering Thermal Physics, The Academy of Sciences, People's Republic of China, at that time. We discussed the possibilities of exchange visits and collaborations.

A project emerged with the following specific objectives:

- (1) To prepare a manuscript that summarizes the work of more than 100 journal articles on S_1 and S_2 methods and three-dimensional flow solutions in turbomachinery that Wu and his colleagues developed in the last 40 years
- (2) To give two lecture series on the above subjects, one at NASA Lewis Research Center and the other at the University of Cincinnati
- (3) To discuss, on a regular basis, research problems in internal flows with graduate students and faculty of the Department of Mechanical Engineering of Clemson University

Thanks to the assistance of Dr. Melvin J. Hartmann, Director of University Programs at NASA Lewis, the above objectives materialized in 1990 with the support of a grant for NASA Lewis. Clemson University was privileged to have had Professor Wu and his wife, Professor Min-Hua Li, reside on Clemson's campus from January 1990 until May 1990. The lecture series at NASA Lewis was held March 19-21, 1990, and April 16-17, 1990, in Cincinnati. The manuscript draft was completed prior to Professor Wu's return to China.

On the eve of publishing this report, I would like to recognize the efforts of Dr. Lonnie Reid, Chief of Internal Fluid Mechanics Division, and his colleagues who reviewed the manuscripts, and to express my appreciation to many others at NASA Lewis who made this report possible.

It was a fulfilling experience and an inspiration for me to work with Professor Wu on this project. Persons who were involved with this project hope that this report will serve a useful purpose not only to document the work of computational fluid mechanics in turbomachinery, but also to encourage those of us who continue to toil in turbomachinery research.

On September 19, 1992, Professor Chung Hua Wu died in Beijing after a prolonged illness. While in the hospital, he read the final typing of the manuscript. We are sorry that he did not see his report released. The subject of this report is Professor Wu's lifetime effort. We hope this report will inspire those of us who toil in the field of turbomachinery.

March 1991

Project Coordinator

Tah-teh Yang

Professor of Mechanical Engineering

Clemson University

SYMBOLS

a	Jacobian of matrix $a_{\alpha\beta}$; velocity of sound
$a_{\alpha\beta}$	basic metric tensor of two-dimensional x^α coordinate system
b, B	integrating factor in the continuity equation for S_1 and S_2 stream surfaces
C	blade chord in z-direction; artificial compressibility coefficient
c_p	specific heat at constant pressure
c_v	specific heat at constant volume
D/Dt	differentiation with respect to time following relative motion of fluid particle
e	internal energy of fluid per unit mass
e_j, e^i	base vector and reciprocal vector of x^1 coordinate system
F	force acting on S_2 surface per unit mass of fluid, $-\left(\frac{1}{n_\varphi \rho r} \frac{\partial p}{\partial \varphi}\right)_n$
g	Jacobian of matrix g_{ij}
g_{ij}	covariant metric tensor of x^1 coordinate system
g^{ij}	contravariant metric tensor of x^1 coordinate system
H	absolute stagnation enthalpy, $h + V^2/2$
h	enthalpy per unit mass of fluid, $u + p/\rho$
I	relative stagnation rothalpy per unit mass, $I = i + W^2/2 = H - \omega V_\theta r$
i	rothalpy per unit mass, $h - U^2/2$
J	station along x^1 coordinate lines
K	station along x^2 coordinate lines
t, φ	orthogonal coordinates on surface of revolution
M	Mach number
N	number of blades

n	unit vector normal to stream surface
P	cascade spacing (pitch)
p	pressure
q	any fluid quantity
q̇	heat transfer to fluid per unit mass per unit time
R	gas constant
r	radius vector
r,θ,z	absolute cylindrical coordinates
r,φ,z	relative cylindrical coordinates
S₁	relative stream surface passing through fluid particles lying on a circular arc upstream of or midway in blade row
S₂	relative stream surface passing through fluid particles lying on a radial or curved line upstream of or midway in blade row
s	entropy per unit mass of fluid
T	absolute temperature
t	time or circumferential thickness of blade
U	blade velocity at radius <i>r</i>
u	$du = c_v dT$
u_i,uⁱ	unit base vector and reciprocal vector
V	absolute velocity of fluid
V_{θr}	angular momentum of fluid about axis of rotation
W	relative velocity of fluid
W¹	physical component of relative velocity tangent to x^i
ẇ	work done by fluid element per unit mass per unit time
w^j	contravariant component of W

w_j	covariant component of W
x^i	general curvilinear coordinates ($i = 1,2,3$)
z	distance along turbomachine axis
β	angle between W and its meridional component
γ	ratio of specific heats
θ_{ij}	angle included by the coordinate lines x^i and x^j
μ	coefficient of viscosity, coefficient of artificial viscosity, or Mach angle
Ξ	absolute vorticity, $\nabla \times V$
π'	viscous stress tensor
ρ	fluid density
$\tilde{\rho}$	artificial density
σ	angle between z and $t = \tan^{-1}(dr/dz)$
τ	normal, circumferential, or radial thickness of stream filament
Φ	dissipation function
Ψ	stream function
ω	angular speed of blade
$\partial/\partial x^i$	partial differentiation of a flow variable on stream surface with respect to coordinate x^i

Subscripts:

c	casing
e	exit station
h	hub
i	inlet
t	meridional component
L.E.	leading edge

m mean (midchannel)
n component in the direction normal to hub or casing
p pressure surface of blade
r,φ,z radial, circumferential, and axial component
s suction surface of blade
T.E. trailing edge

Superscripts:

° stagnation state
* dimensionless quantity

CHAPTER 1

INTRODUCTION

As a result of studying the effect of the radial equilibrium condition on the radial flow field in the axial-flow turbomachine (refs. 1 and 2), a general theory of three-dimensional flow in turbomachines (ref. 3) was proposed in 1950. It was intended for solving the three-dimensional flow in a turbomachine

- (1) Having arbitrary hub and casing shapes—the theory applicable to axial-flow, radial-flow, and mixed-flow turbomachines
- (2) With a finite number of blades which have finite thickness and arbitrary shape
- (3) With fluid moving through it at a high speed—the speed of flow being purely subsonic or supersonic

The fluid flow through the stator and rotor blade row was assumed to be steady with respect to the stationary blades and rotating blades, respectively. It was proposed to obtain steady flow relative to the blades by an iterative solution between two families of relative stream surfaces. The families were the S_1 family and the S_2 family. The problem of determining the flow field with three independent variables was reduced to a number of flow fields having only two independent variables. Thus, the purely subsonic or purely supersonic flow along an S_1 or S_2 relative stream surface could be accurately solved by the mathematical techniques available at that time. The relaxation or direct matrix method was used for the subsonic flow, and the method of characteristics was used for supersonic flows. References 4 to 10 contain the solutions obtained by these methods and the approximate solutions obtained by series expansion in the circumferential direction from a mean streamline on the S_1 stream surface in axial flow

turbomachines and centrifugal compressors. Almost all of these calculations were obtained by mechanical, digital computers. This was a laborious endeavor and consumed a great deal of time, but provided insight into the characteristics of three-dimensional compressible flow in turbomachines. Those insights were useful to the development of the three-dimensional flow in turbomachine theory.

The flow computations reported in references 10 and 11 are probably the first two turbomachine calculations ever performed on large-scale, high-speed, electronic digital computers. Reference 10 includes calculations along the mid-channel S_2 relative stream surface for high subsonic flow. Reference 8 contains computations along the mid-span S_1 relative stream surface for incompressible flow at design and off-design inlet angles. The number of interior grid points for the two problems was 400 and 200, respectively. The fourth degree differential formula was used. It took approximately 60 hr on an IBM CPEC computer to factorize the coefficient matrix into lower and upper triangular matrices for the turbine problem. The compressor problem was also factorized in 60 hr on an IBM 604 computer. The gas turbine problem was also solved on an UNIVAC computer later and took a relatively shorter period of time—11 min for factorization and 2.5 min for each cycle of stream function calculation.

With the advent of the faster, modern digital computers, solutions for the subsonic flow along the S_1 and S_2 stream surfaces were obtained by many turbomachine investigators (refs. 12 to 26). Solutions obtained on IBM 360, 370, KDF9, and Facom 230-26 took about 0.5 to 35 min. In addition to the S_1 and S_2 stream surface flow solutions, quasi- (refs. 22 to 25) and full-three-dimensional flows (ref. 25) were obtained on IBM, Facon, and CDC 7600 in about 2 to 16 min (refs. 22 to 25). The S_1 surfaces were assumed to be surfaces of revolution in calculating the quasi-three-dimensional flow.

Along with the development of high speed digital computers, the development of mathematical calculation techniques continued. One major development of the latter was avoiding the inconvenience

and inaccuracy caused by unequal grid spacing near an arbitrarily shaped boundary surface, which exists in all practical applications. One approach used more accurate, high-order differentiation at such points (ref. 27). A second approach used body-fitted finite elements to discretize the differential equations (refs. 19, 20 and 25). A third approach used the body-fitted, nonorthogonal, curvilinear coordinate system (refs. 28 to 33). A second major development in mathematical techniques was the solution of transonic turbomachine flow using the time-marching method (refs. 34 to 36), separate-region calculation and shock fitting (refs. 37 to 39), and artificial compressibility (refs. 40 to 42).

This report is a slightly expanded version of a series of lectures given at NASA Lewis and at Cincinnati University during the spring of 1990.

Chapter 2 briefly reviews the fundamental aerothermodynamic equations governing three-dimensional flow in turbomachines. The equations, in the beginning, are for the most general case of unsteady flow of a viscous fluid relative to a rotating blade. The two independent thermodynamic properties selected were entropy and relative stagnation rothalpy of the fluid. The latter is a thermodynamic property introduced especially for calculating three-dimensional flow in the rotating blade row. The implication of assuming steady absolute flow in the stator and the steady relative flow in the rotor at the same time is also discussed. After a discussion on the effect of viscosity in the governing equations, a practical method for considering the viscous effect on the flow field is given.

Chapter 3 presents the basic idea of expressing flow variables on a general stream surface in terms of two independent variables, i.e., the two coordinates. This chapter continues conservation of mass in a fluid element. In such a case, the governing equations naturally contain a stream filament thickness term, a general function of the two coordinates. The flow along the stream filament is obtained by

solving the principal equation with the stream function as the single dependent variable. Procedures for solving direct (analysis) and inverse (design) problems are described.

To have high accuracy in the finite-difference approximation at grid points near a curved boundary wall and to satisfy the boundary condition at the curved wall accurately, the body fitted, general, nonorthogonal, curvilinear coordinate system is used for both S_1 and S_2 stream filaments. By using tensor calculus—the continuity equation, the vorticity equation, the dynamic equation, the energy equation, and the principal equation are easily expressed in terms of the general, nonorthogonal, curvilinear coordinates and corresponding nonorthogonal velocity components. These equations and methods of solution for flow along S_1 and S_2 stream filaments are given in Chapter 4.

The first part of Chapter 5 presents a simple, approximate solution for subsonic flow along the S_1 stream filament of revolution by circumferentially extending the known solution on the mid-channel streamline. Also in this chapter a simple, approximate three-dimensional solution is obtained by circumferentially extending the known values on the mid-channel stream surface. The second part of this chapter presents results obtained in subsonic S_1 solutions employing H type and C type nonorthogonal, curvilinear coordinates. The third part describes procedures for quasi-three-dimensional blade design and full-three-dimensional analysis of given blades. A comparison of the calculated three-dimensional flow field and measured data is also included.

Chapter 6 describes several relatively quick methods for calculating the transonic flow along S_1 and S_2 relative stream filaments. The method of separate-region calculation with shock-fitting, elliptic solution of the stream-function principal equation, to which artificial viscosity is introduced in the density term to stabilize the transonic calculation for both the S_1 and S_2 stream filament, and the elliptic

algorithm for the inverse solution of S_2 flow ($V_{\theta r}$ prescribed), which is modified for obtaining a sharp shock discontinuity, are presented. The calculated results are compared with experimental data.

Applying the quick solution methods described in Chapter 6, the quasi-three- and full-three-dimensional transonic flow solutions in two compressor rotors were obtained and are presented in Chapter 7. The solutions are presented with emphasis on the convergence process and the geometry of individual S_1 and S_2 stream filaments obtained in the three-dimensional solution. These solutions are also compared to experimental data and are included in Chapter 7.

Based on the analytical solutions of three-dimensional subsonic and transonic flows and their respective experimental data, practical methods for three-dimensional turbomachine blade design and blade element test data correction emerged and are proposed in Chapters 6 and 7.

CHAPTER 2

FUNDAMENTAL AEROTHERMODYNAMIC EQUATIONS GOVERNING THE THREE-DIMENSIONAL FLOW IN TURBOMACHINES

2.1 Basic Aerothermodynamic Equations Governing the Three-Dimensional Flow of a Viscous Fluid Through a Stationary Blade Row

The general basic aerothermodynamic equations governing the flow of a viscous fluid through a stationary blade row which were formulated in reference 1 in connection with the calculation of a radial-equilibrium condition for the design of turbomachine blades are as follows:

Continuity Equation: From the principle of conservation of matter, the equation of continuity is

$$\frac{\partial \rho}{\partial t} + \nabla \cdot (\rho \mathbf{V}) = 0 \quad (2.1)$$

or

$$\nabla \cdot \mathbf{V} + \frac{D \ln \rho}{Dt} = 0 \quad (2.1a)$$

Dynamic Equation: Newton's second law of motion is expressed for viscous fluid by the Navier-Stoke's equation.

$$\rho \frac{D\mathbf{V}}{Dt} = -\nabla p + \mu \left[\nabla^2 \mathbf{V} + \frac{1}{3} \nabla (\nabla \cdot \mathbf{V}) + \dots \right] \quad (2.2)$$

where ... represents high order terms due to viscosity change with temperature.

Energy Equation: From the first law of thermodynamics, one form of the energy equation is

$$\frac{Du}{Dt} + \rho \frac{D(1/\rho)}{Dt} = \dot{q} + \frac{\Phi}{\rho} \quad (2.3)$$

in which

$$du = c_v dT \quad (2.4)$$

$$\dot{q} = \frac{1}{\rho} \nabla \cdot (k \nabla T) \quad (2.5)$$

and

$$\Phi = \mu \left\{ 2 \nabla \cdot (\mathbf{V} \cdot \nabla) \mathbf{V} + (\nabla \times \mathbf{V})^2 - 2(\mathbf{V} \cdot \nabla)(\nabla \cdot \mathbf{V}) - \frac{2}{3}(\nabla \cdot \mathbf{V})^2 \right\} \quad (2.6)$$

For turbomachine calculations it is convenient to take specific stagnation enthalpy H and specific entropy s as the two independent thermodynamic properties defining the thermodynamic state of the gas. They are related to other thermodynamic properties and velocity by

$$H \equiv h + \frac{1}{2} V^2 = (u + p/\rho) + \frac{1}{2} V^2 \quad (2.7)$$

and

$$T ds = du + p d(1/\rho) \quad (2.8)$$

By the use of equations (2.2), (2.7), and (2.8) the following forms of dynamic equation and energy equation were obtained (ref. 1):

$$\frac{\partial \mathbf{V}}{\partial t} - \mathbf{V} \times (\nabla \times \mathbf{V}) = -\nabla H + T\nabla s + \frac{\mu}{\rho} \left[\nabla^2 \mathbf{V} + \frac{1}{3} \nabla(\nabla \cdot \mathbf{V}) + \dots \right] \quad (2.2a)$$

and

$$\frac{DH}{Dt} = \dot{q} + \frac{1}{\rho} \frac{\partial p}{\partial t} + \frac{\Phi}{\rho} + \mathbf{V} \cdot \left[\frac{\mu}{\rho} \left(\nabla^2 \mathbf{V} + \frac{1}{3} \nabla(\nabla \cdot \mathbf{V}) \right) + \dots \right] \quad (2.3a)$$

In the case of steady invicid flow, equation (2.2a) becomes

$$\mathbf{V} \times (\nabla \times \mathbf{V}) = \nabla H - T\nabla s \quad (2.2b)$$

which is the Coroco equation originally deduced for the investigation of flow with shock and vorticity.

The second law of thermodynamics states

$$T \frac{Ds}{Dt} \geq \dot{q} \quad (2.9)$$

Combining equation (2.8) with the first law of thermodynamics, equation (2.3), yields

$$T \frac{Ds}{Dt} = \dot{q} + \frac{\Phi}{\rho} \quad (2.10)$$

which conforms with the second law of thermodynamics, equation (2.9).

From the preceding general, basic equations the following can be noticed:

(1) In the stationary frame of reference the flow unsteadiness is represented by the partial derivative, with respect to time, of density in the continuity equation, of velocity in the dynamic equation, and of pressure in the energy equation.

(2) Stagnation enthalpy is, in general, affected by the viscosity of the fluid through the last two terms on the right side of equation (2.3a). If the last term on the right side of equation (2.1a), the viscous force per unit mass of fluid, is denoted by F_v , then the two viscous terms in equation (2.3a) are Φ/ρ and $V \cdot F_v$. Thus the effect of viscosity on the stagnation enthalpy is not represented by $V \cdot F_v$ alone.

2.2 Effect of Viscosity on Basic Equations

In order to more clearly see the effects of viscosity on the changes in stagnation enthalpy and entropy, the dynamic equation (2.2a), the energy equation (2.3a), and the entropy equation (2.10) are further examined using the stress tensor π (ref. 43).

Newton's Second Law of Motion

Let the resultant stress (force per unit area) acting on the surfaces of an infinitesimally small fluid element be denoted by π (fig. 2.1) where π is related to the hydraulic pressure p , uniform in all directions, and a viscous stress π' by the following equation:

$$\pi = \begin{bmatrix} \sigma_x & \tau_{xy} & \tau_{xz} \\ \tau_{yx} & \sigma_y & \tau_{yz} \\ \tau_{zx} & \tau_{zy} & \sigma_z \end{bmatrix} = \begin{bmatrix} \sigma'_x & \tau_{xy} & \tau_{xz} \\ \tau_{yx} & \sigma'_y & \tau_{yz} \\ \tau_{zx} & \tau_{zy} & \sigma'_z \end{bmatrix} + \begin{bmatrix} -p & 0 & 0 \\ 0 & -p & 0 \\ 0 & 0 & -p \end{bmatrix} \quad (2.11)$$

or

$$\pi_{ij} = -p \delta_{ij} + \pi'_{ij} \quad (2.12)$$

where

$$\delta_{ij} = \begin{cases} 1, & i = j \\ 0, & i \neq j \end{cases}$$

The vector and tensor form of Newton's second law of motion are, respectively

$$\frac{DV}{Dt} = -\frac{1}{\rho} \nabla p + \frac{1}{\rho} \nabla \cdot \pi' \quad (2.13a)$$

and

$$\frac{DV_i}{Dt} = \frac{\partial V_i}{\partial t} + V_j \frac{\partial V_i}{\partial x_j} = -\frac{1}{\rho} \frac{\partial p}{\partial x_i} + \frac{1}{\rho} \frac{\partial \pi'_{ij}}{\partial x_j} \quad (2.13b)$$

where Einstein's summation convention is used.

By using equations (2.1), (2.2), and (2.3), Newton's second law of motion can also be put into the following form:

$$\frac{\partial \mathbf{V}}{\partial t} - \mathbf{V} \times (\nabla \times \mathbf{V}) = -\nabla H + \mathbf{T} \times \nabla \mathbf{s} + \frac{1}{\rho} \nabla \cdot \boldsymbol{\pi}' \quad (2.14)$$

First Law of Thermodynamics

The first law of thermodynamics is, in general, expressed by

$$\frac{De}{Dt} = \dot{q} - \dot{w} \quad (2.15)$$

The time rate of work done by the force acting on the fluid element surface, per unit mass of fluid, as seen by a stationary observer is

$$\dot{w} = \frac{1}{\rho} \frac{\partial(\pi_{ij} V_j)}{\partial x_i} = -\frac{1}{\rho} \frac{\partial(p V_i)}{\partial x_i} + \frac{1}{\rho} \frac{\partial(\pi'_{ij} V_j)}{\partial x_i} \quad (2.16a)$$

or

$$\dot{w} = \frac{1}{\rho} \nabla \cdot (\boldsymbol{\pi} \cdot \mathbf{V}) = -\frac{1}{\rho} \nabla \cdot (p \mathbf{V}) + \frac{1}{\rho} \nabla \cdot (\boldsymbol{\pi}' \cdot \mathbf{V}) \quad (2.16b)$$

where

$$\boldsymbol{\pi}' \cdot \mathbf{V} = \pi'_{ij} V_j \quad (2.17)$$

The first term on the right side of equation (2.16b) can be written as

$$\frac{1}{\rho} \nabla \cdot (p \mathbf{V}) = \frac{1}{\rho} (\mathbf{V} \cdot \nabla p + p \nabla \cdot \mathbf{V}) = \frac{1}{\rho} \left(\frac{Dp}{Dt} - \frac{\partial p}{\partial t} \right) + \frac{p}{\rho} \nabla \cdot \mathbf{V}$$

Substituting the continuity equation (2.1a) into the preceding equation results in

$$\frac{1}{\rho} \nabla \cdot (p\mathbf{V}) = \frac{1}{\rho} \left(\frac{Dp}{Dt} - \frac{\partial p}{\partial t} \right) - \frac{p}{\rho} \frac{1}{\rho} \frac{D\rho}{Dt} = \frac{D(p/\rho)}{Dt} - \frac{1}{\rho} \frac{\partial p}{\partial t}$$

Substituting the preceding equation into equation (2.16b) results in

$$\dot{w} = \frac{D(p/\rho)}{Dt} - \frac{1}{\rho} \frac{\partial p}{\partial t} + \frac{1}{\rho} \nabla \cdot (\pi' \cdot \mathbf{V}) \quad (2.18)$$

To this observer the time rate of increase of internal energy is

$$\frac{De}{Dt} = \frac{D}{Dt} \left(u + \frac{V^2}{2} \right) \quad (2.19)$$

Substituting equations (2.18) and (2.19) into equation (2.15) yields

$$\frac{DH}{Dt} = \frac{1}{\rho} \frac{\partial p}{\partial t} + \dot{q} + \frac{1}{\rho} \nabla \cdot (\pi' \cdot \mathbf{V}) \quad (2.20)$$

The energy equation (2.20) can be put into a slightly different form by expanding the last term on the right side of the equation as follows:

$$\frac{1}{\rho} \frac{\partial (\pi'_{ij} V_j)}{\partial x_i} = \frac{1}{\rho} \left[\pi'_{ij} \frac{\partial V_j}{\partial x_i} + V_j \frac{\partial \pi'_{ij}}{\partial x_i} \right] \quad (2.21)$$

But

$$\pi'_{ij} \frac{\partial V}{\partial x_i} = \Phi \quad (2.22a)$$

and

$$\frac{1}{\rho} \frac{\partial \pi'_{ij}}{\partial x_i} = F_f \quad (2.22b)$$

Therefore, the energy equation (2.20) can be written as

$$\frac{DH}{Dt} = \frac{1}{\rho} \frac{\partial p}{\partial t} + \dot{q} + \frac{\Phi}{\rho} + \mathbf{F}_f \cdot \mathbf{V} \quad (2.23)$$

which is the same as equation (2.39).

The energy equation (2.20) can also be transformed to the form of equation (2.3) as follows by multiplying terms on the left side of equation (2.13b) by V_i :

$$\rho \frac{D}{Dt} \frac{V^2}{2} = V_i \frac{\partial p}{\partial x_i} - V_i \frac{\partial \pi'_{ij}}{\partial x_j} \quad (2.24)$$

Using equations (2.21), (2.22a), and the continuity equation (2.1a), equation (2.14) is transformed into the following equation:

$$\dot{w} = \left[p \frac{D(1/\rho)}{Dt} - \frac{\Phi}{\rho} \right] - \frac{D}{Dt} \frac{V^2}{2} \quad (2.25)$$

Substituting equations (2.25) and (2.19) into the first law of thermodynamics, equation (2.14) results in

$$\frac{Du}{Dt} + \rho \frac{D(1/\rho)}{Dt} = \dot{q} + \frac{\Phi}{\rho}$$

which is identical to equation (2.3).

The physical meaning of this form of the energy equation can best be seen by deriving the equation from the point of view of an observer moving with the fluid element. To this observer the time rate of the increase of its internal energy is

$$\frac{De}{Dt} = \frac{Du}{Dt} \tag{2.26}$$

and the rate of doing work against the surroundings by unit mass of the fluid element per unit time is

$$\dot{w}_\xi = -\frac{1}{\rho} \pi_{ij} \frac{\partial v_i}{\partial \xi_j} = \frac{1}{\rho} \left(p \frac{\partial v_i}{\partial \xi_j} - \pi'_{ij} \frac{\partial v_i}{\partial \xi_j} \right) = p \frac{D(1/\rho)}{Dt} - \frac{\Phi}{\rho} \tag{2.27}$$

In equation (27) \dot{w}_ξ is the rate of work done by unit mass of fluid element as seen by an observer moving with the fluid element and ξ_i are the coordinates moving with the fluid element.

Substituting equations (2.26) and (2.27) into equation (2.15) yields

$$\frac{Du}{Dt} = \dot{q} - \left[p \frac{D(1/\rho)}{Dt} - \frac{\Phi}{\rho} \right] \quad (2.28)$$

Equation (2.28) is exactly the same as equation (2.21) which is obtained by modifying the energy equation (2.26) obtained from the point of view of a stationary observer with the use of Newton's second law of motion (eq. (2.13)).

It is important to notice the following:

(1) To a stationary observer, the rate of work done by unit mass of fluid against viscous forces and the rate of increase of internal energy are, respectively,

$$-\frac{1}{\rho} \nabla \cdot (\pi' \cdot \mathbf{V}) \quad \text{and} \quad \frac{D(u + V^2/2)}{Dt} \quad (2.29)$$

These two terms appear in the corresponding energy equation (2.20).

(2) To an observer moving with the fluid, the rate of work done by the unit mass of fluid against viscous forces and the rate of increase of internal energy are, respectively,

$$\frac{\Phi}{\rho} \quad \text{and} \quad \frac{Du}{Dt}$$

These two terms appear in the corresponding energy equation (2.28).

In the derivation of the energy equation from the first law of thermodynamics, the expression for work done by the fluid element against its surroundings and the increase in the internal energy of the fluid element must be written for the same observer, either stationary or moving with the fluid. If one is written for the stationary observer and the other is written for the observer moving with the fluid, the resulting equation is erroneous. Unfortunately this kind of mixup has appeared in some publications.

Two-Dimensional Laminar Boundary Layer Flow In order to clearly see the effects of fluid viscosity and heat transfer on the energy equation and entropy equation, the following general analysis of steady laminar boundary layer flow is made. The velocity and temperature distributions in the boundary layer and an infinitesimally small element whose width and height are δx and δy are shown in figure 2.2. The x and y coordinates are chosen, respectively, to lie along and perpendicular to the tangent of the blade surface. The approximate relation commonly used to treat boundary layer problems is employed in the analysis. Fluid pressure may have a gradient in the x direction.

(1) To a stationary observer, the time rate of work done by the fluid, per unit mass, is

$$\begin{aligned} \dot{w} &= \frac{1}{\rho} \left[\frac{\partial}{\partial x} (p V_x - r V_y) + \frac{\partial}{\partial y} (-r V_x + p V_y) \right] \\ &= \frac{1}{\rho} \left[\nabla \cdot (p \mathbf{V}) - \nabla \cdot (\boldsymbol{\pi}' \cdot \mathbf{V}) \right] \end{aligned} \quad (2.30)$$

and after employing the continuity equation

$$\dot{w} = \frac{D(p/\rho)}{Dt} - \frac{1}{\rho} \nabla \cdot (\boldsymbol{\pi}' \cdot \mathbf{V}) \quad (2.30a)$$

The time rate of heat transfer to the fluid element, per unit mass, is

$$\dot{q} = \frac{1}{\rho} \nabla \cdot \frac{\partial}{\partial y} \left(k \frac{\partial T}{\partial y} \right) \quad (2.31)$$

Substituting equations (2.30a) and (2.31) into the first law of thermodynamics equation (2.15), the following is obtained:

$$\frac{1}{\rho} \frac{\partial}{\partial y} \left(k \frac{\partial T}{\partial y} \right) - \left\{ \frac{D(p/\rho)}{Dt} - \frac{1}{\rho} \left[\frac{\partial(\tau V_y)}{\partial x} + \frac{\partial(\tau V_x)}{\partial y} \right] \right\} = \frac{D}{Dt} \left(u + \frac{V^2}{2} \right) \quad (2.32)$$

Rearranging terms gives

$$\frac{DH}{Dt} \simeq \frac{1}{\rho} \left[\frac{\partial}{\partial y} \left(\frac{k}{C_p} \frac{\partial h}{\partial y} \right) + \frac{\partial(\tau V_y)}{\partial x} + \frac{\partial(\tau V_x)}{\partial y} \right] \quad (2.33)$$

In equation (2.33), $\frac{\partial(\tau V_y)}{\partial x}$ is much smaller than $\frac{\partial(\tau V_x)}{\partial y}$ and can be neglected. Equation (2.33) then becomes

$$\frac{dH}{dt} \simeq \frac{1}{\rho} \left[\frac{\partial}{\partial y} \left(\frac{k}{C_p} \frac{\partial h}{\partial y} \right) + \frac{\partial}{\partial y} \left(\mu V_x \frac{\partial V_x}{\partial y} \right) \right] \quad (2.34)$$

If $\mu = \text{constant}$, $Pr = 1$, and the difference between V and V_x is neglected, then equation (2.34)

becomes

$$\frac{dH}{dt} \approx \frac{\mu}{\rho} \left(\frac{\partial^2 h}{\partial y^2} + \frac{\partial^2}{\partial y^2} \frac{V_x^2}{2} \right) \approx \frac{\mu}{\rho} \frac{\partial^2 H}{\partial y^2} \quad (2.35)$$

$H = \text{constant}$ everywhere in the boundary layer is a particularly useful solution to the above equation. In this case, the wall temperature T_w equals the fluid stagnation temperature T_o . When c_p of the gas is a constant,

$$T_o = T + \frac{V^2}{2c_p} = \text{constant} \quad (2.36)$$

Differentiating equation (2.36) results in

$$\frac{\partial T}{\partial y} = - \frac{V}{c_p} \frac{\partial V}{\partial y} \quad (2.37)$$

It can be seen from equations (2.37) and (2.31) that

(a) at the lower boundary of the boundary layer, $V = 0$ and $\partial V / \partial y > 0$, therefore, $\tau > 0$ and

$$\partial T / \partial y = \dot{q} = 0;$$

(b) at the upper boundary of the boundary layer, $V = V_1$ and $\partial V / \partial y = 0$, therefore, $\tau = 0$ and

$$\partial T / \partial y = \dot{q} = 0;$$

(c) between these two boundaries, $\partial W / \partial y > 0$, $\tau > 0$, $\partial T / \partial y < 0$, and therefore, heat transfer is in the y direction.

Since $H = \text{constant}$, equation (2.34) indicates that, under the present approximation, the amount of heat transferred into (or out of) the fluid element is equal to the work done by the fluid element on the surrounding (or by the external viscous shear stress on the fluid element), i.e.,

$$\frac{\partial}{\partial y} \left(k \frac{\partial T}{\partial y} \right) = - \frac{\partial}{\partial y} (\tau V_x) = - \left(\tau \frac{\partial V_x}{\partial y} \right) - \left(V_x \frac{\partial \tau}{\partial y} \right) \quad (2.38)$$

Of the two terms on the right side of equation (2.38) the first one is always negative and the second one is always positive.

2. To an observer moving with the fluid the time rate of work done by the fluid element, per unit mass, on its surrounding is

$$\dot{w} = p \frac{D(1/\rho)}{Dt} - \frac{\tau}{\rho} \left(\frac{\partial W_\xi}{\partial \eta} + \frac{\partial W_\eta}{\partial \xi} \right) \simeq p \frac{D(1/\rho)}{Dt} - \frac{\tau}{\rho} \frac{\partial V_x}{\partial y} \quad (2.39)$$

where ξ and η are coordinates moving with the fluid, with the velocity W . Since $\partial W_\eta / \partial \xi \ll \partial W_\xi / \partial \eta$

$$\Phi = \tau \left(\frac{\partial W_\xi}{\partial \eta} + \frac{\partial W_\eta}{\partial \xi} \right) \simeq \tau \frac{\partial V_x}{\partial y} \simeq \mu \left(\frac{\partial V_x}{\partial y} \right)^2 > 0 \quad (2.40)$$

Substituting equations (2.39) and (2.32) into the first law of thermodynamics, the following is obtained:

$$\frac{Du}{Dt} = \frac{1}{\rho} \frac{\partial}{\partial y} \left(k \frac{\partial T}{\partial y} \right) - \left(p \frac{D(1/\rho)}{Dt} - \tau \frac{\partial V_x}{\partial y} \right) \quad (2.41)$$

Substituting equation (2.41) into the entropy equation (2.61) results in

$$T \frac{Ds}{Dt} = \frac{1}{\rho} \left[\frac{\partial}{\partial y} \left(k \frac{\partial T}{\partial y} \right) + \tau \frac{\partial V_x}{\partial y} \right] \quad (2.42)$$

The preceding two equations give, respectively, rate of increase of internal energy and entropy in the fluid element due to the work done on the fluid element by viscous force acting on the fluid element.

In the particular solution above, substituting equation (2.38) into equations (2.41) and (2.42) results in the following equations, respectively:

$$\frac{Du}{Dt} = - \frac{1}{\rho} V_x \frac{\partial \tau}{\partial y} - p \frac{D(1/\rho)}{Dt} = \frac{\mu}{\rho} \frac{\partial^2}{\partial y^2} \frac{V_x^2}{2} - p \frac{D(1/\rho)}{Dt} \quad (2.43)$$

and

$$T \frac{Ds}{Dt} = - \frac{1}{\rho} V_x \frac{\partial \tau}{\partial y} = - \frac{\mu}{\rho} \frac{\partial^2}{\partial y^2} \frac{V_x^2}{2} \quad (2.44)$$

The first term on the right side of these two equations is always positive because $\partial \tau / \partial y$ is always negative.

In this example it is quite clear that

(a) the rate of work done by the viscous forces on the fluid element, per unit mass, seen by a stationary observer at rest is $1/\rho \partial(\tau V_x)/\partial y = 1/\rho (\tau \partial V_x/\partial y + V_x \partial \tau/\partial y)$, where the first term is always positive and the second term is always negative.

In the particular solution above, because the work done by the fluid element and heat transfer to the fluid element just cancel each other, the stagnation enthalpy remains constant along the relative streamline.

(b) The rate of work done on unit mass of fluid by the viscous force seen by an observer moving with the gas is $\tau(1/\rho) \partial V_x/\partial y$, which is always greater than zero.

In the particular solution above, $(\dot{q} - \dot{w}) = -\frac{1}{\rho} V_x \frac{\partial \tau}{\partial y} - \frac{p D(1/\rho)}{Dt}$, in which the first term is always greater than zero, thereby causing Du/Dt and Ds/Dt always to be greater than zero.

It is quite obvious that the work done by the fluid element seen by a stationary observer and by an observer moving with the fluid element are not the same. In writing out the energy equation, they should be used with the increase in internal energy of the fluid element seen by the same observer.

2.3 Basic Aerothermodynamic Equations Governing the Three-Dimensional Flow of a Viscous Fluid Through a Rotating Blade Row

General basic aerothermodynamic equations governing the fluid flow through a blade row rotating at a constant angular velocity were formulated in reference 3 for a nonviscous fluid, in which the entropy s and a new thermodynamic property I , first called "modified total enthalpy" and later named "relative stagnation rothalpy" (ref. 44), were taken as the two independent thermodynamic properties defining the thermodynamic state of the gas. Later this formulation was extended to viscous gases in reference 43.

Continuity Equation: From the principle of conservation of matter, the equation of continuity is

$$\frac{\partial \rho}{\partial t} + \nabla \cdot (\rho \mathbf{W}) = 0 \quad (2.45)$$

or

$$\nabla \cdot \mathbf{W} + \frac{D \ln \rho}{Dt} = 0 \quad (2.45a)$$

Dynamic Equation: For a blade rotating at a constant angular velocity ω about the z axis, Newton's second law of motion is

$$\frac{D\mathbf{W}}{Dt} = \omega^2 \mathbf{r} + 2 \boldsymbol{\omega} \times \mathbf{W} = -\frac{1}{\rho} \nabla p + \frac{1}{\rho} \nabla \cdot \boldsymbol{\pi}' \quad (2.46)$$

Where $\boldsymbol{\pi}'$ is the viscous stress tensor acting on a fluid element.

The relative acceleration in equation (2.46) can be written as

$$\frac{D\mathbf{W}}{Dt} = \frac{\partial \mathbf{W}}{\partial t} + (\mathbf{W} \cdot \nabla) \mathbf{W} = \frac{\partial \mathbf{W}}{\partial t} + \frac{1}{2} \nabla W^2 - \mathbf{W} \times (\nabla \times \mathbf{W}) \quad (2.47)$$

Rothalpy and relative stagnation rothalpy are defined, respectively, by (ref. 44)

$$i \equiv h - \frac{(\omega r)^2}{2} \quad (2.48)$$

$$I \equiv i + \frac{W^2}{2} = h - \frac{(\omega r)^2}{2} + \frac{W^2}{2} \quad (2.49)$$

By using equations (2.4), (2.8), and (2.49) the following form of Newton's second law of motion is obtained:

$$\frac{\partial W}{\partial t} - W \times (\nabla \times V) = -\nabla I + T \nabla s - \frac{1}{\rho} \nabla \pi' \quad (2.50)$$

Energy Equation: The energy equation for fluid flow passing through a rotating blade can be obtained from the first law of thermodynamics in the same manner as in the case of fluid flow passing through a stationary blade row. First, from a stationary observer's point of view, the rate of work done by the fluid element, per unit mass, against its surrounding is

$$\begin{aligned} \dot{w} &= -\Sigma F \cdot V = -\Sigma F \cdot (W + U) \\ &= -\frac{1}{\rho} \nabla \cdot (\pi \cdot W) - \Sigma F_{\phi} \omega r \\ &= \frac{1}{\rho} \nabla \cdot (pW) - \frac{1}{\rho} \nabla \cdot (\pi' \cdot W) - \omega \frac{D(V_{\phi r})}{Dt} \end{aligned} \quad (2.51)$$

where U is the blade speed ωr . To the same observer the rate of increase of the fluid element's internal energy per unit mass is

$$\frac{De}{Dt} = \frac{D}{Dt} \left(u + \frac{V^2}{2} \right) = \frac{D}{Dt} \left[u + \frac{W^2 + 2W_{\phi} \omega r + \omega^2 r^2}{2} \right] \quad (2.52)$$

Substituting equations (2.51) and (2.52) into equation (2.15) yields

$$\frac{DI}{Dt} = \frac{1}{\rho} \frac{\partial p}{\partial t} + \dot{q} + \frac{1}{\rho} \nabla \cdot (\pi' \cdot \mathbf{W}) \quad (2.53)$$

Just as in the case of fluid flow passing through a stationary blade row, the energy equation in the form of the preceding equation can be transformed into the form similar to equation (2.28). For instance the dot product of \mathbf{W} and equation (2.46) is

$$\rho \frac{D}{Dt} \frac{W^2}{2} = \mathbf{W} \cdot (\omega^2 \mathbf{r} - 2\omega \times \mathbf{W}) = W_i \frac{\partial p}{\partial x_i} - W_i \frac{\partial \pi'_{ij}}{\partial x_j} \quad (2.54)$$

The last term in the preceding equation can be written as

$$W_i \frac{\partial \pi'_{ij}}{\partial x_j} = \frac{\partial (\pi'_{ij} W_i)}{\partial x_j} - \pi'_{ij} \frac{\partial W_i}{\partial x_j} \quad (2.55)$$

and the dissipation function for the fluid element moving with respect to the rotating blade is

$$\phi' = \pi'_{ij} \frac{\partial W_i}{\partial x_j} \quad (2.56)$$

By using equations (2.55), (2.56), and the continuity equation (2.45); equation (2.51) can be transformed into the following equation:

$$\dot{w} = \left(p \frac{D(1/\rho)}{Dt} - \frac{\phi'}{\rho} \right) - \frac{D}{Dt} \frac{W^2 - \omega^2 r^2}{2} - \omega \frac{D(V_{\theta} r)}{Dt} \quad (2.57)$$

Substituting equation (2.57) and (2.52) into equation (2.14) yields the following form of the energy equation:

$$\frac{Du}{Dt} = \dot{q} - \left(p \frac{D(1/\rho)}{Dt} - \frac{\Phi'}{\rho} \right) \quad (2.58)$$

Again the physical meaning of this form of energy equation can be seen more clearly by deriving the equation from the point of view of an observer moving with the fluid element. To this observer the time rate of the increase in the internal energy is given by equation (2.26) and the time rate of work done by the fluid element against its surroundings is

$$\dot{w} = - \frac{1}{\rho} \pi_{ij} \frac{\partial W_i}{\partial \xi_j} = p \frac{D(1/\rho)}{Dt} - \frac{\Phi'}{\rho} \quad (2.59)$$

where ξ is the coordinate moving with the fluid.

Substituting equations (2.59) and (2.26) into equation (2.14) yields equation (2.58).

Entropy Equation: From the second law of thermodynamics,

$$T \frac{Ds}{Dt} \geq \dot{q} \quad (2.60)$$

substituting (2.58) into the entropy equation (2.8) the following is obtained:

$$T \frac{Ds}{Dt} = \dot{q} + \frac{\Phi'}{\rho} \quad (2.61)$$

Equations (2.53) and (2.61) are two important equations. They appear quite similar to equation (2.20) and (2.10), respectively, but the total derivative with respect to time now means following motion along the relative streamline, and the partial derivative with respect to time now refers to the derivative at a coordinate point relative to the rotating blade.

2.4 Steady Fluid Flow Through a Stationary Blade Row and Steady Relative Flow Through a Rotating Blade Row

Under steady operating conditions, fluid flow through a single stationary blade row is steady and the unsteady terms in the governing equations can be neglected. Similarly under steady operating conditions fluid flow through a single rotating blade row is steady and the unsteady terms in the governing equations can be neglected. However, even in a single-stage turbomachine, there is always a stationary blade row upstream (in the case of a turbine) or downstream (in the case of a compressor) of a rotating blade row. Usually they are spaced not too far apart and the fluid flow relative to either blade row is

unsteady. Because of the mathematical difficulty, in practically all of the design calculations and analysis calculations, fluid flow relative to either the stator or rotor, is assumed to be steady.

Steady absolute flow in stationary blade rows means that the unsteady terms in governing equations (2.1), (2.14), (2.20), and (2.28) at a fixed coordinate point, say $(r, \theta, z)_o$ are equal to zero.

In the case of fluid flow through a rotating blade row, steady relative flow means that all of the partial derivatives with respect to time in governing equations (2.45), (2.50), (2.53) and (2.61) at a fixed coordinate point, say $(r, \phi, z)_o$, with the origin of the coordinates fixed in the blade (i.e., $\phi = \theta - \omega t$), are equal to zero. Furthermore, since the absolute velocity V is related to the relative velocity W by

$$V = W + U \quad (2.62)$$

or

$$\left. \begin{aligned} V_r &= W_r \\ V_z &= W_z \\ V_\theta &= W_\phi + \omega r \end{aligned} \right\} \quad (2.63)$$

When the relative velocity at a relative coordinate point (r, ϕ, z) is steady, the absolute velocity at a relative point, $V_{r, \phi, z}$ is also steady with respect to the rotating blade, so is $\nabla \times V$.

Because the absolute flow is calculated for the stationary blade row, whereas the relative flow is calculated for the rotating blade row, there is an abrupt change in the tangential component of the fluid velocity, and consequently, in the streamline when the fluid motion is referred to the different coordinate

system moving from one blade row to the next (fig. 2.3). However, the projection of the streamlines on the meridional plane is continuous because the meridional components of the absolute and relative velocities are continuous (fig. 2.4).

In the following presentation, as well as in computer codes, only the governing equations for steady relative flow through the rotating blade row will be given. It is understood that when the blade row is stationary, $\omega = 0$, $\varphi \rightarrow \theta$, $W \rightarrow V$, $I \rightarrow H$, and $\Phi' \rightarrow \Phi$.

2.5 Viscous Terms in the Governing Equations

An analysis will now be made on the magnitude of the viscous terms in the governing equations.

Continuity Equation: For steady flow the continuity equation (2.45) becomes

$$\nabla \cdot (\rho \mathbf{W}) = 0 \quad (2.64)$$

Equation (2.64) does not contain a viscous term. The effect of viscosity on the fluid flow comes through the entropy increase in the flow in the following equation of fluid density:

$$\frac{\rho_b}{\rho_a} = \left[\frac{(I - W^2/2 + U^2/2)_b}{(I - W^2/2 + U^2/2)_a} \right]^{\frac{1}{\gamma-1}} e^{\frac{S_b - S_a}{R}} \quad (2.65)$$

The effect of entropy increase in density is quite large and consequently cannot be ignored.

Energy Equation: Of the two forms of energy equation (2.53) and (2.58), it is more convenient to use (2.53). For steady flow it becomes

$$\frac{DI}{Dt} = \dot{q} + \frac{1}{\rho} \nabla \cdot (\pi' \cdot \mathbf{W}) \quad (2.66)$$

In the core region the viscous stress and heat transfer are negligible. In the boundary layer region near the blade surfaces and hub and casing walls, if the boundary layer is laminar, the Pr number of the fluid is equal to unity, and the boundary walls are adiabatic walls, the viscous work term and heat transfer term cancel each other. In actual turbomachines the boundary layer flow is turbulent and the Pr number is different from 1, and the summation of these two terms will not be equal to zero, but the magnitude is expected to be small. The following equation is usually considered to be a good approximation for the entire flow region:

$$\frac{DI}{Dt} = 0 \quad (2.67)$$

Dynamic Equation: For steady flow equation (2.34) becomes

$$\mathbf{W} \times (\nabla \times \mathbf{V}) = \nabla I - T \nabla s + \frac{1}{\rho} \nabla \cdot \pi' \quad (2.68)$$

When I is taken to be constant on all streamlines, the magnitude of ∇I depends on the magnitude of ∇I at the inlet. ∇s is quite small in the core region, but quite large near the solid wall. For instance the radial entropy profile at the exit of a rotor blade row may look something like that shown in figure 2.5. From the dynamic equation in the radial direction.

When the viscous stresses are neglected, equation (2.68) is simplified to

$$\mathbf{W} \times (\nabla \times \mathbf{V}) = \nabla I - T \nabla s \quad (2.69)$$

Equation (2.69) in the radial direction is

$$W_z \frac{\partial W_z}{\partial r} \simeq - \frac{W_\varphi}{r} \frac{\partial (V_{\theta r})}{\partial r} + W_z \frac{\partial W_r}{\partial z} + \frac{\partial I}{\partial r} - T \frac{\partial s}{\partial r} \quad (2.70)$$

The effect of radial entropy gradient on the radial variation of velocity is indicated in figure 2.5.

The inclusion of entropy gradient in the dynamic equations is necessary for a better prediction of velocity variations near the solid wall.

Entropy Increase: Evaluation of entropic increase along the streamlines by equation (2.61) requires a solution of the complete set of governing equations for viscous fluid. At the present time approximate value of entropy increase along the streamlines may be estimated by an appropriate value of the polytropic exponent of a polytropic process which represents the actual flow process (ref. 1). It may also be estimated by the pressure recovery factor and the isentropic rotor efficiency obtained in experimental investigation and tests (ref. 47). For the flow through a stator blade row the entropy increase across the blade row is calculated from the recovery factor in stagnation pressure as follows:

$$s_c - s_b = R \frac{\gamma}{\gamma - 1} \ln \frac{1}{\sigma} \quad (2.71)$$

or

$$s_c - s_b = R \frac{\gamma}{\gamma - 1} \ln \frac{P_{b^{\circ}}}{P_{c^{\circ}}} \quad (2.71a)$$

For the flow passing a rotor blade row, the increase of entropy across the blade row is calculated from the isotropic rotor efficiency as follows:

$$s_b - s_a = R \frac{\gamma}{\gamma - 1} \ln \frac{T_{b^{\circ}}/T_{a^{\circ}}}{1 + \xi(T_{b^{\circ}}/T_{a^{\circ}} - 1)} \quad (2.72)$$

where

$$\xi = \eta_s \text{ for compressor rotor}$$

$$= 1/\eta_s \text{ for turbine rotor}$$

2.6 Some Remarks on the Energy Equation and the Entropy Equation

The First Law of Thermodynamics and the Second Law of Thermodynamics are two important physical laws governing the flow of a compressible viscous fluid in a turbomachine. The following remarks are made here regarding the energy equation and entropy equation derived from these two laws.

1. Energy equations in two different forms were described in Section 2.1 and 2.2 for flow through, a stationary blade row and a rotating blade row respectively. In one form of the energy equation, equation (2.28) or (2.58), the increase of internal energy of a fluid element along the streamline is given directly by the heat transfer from the surroundings to the fluid element minus the work done by the fluid element against its surroundings. The equation is the same as the one universally used in thermodynamic

calculations, except that there is an additional work done term by the fluid element against the external viscous force. In the other form of energy equation, equation (2.2) or (2.53), however, the increase of stagnation enthalpy or stagnation rothalpy is given by three terms, namely, the heat transfer to the fluid element, the work done by the fluid element against the viscous forces, and an unsteady pressure term. It should be noted here that the work done by the fluid element against external pressure is included in the first form of the energy equation, but not in the second form of the energy equation. (Equation (2.18) will help to explain this difference.)

2. It should be emphasized that the heat transfer term \dot{q} refers to the heat transferred to the fluid element from its surrounding fluid elements and that it is not equal to zero for the fluid element in the viscous region, even when the flow of the fluid as a whole is adiabatic, i.e., there is no heat transfer between the fluid and the bounding wall. For instance, in the preceding analysis of a two-dimensional boundary layer flow, it is seen that (i) there is a positive heat transfer into the fluid element in the boundary layer, and (ii) when the Prandtl number of the fluid is equal to one, this amount of heat transfer into the fluid element is equal to just the work done by the fluid element against the viscous forces acting on the fluid element, thereby keeping the stagnation enthalpy constant along the streamline. This is a very useful result, which provides a sound basis in taking stagnation enthalpy or stagnation rothalpy constant along the streamline in current engineering calculation for turbomachine flows. Because of this canceling effect, it should be kept in mind that when the viscous effect on the stagnation enthalpy is considered in the calculation, it is not correct to keep one viscous work term in equation (2.20) or equation (2.53), or two viscous work terms in equation (2.23) and to neglect the heat transfer term in these equations.

3. Entropy equation (2.10) or (2.61) clearly shows that the increase of entropy of the fluid element along the streamline is made of two parts, namely the heat transfer to the fluid element \dot{q} and the work done by the fluid element against the external viscous forces as seen by an observer moving with the fluid

element, the dissipation function Φ (see eq. (2.27)). Depending on the nature of problem, \dot{q} may be positive or negative (usually positive), but Φ is always positive.

4. The heat transfer term \dot{q} in the energy equation and entropy equation is heat transfer to the fluid element from its surroundings due to temperature difference. The viscous term in the energy equation and entropy equation is work done by the fluid element against the viscous force acting on the fluid element. They are independently evaluated according to their own definition, which is set up to the heat transfer term and work done term in the First Law of Thermodynamics (eq. (2.15)). In light of the preceding argument, it is easy to see that the frequently-appearing saying “work done by the frictional forces acting on the fluid element turns into frictional heat and is added to the fluid element,” $dH/dt = \mathbf{F}_f \cdot \mathbf{V}$, $T ds/dt = \mathbf{F}_f \cdot \mathbf{V}$ (for instance, eq. (3.19) on p. 51 of ref. 45 and equations in the middle of p. 277 of ref. 46) are incorrect.

CHAPTER 3

GOVERNING EQUATIONS FOR FLUID FLOW ALONG RELATIVE STREAM FILAMENTS

3.1 Following Fluid Flow on Relative Stream Surfaces

In order to solve the steady three-dimensional irrotational or rotational flow in a relatively simple manner, an approach was taken in reference 3 to obtain the three-dimensional solution by an appropriate combination of mathematically two-dimensional flows on two different kinds of relative stream surfaces (figs. 3.1 to 3.3). The first kind of relative stream surface is one whose intersection with a z -plane, either upstream of the blade row or somewhere in the blade row, forms a circular arc (fig. 3.1). The second kind of relative stream surface is one whose intersection with a z -plane, either upstream of the blade row or somewhere inside the blade row, forms a radial line (fig. 3.2). These two kinds of relative stream surfaces were designated as stream surface S_1 and S_2 , respectively.

STREAM SURFACE OF THE FIRST KIND— S_1

Shown in figure 3.1 is a stream surface of the first kind formed by fluid particles lying on a circular arc ab of radius oa upstream from the blade row. It is a generalization for three-dimensional flow from the cylindrical surfaced usually considered in the two-dimensional design of turbomachines.

STREAM SURFACE OF THE SECOND KIND— S_2

A stream surface of the second kind is shown in figure 3.2. The important surface of this family is the one that lies about midway between two adjacent blades, and divides the mass flow in the channel formed by the two blades into approximately two equal parts. This surface is designated as the mean

stream surface or mid-channel stream surface $S_{2,m}$. For blades with all radial elements, such as the one shown in figure 3.2, it is convenient to consider a mid-channel stream surface formed by fluid particles originally lying on a radial line ab upstream from the blade row. Otherwise the radial line is chosen about midway in the passage with the fluid particles originally starting out from a curved line upstream from the blade row as shown in figure 3.3.

In general, both of these two kinds of stream surfaces are employed in the solution of the three-dimensional problem flow field in turbomachines. The correct solution of one surface requires some data from the other, and consequently, successive solutions between the solution of one of these two surfaces are involved. Yet, the solution of flow on each surface is manageable with the efficient technique for mathematically two-dimensional problems.

Relations Among Relative Velocity of Fluid, Coordinates of Stream Surface, and Normal to Stream Surface

In general, the coordinates of the relative stream surfaces, the components of the unit normal n (figs. 3.1 and 3.2), and the velocity components are related by the following equations:

$$S(r, \varphi, z) = 0 \tag{3.1}$$

$$n_r dr + n_\phi d\phi + n_z dz = 0 \tag{3.2}$$

$$n_r W_r + n_\phi W_\phi + n_z dz = 0 \tag{3.3}$$

3.2 Equation Governing Fluid Flow Along S_2 Stream Surface of S_2 Stream Filament

Because S_2 stream surface involved in the three-dimensional flow calculation is always a general twisted surface, whereas the S_1 stream surface involved can be a surface of revolution, the S_2 stream surface will be considered first in the following treatment.

When the fluid motion on S_2 stream surface is followed, equations (3.1) and (3.2) are used to eliminate one of the three independent variables, the φ coordinate. That is, any quantity q on S_2 is now considered as

$$q = f [r, z, \varphi(r, z)] \quad (3.3a)$$

The change in the quantity q along S_2 due to a small change in r while z is held constant is (see fig. 3.4)

$$dq = \left(\frac{\partial q}{\partial r} + \frac{\partial q}{\partial \varphi} \frac{\partial \varphi}{\partial r} \right) dr \quad (3.4)$$

Substituting $\partial \varphi / \partial r$ from equation (3.2), for $dz = 0$, into the preceding equation gives

$$\frac{\partial q}{\partial r} = \frac{\partial q}{\partial r} - \frac{n_r}{n_\phi} \frac{1}{r} \frac{\partial q}{\partial \varphi} \quad (3.4a)$$

in which the bold partial derivative sign is used to indicate this differentiation following the stream surface.

Similarly,

$$\frac{\partial q}{\partial z} = \frac{\partial q}{\partial z} - \frac{n_z}{n_\phi} \frac{1}{r} \frac{\partial q}{\partial \phi} \quad (3.5)$$

Along streamline on S_2

$$\frac{Dq}{Dt} = W_r \frac{\partial q}{\partial r} + W_z \frac{\partial q}{\partial z} \quad (3.6)$$

Continuity Equation

When the fluid motion is followed along the S_2 stream surface and equation (3.4) and (3.5) are used, the continuity equation for steady relative motion becomes

$$\frac{1}{r} \frac{\partial(\rho W_r r)}{\partial r} + \frac{\partial(\rho W_z)}{\partial z} = \rho C(r, z) \quad (3.7)$$

where

$$C(r, z) = - \frac{1}{n_\phi r} + \left(n_r \frac{\partial W_r}{\partial \phi} + n_\phi \frac{\partial W_\phi}{\partial \phi} + n_z \frac{\partial W_z}{\partial \phi} \right) \quad (3.8)$$

This continuity equation is put into the following form:

$$\frac{\partial(rB\rho W_r)}{\partial r} + \frac{\partial(rB\rho W_z)}{\partial z} = 0 \quad (3.9)$$

by using an integrating factor B , which is related to C by the following equation:

$$\frac{D \ln B}{Dt} = W_r \frac{\partial \ln B}{\partial r} + W_z \frac{\partial \ln B}{\partial z} = -C \quad (3.10)$$

or

$$\ln \frac{B}{B_i} = - \int_{t_i}^t C dt = - \int_{L_i}^L \frac{C}{W} dx \quad (3.11)$$

Equation (3.9) is the necessary and sufficient condition that a stream function Ψ exists. Ψ is related to velocity components by

$$\frac{\partial \Psi}{\partial r} = rB\rho W_z \quad (3.12a)$$

$$\frac{\partial \Psi}{\partial z} = rB\rho W_r \quad (3.12b)$$

The difference in Ψ at two points j and k on the S_2 surface is

$$\Psi^k - \Psi^j = \int_j^k d\Psi = \int_j^k rB\rho (W_z dr - W_r dz) \quad (3.13)$$

The preceding equation indicates that B is proportional to the angular thickness of a thin stream filament whose mid-surface is the stream surface S_2 considered herein and whose circumferential thickness is equal to rB . Indeed, if the mass flow into and out of the element of such a stream sheet (cut between two planes normal to the z -axis, and a distance dz apart (see fig. 3.5)) is equated to zero, and the distances dr and dz approach zero as a limit, the following equation is obtained:

$$\frac{\partial(\tau\rho W_r)}{\partial r} + \frac{\partial(\tau\rho W_s)}{\partial z} = 0 \quad (3.14)$$

Comparing this equation with equation (3.9) and considering the mass flow relations show τ to be proportional to rB . This proportionality means that physically B is a quantity which is proportional to the angular thickness of a stream filament whose mid-surface is the S_2 surface considered herein. With this interpretation, B is immediately seen to be closely related to the angular distance between two adjacent blades. In actual calculation, only the ratio rB to $(rB)_i$ or τ to τ_i is important. In general it is easier to obtain the variation in rB from the distance between adjacent streamlines obtained on S_1 surface than to evaluate B/B_i by equations (3.11) and (3.8) using data obtained on S_1 surfaces.

It is seen from the preceding section that in following the fluid flow along a stream surface, a consideration of conservation of matter automatically changes the fluid flow on the stream surface to the fluid flow along the stream filament. In general three-dimensional flow, the thickness of the stream filament changes with respect to the two coordinates r and z . In the case of S_2 stream filament (see fig. 3.6) it is easy to see that: (1) in the radial direction, τ increases with the radius as the circumferential distance between the adjacent blades increases in the radial direction and (2) in the flow direction, due to the blade thickness, τ decreases as the fluid enters the blade channel and then increases as the fluid moves toward the trailing edge of the blade.

Dynamic Equation

For general rotational flow, the dynamic equation (2.69) in the three perpendicular directions are

$$-\frac{W_\varphi}{r} \left(\frac{\partial(V_\theta r)}{\partial r} - \frac{\partial W_r}{\partial \varphi} \right) + W_s \left(\frac{\partial W_r}{\partial z} - \frac{\partial W_s}{\partial r} \right) = -\frac{\partial I}{\partial r} + T \frac{\partial s}{\partial r} \quad (3.15a)$$

$$\frac{W_r}{r} \left(\frac{\partial(v_{\theta r})}{\partial r} - \frac{\partial W_r}{\partial \varphi} \right) - W_s \left(\frac{1}{r} \frac{\partial W_s}{\partial \varphi} - \frac{\partial W_\phi}{\partial z} \right) = -\frac{1}{r} \frac{\partial I}{\partial \varphi} + \frac{T}{r} \frac{\partial s}{\partial \varphi} \quad (3.15b)$$

$$-W_r \left(\frac{\partial W_r}{\partial z} - \frac{\partial W_s}{\partial r} \right) + W_\phi \left(\frac{1}{r} \frac{\partial W_s}{\partial \varphi} - \frac{\partial W_\phi}{\partial z} \right) = -\frac{\partial I}{\partial z} + T \frac{\partial s}{\partial z} \quad (3.15c)$$

In following the motion on S_2 equation (3.15) are reduced to the following forms by using equations (3.3) to (3.6):

$$-\frac{W_\varphi}{r} \frac{\partial(v_{\theta r})}{\partial r} + W_s \left(\frac{\partial W_r}{\partial z} - \frac{\partial W_s}{\partial r} \right) = -\frac{\partial I}{\partial r} + T \frac{\partial s}{\partial r} + F_r \quad (3.16a)$$

$$F_{\varphi r} = \frac{D(v_{\theta r})}{Dt} \quad (3.16b)$$

$$-W_r \left(\frac{\partial W_r}{\partial z} - \frac{\partial W_s}{\partial r} \right) - \frac{W_\varphi}{r} \frac{\partial(v_{\theta r})}{\partial z} = -\frac{\partial I}{\partial z} + T \frac{\partial s}{\partial z} + F_s \quad (3.16c)$$

where \mathbf{F} is a vector having the unit of force per unit mass of gas defined by

$$\mathbf{F} = - \left(\frac{1}{n_\phi} \frac{1}{\rho} \frac{1}{r} \frac{\partial p}{\partial \phi} \right) \mathbf{n} \quad (3.17)$$

3.3 Principal Equation for Fluid Flow Along S_2 Stream Filament

By considering the fluid flow along an S_2 stream filament and using the partial derivative of fluid quantities as functions of two independent variables r and z , the principle of conservation of matter leads to the continuity equation given by either equation (3.9) or (3.14), which are the necessary and sufficient conditions for a stream function Ψ to exist. The relative velocity components W_r and W_z are related to the partial derivatives of Ψ by equation (3.12). When this relation is used, the dynamic equation in the radial direction can be used to form a principal equation governing the fluid flow on S_2 stream filament. The solution of the fluid flow on S_2 stream filament is concentrated on solving this principal equation for the single dependent variable Ψ . It is much better than solving a number of dependent variables from a set of partial differential equations. The form of the principal equation will be given for the direct problem and the inverse problem in the next two sections.

Principal Equation for Direct Problem

In the direct problem the shape of the S_2 stream surface is given. In practice the shape is specified by a number of coordinate points lying on the surface. The components of the unit normal are then calculated by equation (3.2) as follows:

Along the intersection of the S_2 surface and a constant- z plane

$$\frac{n_r}{n_\phi} = -r \left(\frac{\partial \phi}{\partial r} \right)_{z = z_0} \quad (3.18)$$

and along the intersection of the S_2 surface and a constant r -surface

$$\frac{n_z}{n_\phi} = -r \left(\frac{\partial \phi}{\partial z} \right)_{r=r_0} \quad (3.19)$$

Components n_r , n_ϕ , and n_z are determined by the preceding two equations along with the following equation:

$$n_r^2 + n_\phi^2 + n_z^2 = 1 \quad (3.20)$$

Let

$$\mu = \frac{n_r}{n_\phi} = \frac{F_r}{F_\phi} \quad (3.21a)$$

$$\nu = \frac{n_z}{n_\phi} = \frac{F_z}{F_\phi} \quad (3.21b)$$

From equation (3.3)

$$W_\phi = -(\mu W_r + \nu W_z) \quad (3.22)$$

Using equations (3.21a) and (3.21b) and other basic relations, the dynamic equation in the radial direction can be transformed into the following form (ref. 48).

$$\begin{aligned}
& \left[(1 + \nu^2) - (1 + \mu^2 + \nu^2) \frac{W_r^2}{a^2} \right] \frac{\partial^2 \Psi}{\partial r^2} - 2 \left[\mu\nu + (1 + \mu^2 + \nu^2) \frac{W_r W_s}{a^2} \right] \frac{\partial^2 \Psi}{\partial r \partial z} \\
& + \left[(1 + \mu^2) - (1 + \mu^2 + \nu^2) \frac{W_s^2}{a^2} \right] \frac{\partial^2 \Psi}{\partial z^2} + N \frac{\partial \Psi}{\partial r} + M \frac{\partial \Psi}{\partial z} = 0
\end{aligned} \tag{3.23}$$

where

$$\begin{aligned}
N = & -(1 + \nu^2) \left[\frac{\partial \ln \tau}{\partial r} - \frac{1}{R} \frac{\partial s}{\partial r} + \frac{1}{a^2} \left(\frac{\partial I}{\partial r} + \omega^2 r + W_r W_\varphi \frac{\partial \mu}{\partial r} + W_\varphi W_s \frac{\partial \nu}{\partial r} \right) \right] \\
& + \mu\nu \left[\frac{\partial \ln \tau}{\partial z} - \frac{1}{R} \frac{\partial s}{\partial z} + \frac{1}{a^2} \left(\frac{\partial I}{\partial r} + W_r W_\varphi \frac{\partial \mu}{\partial z} + W_\varphi W_s \frac{\partial \nu}{\partial r} \right) \right] \\
& + \frac{a^2 - W^2}{a^2} \left[\nu \frac{\partial \nu}{\partial r} - \mu \frac{\partial \nu}{\partial z} - \frac{\nu W_\varphi}{r W_s} - \frac{2\omega\nu}{W_s} - \frac{1}{W_s^2} \left(\frac{\partial I}{\partial r} - T \frac{\partial s}{\partial r} \right) \right]
\end{aligned}$$

$$\begin{aligned}
M = & \mu\nu \left[\frac{\partial \ln \tau}{\partial r} - \frac{1}{R} \frac{\partial s}{\partial r} + \frac{1}{a^2} \left(\frac{\partial I}{\partial r} + \omega^2 r + W_r W_\varphi \frac{\partial \mu}{\partial r} + W_\varphi W_s \frac{\partial \nu}{\partial r} \right) \right] \\
& - (1 + \mu^2) \left[\frac{\partial \ln \tau}{\partial z} - \frac{1}{R} \frac{\partial s}{\partial z} + \frac{1}{a^2} \left(\frac{\partial I}{\partial z} + W_r + W_\varphi \frac{\partial \mu}{\partial z} + W_\varphi W_s \frac{\partial \nu}{\partial z} \right) \right] \\
& + \frac{a^2 - W^2}{a^2} \left(\nu \frac{\partial \mu}{\partial r} - \mu \frac{\partial \mu}{\partial z} \right)
\end{aligned}$$

It is seen from the coefficients of the second order partial derivatives that when $W > a$ or $< a$, equation (3.23) is hyperbolic or elliptic.

Procedure of Solution for Direct Problem

In the direct problem of fluid flow along the S_2 stream filament the variation of filament thickness r (or rB) relative to its inlet value and equation (3.21) are given. There are nine independent equations governing the fluid flow, namely equations (3.12a), (3.12b), (3.22), (3.16b), (3.21a), (3.21b), (2.67), (2.71), or (2.72). The nine independent variables to be determined are W_r , W_φ , W_s , F_r , F_φ , F_s , I , S , and Ψ . (It may be noted here that, when equation (2.67) instead of the complete viscous equation (2.66) is used for the energy equation in the calculation, there are only three independent equations among the dynamic equations in three directions and the energy equation, because the latter can be obtained from the former and the normality conditions between F and W .) The procedure of calculation is as follows:

- (1) Starting from an estimated Ψ field at the beginning of calculation or from the Ψ field determined in the previous cycle, compute W_r and W_z from equations (3.12a) and (3.12b), respectively.
- (2) Compute W_φ from equation (3.22).
- (3) Compute $V_\theta = W_\varphi + \omega r$ and then F_φ from the dynamic equation in the circumferential direction, equation (3.16b).
- (4) Compute F_r and F_z from equations (3.21a) and (3.21b).
- (5) When the approximate equation, equation (2.67) is used for the whole flow region, stagnation rothalpy I is taken to be constant along all streamlines.
- (6) For an invicid isentropic calculation, entropy s is taken to be constant over the whole region.

For an analysis and design calculation, which tries to approximate the real flow as closely as possible, a certain empirical variation along the streamline with the difference between the exit and inlet value given by equations (2.71) or (2.72) is considered. In transonic turbomachines the abrupt entropy increase across the shock is also taken into consideration.

- (7) Solve Ψ from the principal equation (3.23).

Repeat calculations 1 to 7 until the desired accuracy is reached.

Principal Equation for Inverse Problem

In the inverse or design problem of fluid flow along the mid-channel S_2 filament the variation of the filament thickness τ (or rB) relative to its inlet value is empirically determined by the desirable blade thickness distribution. (In three-dimensional solution the S_2 filament thickness is taken from the solution of S_1 filaments obtained in a previous cycle.) Now there are only seven independent equations governing the fluid flow, namely equations (3.12a) and (3.12b), (3.16a) to (3.16c), (c), (2.67), and (2.71) or (2.72), two less than that in the direct problem. On the other hand, however, there are nine independent variables to be determined.

The differential of the coordinates of the S_2 stream surface are related to the \mathbf{F} components by

$$F_r dr + F_\varphi r d\varphi + F_z dz = 0 \quad (3.24)$$

In order for this differential equation to lead to an integral surface of the form represented by equation (3.1), \mathbf{F} must satisfy the following condition of integrability:

$$\mathbf{F} \cdot \nabla \times \mathbf{F} = 0 \quad (3.25)$$

Writing equation (3.25) in scalar form and using the relations (3.12a) and (3.12b) gives

$$\frac{\partial}{\partial r} \left(\frac{F_z}{F_{\varphi r}} \right) = \frac{\partial}{\partial z} \left(\frac{F_r}{F_{\varphi r}} \right) \quad (3.26)$$

By integrating along a constant r -line equation (3.26) gives

$$\frac{F_r}{F_{\varphi r}} = \left(\frac{F_z}{F_{\varphi r}} \right)_0 + \int_{z_0}^z \frac{\partial}{\partial r} \left(\frac{F_z}{F_{\varphi r}} \right) dz \quad (3.27)$$

If $F_r = 0$ at z_0

$$F_r = F_{\varphi r} \int_{z_0}^z \frac{1}{r} \left(\frac{F_z}{F_{\varphi r}} \right) dz \quad (3.28)$$

Thus, there is only one degree of freedom left to the designer. Of all of the appropriate ways of utilizing this degree of freedom, the one found most useful is to prescribe an appropriate variation of V_θ or $V_{\theta r}$ on the $S_{2,m}$ surface, i.e., the following equation is prescribed:

$$V_{\theta r} = G(r, z) \quad (3.29)$$

The principal equation formed by combining the continuity equation and the dynamic equation in the radial direction is

$$\left(1 - \frac{W_r^2}{a^2}\right) \frac{\partial^2 \Psi}{\partial r^2} - 2 \frac{W_r W_z}{a^2} + \left(1 - \frac{W_z^2}{a^2}\right) \frac{\partial^2 \Psi}{\partial z^2} + N \frac{\partial \Psi}{\partial r} + M \frac{\partial \Psi}{\partial z} = 0 \quad (3.30)$$

where

$$M = \frac{\partial \ln r}{\partial z} + \frac{1}{R} \frac{\partial s}{\partial z} - \frac{1}{a^2} \left(\frac{\partial I}{\partial z} - W_\varphi \frac{\partial W_\varphi}{\partial z} \right)$$

$$N = - \frac{\partial \ln r}{\partial r} + \frac{1}{R} \frac{\partial s}{\partial r} - \frac{1}{a^2} \left(\frac{\partial I}{\partial r} + W_\varphi \frac{\partial W_\varphi}{\partial r} + \omega^2 r \right) \\ + \frac{a^2 - (W_r^2 + W_z^2)}{a^2 W_z^2} \left[- \frac{\partial I}{\partial r} + T \frac{\partial s}{\partial r} + F_r + \frac{W_\varphi}{r} \frac{\partial (V_{\theta r})}{\partial r} \right]$$

From the coefficients of this second order partial derivative, the principal equation (3.27) is seen to be hyperbolic or elliptic then the meridional velocity $W_t = \sqrt{W_r^2 + W_z^2}$ is greater or less than the speed of sound.

In turbomachine design the $S_{2,m}$ surface may be specified in some manner other than equation (3.29). For instance in the case of an axial-flow turbine, in order to design the cooled rotor 54 blades with no or minimum radial twist, the following function may be specified on the mid-channel S_2 stream surface:

$$\frac{W_{\varphi}}{W_s} = g_1(z) \quad (3.31)$$

In the case of a centrifugal compressor, in order to design the impeller blades with minimum deformation and stress during operation, the mid-channel S_2 stream surface may be specified to consist of all radial elements, i.e.,

$$\frac{W_{\varphi}}{W_s} = r g_2(z) \quad (3.32)$$

In general then, the S_2 stream surface may be specified by the following relation:

$$\frac{W_{\varphi}}{W_s} = g(r, z) \quad (3.33)$$

By using equation (3.33) and other basic relations the dynamic equation in the radial direction can be transformed into the following form (ref. 48):

$$(1 + g^2) \left(1 - \frac{W_r^2}{a^2} \right) \frac{\partial^2 \Psi}{\partial r^2} - 2(1 + g^2) \frac{W_r W_s}{a^2} \frac{\partial^2 \Psi}{\partial r \partial z} + \left(1 - \frac{W_{\varphi}^2 + W_s^2}{a^2} \right) \frac{\partial^2 \Psi}{\partial z^2} + N \frac{\partial \Psi}{\partial r} + M \frac{\partial \Psi}{\partial z} = 0 \quad (3.34)$$

where

$$M = -\frac{\partial \ln B}{\partial z} + \frac{\partial s^*}{\partial z} - \frac{1}{a^2} \left(\frac{\partial I}{\partial z} - \frac{W_z^2}{a^2} g \frac{\partial g}{\partial z} \right)$$

$$N = -\left(1 + g^2\right) \left[\frac{1}{r} + \frac{\partial \ln B}{\partial r} - \frac{\partial s^*}{\partial r} + \frac{1}{a^2} \left(\frac{\partial I}{\partial r} + \omega^2 r - W_z^2 g \frac{\partial g}{\partial r} \right) \right] + \frac{a^2 - W^2}{a^2} g \left(\frac{g}{r} + \frac{\partial g}{\partial r} \right) \\ + \frac{a^2 - W^2}{a^2 W_z^2} \left(-\frac{\partial I}{\partial r} + T \frac{\partial s}{\partial r} + F_r + 2\omega W_\varphi \right)$$

Procedure of Solution for Inverse Problem

The procedure of calculation of $S_{2,m}$ stream filament is as follows:

- (1) Starting from an estimated Ψ field at the beginning of calculation or from the Ψ field determined in the previous cycle, compute W_r and W_z from equations (3.12a) and (3.12b), respectively.
- (2) When $(V_{\theta r})$ is prescribed, compute W_φ from V_θ . When (W_φ/W_z) is prescribed, compute W_φ from equation (3.30) and W_z is computed from step 1.
- (3) Compute F_φ and F_z from, respectively, equations (3.16b) and (3.16c).
- (4) When the approximate equation (2.67) is used for the whole flow region, the stagnation rothalpy I is taken to be constant along all streamlines.
- (5) For an invicid isentropic calculation, entropy s is taken to be constant over the whole region. For an analysis and design calculation, which tries to approximate the real flow as closely as possible, a certain empirical variation along the streamline with the difference between exit and inlet value given by equation (2.71) or (2.77) is considered. In transonic turbomachines the abrupt entropy increase across the shock is also taken into consideration.

(6) Solve Ψ from the principal equation (3.30) or (3.34).

Repeat steps 1 to 6 until the desired accuracy is reached.

3.4 Principal Equations for Fluid Flow Along S_1 Stream Filament

The S_1 stream surfaces near the hub and casing walls are usually considered to be surfaces of revolution. If the radius of the hub wall increases (or decreases) in the flow direction while the radius of the casing wall decreases (or increases) in the flow direction, the S_1 surface in the mid-span region may be close to surface of revolution. Just like in the case of S_2 flow, the continuity equation requires that the mass of fluid flow in a thin stream filament be conserved.

The flow equations expressed by a set of orthogonal curvilinear coordinates (ℓ, φ) (fig. 3.6) are as follows (refs. 2 and 4):

Continuity Equation:

$$\frac{\partial(\tau\rho W_\ell)}{\partial\ell} + \frac{\partial(\tau\rho W_\varphi)}{\partial\varphi} = 0 \quad (3.35)$$

Ψ - W relations

$$\frac{\partial\Psi}{\partial\ell} = -\tau\rho W_\varphi \quad (3.36a)$$

$$\frac{1}{r} \frac{\partial \Psi}{\partial \varphi} = \tau \rho W_t \quad (3.36b)$$

Dynamic Equation:

$$\frac{1}{r} \frac{\partial W_t}{\partial \varphi} - \frac{\partial W_\varphi}{\partial \ell} - \left(\frac{W_\varphi}{r} + 2\omega \right) \sin \sigma = \frac{1}{W_t} \left(\frac{1}{r} \frac{\partial I}{\partial \varphi} - \frac{T}{r} \frac{\partial s}{\partial \varphi} \right) = 0 \quad (3.37)$$

Principal Equation:

$$\frac{\partial^2 \Psi}{\partial \ell^2} + \left(\frac{\sin \sigma}{r} - \frac{\partial \tan r}{\partial \ell} \right) \frac{\partial \Psi}{\partial \ell} + \frac{1}{r^2} \frac{\partial^2 \Psi}{\partial \varphi^2} = N \quad (3.38)$$

where

$$N = \frac{1}{\rho} \left(\frac{\partial \rho}{\partial \ell} \frac{\partial \Psi}{\partial \ell} + \frac{1}{r^2} \frac{\partial \rho}{\partial \varphi} \frac{\partial \Psi}{\partial \varphi} \right) + 2\omega \tau \rho \sin \sigma + \frac{\tau \rho}{W_t} \left(\frac{1}{r} \frac{\partial I}{\partial \varphi} - \frac{I}{r} \frac{\partial s}{\partial \varphi} \right) = 0$$

For general S_1 surface or filament, where the surface twists in the circumferential direction, one may formulate the governing equation with respect to the coordinates as follows:

- (1) For turbomachines with axial inflow and axial outflow any quantity q on the S_1 surface is considered a function of φ and z .
- (2) For turbomachines with radial inlet and radial discharge, any quantity on the S_1 surface is considered a function of φ and r .

- (3) For turbomachines with axial (or radial) inflow and radial (or axial) outflow, any quantity on the S_1 surface is considered a function of (φ, θ) .
- (4) Same as that in case (3) but considered a function of noncurvilinear coordinates x^1 and x^2 .

CHAPTER 4

THREE-DIMENSIONAL FLOW EQUATIONS EXPRESSED IN TERMS OF NONORTHOGONAL CURVILINEAR COORDINATES AND CORRESPONDING NONORTHOGONAL VELOCITY COMPONENTS

Equations governing the fluid flow along S_1 and S_2 stream filaments were first derived in references 2 to 4 employing orthogonal curvilinear coordinates (r, φ, z) or (φ, ℓ, n) . These equations have been adopted in treatises on turbomachinery (for instance refs. 45 to 47), programmed into computer codes (for instance, refs. 8, 10 to 19, 22, and 23) and used in analysis and design of turbomachines (for instance, refs. 21 to 26). During calculation of actual engineering problems it soon becomes evident that in order to improve the relatively low accuracy of numerical differentiation (ref. 27) occurring at grid points, unequally spaced near a curved boundary the coordinate line may coincide with the leading and trailing edges of the blade (see fig. 4.1) and a computer code may be used universally for turbomachines of different geometry. Work to employ general nonorthogonal curvilinear coordinates for the calculation of fluid flow along S_1 and S_2 stream filaments began in the sixties (refs. 28 and 29). Presented in the following sections are some basic relations of general nonorthogonal curvilinear coordinates, equations governing fluid flow along S_1 and S_2 stream filaments employing general nonorthogonal curvilinear coordinates and the methods of solution.

4.1 General Curvilinear Coordinates in a Three-Dimensional Space

Let (y^1, y^2, y^3) be the usual orthogonal Cartesian coordinates of point P and (x^1, x^2, x^3) be its nonorthogonal curvilinear coordinates. In general the square of the element of arc ds is

$$ds^2 = g_{ij} dx^i dx^j \quad (i, j = 1, 2, 3) \quad (4.1)$$

where g_{ij} is the covariant metric tensor of the three-dimensional space

$$g_{ij} = \frac{\partial y^k}{\partial x^i} \frac{\partial y^k}{\partial x^j} = \mathbf{e}_i \cdot \mathbf{e}_j = g_{ji} \quad (k = 1, 2, 3) \quad (4.2)$$

$$g_{ij} = \sqrt{g_{ii} g_{jj}} \cos \theta_{ij} \quad (4.3)$$

where θ_{ij} is the angle between the two basic vectors \mathbf{e}_i and \mathbf{e}_j .

The lengths of the elements of arc measured along the coordinates lines of our curvilinear systems, are

$$ds_{(i)} = \sqrt{g_{ii}} dx^i \quad (4.4)$$

The element of volume dv is

$$dv = \sqrt{g} dx^1 dx^2 dx^3 \quad (4.5)$$

where g is the determinant $|g_{ij}|$. Let \mathbf{e}^i denote the reciprocal base vectors defined by

$$\mathbf{e}_i \cdot \mathbf{e}^j = \delta_i^j \text{ or } \mathbf{e}^i = \frac{\mathbf{e}_j \times \mathbf{e}_k}{\sqrt{g}} \quad (4.6)$$

The corresponding contravariant metric tensor of the three-dimensional space is

$$g^{ij} = \frac{G^{ij}}{g} = \mathbf{e}^i \cdot \mathbf{e}^j = g^{ji} \quad (4.7)$$

where G^{ij} is the cofactor of the element g_{ij} in g .

For both systems it is convenient to use base vectors of unit length defined by

$$\mathbf{u}_i = \mathbf{e}_i \div \sqrt{g_{ii}} \quad (4.8)$$

$$\mathbf{u}^i = \mathbf{e}^i \div \sqrt{g^{ii}} \quad (4.9)$$

A vector \mathbf{B} in the three-dimensional space is now either expressed in terms of the base vectors \mathbf{e}_i and \mathbf{u}_i , or the reciprocal vectors \mathbf{e}^i and \mathbf{u}^i , as follows:

$$\mathbf{B} = b^i \mathbf{e}_i \quad (4.10)$$

$$\mathbf{B} = B^i \mathbf{u}_i \quad (4.11)$$

$$\mathbf{B} = b_i \mathbf{e}^i \quad (4.12)$$

$$\mathbf{B} = B_i \mathbf{u}^i \quad (4.13)$$

where b^i and B^i are, respectively, the contravariant components and the physical components along \mathbf{e}_i of the vector \mathbf{B} ; and b_i and B_i are, respectively, the covariant components and the physical components along \mathbf{e}^i of the vector \mathbf{B} . The covariant component and its corresponding physical component can be calculated from the contravariant component with the following formula:

$$b_i = \mathbf{B} \cdot \mathbf{e}_i = g_{ij} b^j \quad (4.14)$$

Finally the differential operators in general curvilinear coordinates are as follows: the gradient of a scalar I is given by

$$\nabla I = \mathbf{e}^i \frac{\partial I}{\partial x^i} \quad (4.15)$$

the divergence of vector \mathbf{W} is

$$\nabla \cdot \mathbf{W} = \frac{1}{\sqrt{g}} \frac{\partial(\sqrt{g} w^i)}{\partial x^i} \quad (4.16)$$

and the contravariant components ξ^i of vector $\Sigma = \nabla \times \mathbf{V} = \xi^i \mathbf{e}_i$ are

$$\left. \begin{aligned} \xi^1 &= \frac{1}{\sqrt{g}} \left(\frac{\partial v_3}{\partial x^2} - \frac{\partial v_2}{\partial x^3} \right) \\ \xi^2 &= \frac{1}{\sqrt{g}} \left(\frac{\partial v_1}{\partial x^3} - \frac{\partial v_3}{\partial x^1} \right) \\ \xi^3 &= \frac{1}{\sqrt{g}} \left(\frac{\partial v_2}{\partial x^1} - \frac{\partial v_1}{\partial x^2} \right) \end{aligned} \right\} \quad (4.17)$$

4.2 General Curvilinear Coordinates on a Surface

In the investigation of fluid flow along an S_1 or S_2 stream filament the governing equations are written for the fluid flow on the mid-surface of the filament. Such a surface is a two-dimensional manifold embedded in a three-dimensional enveloping space and is usually described by coordinates u^α ($\alpha = 1, 2$), called the curvilinear or Gaussian coordinates on the surface.

Under this notation the relevant equations corresponding to those in the preceding section are as follows:

$$ds^2 = a_{\alpha\beta} dx^\alpha dx^\beta \quad (\alpha, \beta = 1, 2) \quad (4.18)$$

where $a_{\alpha\beta}$ is the covariant metric tensor of the surface

$$a_{\alpha\beta} = \frac{\partial y^k}{\partial u^\alpha} \frac{\partial y^k}{\partial u^\beta} = \mathbf{e}_\alpha \cdot \mathbf{e}_\beta = a_{\beta\alpha} \quad (4.19)$$

$$a_{\alpha\beta} = \sqrt{a_{\alpha\alpha} a_{\beta\beta}} \cos \theta_{\alpha\beta} \quad (4.20)$$

The lengths of elements of arc measured along the coordinate lines are

$$ds_{(\alpha)} = \sqrt{a_{\alpha\alpha}} dx^\alpha \quad (4.21)$$

An element of area dA is

$$dA = \sqrt{a} du^1 du^2 \quad (4.22)$$

where a is the determinant $|a_{\alpha\beta}|$.

$$a = |a_{\alpha\beta}| = a_{11} a_{22} \sin^2 \theta_{12} \quad (4.23)$$

The contravariant metric tensor of the two-dimensional surface is

$$\begin{aligned} \mathbf{a}^{\alpha\beta} &= \mathbf{e}^\alpha \cdot \mathbf{e}^\beta = \mathbf{a}^{\beta\alpha} \\ \mathbf{a}^{11} &= \mathbf{a}_{22} \div \mathbf{a} = \left(\mathbf{a}_{11} \sin^2 \theta_{12} \right)^{-1} \\ \mathbf{a}^{22} &= \mathbf{a}_{11} \div \mathbf{a} = \left(\mathbf{a}_{11} \sin^2 \theta_{12} \right)^{-1} \end{aligned} \tag{4.24}$$

$$\mathbf{a}^{12} = \mathbf{a}^{21} = -\mathbf{a}_{12} \div \mathbf{a} = -\cos \theta_{12} / \left(\sqrt{\mathbf{a}_{11}\mathbf{a}_{22}} \sin^2 \theta_{12} \right) \tag{4.25}$$

In the investigation of S_1 and S_2 flow employing nonorthogonal curvilinear coordinates the two Gaussian coordinates, u^1 and u^2 , on the surface, are selected to be the same as two of the three curvilinear coordinates in the three-dimensional space. For instance, in the case of S_1 flow, x^1 and x^2 shown in figure 4.1 are two nonorthogonal curvilinear coordinates of the three general curvilinear coordinates referring to the three-dimensional space and are the same as the two Gaussian coordinates which refer to the two-dimensional surface. The third coordinate x^3 , which refers to the three-dimensional space, may be selected as normal to the $x^1 - x^2$ surface. In that case $W^3 = w^3 = W_3 = w_3 = 0$.

In the following, distinctions between (u^1, u^2) and (x^1, x^2) will not be made, but $\mathbf{e}_\alpha, \mathbf{a}_{\alpha\beta}, \mathbf{a} \dots (\alpha, \beta = 1, 2)$ will be used for the S_1 surface, whereas $\mathbf{e}_i, \mathbf{g}_{ij}, \mathbf{g} \dots (i, j = 1, 2, 3)$ will be used for the three-dimensional space in which the surface is embedded. For a given problem, $\mathbf{a}_{\alpha\beta}$ are computed from equation (4.19) through numerical differentiation.

For vector \mathbf{W} on the S_1 surface the following are obtained:

$$\left. \begin{aligned} w_1 &= \mathbf{W} \cdot \mathbf{e}_1 = a_{11} w^1 + a_{12} w^2 = \sqrt{a_{11}} (W^1 + W^2 \cos \theta_{12}) \\ w_2 &= \mathbf{W} \cdot \mathbf{e}_2 = a_{21} w^1 + a_{22} w^2 = \sqrt{a_{22}} (W^1 \cos \theta_{12} + W^2) \end{aligned} \right\} \quad (4.26)$$

$$\left. \begin{aligned} W_1 &= \sqrt{a^{11}} w_1 = (W^1 + W^2 \cos \theta_{12}) \div \sin \theta_{12} \\ W_2 &= \sqrt{a^{22}} w_2 = (W^1 \cos \theta_{12} + W^2) \div \sin \theta_{12} \end{aligned} \right\} \quad (4.27)$$

The preceding equations can also be obtained by the geometrical relations indicated in figure 4.2.

4.3 Basic Equations Governing Fluid Flow on S_1 Surface of Revolution

General Equations: Denoting the normal distance between two adjacent surfaces of revolution by r , the continuity equation of steady relative flow along the stream filament is

$$\nabla \cdot (r\rho\mathbf{W}) = 0 \quad (4.28)$$

Substituting equation (4.16) into (4.28) results in

$$\frac{\partial(\tau\rho W^1 \sqrt{a_{22}} \sin \theta_{12})}{\partial x^1} + \frac{\partial(\tau\rho W^2 \sqrt{a_{11}} \sin \theta_{12})}{\partial x^2} = 0 \quad (4.29)$$

This equation can also be obtained by considering the mass flow into and out of the elementary volume (ds_1, ds_2, τ) (see fig. 4.3).

When expressions (4.10), (4.15), and (4.17) are used, the dynamic equation (2.53) in the \mathbf{e}^2 direction is

$$-w^1 \mathbf{e}_1 \times \zeta^3 \mathbf{e}_3 = \left(\frac{\partial I}{\partial x^2} - T \frac{\partial s}{\partial x^2} \right) \mathbf{e}^2 \quad (4.30)$$

When equation (4.10) and the following relation between the absolute and relative vorticities are used:

$$\nabla \times \mathbf{V} = \nabla \times \mathbf{W} + 2\boldsymbol{\omega} \quad (4.31)$$

the dynamic equation in the \mathbf{e}^2 direction for steady relative flow is (fig. 4.4).

$$-w^1 \left[\left(\frac{\partial w_2}{\partial x^1} - \frac{\partial w_1}{\partial x^2} \right) - 2\omega \sqrt{a} \sin \sigma \right] = \frac{\partial I}{\partial x^2} - T \frac{\partial s}{\partial x^2} \quad (4.32)$$

By using equation (4.26) the preceding equation becomes

$$\begin{aligned} \frac{\partial}{\partial x^2} (W^1 + W^2 \cos \theta_{12}) \sqrt{a_{11}} - \frac{\partial}{\partial x^1} [(W^1 \cos \theta_{12} + W^2) \sqrt{a_{22}}] \\ = -2 \sqrt{a_{11} a_{22}} \omega \sin \sigma \sin \theta_{12} + \frac{\sqrt{a_{11}}}{W^1} \left(\frac{\partial I}{\partial x^2} - T \frac{\partial s}{\partial x^2} \right) \end{aligned} \quad (4.33)$$

This equation can also be obtained by applying Stokes theorem to the surface element of figure 4.3.

Using relations (4.10) and (4.15) the energy equation (2.51) for steady relative flow becomes

$$\frac{DI}{Dt} = \mathbf{W} \cdot \nabla I = w^i \mathbf{e}_i \cdot \frac{\partial I}{\partial x^i} \mathbf{e}^i = w^i \frac{\partial I}{\partial x^i} = 0 \quad (4.34)$$

or

$$\frac{DI}{Dt} = \frac{W^1}{\sqrt{a_{11}}} \frac{\partial I}{\partial x^1} + \frac{W^2}{\sqrt{a_{22}}} \frac{\partial I}{\partial x^2} = 0 \quad (4.35)$$

Special Forms of Flow Equations on S_1 :

A number of useful special forms of equations presented in the preceding section can be obtained by selecting a number of different x^1 - and x^2 -coordinate lines, as follows:

(a) x^1 -lines coincident with streamlines. In this case $W^2 = w^2 = 0$, $W^1 = W$, equations (4.29), (4.33), and (4.35) simplify to, respectively,

$$\frac{\partial}{\partial x^1} \left(r \rho W^1 \sqrt{a_{22}} \sin \theta_{12} \right) = 0 \quad (4.29a)$$

$$\begin{aligned} \frac{\partial}{\partial x^2} \left(W^1 \sqrt{a_{11}} \right) &= \frac{\partial}{\partial x^1} \left(W^1 \sqrt{a_{22}} \cos \theta_{12} \right) - 2 \sqrt{a_{11} a_{12}} \omega \sin \sigma \sin \theta_{12} \\ &+ \frac{\sqrt{a_{11}}}{W} \left(\frac{\partial I}{\partial x^2} - T \frac{\partial s}{\partial x^2} \right) \end{aligned} \quad (4.33a)$$

$$\frac{\partial I}{\partial x^1} = 0 \quad (4.35a)$$

If at the same time x^2 is taken to be normal to x^1 , the preceding equations are further simplified with $\cos \theta_{12} = 0$ and $\sin \theta_{12} = 1$.

(b) x^1 -line coincident with the meridional coordinate line ℓ and $x^2 = \varphi$. In this case, $\theta_{12} = 270^\circ$, $W^1 = W_\theta$, $W^2 = -W_\varphi$, $\sqrt{a_{11}} = 1$, $\sqrt{a_{22}} = r$, equations (4.29), (4.33), and (4.35) become those used in references 4 to 9.

(c) S_1 surface is a cylindrical surface of radius r . If $y = x^2 = r\varphi$ and $x^1 = z$, equations (4.29), (4.33), and (4.35) become those of plane flow as used in reference 54. If, however, x^1 -line is taken to be coincident with the streamline $W^1 = W$, $W^2 = 0$ and the equations are further simplified to

$$\frac{\partial}{\partial x^1} \left(r \rho W \sqrt{a_{22}} \sin \theta_{12} \right) = 0 \quad (4.29c)$$

$$\frac{\partial}{\partial y} \left(W \sqrt{a_{11}} \right) = \frac{\partial}{\partial x^1} \left(W \sqrt{a_{22}} \cos \theta_{12} \right) + \frac{\sqrt{a_{11}}}{W} \left(\frac{\partial I}{\partial y} - T \frac{\partial s}{\partial y} \right) \quad (4.33c)$$

$$\frac{\partial I}{\partial x^1} = 0 \quad (4.35c)$$

Furthermore, if x^2 -line is taken to be normal to x^1 -line, an interesting result is obtained—the quantity $W \sqrt{a_{11}}$ is an invariant along an x^2 -line in the case where the variations of I and s along the x^2 -line are equal to zero.

As seen in the preceding equations, dynamic equations (4.33) and (4.33a) contain the variations of I and s of the fluid in the e_2 direction. When they are uniform at the blade inlet and no change occurs along the streamline, they are uniform everywhere—this is usually assumed on S_1 flow calculation and will also be assumed in the following discussion of methods of solution. In cases where their derivatives are not very small, they should, of course, be properly considered.

4.4 Methods of Solution for S_1

When the x^1 -lines are corrected during calculation to coincide with the streamlines, equation (4.29), along the x^1 -line, gives

$$\rho W = (\rho W)_i \frac{(\gamma \sqrt{a_{22}} \sin \theta_{12})_i}{\gamma \sqrt{a_{22}} \sin \theta_{12}} \quad (4.36)$$

in which $\sqrt{a_{22}}$ and θ_{12} are computed after each correction of the streamline coordinates. For nonisentropic flow of a perfect gas

$$\frac{\rho}{\rho_{1^{\circ}}} = \left(\frac{h}{H_1'} \right)^{\frac{1}{\gamma-1}} e^{-\frac{s-s_i}{R}} = \left[1 - \frac{\gamma-1}{2} \frac{(\rho W)^2}{(\rho_1 \alpha_i)^2 (\rho/\rho_i)^2} \right]^{\frac{1}{\gamma-1}} e^{-\frac{s-s_i}{R}} \quad (4.37)$$

The values of ρ and W can be determined from their product by rewriting equation (4.37) as (ref. 3)

$$\Sigma^2 = \left(1 - \frac{\Phi}{\Sigma^2} \right)^{\frac{2}{\gamma-1}} \quad (4.38)$$

where

$$\Sigma = \frac{\rho}{\rho_i} e^{-\frac{s-s_i}{R}} \quad (4.39)$$

$$\Phi = \frac{\gamma - 1}{2} \left(\frac{\rho W}{\rho_i/a_i} \right) e^{-2 \frac{s-s_i}{R}}$$

The table in reference 3 can then be used find Σ (i.e., ρ) from the known value of Φ (i.e., ρW). W is then computed from ρW after ρ obtained.

When the derivatives of I and s are neglected, equation (4.33a) yields

$$\frac{\partial}{\partial x^2} (W \sqrt{a_{11}}) = \frac{\partial}{\partial x^1} (W \sqrt{a_{22}} \cos \theta_{12}) - 2 \sqrt{a_{11} a_{22}} \omega \sin \sigma \sin \theta_{12} \quad (4.41)$$

This equation is used to obtain a new set of values of W at the grid points by integrating along the x^2 -lines with the right side of the equation computed from known values of the preceding cycle. The integration may be started from the mid-channel streamline as in references 4 to 6 or from the stagnation streamline. The mass flow along the x^2 -line is then computed by

$$\dot{m} = \int_{(x^2)_0}^{x^2} r \rho W \sin \theta_{12} \sqrt{a_{22}} dx^2 \quad (4.42)$$

A comparison between the computed mass flow and the correct mass flow leads to new values of streamline positions. This process of correction should be applied at each station along the streamlines, quite similar to the method employed in references 4 and 6. It may be noticed, however, that with the use of the present nonorthogonal curvilinear coordinates the tangency of the relative fluid velocity at the

blade surfaces is automatically satisfied. This method, of course, can also be employed to modify existing blading or to design new blading as in references 4 and 35.

If it is desirable to keep the x^1 -line fixed during calculation, then

- (1) ρW^1 along the x^1 -line is corrected by the complete continuity equation (4.29).
- (2) compute ρW by

$$\rho W = \left[(\rho W^1)^2 + (\rho W^2)^2 - 2(\rho W^1)(\rho W^2)\cos \theta_{12} \right]^{1/2} \quad (4.43)$$

- (3) integrate $(W^2 \sqrt{a_{11}})$ along x^1 -line by

$$\begin{aligned} \frac{\partial (W^1 \sqrt{a_{11}})}{\partial x^2} = & - 2 \sqrt{a_{11} a_{12}} \omega \sin \sigma \sin \theta_{12} + \frac{\partial}{\partial x^1} \left[(W^1 \cos \theta_{12} + W^2) \sqrt{a_{22}} \right] \\ & - \frac{\partial}{\partial x^2} \left[W^2 \sqrt{a_{11}} \cos \theta_{12} \right] \end{aligned} \quad (4.44)$$

- (4) compute mass flow along x^2 -line by

$$\dot{m} = \int_{(x^2)_0}^{x^2} r \rho W^1 \sin \theta_{12} \sqrt{a_{22}} dx^2 \quad (4.45)$$

- (5) correct the W^1 values at the grid points in the same manner as in the previous case.

The method described above is quite similar to that used in references 4, 6, and 54 except that the solution of the latter is extended in the circumferential direction from the mean streamline by using a Taylor series consisting of three terms. Whereas, the solution of the former is extended circumferentially to successive streamlines by a Taylor series of only two terms.

In general the continuity equation and the dynamic equation are to be solved simultaneously through the use of the stream function Ψ . Equation (4.29) is necessary and sufficient condition that a function Ψ exists with

$$\left. \begin{aligned} \frac{\partial \Psi}{\partial x^1} &= -\tau \rho W^2 \sqrt{a_{11}} \sin \theta_{12} \\ \frac{\partial \Psi}{\partial x^2} &= \tau \rho W^1 \sqrt{a_{22}} \sin \theta_{12} \end{aligned} \right\} \quad (4.46)$$

Substituting equations (4.46) into (4.33), the following principal equation governing the fluid flow along the S_1 filament of revolution expressed in terms of nonorthogonal curvilinear coordinates x^1 - and x^2 is obtained.

$$\frac{1}{a_{11}} \frac{\partial^2 \Psi}{\partial (x^1)^2} - 2 \frac{\cos \theta_{12}}{\sqrt{a_{11} a_{22}}} \frac{\partial^2 \Psi}{\partial x^1 \partial x^2} + \frac{1}{a_{22}} \frac{\partial^2 \Psi}{\partial (x^2)^2} + \frac{J}{\sqrt{a_{11}}} \frac{\partial \Psi}{\partial x^1} + \frac{K}{\sqrt{a_{22}}} \frac{\partial \Psi}{\partial x^2} = M \quad (4.47)$$

where

$$J = - \frac{\partial \ln \left(\sqrt{a_{11}/a_{22}} \tau \sin \theta_{12} \right)}{\sqrt{a_{11}} \partial x^1} + \frac{\cos \theta_{12} \partial \ln \tau}{\sqrt{a_{22}} \partial x^2} + \frac{1}{\sin \theta_{12} \sqrt{a_{22}}} \cdot \frac{\partial \theta_{12}}{\partial x^2}$$

$$K = - \frac{\partial \ln \left(\sqrt{a_{22}/a_{11}} \tau \sin \theta_{12} \right)}{\sqrt{a_{22}} \partial x^2} + \frac{\cos \theta_{12} \partial \ln \tau}{\sqrt{a_{11}} \partial x^1} + \frac{1}{\sin \theta_{12} \sqrt{a_{11}}} \cdot \frac{\partial \theta_{12}}{\partial x^1}$$

$$M = \left(\frac{1}{\sqrt{a_{11}}} \frac{\partial \ln \rho}{\partial x^1} - \frac{\cos \theta_{12}}{\sqrt{a_{11}}} \frac{\partial \ln \rho}{\partial x^2} \right) \frac{1}{\sqrt{a_{11}}} \frac{\partial \Psi}{\partial x^1} + \left(\frac{1}{\sqrt{a_{22}}} \frac{\partial \ln \rho}{\partial x^2} - \frac{\cos \theta_{12}}{\sqrt{a_{11}}} \frac{\partial \ln \rho}{\partial x^1} \right) \\ + \frac{1}{\sqrt{a_{22}}} \frac{\partial \Psi}{\partial x^2} - 2\omega r \rho \sin \sigma \sin^2 \theta_{12}$$

Equation (4.47) may be considered as a generalization of the principal equation (3.38) in which the orthogonal curvilinear coordinates (ℓ, φ) are used. When x^1 and x^2 become ℓ and φ , respectively, equation (4.47) reduces to equation (3.38).

When the Ψ -derivatives are evaluated with suitable numerical differentiation formulas, including those at the unequally spaced grid points (ref. 27) the resulting set of a large number of algebraic equations involving the unknown Ψ 's at the grid points may be solved either by the direct matrix method (refs. 3, 4, 8, 10 to 12, and 27) or by the relaxation method (refs. 3, 4, 10, 11, and 27). The boundary conditions of the periodic variation of flow and the flow angles at the inlet and outlet stations are to be satisfied in the same manner as described in references 4 and 8. Inasmuch as fixed (x^1, x^2) coordinates are generally used in solving the principal equation (4.47), J and K are then a function of a

fixed geometry and have to be computed only once. The exclusion of derivatives W^1 and W^2 on the right side of equation (4.47) is helpful in the convergence of the solution.

4.5 Equations Governing Fluid Flow on a General S_2 Surface

Vorticity Equation and Dynamic Equation: In general, the problem of fluid flow along S_2 stream filament is treated in the same manner as described for S_1 stream filament in the preceding sections. But there is an important difference in the S_2 surface inverse problem in that the shape of the S_2 surface is known only after the solution is obtained. Because of this and also for the elimination of the angular derivatives in the governing equations, the independent variables, i.e., the nonorthogonal curvilinear coordinates x^1 and x^2 are selected to lie on the meridional plane (see fig. 4.5) while following the fluid motion on the S_2 surface in exactly the same manner as was done in references 3, 10, and 11 in which orthogonal coordinates z and r on the meridional plane were used. The third coordinate x^3 for three-dimensional flow is chosen to be the angular coordinate φ , which is the same as that used in the cylindrical coordinate system previously employed in references 3, 10, and 11.

Corresponding to this choice of x^3 , $\sqrt{g_{33}} = r$, $g = r^2 a$, $\sqrt{g^{33}} = r^{-1}$, $W^3 = W_\varphi$, $w^3 = W_\varphi \div r$, $V^3 = V_\theta$, $v^3 = V_\theta \div r$, $W_3 = W_\varphi$, $w_3 = W_\varphi r$, $V^3 = V_\theta$ and $v_3 = V_\theta r$.

It was found in references 2 and 3 that it is more convenient to use the absolute vorticity than to use the relative vorticity in treating the relative flow on S_2 surface. Under the present nonorthogonal curvilinear coordinate system, the three contravariant components of $\nabla \times \mathbf{V}$ (eq. (4.17)) becomes

$$\left. \begin{aligned} \xi^1 &= \frac{1}{r\sqrt{a}} \left[\frac{\partial(V_{\theta r})}{\partial x^2} - \frac{\partial w_2}{\partial \varphi} \right] \\ \xi^2 &= \frac{1}{r\sqrt{a}} \left[\frac{\partial w_1}{\partial \varphi} - \frac{\partial(V_{\theta r})}{\partial x^1} \right] \\ \xi^3 &= \frac{1}{r\sqrt{a}} \left[\frac{\partial w_2}{\partial x^1} - \frac{\partial w_1}{\partial x^2} \right] \end{aligned} \right\} \quad (4.48)$$

By using these expressions, the three nonorthogonal dynamic equations in the \mathbf{e}_i directions are

$$\frac{W^2}{\sqrt{a_{22}}} \left[\frac{\partial w_2}{\partial x^1} - \frac{\partial w_1}{\partial x^2} \right] - \frac{W_{\varphi}}{r} \left[\frac{\partial w_1}{\partial \varphi} - \frac{\partial(V_{\theta r})}{\partial x^1} \right] = \frac{\partial I}{\partial x^1} - T \frac{\partial s}{\partial x^1} \quad (4.49a)$$

$$\frac{W_{\varphi}}{r} \left[\frac{\partial(V_{\theta r})}{\partial x^2} - \frac{\partial w_2}{\partial \varphi} \right] - \frac{W^1}{\sqrt{a_{11}}} \left[\frac{\partial w_2}{\partial x^1} - \frac{\partial w_1}{\partial x^2} \right] = \frac{\partial I}{\partial x^2} - T \frac{\partial s}{\partial x^2} \quad (4.49b)$$

$$\frac{W^1}{\sqrt{a_{11}}} \left[\frac{\partial w_1}{\partial \varphi} - \frac{\partial(V_{\theta r})}{\partial x^1} \right] - \frac{W^2}{\sqrt{a_{22}}} \left[\frac{\partial(V_{\theta r})}{\partial x^2} - \frac{\partial w_2}{\partial \varphi} \right] = \frac{\partial I}{\partial \varphi} - T \frac{\partial s}{\partial \varphi} \quad (4.49c)$$

Alternatively these equations may also be obtained by using the following expressions of the rectangular components of \mathbf{W} and $\nabla \times \mathbf{V}$ in the \mathbf{e}^1 , \mathbf{e}^2 , and \mathbf{e}^3 directions (see fig. 4.2).

$$W_c = W^1 \sin \theta_{12}, W_d = W^2 \sin \theta_{12}, W_\varphi = W_\varphi \quad (4.50)$$

$$\left. \begin{aligned} \Xi_c &= (\sqrt{a_{11}} \xi^1) \sin \theta_{12} = \frac{1}{r \sqrt{a_{22}}} \left[\frac{\partial(V_\theta r)}{\partial x^2} - \frac{\partial w_2}{\partial \varphi} \right] \\ \Xi_d &= (\sqrt{a_{22}} \xi^2) \sin \theta_{12} = \frac{1}{r \sqrt{a_{11}}} \left[\frac{\partial w_1}{\partial \varphi} - \frac{\partial(V_\theta r)}{\partial x^1} \right] \\ \Xi_\varphi &= r \xi^3 = \frac{1}{\sqrt{a_{11} a_{22}} \sin \theta_{12}} \left[\frac{\partial w_2}{\partial x^1} - \frac{\partial w_1}{\partial x^2} \right] \end{aligned} \right\} \quad (4.51)$$

We notice that the form of equations (4.49) and (4.51) are quite similar to equations (19) and (75), respectively, of reference 3 employing orthogonal curvilinear coordinates (z, r, φ) , but that the w 's are now more complicated covariant components of the relative velocity \mathbf{W} .

With different choices of x^1 - and x^2 -coordinate lines suitable for different problems, the general form of equations (4.49) reduces correspondingly to a number of special forms. For instance, if it is selected that

(1) x^1 -line is coincident with the projection of the streamline on the meridional plane, then

$$\theta_1 = \sigma, W^2 = 0, W^1 = W_\sigma \text{ and } w_1 = \sqrt{a_{11}} W_1, w_2 = W \sqrt{a_{22}} \cos \theta_{12}, \text{ and equation (4.49)}$$

becomes

$$-\frac{W_\varphi}{r} \left[\frac{\partial(W_\ell \sqrt{a_{11}})}{\partial \varphi} - \frac{\partial(V_{\theta r})}{\partial \ell} \right] = \frac{\partial I}{\partial \ell} - T \frac{\partial s}{\partial \ell}$$

$$\frac{W_\varphi}{r} \left[\frac{\partial(V_{\theta r})}{\partial x^2} - \frac{\partial(W_\ell \sqrt{a_{22}} \cos \theta_{12})}{\partial \varphi} \right] - \frac{W_\ell}{\sqrt{a_{11}}} \left[\frac{\partial(W_\ell \sqrt{a_{22}} \cos \theta_{12})}{\partial \ell} - \frac{\partial(W_\ell \sqrt{a_{11}})}{\partial x^2} \right] = \frac{\partial I}{\partial x^2} - T \frac{\partial s}{\partial x^2} \quad (4.52)$$

$$\frac{W_\ell}{\sqrt{a_{11}}} \left[\frac{\partial(W_\ell \sqrt{a_{11}})}{\partial \varphi} - \frac{\partial(V_{\theta r})}{\partial \ell} \right] = \frac{\partial I}{\partial \varphi} - T \frac{\partial s}{\partial \varphi}$$

(2) x^1 -line is coincident with the projection of the streamline on the meridional plane and x^2 -line to

be radial line normal to the z -axis, then $\theta_1 = \sigma$, $\theta_2 = 0$, $\theta_{12} = 90^\circ - \sigma$,

$a = \sqrt{a_{11}a_{12}} \cos \sigma$, $w_2 = W_\ell \sqrt{a_{22}} \sin \sigma$, equation (4.51) becomes

$$\left. \begin{aligned}
 \xi^1 &= \frac{1}{r \sqrt{a_{11} a_{22}} \cos \sigma} \left[\frac{\partial(V_{\theta r})}{\partial r} - \frac{\partial(W_{\ell} \sqrt{a_{22}} \sin \sigma)}{\partial \varphi} \right] \\
 \xi^2 &= \frac{1}{r \sqrt{a_{11} a_{22}} \cos \sigma} \left[\frac{\partial(W_{\ell} \sqrt{a_{11}})}{\partial \varphi} - \frac{\partial(V_{\theta r})}{\partial \ell} \right] \\
 \xi^3 &= \frac{1}{r \sqrt{a_{11} a_{22}} \cos \sigma} \left[\frac{\partial(W_{\ell} \sqrt{a_{22}} \sin \sigma)}{\partial \ell} - \frac{\partial(W_{\ell} \sqrt{a_{11}})}{\partial r} \right]
 \end{aligned} \right\} \quad (4.53)$$

and (4.49b) becomes

$$\frac{W_{\varphi}}{r} \left[\frac{\partial(V_{\theta r})}{\partial r} - \frac{\partial(W_{\ell} \sqrt{a_{22}} \sin \theta_{12})}{\partial \varphi} \right] - \frac{W_{\ell}}{\sqrt{a_{11}}} \left[\frac{\partial(W_{\ell} \sqrt{a_{22}} \sin \theta_{12})}{\partial \ell} - \frac{\partial(W_{\ell} \sqrt{a_{11}})}{\partial r} \right] = \frac{\partial I}{\partial r} - T \frac{\partial s}{\partial r} \quad (4.54)$$

and (4.49a) and (4.49c) remain unchanged. Equation (4.54) may be used to evaluate the change of W_{ℓ} along the r -coordinate lines for axial-flow machines.

Under this coordinate system, the correct expressions of $\nabla \times \mathbf{V}$ in the r , φ and z directions in terms of the rectangular components W_{ℓ} and W_{φ} or V_{θ} are

$$\begin{aligned}
\Xi_r &= \Xi^1 \sin \sigma + \Xi^2 = \frac{\tan \sigma}{r} \left[\frac{1}{\sqrt{a_{22}}} \frac{\partial(V_{\theta r})}{\partial r} - \frac{1}{\sin \sigma \sqrt{a_{11}}} \frac{\partial(V_{\theta r})}{\partial \ell} + \frac{1}{\sin \sigma} \frac{\partial W_{\ell}}{\partial \phi} - \frac{\partial(W_{\ell} \sin \sigma)}{\partial \phi} \right] \\
\Xi_{\phi} &= \Xi^3 = \frac{\tan \sigma}{\sqrt{a_{11}}} \frac{\partial W_{\ell}}{\partial \ell} - \frac{W_{\ell}}{r_m} - \frac{1}{\cos \sigma \sqrt{a_{22}}} \frac{\partial W_{\ell}}{\partial r} \\
\Xi_x &= \Xi^1 \cos \sigma = \frac{1}{r} \left[\frac{1}{\sqrt{a_{22}}} \frac{\partial(V_{\phi r})}{\partial r} - \frac{\partial(W_{\ell} \sin \sigma)}{\partial \phi} \right]
\end{aligned} \tag{4.55}$$

(c) x^2 -line is normal to x^1 -line and $\theta_1 = \theta_2 \neq 0$, then $w_1 = W^1 \sqrt{a_{11}}$, $w_2 = W^2 \sqrt{a_{22}}$, $a = \sqrt{a_{11} a_{22}}$, equation (4.51) reduces to

$$\left. \begin{aligned}
\xi^1 &= \frac{1}{r \sqrt{a_{11} a_{22}}} \left[\frac{\partial(V_{\theta r})}{\partial x^2} - \frac{\partial(W^2 \sqrt{a_{22}})}{\partial \phi} \right] \\
\xi^2 &= \frac{1}{r \sqrt{a_{11} a_{22}}} \left[\frac{\partial(W^1 \sqrt{a_{11}})}{\partial \phi} - \frac{\partial(V_{\theta r})}{\partial x^1} \right] \\
\xi^3 &= \frac{1}{r \sqrt{a_{11} a_{22}}} \left[\frac{\partial(W^2 \sqrt{a_{22}})}{\partial x^1} - \frac{\partial(W^1 \sqrt{a_{11}})}{\partial x^2} \right]
\end{aligned} \right\} \tag{4.56}$$

and (4.49) reduces to

$$\frac{W^2}{\sqrt{a_{22}}} \left[\frac{\partial(W^2 \sqrt{a_{22}})}{\partial x^1} - \frac{\partial(W^1 \sqrt{a_{11}})}{\partial x^2} \right] - \frac{W_\varphi}{r} \left[\frac{\partial(W^1 \sqrt{a_{11}})}{\partial \varphi} - \frac{\partial(V_{\theta r})}{\partial x^1} \right] = \frac{\partial I}{\partial x^1} - T \frac{\partial s}{\partial x^1}$$

$$\frac{W_\varphi}{r} \left[\frac{\partial(V_{\theta r})}{\partial x^2} - \frac{\partial(W^2 \sqrt{a_{22}})}{\partial \varphi} \right] - \frac{W^1}{\sqrt{a_{11}}} \left[\frac{\partial(W^2 \sqrt{a_{22}})}{\partial x^1} - \frac{\partial(W^1 \sqrt{a_{11}})}{\partial x^2} \right] = \frac{\partial I}{\partial x^2} - T \frac{\partial s}{\partial x^2} \quad (4.57)$$

$$\frac{W^1}{\sqrt{a_{11}}} \left[\frac{\partial(W^1 \sqrt{a_{11}})}{\partial \varphi} - \frac{\partial(V_{\theta r})}{\partial x^1} \right] - \frac{W^2}{\sqrt{a_{22}}} \left[\frac{\partial(V_{\theta r})}{\partial x^2} - \frac{\partial(W^2 \sqrt{a_{22}})}{\partial \varphi} \right] = \frac{\partial I}{\partial \varphi} - T \frac{\partial s}{\partial \varphi}$$

If $\theta_{12} = 90^\circ$ and $\theta_1 = \theta_2 = 0$, then $\sqrt{a_{11}} = \sqrt{a_{22}} = 1$, equations (4.55) and (4.56) reduce to, respectively, (19) and (95) of reference 3 in which the orthogonal cylindrical coordinates r, ϕ, z are used.

(d) x^2 -line is normal to x^1 -line and x^1 -line is coincident with the projection of streamline on the meridional plane, then $\theta_1 = \theta_2 = \sigma$, $W^2 = 0$, $W^1 = W_\theta$, $w_1 = W_\theta \sqrt{a_{11}}$, $w_2 = 0$, $\sqrt{a} = \sqrt{a_{11} a_{22}}$ and equation (4.48) simplifies to

$$\begin{aligned}
\xi^1 &= \frac{1}{r\sqrt{a_{11}a_{22}}} \frac{\partial(V_{\theta r})}{\partial x^2} \\
\xi^2 &= \frac{1}{r\sqrt{a_{11}a_{22}}} \left[\frac{\partial(W^1\sqrt{a_{11}})}{\partial\varphi} - \frac{\partial(V_{\theta r})}{\partial\ell} \right] \\
\xi^3 &= - \frac{1}{r\sqrt{a_{11}a_{22}}} \frac{\partial(W^1\sqrt{a_{11}})}{\partial x^2}
\end{aligned} \tag{4.58}$$

and correspondingly

$$\begin{aligned}
\Xi^1 &= \frac{1}{r\sqrt{a_{22}}} \frac{\partial(V_{\theta r})}{\partial x^2} \\
\Xi^2 &= \frac{1}{\sqrt{a_{11}}} \left[\frac{\partial(W^1\sqrt{a_{11}})}{\partial\varphi} - \frac{\partial(V_{\theta r})}{\partial\ell} \right] \\
\Xi^3 &= - \frac{1}{\sqrt{a_{11}a_{22}}} \frac{\partial(W^1\sqrt{a_{11}})}{\partial x^2}
\end{aligned} \tag{4.59}$$

It is interesting to notice that in the present coordinate system the components of the absolute vorticity Ξ^1 and Ξ^3 contain only one term each, and that for flow, in which the absolute vorticity remains zero, both $V_{\theta r}$ and $W^1\sqrt{a_{11}}$ remain constant along the x^2 -line, while $W^1\sqrt{a_{11}}$ must vary with respect to the angular coordinate φ according to the variation of $V_{\theta r}$ with respect to the meridional coordinate ℓ as the fluid moves through the blade passage. In this coordinate system, equations (4.49) simplify to

$$\frac{W_\varphi}{r} \left[\frac{\partial(W_\ell \sqrt{a_{11}})}{\partial \varphi} - \frac{\partial(V_\theta r)}{\partial \ell} \right] = \frac{\partial I}{\partial \ell} - T \frac{\partial s}{\partial \ell} \quad (4.60a)$$

$$\frac{W_\varphi}{r} \frac{\partial(V_\theta r)}{\partial x^2} + \frac{W_\ell}{\sqrt{a_{11}}} \frac{\partial(W_1 \sqrt{a_{11}})}{\partial x^2} = \frac{\partial I}{\partial x^2} - T \frac{\partial s}{\partial x^2} \quad (4.60b)$$

$$\frac{W_\ell}{\sqrt{a_{11}}} \left[\frac{\partial(W^1 \sqrt{a_{11}})}{\partial \varphi} - \frac{\partial(V_\theta r)}{\partial \ell} \right] = \frac{\partial I}{\partial \varphi} - T \frac{\partial s}{\partial \varphi} \quad (4.60c)$$

4.6 Governing Equations for S_2 with Independent Variable φ Eliminated

The unit vector normal to the S_2 surface is expressed as

$$\mathbf{n} = n_i \mathbf{e}^i = N_i \mathbf{u}^i \quad (4.61)$$

the orthogonal relation is expressed by

$$n_i \mathbf{e}^i \cdot dx^i \mathbf{e}_i = n_1 dx^1 + n_2 dx^2 + n_\varphi d\varphi = \frac{N_1}{\sqrt{a^{11}}} dx^1 + \frac{N_2}{\sqrt{a^{22}}} dx^2 + N_\varphi r d\varphi = 0 \quad (4.62)$$

The derivative of fluid quantity on S_2 stream surface with respect to x^1 or x^2 with the other kept constant is

$$\frac{\partial}{\partial x^1} = \frac{\partial}{\partial x^1} + \frac{\partial}{\partial x^3} \frac{\partial x^3}{\partial x^1} = \frac{\partial}{\partial x^1} + \frac{\partial}{\partial \varphi} \frac{\partial \varphi}{\partial x^1} = \frac{\partial}{\partial x^1} - \frac{n_1}{n_\varphi} \frac{\partial}{\partial \varphi} = \frac{\partial}{\partial x^1} - \frac{N_1}{N_\varphi r \sqrt{a^{11}}} \frac{\partial}{\partial \varphi} \quad (4.63a)$$

$$\frac{\partial}{\partial x^2} = \frac{\partial}{\partial x^2} + \frac{\partial}{\partial x^3} \frac{\partial x^3}{\partial x^2} = \frac{\partial}{\partial x^2} + \frac{\partial}{\partial \varphi} \frac{\partial \varphi}{\partial x^2} = \frac{\partial}{\partial x^2} - \frac{n_2}{n_\varphi} \frac{\partial}{\partial \varphi} = \frac{\partial}{\partial x^2} - \frac{N_2}{N_\varphi r \sqrt{a^{22}}} \frac{\partial}{\partial \varphi} \quad (4.63b)$$

When equations (4.63) are used the continuity equation for steady relative flow becomes

$$\frac{\partial}{\partial x^1} \left(\tau \rho W^1 \sqrt{a_{22}} \sin \theta_{12} \right) + \frac{\partial}{\partial x^2} \left(\tau \rho W^2 \sqrt{a_{11}} \sin \theta_{12} \right) = 0 \quad (4.64)$$

where τ is the circumferential distance between two adjacent S_2 surfaces and the dynamic equations become

$$\frac{W^2}{\sqrt{a_{22}}} \left[\frac{\partial w_2}{\partial x^1} - \frac{\partial w_1}{\partial x^2} \right] + \frac{W_\varphi}{r} \frac{\partial (V_\theta r)}{\partial x^1} = \frac{\partial I}{\partial x^1} - T \frac{\partial s}{\partial x^1} - f_1 \quad (4.65a)$$

$$\frac{W_\varphi}{r} \frac{\partial(V_{\theta r})}{\partial x^2} - \frac{W^1}{\sqrt{a_{11}}} \left(\frac{\partial w_2}{\partial x^1} - \frac{\partial w_1}{\partial x^2} \right) = \frac{\partial I}{\partial x^2} - T \frac{\partial s}{\partial x^2} - f_2 \quad (4.65b)$$

$$\frac{D(V_{\theta r})}{Dt} = \frac{W^1}{\sqrt{a_{11}}} \frac{\partial(V_{\theta r})}{\partial x^1} + \frac{W^2}{\sqrt{a_{22}}} \frac{\partial(V_{\theta r})}{\partial x^2} = f_\varphi = F_{\varphi r} \quad (4.65c)$$

Alternatively, these equations can be obtained by projecting the three components of equation (96) of reference 2 in $\mathbf{e}^1, \mathbf{e}^2, \mathbf{e}^3$ directions. \mathbf{F} in these equations is the same \mathbf{F} of reference 2, f_i being its covariant components

$$\mathbf{F} = - \left(\frac{1}{n_\varphi} \frac{1}{\rho} \frac{\partial p}{\partial \varphi} \right) \mathbf{n} = - \frac{1}{N_{\varphi r}} \frac{1}{\rho} \frac{\partial p}{\partial \varphi} \mathbf{n} = f_i \mathbf{e}^i = F_i \mathbf{u}^i \quad (4.66)$$

From equations (4.26),

$$\frac{\partial w_2}{\partial x^1} - \frac{\partial w_1}{\partial x^2} = \frac{\partial}{\partial x^1} \left[(W^1 \cos \theta_{12} + W^2) \sqrt{a_{22}} \right] - \frac{\partial}{\partial x^2} \left[(W^1 + W^2 \cos \theta_{12}) \sqrt{a_{22}} \right] \quad (4.67)$$

Substituting equation (4.67) into equation (4.65) gives

$$\frac{W^2}{\sqrt{a_{22}}} \left\{ \frac{\partial}{\partial x^1} \left[(W^1 \cos \theta_{12} + W^2) \sqrt{a_{22}} \right] - \frac{\partial}{\partial x^2} \left[(W^1 + W^2 \cos \theta_{12}) \sqrt{a_{11}} \right] \right\} + \frac{W_\varphi}{r} \frac{\partial (V_{\theta r})}{\partial x^1} - \frac{\partial I}{\partial x^1} + T \frac{\partial s}{\partial x^1} = -f_1 \quad (4.68a)$$

$$\frac{\partial}{\partial x^2} \left[(W^2 + W^2 \cos \theta_{12}) \sqrt{a_{11}} \right] - \frac{\partial}{\partial x^1} \left[(W^1 \cos \theta_{12} + W^2) \sqrt{a_{22}} \right] = \frac{\sqrt{a_{11}}}{W^1} \left[-\frac{W_\varphi}{r} \frac{\partial (V_{\theta r})}{\partial x^2} + \frac{\partial I}{\partial x^2} - T \frac{\partial s}{\partial x^3} - f_2 \right] \quad (4.68b)$$

$$\frac{D(V_{\theta r})}{Dt} = \frac{W^1}{\sqrt{a_{11}}} \frac{\partial (V_{\theta r})}{\partial x^1} + \frac{W^2}{\sqrt{a_{22}}} \frac{\partial (V_{\theta r})}{\partial x^2} = f_\varphi = F_{\varphi r} \quad (4.68c)$$

Equation (4.68b) is the most important equation for S_2 flow just as equation (4.33) for S_1 surface flow.

Corresponding to the different choice of the x^1 - and x^2 -coordinates, equations (4.64) and (4.68) reduce to the following special equations:

(1) x^1 -line coincides with the projection of the streamline on the meridional plane.

$W^2 = 0$ and equations (4.64) and (4.68) simplify to, respectively

$$\frac{\partial}{\partial t} \left(r \rho W^1 \sqrt{a_{22}} \sin \theta_{12} \right) = 0 \quad (4.69)$$

and

$$\frac{W_\phi}{r} \frac{\partial(V_{\theta r})}{\partial t} - \frac{\partial I}{\partial t} + T \frac{\partial s}{\partial t} = -f_1 \quad (4.70a)$$

$$\frac{\partial(W_\ell \sqrt{a_{11}})}{\partial x^2} = \frac{\partial(W_\ell \sqrt{a_{22}} \cos \theta_{12})}{\partial t} + \frac{\sqrt{a_{11}}}{W_\ell} \left[-\frac{W_\phi}{r} \frac{\partial(V_{\theta r})}{\partial x^2} + \frac{\partial I}{\partial x^2} - T \frac{\partial s}{\partial x^2} - f_2 \right] \quad (4.70b)$$

$$\frac{D(V_{\theta r})}{Dt} = \frac{W_\ell}{\sqrt{a_{11}}} \frac{\partial(V_{\theta r})}{\partial t} = f_\phi = F_{\phi r} \quad (4.70c)$$

Equations (4.69) and (4.70b) of S_2 surface are quite similar to equations (4.29a) and (4.33a), respectively, of S_1 surface.

(2) x^1 -line coincides with the projection of the streamline on the meridional plane and x^2 -line is in the radial direction normal to the z -axis. Equations (4.69), (4.70a), and (4.70c) remain unchanged, but (4.70b) becomes

$$\frac{\partial(W_\ell \sqrt{a_{11}})}{\partial r} = \frac{\partial(W \sqrt{a_{22}} \sin \sigma)}{\partial \ell} + \frac{\sqrt{a_{11}}}{W_\ell} \left[-\frac{W_\varphi}{r} \frac{\partial(V_{\theta r})}{\partial r} + \frac{\partial I}{\partial r} - T \frac{\partial s}{\partial r} - f_r \right] \quad (4.71)$$

(3) x^1 -line coincides with the projection of the streamline on the meridional plane and x^2 -line is normal to x^1 -line. Equations (4.64), (4.70a) and (4.70c) remain unchanged, but (4.64) simplifies to

$$\frac{\partial(W_\ell \sqrt{a_{11}})}{\partial x^2} = \frac{\sqrt{a_{11}}}{W_\ell} \left[-\frac{W_\varphi}{r} \frac{\partial(V_{\theta r})}{\partial x^2} + \frac{\partial I}{\partial x^2} - T \frac{\partial s}{\partial x^2} - f_2 \right] \quad (4.72)$$

It is noticed that equation (4.70b) contains an f_2 term which is, in general, not equal to zero inside the blade passage.

By the use of equations (4.63), the energy equation (4.35) becomes

$$\frac{DI}{Dt} = \frac{W^1}{\sqrt{a_{11}}} \frac{\partial I}{\partial x^1} + \frac{W^2}{\sqrt{a_{22}}} \frac{\partial I}{\partial x^2} = 0 \quad (4.73)$$

For the special case where x^1 -line is coincident with the projection of the streamline on the meridional plane it simplifies to

$$\frac{\partial I}{\partial x^1} = 0 \quad (4.74)$$

4.7 Methods of Solution For S_2 Flow

Since the equations governing the flow along S_2 stream filament are quite similar to those along S_1 stream filament (the main difference being the difference in the partial derivatives involved), the methods of solution are also quite similar. In the first group of methods of solution, W^1 or Ψ is integrated along successive x^2 -coordinate lines, whereas in the second group of methods of solution Ψ -values at all grid points on the mid- S_2 surface are solved at the same time.

In the first group, if the x^1 -lines are corrected during calculation to coincide with the projection of the streamlines on the meridional plane, the continuity equation (4.64) gives

$$\rho W_t = (\rho W_\theta)_i \frac{(\tau \sqrt{a_{22}} \sin \theta_{12})_i}{\tau \sqrt{a_{22}} \sin \theta_{12}} \quad (4.75)$$

S_2 filament flow is calculated by considering the effect of entropy increase in the density equation

$$\Sigma = \frac{\rho}{\rho_o} \left(\frac{H - \frac{1}{2} V_\theta^2}{H_i} \right)^{-\frac{1}{\gamma-1}} e^{\frac{s-s_i}{R}} \quad (4.76)$$

$$\phi = \frac{\gamma-1}{2} \left(\frac{\rho W_t}{\rho_i a_i} \right)^2 \left(\frac{H_i}{H_i - \frac{1}{2} V_\theta^2} \right)^{\frac{\gamma+1}{\gamma-1}} e^{2\frac{s-s_i}{R}}$$

The values of ρ and W can be determined from their product by rewriting equation (4.75) in the form of equation (4.38) with

$$\frac{\partial(W_\ell \sqrt{a_{11}})^2}{\partial x^2} = 2a_{11} \left[-\frac{W_\varphi}{r} \frac{\partial(V_{\theta r})}{\partial x^2} + \frac{\partial I}{\partial x^2} - T \frac{\partial s}{\partial x^2} - f_2 \right] \quad (4.77)$$

The table in reference 3 can be used to find Σ (or ρ) from the known value of Φ (or ρW_ℓ). W_ℓ is then computed from ρW_ℓ after ρ is obtained.

The right side of equation (4.70b) is more complicated than equation (4.41) of S_1 flow. In the inverse or design problem, the variation of $V_{\theta r}$ is specified by the designer, whereas in the direct or analysis problem it is obtainable from the given shape of the S_2 surface (see next section for further discussion). The variation of I is obtained from its inlet value and equation (4.73). The variation of s is estimated from its inlet value and the empirical equation. $W_\ell \sqrt{a_{11}}$ is then integrated along the x^2 -lines from a streamline along the inner boundary or in the middle of the flow region in the same manner as that in the S_1 surface flow calculation. In the case where the x^2 -line is chosen normal to the x^1 -line it is convenient to rewrite equation (4.72) as

$$\dot{m} = K_\zeta \int_{(x^2)_h}^{x^2} \tau \rho W_\ell \sin \theta_{12} \sqrt{a_{22}} dx^2 \quad (4.78)$$

and integrate $(W_\ell \sqrt{a_{11}})^2$ along the x^2 -lines. After variation of W_ℓ along x^2 is obtained, the mass flow along x^2 is computed.

with

$$K_\zeta = \frac{2\pi r - Nt}{\zeta} = \frac{2\pi r}{\zeta} \left(1 - \frac{Nt}{2\pi r} \right) = \frac{2\pi r}{\zeta} \left(1 - \frac{t}{P} \right) = \frac{2\pi r}{\zeta} \left(\frac{P - t}{P} \right) \quad (4.79)$$



where ζ is a correction factor as indicated by figure 19 of reference 7. If the range of integration includes the wall boundary-layer regions, m calculated should be slightly greater than the actual mass flow because the calculated velocity in the wall boundary-layer region is greater than the actual value (see fig. 2.5). In the design problem we may either specify the mean streamline and obtain the coordinates of the inner and outer boundaries from given mass flow, or specify one boundary and obtain the other boundary. In the analysis problem, the mass flow calculation is used to correct the values of W_θ and ρ on the streamlines (see ref. 6).

If it is preferred to use fixed x^1 -lines, then the variation of ρW^1 along the x^2 -lines should be corrected according to continuity equation (4.64). Compute ρW by

$$\rho W = \left\{ [(\rho W^1)^2 + (\rho W^2)^2 - 2(\rho W^1)(\rho W^2) \cos \theta_{12}] + (\rho W_\varphi)^2 \right\}^{\frac{1}{2}} \quad (4.80)$$

integrate $W^1 \sqrt{a_{11}}$ along x^2 -line by

$$\begin{aligned} \frac{\partial(W^1 \sqrt{a_{11}})}{\partial x^2} = & \frac{\sqrt{a_{11}}}{W^1} \left[-\frac{W_\varphi}{r} \frac{\partial(V_\theta r)}{\partial x^2} + \frac{\partial I}{\partial x^2} - T \frac{\partial s}{\partial x^2} - f_2 \right] \\ & + \frac{\partial}{\partial x^1} \left[(W^1 \cos \theta_{12} + W^2) \sqrt{a_{22}} \right] - \frac{\partial}{\partial x^2} \left[W^2 \sqrt{a_{11}} \cos \theta_{12} \right] \end{aligned} \quad (4.81)$$

compute mass flow along x^2 -line by

~~0-2~~

$$\dot{m} = K \zeta \int_{(x^2)_h}^{x^2} \tau \rho W^1 \sin \theta_{12} \sqrt{a_{22}} dx^2 \quad (4.82)$$

and correct W^1 values at the fixed grid points in the same manner as in the previous case.

Analogous to the S_1 -surface problem, the continuity equation and dynamic equation may be solved simultaneously through the use of stream function. From equation (4.64) a stream function can be defined with

$$\left. \begin{aligned} \frac{\partial \Psi}{\partial x^1} &= -\tau \rho W^2 \sqrt{a_{11}} \sin \theta_{12} \\ \frac{\partial \Psi}{\partial x^2} &= \tau \rho W^1 \sqrt{a_{22}} \sin \theta_{12} \end{aligned} \right\} \quad (4.83)$$

Substituting equation (4.83) into the dynamic equation (4.65b) gives the following principal equation for flow along S_2 stream filament.

$$\frac{1}{a_{11}} \frac{\partial^2 \Psi}{\partial (x^1)^2} - 2 \frac{\cos \theta_{12}}{\sqrt{a_{11} a_{22}}} \frac{\partial^2 \Psi}{\partial x^1 \partial x^2} + \frac{1}{a_{22}} \frac{\partial^2 \Psi}{\partial (x^2)^2} + \frac{J}{\sqrt{a_{11}}} \frac{\partial \Psi}{\partial x^1} + \frac{K}{\sqrt{a_{22}}} \frac{\partial \Psi}{\partial x^2} = M \quad (4.84)$$

where

$$\begin{aligned}
J &= -\frac{\partial \ln \left(\sqrt{a_{11}/a_{22}} \tau \sin \theta_{12} \right)}{\sqrt{a_{11}} \partial x^1} + \frac{\cos \theta_{12}}{\sqrt{a_{22}}} \frac{\partial \ln \tau}{\partial x^2} + \frac{1}{\sin \theta_{12} \sqrt{a_{22}}} \frac{\partial \theta_{12}}{\partial x^2} \\
K &= -\frac{\partial \ln \left(\sqrt{a_{22}/a_{11}} \tau \sin \theta_{12} \right)}{\sqrt{a_{22}} \partial x^2} + \frac{\cos \theta_{12}}{\sqrt{a_{11}}} \frac{\partial \ln \tau}{\partial x^1} + \frac{1}{\sin \theta_{12} \sqrt{a_{11}}} \frac{\partial \theta_{12}}{\partial x^1} \\
M &= \left(\frac{1}{\sqrt{a_{11}}} \frac{\partial \ln \rho}{\partial x^1} - \frac{\cos \theta_{12}}{\sqrt{a_{22}}} \frac{\partial \ln \rho}{\partial x^2} \right) \frac{1}{\sqrt{a_{11}}} \frac{\partial \Psi}{\partial x^1} \\
&+ \left(\frac{1}{\sqrt{a_{22}}} \frac{\partial \ln \rho}{\partial x^2} - \frac{\cos \theta_{12}}{\sqrt{a_{11}}} \frac{\partial \ln \rho}{\partial x^1} \right) \frac{1}{\sqrt{a_{22}}} \frac{\partial \Psi}{\partial x^2} + \frac{\tau \sin \theta_{12}}{\sqrt{a_{11} a_{22}}} \rho C
\end{aligned}$$

Equation (4.84) may be considered as a generalization of the principal equation (107a) of reference 3 where orthogonal curvilinear coordinates r, φ, z are used. When x^1 and x^2 become z and r , respectively, equation (4.85) reduces to equation (107a) of reference 3.

When the Ψ -derivatives are evaluated by suitable numerical differentiation formulas of equal or unequal spacing (ref. 27), the resulting set of a large number of algebraic equations containing the unknown Ψ -values at the grid points are obtained. Also the dynamic equation may be written as

$$\begin{aligned}
\oint \mathbf{t} \cdot \mathbf{W} dL &= \iint (\nabla \times \mathbf{W})_{\varphi} \sqrt{a_{11} a_{22}} \sin \theta_{12} dx^1 dx^2 \\
&= \iint \frac{\sqrt{a_{11}}}{W^1} \left[\frac{W_{\varphi}}{r} \frac{\partial (V_{\theta} r)}{\partial x^2} - \frac{\partial I}{\partial x^2} + T \frac{\partial s}{\partial x^2} - f_2 \right] dx^1 dx^2
\end{aligned} \tag{4.85}$$

and integration along 1, 2, ..., 8, 1 around the grid point E results in an algebraic equation containing the Ψ -values at the grid points A, B, ..., I, (fig. 4.7). The resulting set of algebraic equations containing

unknown Ψ -values at the grid points in the order of several hundred for one stream filament, can be solved by either the direct matrix method or relaxation method as employed in references 3 to 8, 11 and 12.

4.8 Computation of \mathbf{F} Term in Inverse Problem

It is pointed out in Chapter 3 that in the inverse or design problem the following condition of integrability should be used in the solution in the fluid flow along the S_2 stream filament.

$$\mathbf{F} \cdot \nabla \times \mathbf{F} = 0 \quad (4.86)$$

When general curvilinear coordinates are employed, substituting equations (4.12), (4.17) and (4.63) into equation (4.86) gives

$$\frac{\partial}{\partial x^1} \left(\frac{f_2}{f_\varphi} \right) = \frac{\partial}{\partial x^2} \left(\frac{f_1}{f_\varphi} \right) \quad (4.87)$$

Then

$$\frac{f_2}{f_\varphi} = \left(\frac{f_2}{f_\varphi} \right)_0 + \int_{(x^1)_0}^{x^1} \frac{\partial}{\partial x^2} \left(\frac{f_1}{f_\varphi} \right) dx^1 \quad (4.88)$$

or

$$\frac{F_2}{\sqrt{a^{22}} F_{\varphi r}} = \left(\frac{F_2}{\sqrt{a^{22}} F_{\varphi r}} \right)_o + \int_{(x^1)_o}^{x^1} \frac{\partial}{\partial x^2} \left(\frac{F_1 / \sqrt{a_{11}}}{F_{\varphi r}} \right) dx^1 \quad (4.89)$$

The procedure of calculating f_2 is similar to f_r of references 2, 12 and 16. Compute f_1 from equation (4.68a), f_{φ} from (4.68c), the derivative of f_1/f_{φ} with respect to x^2 , then integrate f_2 along x^1 from $(x^1)_o$, where f_2 is known. It is convenient to choose $(x^1)_o$ at a station where F_r is equal to zero because F_2 can then be computed from F_1 .

4.9 Computation of Components of Normal and W_{φ} In Direct Problem

In the direct or analysis problem, the known S_2 surface offers two relations between the \mathbf{n} - or \mathbf{F} -components. Since \mathbf{n} is normal to \mathbf{W} ,

$$\mathbf{n} \cdot \mathbf{W} = n_1 w^1 + n_2 w^2 + n_{\varphi} w_{\varphi} = \frac{N_1}{\sqrt{a^{11}}} \frac{W^1}{\sqrt{a_{11}}} + \frac{N_2}{\sqrt{a^{22}}} \frac{W^2}{\sqrt{a_{22}}} + N_{\varphi} W_{\varphi} = 0 \quad (4.90)$$

or

$$N^1 W^1 \sin \theta_{12} + N^2 W^2 \sin \theta_{12} + N_{\varphi} W_{\varphi} = 0 \quad (4.91)$$

then

$$W_\varphi = - \left(\frac{N_1}{N_\varphi} W^1 + \frac{N_2}{N_\varphi} W^2 \right) \sin \theta_{12} \quad (4.92)$$

This equation is similar to the equation appearing in section 3.3. The ratio of the N-components may be obtained by the following consideration: Along the intersection of the S_2 surface and a constant x^2 surface

$$\frac{N_1}{N_\varphi} = - r \left(\frac{\partial \varphi}{\partial x^1} \right) \sqrt{a^{11}} = - r \left(\frac{\partial \varphi}{\partial x^1} \right)_{x^2=(x^1)_o} \left(\sqrt{a_{11}} \sin \theta_{12} \right)^{-1} \quad (4.93)$$

Along the intersection of the S_2 surface and a constant x^1 surface

$$\frac{N_2}{N_\varphi} = - r \left(\frac{\partial \varphi}{\partial x^2} \right) \sqrt{a^{22}} = - r \left(\frac{\partial \varphi}{\partial x^2} \right)_{x^1=(x^1)_o} \left(\sqrt{a_{22}} \sin \theta_{12} \right)^{-1} \quad (4.94)$$

Knowing these N-ratios W_φ can be computed from equation (4.92) and V_θ computed from W_φ . F_φ is then calculated by equation (4.68c) and F_2 by

$$F_2 = \frac{N_2}{N_\varphi} F_\varphi \quad (4.95)$$

CHAPTER 5

TWO- AND THREE-DIMENSIONAL SUBSONIC FLOW IN TURBOMACHINES

5.1 Series Expansion on S_1 Surface of Revolution

The intersection of an S_1 surface with a mid-channel S_2 surface is a streamline lying in the mid-passage on the S_1 surface (fig. 5.1) and is referred to as the "mean streamline" in references 54 and 4 to 6. In order to get an idea about fluid flow along the $S_{2,m}$ filament with reference to the flow in the three-dimensional channel, the fluid flow along the mean streamline was examined in that reference based on the solution of compressible (subsonic) flow in a typical two-dimensional turbine cascade obtained by an electro-mechanical hand computer in the late forties.

Figure 5.2 shows that as the inlet Mach number increases, the increase in the velocity along the mean streamline is larger toward the suction surface. The dip in velocity variation along the suction surface is also seen along the mean streamline. In figure 5.3 the shape of the mean streamline is compared to those of the mid-channel line and the mean chamber line.

Figure 5.4 compares the variation of the specific mass flow along the mean streamline to the one-dimensional variation, the passage width. Inside the blade passage the former is a few percent greater than the latter, however the difference at the leading edge is large (25 percent). The effect of the blade thickness extends 40 percent upstream and downstream of the blade is also apparent.

The variation of tangential velocity and its rate along the mean streamline are shown in figure 5.5. The two begin to vary at 60 percent chord length upstream of the blade and end at 60 percent chord length downstream of the blade.*

Based on the preceding observation a very simple, quick approximate solution of the inverse or direct problem for fluid flow along an arbitrary S_1 stream filament or revolution was proposed in references 5 and 6. Any flow variable on the mean streamline is considered a function of the meridional coordinate ℓ .

$$q = q[\ell, \varphi(\ell)] \quad (5.1)$$

Its total variation with respect to ℓ is

$$\frac{dq}{d\ell} = \frac{\partial q}{\partial \ell} + \frac{\partial q}{\partial \varphi} \frac{d\varphi}{d\ell} = \frac{\partial q}{\partial \ell} + \frac{\tan \beta}{r} \frac{\partial q}{\partial \varphi} \quad (5.2)$$

From the continuity and dynamic equation the following equations for the first derivatives, with respect to the angular coordinate φ of the velocity components, are

$$\frac{\partial W_\ell}{\partial \varphi} = \left[r \frac{dW_\phi}{d\ell} + \frac{\tan \beta}{r\rho} \frac{d(\tau r \rho W_\ell)}{d\ell} + (W_\phi + 2\omega r) \sin \sigma \right] \cos^2 \beta \quad (5.3)$$

* A variation of tangential velocity, similar to that shown in Fig. 5.5 but simpler, was used in the calculation of fluid flow on $S_{2,m}$ surface in Refs. 10 and 11.

$$\frac{\partial W_\phi}{\partial \phi} = \left\{ \left[r \frac{dW_\phi}{d\ell} + (W_\phi + 2\omega r)\sin \sigma \right] \tan \beta - \frac{1}{r\rho} \frac{d(\tau r \rho W_\ell)}{d\ell} \right\} \cos^2 \beta \quad (5.4)$$

$$\frac{\partial^2 W_\ell}{\partial \phi^2} = r \frac{d}{d\ell} \frac{\partial W_\phi}{\partial \phi} - \tan \beta \frac{\partial^2 W_\phi}{\partial \phi^2} + \sin \sigma \frac{\partial W_\phi}{\partial \phi} \quad (5.5)$$

$$\begin{aligned} \frac{\partial^2 W_\phi}{\partial \phi^2} = & \left\{ \frac{2}{r\rho^2} \frac{\partial \rho}{\partial \varphi} \frac{d(\tau r \rho W_\ell)}{d\ell} - \frac{1}{r\rho} \frac{d}{d\ell} \left[r r \left(\rho \frac{\partial W_\ell}{\partial \varphi} + W_\ell \frac{\partial \rho}{\partial \varphi} \right) \right] \right. \\ & \left. + \tan \beta \left(r \frac{d}{d\ell} \frac{\partial W_\phi}{\partial \phi} + \sin \sigma \frac{\partial W_\phi}{\partial \phi} \right) \right\} \cos^2 \beta \end{aligned} \quad (5.6)$$

The variation of a velocity component W_ℓ or other flow variables in the circumferential direction is given by the Taylor series

$$q(\phi) = q_m + (\phi - \phi_m) \left(\frac{\partial q}{\partial \phi} \right)_m + \frac{(\phi - \phi_m)^2}{2} \left(\frac{\partial^2 q}{\partial \phi^2} \right)_m + \dots \quad (5.7)$$

The mass flow between the mean streamline and suction and pressure surfaces are, respectively,

$$M_s = \tau r \int_{\varphi_s}^{\varphi_m} \rho W_t d\varphi \quad (5.8)$$

and

$$M_p = \tau r \int_{\varphi_m}^{\varphi_p} \rho W_t d\varphi \quad (5.9)$$

The mass flow between the streamline selected in the mid-passage of a radial-flow impeller and the suction surface, is 65 percent of total mass flow (ref. 6). The streamline distribution and the variation of the meridional velocity along the mean streamline are shown in figures 5.7 and 5.8, respectively. It is interesting to see that the final value of W_t obtained in the series (three terms) calculation is quite different from the constant value assumed in the design and compares well with the value obtained in the accurate direct matrix solution (ref. 8).

This method has been improved and further developed in references 55 to 57. Recently a computer code employing fourth order Taylor series has been developed (ref. 58). In the case of a transonic turbine cascade the result obtained by using the fourth order series is generally better than the result obtained by using the second order series (fig. 5.9). It is also seen from the figure that the result agrees with the experimental data better than that obtained by the time-marching method reported in reference 35, especially in the low supersonic region. Yet the code can be put on a TI-59 pocket calculator. (Computing time on this calculator is 3 min per station).

5.2 Series Expansion In φ -Coordinate

The circumferential extension of flow properties on a mean streamline by series expansion along the S_1 surface of revolution, described in the previous section, can readily extend to a circumferential extension of flow properties on a mean S_2 stream surface by series expansion in the three-dimensional blade channel. Because S_1 flow surface of revolution is not assumed here, the three-dimensional series expansion method yields a full-three-dimensional flow field, whereas the use of series expansion on a number of S_1 stream surfaces of revolution yields a quasi-three-dimensional flow field.

Partial Derivatives of Flow Quantities in Nonorthogonal Curvilinear Coordinates: Flow properties at a point in the three-dimensional flow channel are calculated by Taylor series expansion similar to equation (5.7). The first order partial derivative of W^i and ρ , with respect to φ can be obtained from the three-dimensional vorticity components, equation (4.17), for isentropic irrotational flow, is as follows (refs. 59, 61):

$$\begin{bmatrix} \sqrt{a_{22}} \cos \theta_{12} & \sqrt{a_{22}} & r \frac{\partial \varphi}{\partial x^2} \\ \sqrt{a_{11}} & \sqrt{a_{11}} \cos \theta_{12} & r \frac{\partial \varphi}{\partial x^1} \\ \frac{1}{\sqrt{a_{11}}} \frac{\partial \varphi}{\partial x^1} & \frac{1}{\sqrt{a_{22}}} \frac{\partial \varphi}{\partial x^2} & \frac{1}{r} \end{bmatrix} \cdot \begin{bmatrix} \frac{\partial W^1}{\partial \varphi} \\ \frac{\partial W^2}{\partial \varphi} \\ \frac{\partial W_\varphi}{\partial \varphi} \end{bmatrix} = \begin{bmatrix} \frac{\partial(V_\theta r)}{\partial x^2} \\ \frac{\partial(V_\theta r)}{\partial x^1} \\ C \end{bmatrix} \quad (5.10)$$

where

$$C = \left[\frac{\partial}{\partial x^1} \left(r \rho W^1 \sqrt{a_{22}} \sin \theta_{12} \right) + \frac{\partial}{\partial x^2} \left(r \rho W^2 \sqrt{a_{11}} \sin \theta_{12} \right) \right] \frac{1}{r \rho \sqrt{a_{11}}}$$

and

$$\frac{\partial \rho}{\partial \varphi} = \frac{\rho}{(\gamma - 1)h} \left[\frac{\partial I}{\partial \varphi} - \frac{\partial}{\partial \varphi} \left\{ \left[(\rho W^1)^2 + (\rho W^2)^2 - 2(\rho W^1)(\rho W^2) \cos \theta_{12} \right] + (\rho W \varphi)^2 \right\} \right]$$

The higher order derivatives can also be obtained from the basic equations.

5.3 Forming Successive S_2 Surfaces by Progressing Circumferentially from $S_{2,m}$

Similar to that in the two-dimensional series expansion method, the space coordinate φ of the S_2 surfaces can be obtained by the following series (ref. 59)

$$\Delta \varphi = \varphi - \varphi_m = (\Psi_2 - \Psi_{2m}) \left(\frac{\partial \varphi}{\partial \Psi_2} \right)_m + \frac{1}{2} (\Psi_2 - \Psi_{2m})^2 \left(\frac{\partial^2 \varphi}{\partial \Psi_2^2} \right)_m + \dots \quad (5.11)$$

where φ is the circumferential coordinate of any S_2 surface and Ψ_2 is the value of stream function of that S_2 surface.

In reference to figure 5.10 the integrating factor B of S_2 surface in section 4.5 is related to its inlet value by

$$\frac{B}{B_i} = \frac{\Delta \varphi}{(\Delta \varphi)_i} \quad (5.12)$$

The inlet plane Z_i is taken sufficiently far upstream of the blade row where the flow is uniform. The difference of stream function Ψ between two adjacent S_2 surfaces is the mass flow passing through the shaded area in figure 5.10, i.e.,

$$\Delta \Psi_2 = \left[\rho W (r_c^2 - r_h^2) \Delta \varphi \right]_i \quad (5.13)$$

With the use of equations (5.12) and (5.13) the φ coordinate of S_2 surface can be determined step-by-step as shown in figure 5.11. The velocity component W^i and ρ at the S^1, S^2, \dots are then calculated by Taylor series expansion.

The method described in the preceding paragraphs was programmed in Fortran IV and employed to investigate three-dimensional flow in a compressor stator and a turbine rotor. Less than 3 min were needed on a M150 computer (0.4 MIP). The turbine rotor is designed for a pressure ratio of 1.4, inlet absolute Mach number of 0.4, and rotor hub tip ratio of 0.66.

Figure 5.12 shows the projection of the streamlines on $S_{2,m}$ surface on the meridional plane. The blade shape and the velocity distribution around the blade is shown in figure 5.13. The intersections of the S_1 and S_2 surfaces, with the through-flow cross-sections, are shown in figure 5.14.

The twist of the S_1 surface in the radial direction (fig. 5.14) is seen, generally, radially outward toward the suction surface. As this turbine rotor is designed for radially nonuniform work output, the radial twist of S_1 surface is relatively large, but it is still under 3 percent. The differences in the normal distance between the adjacent S_1 stream surface, both in the flow direction and in the circumferential direction of the twisted S_1 surfaces, and the untwisted S_1 surfaces of revolution will explain the difference in flow fields between the two cases.

5.4 Coordinate Transformation and Direct Expansion Method

For a more accurate determination of the coordinates of the S_2 surfaces and flow properties on these surfaces, the following coordinate transformation is made:

$$\begin{aligned}\xi &= x^1(r,z) \\ \eta &= x^2(r,z) \\ \psi_2 &= \psi_2(r,\varphi,z)\end{aligned}\tag{5.16}$$

The surfaces of revolution formed by revolving the x^1 - and x^2 -coordinate lines around the z -axis and the S_2 surfaces are the new coordinate surfaces (fig. 5.15). From the continuity and dynamic equations, the following first order partial derivatives are obtained (refs. 60 and 61):

$$\begin{bmatrix} \sqrt{a_{22}} \cos \theta_{12} & \sqrt{a_{22}} & r \frac{\partial \varphi}{\partial x^2} \\ \sqrt{a_{11}} & \sqrt{a_{11}} \cos \theta_{12} & r \frac{\partial \varphi}{\partial x^1} \\ \frac{1}{\sqrt{a_{11}}} \frac{\partial \varphi}{\partial x^1} & \frac{1}{\sqrt{a_{22}}} \frac{\partial \varphi}{\partial x^2} & \frac{1}{r} \end{bmatrix} \cdot \begin{bmatrix} \frac{\partial W^1}{\partial \psi_2} \\ \frac{\partial W^2}{\partial \psi_2} \\ \frac{\partial W_\varphi}{\partial \psi_2} \end{bmatrix} = \begin{bmatrix} \frac{\partial(V_{\theta r})}{\partial x^2} B \\ \frac{\partial(V_{\theta r})}{\partial x^1} B \\ C' \end{bmatrix} \quad (5.17)$$

where

$$C' = \frac{W^1}{\sqrt{a_{11}}} \frac{\partial B}{\partial x} + \frac{W^2}{\sqrt{a_{22}}} \frac{\partial B}{\partial x}$$

and

$$\frac{\partial \rho}{\partial \psi_2} = \frac{\rho}{(\gamma - 1)h} \left[\frac{\partial I}{\partial \psi_2} - \frac{\partial}{\partial \psi_2} \left\{ [(\rho W^1)^2 + (\rho W^2)^2 - 2(\rho W^1)(\rho W^2) \cos \theta_{12}] + (\rho W_\varphi)^2 \right\} \right] \quad (5.18)$$

In addition second order partial derivatives are also obtained. Then

$$\varphi = \varphi_m + (\psi_2 - \psi_{2m})B_m + \frac{1}{2} (\psi_2 - \psi_{2m})^2 \left(\frac{\partial B}{\partial \psi_2} \right)_m + \frac{1}{6} (\psi_2 - \psi_{2m})^3 \left(\frac{\partial^2 \beta}{\partial \psi_2^2} \right)_m \dots \quad (5.19)$$

$$W_{(\psi_{2s})}^1 = W_{(\psi_{2m})}^1 + (\psi_{2s} - \psi_{2m}) \frac{\partial W^1(\psi_{2m})}{\partial \psi_2} + \frac{1}{2} (\psi_{2s} - \psi_{2m})^2 \frac{\partial^2 W^1(\psi_{2m})}{\partial \psi_2^2} \quad (5.20)$$

This approximate method of solving three-dimensional flow has been programmed in Fortran IV. The complete solution was computed on a UNIVAC-1100 computer in less than 1 min.

The method was used to calculate the three-dimensional flow field in the Chinese Academy of Sciences's (CAS) research compressor (ref. 62). The mass flow is 61 kg/s, the rotor tip M is 1.4, the stage total-pressure ratio is 1.5, the hub-tip ratio at stator inlet is 0.49, and the number of stator blades is 37. Projections of $S_{2,m}$ and its streamline projection on the meridional plane are shown in figure 5.16.

The blade shape and distribution of velocity on the $k = 7$ coordinate surface obtained by this method and the stream surface extension method are compared in figure 5.17. The difference between the two is small. A comparison of Mach number distribution with that obtained by the S_1/S_2 iterative solution (see section 5.9) are shown in figure 5.18. Except near the leading edge, the result obtained from the present method is close to that of the three-dimensional solution. The relative twist of S_1 surfaces at the suction surface (J-4) is shown in figure 5.19. R_m is the value of R on the $S_{2,m}$ surface of the same S_1 surface. (R is the local value to the point $j = 4, k = 1, \dots, 11$.) It is seen that the largest $\Delta R/R$ occurs a short distance from the hub wall and the maximum difference between the present solution and the full-three-dimensional solution also occurs there. It may be noticed that the maximum relative twist is rather small, being less than 1 percent.

5.5 Direct Matrix Solution of Subsonic Flow Along S_1 Filament of Revolution

The method of employing general nonorthogonal curvilinear coordinates and corresponding nonorthogonal velocity components to express the basic equations governing the fluid flow along S_1 and S_2 stream filaments were developed during the sixties (refs. 28 and 29). Since 1969, computer codes using general curvilinear coordinates have become available for flow along the S_2 (ref. 40) and S_1 (ref. 64) stream filaments.

When nonorthogonal curvilinear coordinates (x^1, x^2) are selected on the flow surface of revolution (fig. 4.1) the principal equation (4.48) is to be solved. The metric tensor $a_{\alpha\beta}$ involved in the equation is calculated from the given geometry of the blading in cylindrical coordinate system (ℓ, φ) by the following equations:

$$\begin{aligned}
 a_{11} &= \left(\frac{\partial \ell}{\partial x^1} \right)^2 + r^2 \left(\frac{\partial \varphi}{\partial x^1} \right)^2 \\
 a_{22} &= \left(\frac{\partial \ell}{\partial x^2} \right)^2 + r^2 \left(\frac{\partial \varphi}{\partial x^2} \right)^2 \\
 a_{12} &= \frac{\partial \ell}{\partial x^1} \frac{\partial \ell}{\partial x^2} + r^2 \frac{\partial \varphi}{\partial x^1} \frac{\partial \varphi}{\partial x^2} \\
 \cos \theta_{12} &= \frac{a_{12}}{\sqrt{a_{11} a_{22}}}
 \end{aligned} \tag{5.21}$$

Discretization with the use of second order central numerical differentiation formula leads to a nine-point star in the two coordinates (fig. 4.7). The resulting N algebraic equations for the N interior grid points is written as

$$[M]\{\Psi\} = \{P\} \quad (5.22)$$

The coefficient matrix $[M]$ is a tridiagonal matrix. In order to take advantage of the zero elements in $[M]$, one row of fictitious grid points was added upstream and downstream of the blade and the only coefficient along the diagonals was numbered and stored (ref. 63), thus reducing the storage requirement for the coefficient matrices. For a problem of $m = 47$, $n = 11$, (517 grid points), only 28 000 coefficients are stored. Therefore, 32 K internal storage is sufficient.

As in references 10, 11, and 63, the coefficient matrix is factored to a lower triangular matrix $[L]$ and an upper triangular matrix $[u]$ which has elements along the diagonal equal to unity. Thus, equation (5.22) becomes

$$[L][u]\{\Psi\} = \{P\} \quad (5.23)$$

$\{\Psi\}$ is then obtained by a simple forward and backward substituting process as follows:

$$\text{Calculate } \{Q\} \text{ from } [L]\{Q\} = \{P\} \quad (5.24)$$

$$\text{Calculate } \{\Psi\} \text{ from } [u]\{\Psi\} = \{Q\} \quad (5.25)$$

The preceding direct factorization technique was available in the forties. It was first utilized to solve the $S_{2,m}$ flow in a gas turbine (ref. 10) Only 385 interior points were involved in that problem, and the method was tested on an IBM CPCE and a UNIVAC. Nine digits were used on the former and 11 digits were used on the latter. The results agree up to the fifth digit. The residual left at any grid point is less than one in the eighth digit.

As in references 10, 11, and 63 density is obtained by storing the $\Sigma - \Phi$ table (eqs. 4.39 to 4.41) in the computer. During the iteration process for Ψ and the density terms on the right side of the principal equation (4.47), the relaxation factor for density equal to unity is good for quick convergence, whereas, the relaxation factor for Ψ should be reduced from 1 to 0.5 when the inlet Mach number increases from low subsonic to high subsonic. Depending on the inlet Mach number, usually 10 to 20 iterations are required to reach the following convergence criterion (ref. 63):

$$\frac{\rho^{\nu+1} - \rho^{\nu}}{\rho^{\nu}} < 10^{-5}$$

$$\frac{\psi^{\nu+1} - \psi^{\nu}}{\psi^{\nu}} < 10^{-4}$$
(5.26)

This computer code has been widely used by a number of people on a number of different computers. On a Sun 4/110 (32-bit, 7-MIPS) computer, 20 iterations for an S_1 problem of 500 grid points were computed in less than 30 sec.

This code has been modified slightly by adding a nearly orthogonal C-mesh sub-system around the leading edge of the blade (ref. 65) (fig. 5.20). The Ψ -values at the boundary of this sub-grid-system are taken from the result of the solution formerly obtained with the H-shape grid system. This additional

calculation improves the flow field around the leading edge (fig. 5.20). Not only the peak velocity (fig. 5.21), but also the stagnation point at the leading edge are correctly determined as indicated in figure (5.22). For the blade shown in figure 5.22, the positions of the stagnation point corresponding to a number of inlet angles are shown in figure 5.23.

Alternately an H-C mesh, such as that shown in figure 5.24, may be used in the computation of S_1 flow to obtain flow computation around the leading edge accurately. The H-C grid is obtained by a numerical solution of Poisson's equation incorporating finer grids in areas of the physical plane where large flow gradient exists.

The computer code of reference 43 has been slightly modified to obtain the flow field through a turbomachine blade row having splitter vanes or tandem blades (ref. 66). Division of mass flow by the splitter vane (fig. 5.25) and the outlet flow angle are determined by applying Kutta-Joukosky condition to the trailing edges of the main blade and the splitter vane. Figures 5.25 and 5.26 show some of the results obtained in an investigation of the effects of replacing one half of the main blade by splitter vane. Figure 5.26 reveals that by substituting seven splitter vanes, which have half of the chord length and the same shape as the main blade (except around the leading edge), the peak velocity at the leading edge of the main blade is reduced to about the same value in a cascade of half the solidity. The Mach number at the second peak is also reduced. On the other hand, the outlet angle is reduced only 1.2° compared to 2.3° in cascade of half the solidity.

Iterative SOR and Direct Matrix Solution of Subsonic Flow Along S_2 Filament

The computer code for the solving of the principal equation (4.84) for fluid flow along an S_2 stream filament, employing nonorthogonal curvilinear coordinates and corresponding nonorthogonal velocity components, was first programmed by the use of iterative relaxation method (ref. 64). In order to get an accurate solution, at least six stations are placed inside the blade passage (from leading edge to trailing

edge of the blade). Because of the large number of grid points involved in multistage machines (fig. 2.4) a large internal storage capability is required. However, such storage was not available at that time, the line over-relaxation iterative method was used. Usually 20 to 30 iterations are required to reach the same convergence criterion set for S_1 calculation. (In this way, 1200 grid points can be used on a 32K internal storage.) Recently the same principal of equation has been programmed using the direct matrix method of solution.

Similar to the S_1 flow passing through the blade row having splitter vanes, this code has also been slightly modified for calculating S_2 flow for fan blades, downstream of which the flow is divided into the core compressor and the outer annulus.

Examples of solutions obtained by this computer code will be given in the next section for three-dimensional flow calculation and also in chapters 6 and 7 for transonic flow.

The S_2 computer code is programmed for the inverse problem, i.e., the variation of $V_{\theta r}$ along the S_2 surface is specified by the designer and the condition of integrability is incorporated in the code (see section 3.3). Equations (4.92) to (4.94) are also incorporated in the program so that it may be used to calculate $V_{\theta r}$ from W_{φ} . Thus the same code can also be used for direct problem.

5.6 Three-Dimensional Subsonic Flow in Turbomachine

Three-Dimensional Flow and Quasi-Three-Dimensional Flow in Turbomachines

In general the solution for three-dimensional flow in turbomachines involves the use of a number of S_1 and S_2 stream filaments. Flow through a three-dimensional flow passage formed by two adjacent blades can be considered to consist of a large number of thin S_1 stream filaments (fig. 5.27) and the flow

in each filament can be taken to be the same as that on the S_1 stream surface at mid-height of the filament (fig. 5.28). Similarly, the flow through the passage can be considered to be consist of a large number of S_2 stream filaments (see fig. 5.29) and the flow in each filament can be taken to be the same as that on the S_2 stream surface in the mid-circumferential position of the filament. The two families are related in the following manner: The stream surface of one family is formed by joining the corresponding streamlines lying on the stream surfaces of the other family. Hence iteration between the solutions of the flow through the two families of stream filaments is necessary to obtain the three-dimensional flow. Theoretically the solution becomes exact when the number of filaments becomes very large. However, for engineering accuracy, 8 to 10 filaments in each family is sufficient.

For axial-flow turbomachines the twist of the S_1 stream surface is usually not large. In the so-called "quasi-three-dimensional" solution all of the S_1 -stream surfaces are assumed to be surfaces of revolution. In that case the radius coordinate and the normal thickness of the filament do not vary in the circumferential direction. Any variation in flow direction can be determined by the use of only one S_2 surface. In the following, the S_2 surface lying in the mid-channel, the $S_{2,m}$ surface, will be used (fig. 5.30). This choice is, of course, arbitrary. But, it is preferred, since (1) the shape of that surface bears some resemblance to the mean surface, (2) the flow on that surface is an approximate average flow in the channel, (3) the calculation of the flow on that surface is the first step of practical three-dimensional blade design process, and (4) calculation of flow on more S_2 surfaces will be involved in the full-three-dimensional solution. The geometry of the S_1 stream surface determined by an axially symmetrical solution or by an averaging process of the flow in the circumferential direction would give a quasi-three-dimensional flow solution different from the one described herein.

Three-Dimensional Blade Design Procedure

It is suggested that the following steps may be followed in a three-dimensional blade design process:

- (1) Determine flow path in the meridional plane. Simplified radial equilibrium calculation is made at a number of stations between rows (ref. 1). If desired, this flow path can be modified in the $S_{2,m}$ calculation in the third step.
- (2) Estimate radial variations of stator stagnation pressure loss and rotor isentropic efficiency and compute the corresponding entropy increases across the blade row (see section 2.5). Assume linear variation of entropy in the flow direction except at the passage shock. It is desirable to check the loss with boundary layer calculation in later cycles.
- (3) Assume the variations of τ/τ_i and $(V_{\theta r})/(V_{\theta r})_i$ along the mid-channel S_2 filament (see section 5.1). Solve the $S_{2,m}$ principal equation for Ψ_2 (section 4.6). Compute density and velocity components. Compute coordinates $\varphi(x^1, x^2)$ or (ℓ, φ) and examine the shape of $S_{2,m}$ for its smoothness.
- (4) Obtain the geometry of the S_1 stream filaments of revolution, $[\mathbf{r}(z), r(z)]$ from the meridional projection of streamlines on $S_{2,m}$. Design the blade section by the mean-streamline/series expansion method (section 5.1) or select standard blade section on the conical surface that approximates the S_1 surface in the blade passage. Solve the S_1 principal equation for Ψ (section 4.4). Compute velocity components and density. If the ρ or \mathbf{W} distribution around the blade has to be improved, repeat the design or blade selection process in step 4. An inverse calculation is available to modify the blade shape for a better \mathbf{W} or ρ distribution around the blade (ref. 67). The new values of $V_{\theta r}$ and τ obtained are inputs to the next $S_{2,m}$ calculation.

(5) Repeat step 3 with the $(V_{\theta r})$ and τ values obtained in step 4. Modify the passage geometry in the meridional plane if desirable. Modify the stacking line in the range permitted by stress consideration if desirable.

(6) Steps 4 and 5 are repeated until acceptable convergence and desirable velocity and pressure distributions around the blade surface and along the hub and casing walls are obtained (see fig. 5.31).

The S_1 surface near the hub or casing wall is usually assumed to be surface of revolution. If the angle between the S_1 surface there and the hub or casing wall in the meridional plane is denoted by σ (fig. 5.6), and if the S_1 surface there is a surface of revolution, then

$$\frac{\partial^k \sigma}{\partial \varphi^k} = 0 \quad (5.27)$$

By using the following relation between σ and the velocity components

$$\tan \sigma = \frac{W_r}{W_z} \quad (5.28)$$

and the following equation of vorticity component,

$$(\nabla \times \mathbf{V})_r = \frac{1}{r} \frac{\partial W_z}{\partial \varphi} - \frac{1}{r} \frac{\partial (V_{\theta r})}{\partial z} \quad (5.29)$$

there is obtained (ref. 68)

$$\frac{1}{r} \frac{\partial \sigma}{\partial \varphi} = \frac{1}{W_\theta} \left[\frac{1}{r} \frac{\partial(V_\theta r)}{\partial n} - (\nabla \times \mathbf{V})_\theta \right] \quad (5.30)$$

Equation (5.30) shows how $(V_\theta r)$ and the vorticity affects the twist of the S_1 surface. In particular if S_1 surface is a surface of revolution, $\partial \sigma / \partial \varphi = 0$ and equation (5.30) becomes

$$\frac{\partial(V_\theta r)}{\partial n} = r(\nabla \times \mathbf{V})_\theta \quad (5.31)$$

If the θ -vorticity component is equal to zero, then

$$\frac{\partial(V_\theta r)}{\partial n} = 0 \quad (5.32)$$

Thus, in the third step of the design process described in the preceding section, satisfaction of equation (5.32) in the values of $(V_\theta r)$ specified near the hub and casing wall would help keep the S_1 stream surface near the wall being surface of revolution.

Determination of the Circumferentially Uniform Conditions Far Upstream and Far Downstream of the Blade

In the solution of S_1 flow the uniform condition (in the circumferential direction) at stations far upstream and far downstream of the blade row is required. This is true not only for all of the blade rows in a multistage machine (fig. 2.4), but also for the rotor and stator in a single stage machine (fig. 5.32).

The far field boundary condition upstream of blade row S in figure 5.31 is obtained as follows:

- (1) Calculate $S_{2,m}$ flow with all of the blade rows in the flow passage.

(2) Take off blade row R and make another $S_{2,m}$ flow calculation from station AA to station BB.

In this calculation the Ψ distribution obtained at station AA in step 1 is used as the boundary value at that station. At the far upstream station BB, a boundary condition of the second type (i.e., $V_r = 0$) is considered.

(3) With the Ψ distribution at BB and a second type boundary condition (i.e., $V_r = 0$) specified at far downstream station CC, an $S_{2,m}$ calculation from station BB to station CC is made.

(4) The fluid state obtained at station BB in step 2, and the streamline shape and the fluid state between station BB and CC obtained in step 3 provides the geometry of the S_1 surface and the boundary conditions at the two stations for the calculation of flow along a number of S_1 stream filaments.

The far downstream condition for blade row R is obtained in a similar manner as indicated in the figure.

5.7 Three-Dimensional Flow in a High Subsonic Compressor Stator

Designed by Quasi-Three-Dimensional Flow Method

The quasi-three-dimensional blade design method described in the preceding paragraphs has been used to design a high subsonic stator of a single stage transonic fan. The projection of the stator blade on the meridional plane is shown in figure 5.33. The inlet Mach number at the hub is 0.8. After completion of the blade design a three-dimensional analysis was immediately carried out. The quasi-three-dimensional design took five cycles of iteration, whereas the full-three-dimensional analysis took only three more cycles of iteration.

It was customary in the past that entropy gradient was considered in the S_2 calculation (fig. 2.5), whereas isentropic assumption was considered in subsonic S_1 calculation. Iteration between the two immediately shows divergence of the solution (fig. 5.34). When the same value of entropy was used at the same point on the two surfaces, convergence was quickly reached after only two more cycles of calculation. The criterion used for both convergence consistency is

$$\left| \frac{M_{S_1}^{(n)} - M_{S_2}^{(n)}}{M_{S_1}^{(n)}} \right| < \epsilon \quad (5.33)$$

ϵ was reduced to less than 2 percent. Figure 5.35 shows the streamlines obtained at the root in S_1 and $S_{2,m}$ calculation in the last cycle.

In the followup, full-three-dimensional analysis calculation the S_1 surface is no longer considered as surface of revolution. The nonorthogonal curvilinear coordinates are still placed on the surface. The principal equation is the same as equation (4.84) except for the last term in M . Instead of $(2\omega r \rho \sin \sigma \sin^2 \theta_{12})$ it is now $(2\omega^3 r \rho \sin^2 \theta_{12})$. Actually the computer code needs only one S_1 code and the general S_1 code. By putting $\omega^3 = \omega \sin \sigma$, the same code becomes the S_1 surface of revolution code.

Due to the twist in the general S_1 stream surface, it is not possible to impose the periodic condition immediately downstream of the trailing edge of the blade. Instead the boundary condition of the first kind is used there, that is, Ψ is specified there. After a certain distance downstream the periodic condition is again imposed.

The difference between the two solutions is indicated by the twist of the S_1 surface, that is the deviation of S_1 surface from surface of revolution. Figure 5.36 shows the amount of deviation of the S_1 surface number 3 and number 5 of figure 5.37 at a number of stations along the flow direction. It is apparent that the deviation of surface number 3, located nearly at mid-span, is larger than that of number 5. The deviation measured by the difference in radius, Δr , is less than 1 percent of the radius r . Figure 5.37 also shows twist of S_1 stream surfaces near the leading edge and the trailing edge of the stator.

The difference in the streamline distribution, the variation of $V_{\theta}r$ along the intersecting streamline of S_1 and S_2 surfaces and the variation of the angular thickness of $S_{2,m}$ filament as determined in the S_1 calculation, are shown in figures 5.38 to 5.40, respectively, and are small. Yet these relatively small differences in radius or filament thickness causes a relatively large difference on the Mach number distribution over the blade surface (fig. 5.41). This phenomena can be explained by examining the difference in the variation of r in the two cases. Figure 5.37 shows that r near the suction surface at the blade leading edge is smaller in the full-three-dimensional flow than in the quasi-three-dimensional flow. Thus, the peak Mach number on the suction surface obtained in the full-three-dimensional analysis solution is higher than that obtained in the quasi-three-dimensional design calculation. It exceeds the sonic velocity slightly.

5.8 Three-Dimensional Flow in CAS Research Compressor (Subsonic Case)

CAS Research Compressor

The research compressor designed for experimental investigation of three-dimensional subsonic and transonic flow in an axial-flow compressor is a single-stage compressor with inlet guide vanes. It is designed for a stagnation pressure ratio of 1.5 and isentropic efficiency of 0.85. The tip speed is 400 m/s,

the inlet hub-tip ratio is 0.4. The corrected mass flow per unit frontal area is $188 \text{ kg/m}^2\text{s}$ and the average inlet Mach number is 0.616.

Figure 5.42 shows the flow path with the intersecting lines between the meridional plane and S_1 surfaces. The hub and casing contours are so chosen as to reduce, as much as possible, the severe flow conditions at the tip of the rotor and at the hub of the rotor and stator. The relative Mach number of air entering the rotor varies from 0.68 at the hub to 1.34 at the tip. The MCA blade shape (laid out on conical surfaces) was used for the tip elements. The DCA blade shape was used for the elements in the mid-span and hub regions. Blade solidity varies from 2.3 at the hub to 1.3 at the tip, and the diffusion factor at the tip is limited to less than 0.4. The absolute Mach number of air entering the stator varies from 0.80 at the hub to 0.58 at the casing. Solidity of the stator blade varies from 2.0 at the hub to 1.1 at the casing and the diffusion factor is limited to 0.5 at the hub. The turning angle at the hub is slightly less than 45 degrees for the rotor and slightly less than 45 degrees for the stator. Aerodynamic design details are given in reference 62.

Overall Performance

Rotor test data were taken over a range of mass flows from maximum flow to near stall condition at 60, 70, 80, 90, and 100 percent of equivalent design speed. For each mass flow, measurements were taken at seven radial positions. Measured outlet stagnation pressures, stagnation temperatures, stream static pressure and flow angles were corrected for Mach number effect.

Overall stagnation pressure and stagnation temperature ratios were obtained from a mass average of the survey data at the rotor outlet and the pressure and temperature measured at the inlet station.

Strain-gauge type and Setra capacitance type transducers were used in measuring pressures. Copper resistance temperature detectors were used in measuring temperature at the inlet station and nickel chromel silicon-nickel thermocouplers were used in measuring temperature at the outlet station. Flow through the rotor was determined by the calibrated bell-mouth inlet.

Rotor speed was measured by a magnetic pick-up in conjunction with a gear mounted on the drive motor shaft. A phase difference type torque-meter was used to measure the torque of the drive shaft. A 3000 kW D.C. motor and gear boxes were used to obtain speeds up to 12 000 rpm for the research compressor.

The estimated accuracy of these conventional measurements is as follows:

Inlet pressure, mm H ₂ O	±10
Outlet pressure, mm H ₂ O	±25
Temperature, K	±1
Mass flow, %	±0.5
Speed, %	±0.03
Flow angle, deg.	±1.5
Torque, (0-400 kg/m), %	±1

For overall performance L2F measurements were only made at the inlet and outlet station. At the inlet station, data were taken only at one circumferential position, whereas at the outlet station, data were taken at 16 circumferential positions.

The accuracy of the L2F measurements is estimated to be

Flow speed, %	± 1
Flow angle, deg.	± 1

The overall performance of the rotor is plotted in figure 5.43. The plotted data present rotor stagnation pressure ratio and isentropic efficiency as a function of equivalent mass flow for rotative speeds of 60, 70, 80, 90, and 100 percent of design speed.

Detailed L2F Measurements

Detailed L2F measurements were first made for the peak efficiency point of 70 percent of design speed. The equivalent mass flow was $144.8 \text{ kg/m}^2\text{s}$, the stagnation pressure ratio was 1.21, and the isentropic efficiency was 93.2 percent. Flow speed and flow angle were recorded at 8 axial stations, 6 to 14 radial positions, and 10 to 16 circumferential positions. All of the measured points are on the $S_{2,m}$ and S_1 stream surfaces obtained in the design calculation.

Three-Dimensional Flow Calculation

Before the result of the three-dimensional flow field calculation can be properly compared with the L2F measurements, suitable flow parameters measured at the outlet station should be used in the calculation. The probe measured outlet stagnation pressure p_2° and laser measured outlet flow angle α_2 , shown in figure 5.44 as functions of radius are chosen. The main input to the three-dimensional analysis calculation is then: flow path (in meridional plan), blade geometry (coordinates given on design conical surface or on manufacturing templates), inlet pressure and temperature, rotor speed, mass flow, flow coefficients, and outlet stagnation pressure and outlet absolute flow angle.

The first step in the three-dimensional calculation is computation of flow along an $S_{2,m}$ filament about mid-way between two adjacent blades (fig. 5.31). The radial distribution of rotor efficiency determined by temperature measurement, is shown in figure 5.45. The measured value of torque is considered to be more accurate than the measured value of a small increase in temperature across the rotor. The temperature determined radial distribution of rotor efficiency, used in the initial calculation, has to be corrected so that the radial distribution of stagnation pressure in the calculation at the outlet station should be at least approximately equal to that obtained by the pitot tube measurement. The span-wise averaged value of the corrected efficiencies has to agree with the rotor efficiency determined by torque measurement. The resulting distribution of rotor efficiency also determines the radial distribution of $V_{\theta r}$ at the outlet, which is compared to the values used in the design (fig. 5.45), i.e., 100-percent design speed. The comparison shows that at the peak efficiency point of 70-percent design speed, the load distribution along blade span is quite different from that at the design point. The load near the tip and the efficiency distribution shows that the efficiency at the hub is lower than that at the design point. It seems that is caused by the appearance of a higher angle of attack in the hub region.

In the initial calculation the variation of $V_{\theta r}$ along the flow direction is taken to be the same as that used in reference 11. The variation of the stream filament thickness is estimated according to the blade thickness distribution. (In a later calculation, however, both estimates are not needed, because their variations are given by S_1 solutions.)

With these input values, solution of $S_{2,m}$ flow is obtained. The axial velocity at the outlet station and the experimental flow angle α_2 yield a new set of values for $V_{\theta r}$ at the outlet station. The $S_{2,m}$ calculation is repeated with this set of values until convergence of the solution is obtained.

The converged value of outlet $V_{\theta r}$ is then used with the experimental value of outlet stagnation pressure to correct the radial variation of rotor efficiency. The modified values are used to repeat the preceding calculation of $S_{2,m}$ until the rotor efficiency value converges.

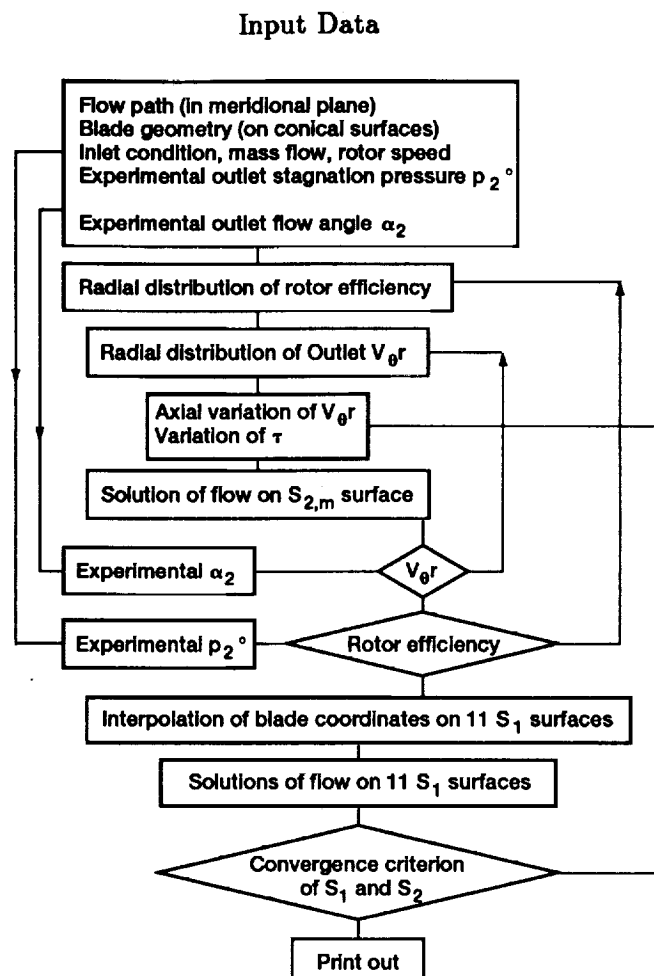
From this solution of $S_{2,m}$ the geometry of 11 surfaces of revolution are formed and interpolated values of coordinates of the corresponding blade surfaces and the variation of the S_1 stream filaments are obtained.

After these solutions of the flow on 11 S_1 surfaces are obtained, a new $S_{2,m}$ surface, together with the corresponding variations of $V_{\theta r}$ and stream filament thickness, is obtained. The flow on this new $S_{2,m}$ surface is computed in the same manner as previously discussed.

The whole calculation process is very similar to the quasi-three-dimensional calculation described in section 5.7, except that input values to the whole calculation are different. The solution of the complete procedure converges rapidly (see fig. 5.46) and only four computation cycles are actually required in the present case.

This quasi-three-dimensional computation could be conveniently followed by a full three-dimensional computation as suggested in the preceding section. It was found in the present case that the difference between the two solutions is rather small. The twist of the S_1 stream surface obtained is very small. Comparisons were made only between the experimental measurement and the quasi-three-dimensional solution.

The following sketch shows the various steps involved in the present calculation:



Comparison and Discussion

From the calculation procedure presented in the preceding section it is seen that the result of the theoretical calculation depends on the accuracy of the experimental data put into the calculation. Because the measured p_2° and α_2 are believed to be relatively more accurate than the others, they are chosen as the input for the calculation, with only a small adjustment in the values (see fig. 5.44).

On the other hand, errors in temperature increase across a single rotor could be quite large, therefore, a relatively large adjustment in local rotor efficiency was made for the overall rotor efficiency determined by the torque-meter to be satisfied (see fig. 5.45).

Figure 5.47 shows the radial variation of the relative flow angle at the inlet and outlet station obtained in the theoretical calculation for 70-percent design speed. It is seen that their variations are quite similar to those of the design values.

The corresponding radial variations of relative Mach number at the inlet and outlet station are shown in figure 5.48. Although the inlet Mach number is only slightly greater than 0.8 at the tip, the calculation shows that supersonic velocity occurs near the leading edge of the blade in the tip region.

The absolute velocities of air flowing past the rotor blade channel obtained in the L2F measurement and in the theoretical calculation on the $S_{2,m}$ surface are compared in figure 5.49. In general, the two agree closely in the trend of variation and agree reasonably well in magnitude. Toward the exit, the calculated value is lower than the L2F measured value. Perhaps this is caused by the inadequacy in the magnitude of the mass flow coefficient used in the theoretical calculation to account for the effect of an annulus boundary layer.

The variation of relative flow angle obtained by the L2F measurement along a streamline near the blade suction surface, along the mean streamline and along a streamline near the blade pressure surface, all on an S_1 surface at 40-percent blade height, are compared to the calculated value in figure 5.50. In general, the agreement is pretty good. Similar to that noticed in the design calculation, the air has an overturning in the blade channel at the outer radius even at 70-percent design speed. Figure 5.51 shows constant Mach contours on three S_1 surfaces.

CHAPTER 6

TRANSONIC FLOW ALONG S_1 AND S_2 STREAM FILAMENTS

Intensive research work on the development of a relatively simple and quick method of computing the transonic flow along S_1 and S_2 relative stream surfaces has been carried out during the last 5 years at the Institute of Engineering Thermophysics, CAS. Once the quick methods for solving transonic S_1 and S_2 flow have been completed, they can be readily utilized to obtain a quick solution of a three-dimensional transonic flow.

Because the computer time required to solve a steady flow problem by using a time-dependent approach is quite long, a solution for the steady flow problem using much shorter computer time has been sought through a number of approaches. The mean streamline/series expansion method, as seen in sections 5.1 to 5.4, is quite simple and is applicable to a low transonic flow without strong passage shock. When strong passage shock in the the blade passage is considered, it immediately appears that using existing methods of calculating the supersonic flow and subsonic flow, separately, on the two sides of the passage shock should work. For instance the method of characteristics can be used for the supersonic region while the direct matrix solution can be used for the subsonic region.

6.1 Transonic Flow Along S_1 Stream Filament of Revolution Solved by Separate Region Computation with Shock Fitting

Calculation of Supersonic Inlet Region

In figure 6.1 a typical compressor cascade with a supersonic inlet flow is shown with the bow-wave/passage-shock. The bow wave region upstream of bow wave can be easily calculated by the method of characteristics. References 37 and 38 give detailed descriptions of this method of solving supersonic

flow along an arbitrary stream filament of revolution. The nonuniform increase of entropy downstream of the detached bow wave is included in this computation. The calculation is carried out from one blade to the next in the circumferential direction for several blades until the periodicity condition is satisfied. Among others, the theoretical inlet flow angle β_1 , which corresponds to the inlet Mach number M_1 , is determined. It was noticed in the calculations that the periodicity of velocity can be satisfied easier than that of entropy (ref. 37). (Usually the former occurs at the fourth blade channel while the latter occurs at the seventh blade.)

Location and Shape of Detached Bow Wave

In the past, the location and shape of the bow wave were usually taken from empirical data of an isolated plane or axially symmetrical body (refs. 70 to 72). Based on experimental data given in reference 73, modification of such data for plane cascade has been done in reference 74. For three-dimensional applications the location and shape of the bow wave on the S_1 surface of revolution is required and their determination by theoretical calculation has been presented in reference 75.

In calculating the transonic flow field for a cascade test, the location and shape of the bow wave may be taken from the middle line of the bow shock band obtained through optical measurement. For the design of a transonic cascade, they may be taken from empirical data (refs. 70, 71, 73, and 74) or may be taken from the shock capturing solution described in section 6.2.

Computation of Subsonic or Transonic Region Downstream of Passage Shock

Depending on the inlet Mach number, the flow downstream of the passage shock may either be subsonic or transonic. The subsonic S_1 code (ref. 63) is modified to take passage shock as the inlet boundary and to take the stream function variation immediately downstream from the passage shock as

the Dirichlet boundary value at the inlet station. The nonorthogonal curvilinear coordinate system is especially suited for use in the downstream region (see fig. 6.2).

The streamline distribution and constant Mach number contours calculated for DCA 2-8-10 cascade (ref. 73) at an inlet Mach number of 1.11 and a static pressure ratio of 1.35 are shown in figure 6.3.

In figure 6.4 the variations of three important flow variables $V_{\theta r}$, β , and M , along the three streamlines are shown. Notice that the change in the flow direction, or angle β , is large at the curved part of the passage shock, whereas the jumps in M and $V_{\theta r}$ are large near the suction surface.

Similar data obtained on a number of S_1 surfaces gives the shape of the mean (and other) S_2 stream surface, the thickness variation of the corresponding S_2 stream filaments, and the variation of $V_{\theta r}$ over the S_2 surface. The accuracy of the calculated flow along the S_2 surface depends on the accuracy of this data.

Improvement of Location and Shape of Passage Shock

According to the calculation for supersonic flow upstream of the passage shock and the assumed location and shape of the passage shock, the Mach number, just upstream of the shock, the angle included by the shock, and incoming flow are completely determined. Then the turning angle across the shock, the Mach number just downstream of the shock, the pressure increase across the shock, the density ratio and the entropy change, etc. are calculated by the Rankine-Hugoniot relations. If the assumed location and shape of the passage shock are correct, these calculated values of aerothermodynamic quantities just downstream of the shock and those at the inlet boundary obtained from the solution of the subsonic flow field, must be the same. Based on this criterion, the correct location and shape of the shock can be obtained. This adjustment process is incorporated in the computer code of reference 38. Figure 6.5

shows the agreement in W and β in the case of a DCA 2-8-10 cascade calculation. On the UNIVAC 1100, computation time for a supersonic region with 90-by-20 mesh points is less than 2 min, and for subsonic region with 13-by-40 mesh points, computation time for each iteration is less than 1 min. To obtain the convergent result, the total computation time is about 10 min. In reference 76, this method was applied to compute the transonic flow along three S_1 stream filaments in the DFVLR rotor and compare the flow with experimental data.

In case the flow downstream of the passage shock is transonic, one of the shock capturing code described in section 6.2, may be used.

6.2 Transonic Stream-Function Principal Equation Solved With the Use of Artificial Compressibility

In the treatment of a transonic flow calculation, the use of the stream function principal equation is preferred to the use of the potential function principal equation. Many good methods are available for quick, accurate solution of the elliptic principal equation corresponding to the direct problem of subsonic flow along an S_1 surface. For transonic flow, however, the stream function approach has inherent difficulty since gas density is not uniquely determined from the mass flux obtained from the derivatives of stream function Ψ after each cycle of iteration of the Ψ field. This is why long computer time was spent to obtain the steady solution through artificial unsteady calculations. Now, with the method of introducing artificial density through the density term (refs. 76 to 78, and 40), the stream function principal equation is elliptic throughout the whole flow field, and quick methods are available for solving the elliptic equation. Several attempts (refs. 41, 42, and 79) to assess this approach are described briefly in the following section.

Principal Equation

The following conservative form of the stream function principal equation is obtained by substituting equation (4.46) into the dynamic equation (4.33):

$$\begin{aligned} & \frac{\partial}{\partial x^2} \left(A_1 \frac{1}{\rho} \frac{\partial \Psi}{\partial x^2} - A_2 \frac{1}{\rho} \frac{\partial \Psi}{\partial x^1} \right) \\ & - \frac{\partial}{\partial x^1} \left(A_2 \frac{1}{\rho} \frac{\partial \Psi}{\partial x^2} - A_3 \frac{1}{\rho} \frac{\partial \Psi}{\partial x^1} \right) = A_4 \end{aligned} \quad (6.1)$$

where

$$\begin{aligned} A_1 &= \sqrt{a_{11}} / \left(\sqrt{a_{22}} \sin \theta_{12} \tau \right) \\ A_2 &= \cos \theta_{12} / \left(\sin \theta_{12} \tau \right) \\ A_3 &= \sqrt{a_{22}} / \left(\sqrt{a_{11}} \sin \theta_{21} \tau \right) \\ A_4 &= \frac{\sqrt{a_{11}}}{W^1} \left(\frac{\partial I}{\partial x^2} - T \frac{\partial s}{\partial x^2} \right) - 2 \sqrt{a_{11}} \sqrt{a_{22}} \omega \sin \omega \sin \theta_{12} \end{aligned} \quad (6.1a)$$

It may be noticed that in the stream function solution it is easy to include entropy variation in the flow field. The density calculation includes entropy increase as follows:

$$\rho = \rho_1 \left(\frac{I + \frac{1}{2} \omega^2 r^2 - \frac{1}{2} (W)^2}{H_1} \right)^{\frac{1}{\gamma-1}} e^{-\frac{S-S_1}{R}} \quad (6.2)$$

The principal equation (6.1) also includes a variation of entropy with respect to x^2 . Entropy increase across a shock is calculated by the usual formula.

Method of Solution

The principal equation (6.1) is a mixed-type equation. It can be solved by modifying the density so numerical dissipation necessary is introduced in the supersonic region. For the present treatment, in which general nonorthogonal curvilinear coordinates are used, modified density is selected as follows:

$$\tilde{\rho} = \rho - \mu \rho_s \Delta s \simeq \rho - \mu \left(\frac{W^1}{W} \rho_{x_1} \Delta x_1 + \frac{W^2}{W} \rho_{x_2} \Delta x^2 \right) \quad (6.3)$$

where

$$\mu = \text{Max} \left[0, C \left(1 - \frac{1}{M^2} \right) \right] \quad (6.4)$$

and

Determination of Density

In transonic flow, the density is not uniquely determined by the value of mass flux, through the Σ - Φ method usually used in subsonic flow cannot be used. Density is now determined in the following manner: By the use of equation (4.46) and artificial density, the dynamic equation (4.33) can be written as (see eq. 4.41)

$$\frac{\partial}{\partial x^2} \left(\sqrt{a_{11}} W^1 \right) = \frac{\partial}{\partial x^1} \left(A_2 \frac{1}{\tilde{\rho}} \frac{\partial \Psi}{\partial x^2} - A_3 \frac{1}{\tilde{\rho}} \frac{\partial \Psi}{\partial x^1} \right) + \frac{\partial}{\partial x^2} \left(A_2 \frac{1}{\tilde{\rho}} \frac{\partial \Psi}{\partial x^1} \right) + A_4 \quad (6.5)$$

This velocity gradient equation is now used to obtain W^2 along the x^2 coordinate line by integrating from an initial x^1 coordinate line. W^1 and W^2 at grid points on this line are first calculated using equation (4.46), in which the density ρ is replaced by the artificial density $\tilde{\rho}$. Then W^1 on other x^1 coordinate lines are obtained by integrating from the initial line either in one direction (ref. 41), successively in reversed direction (ref. 42), or in positive and negative directions (ref. 79). Knowing W^1 , W^2 is calculated by

$$W^2/W^1 = - \left(\sqrt{a_{22}} \partial \Psi / \partial x^1 \right) / \left(\sqrt{a_{11}} \partial \Psi / \partial x^2 \right) \quad (6.6a)$$

W is calculated by

$$W = \left[(W^1)^2 + (W^2)^2 + 2W^1W^2 \cos \theta_{12} \right]^{\frac{1}{2}} \quad (6.6b)$$

and ρ is calculated by equation (4.2).

Discretized algebraic equations obtained by the principal equation (6.1) by conservative central difference formula over a whole flow field can then be solved by a suitable method for the solution of an elliptic equation. In the direct matrix method of solution the coefficient matrix $[M]$ of the discretized equation (6.1) is now a function of $\tilde{\rho}$. To prevent decomposition of the coefficient matrix $[M]$ in every cycle of iteration, equation (5.0) is transformed into (ref. 41).

$$[M'] [\Delta \psi]^{(n+1)} = \tilde{\rho} [R]^{(n)} \quad (6.7)$$

so that the decomposition of $[M']$ is needed only the first time, and subsequent solutions can be obtained with relatively few forward and backward substitutions.

In addition to this direct matrix solution, strong implicit approximate factorization procedures (refs. 80 and 81) and vertical line relaxation procedures were also programmed in reference 41.

It was found when calculating for a transonic cascade with a mesh of 61-by-11, the strong implicit algorithm and the relaxation algorithm took about 2 sec per iteration on an UNIVAC-1100 computer whereas the direct matrix algorithm took about 3 sec on the same computer. But convergence obtained after 40 iterations (120 sec) in the latter is better than the convergence obtained after 100 iterations (200 sec) in the former. The Mach number obtained by the direct matrix algorithm for a turbine cascade

and a compressor cascade are compared with other theoretical calculations and experimental data in figures 6.6 and 6.7 respectively. Fifty to sixty and 11 to 15 grid points were used, respectively, along x^1 and x^2 coordinate lines, and 200 to 300 iterations were carried out to reach an $\epsilon_{L(\Psi)}$ level of 10^{-3} . It is interesting to see that in the case of the turbine cascade, the result obtained by the present method agrees quite well with experimental value. It seems that both this method and the mean streamline/series expansion method gives a Mach number distribution in the supersonic region better than that given by the time-marching method. In the case of the T-1 compressor cascade, it is seen that the present method captured the second shock better than the relaxation method and time-marching method, and that the position of the captured first shock is a little ahead of that given by the experiment data.

Improvement of Velocity Distribution for Transonic Blading

On the basis of this treatment of the transonic direct problem, a method of solution for the transonic inverse problem was developed and reported in reference 67. This method is very useful in improving the aerodynamic performance of cascade blades. For instance, the velocity distribution on the suction of $T_1(18A_6I_{4b})08$ cascade shows two high velocity peaks (fig. 6.8). This method enables one to modify the velocity distribution so that the magnitude of the two velocity peaks is reduced, but the blade circulation is kept the same (see fig. 6.8). Blade coordinates obtained in the inverse solution are shown in figure 6.9. It is seen that the change in the blade shape is very small. Maximum blade thickness and outlet flow angle are practically the same.

6.3 Effect of Axial-Velocity Density Ratio and Viscous Effect

In comparing theoretical calculations presented in the preceding sections with experimental data, it is important to notice that the cascade experimental data is usually obtained at a certain axial-velocity

density ratio. In the case of compressor cascade it exceeds unity. Therefore, the theoretical calculation should consider a variation of the stream filament r corresponding to the axial velocity density ratio in the experiment.

It is also important to consider the viscous effect. If flow does not separate from the blade, the viscous effect is reflected by the reduction in flow area due to boundary layer development on the blade surface and the increase of entropy in the fluid.

At a relatively low supersonic inlet Mach number, inclusion of the effect of entropy increase in the theoretical calculation (shock capturing method) seems to give a pressure distribution in agreement with the experimental data (ref. 73) (fig. 6.10). The variations of $V_{\theta r}$, M , and β along three streamlines are shown in figure 6.11.

In the case of an inlet Mach number of 1.11, the inclusion of both entropy increase and axial-velocity density ratio ($\Omega = 1.16$) in the theoretical calculation yields a fair comparison between the calculated and experimental pressure distribution (ref. 73) around the blade surface (fig. 6.12). The variations of $V_{\theta r}$, M , and β along three streamlines are also shown in figure 6.13.

At an even higher inlet Mach number of 1.34, probably due to boundary layer separation, an Ω value of 1.18, which is much higher than the experimental data of 1.04, is required to bring the pressure distribution close to the experimental level (fig. 6.14). The corresponding variation along three streamlines is shown in figure 6.15.

Calculations (ref. 85) have also been made to obtain the flow along three S_1 surfaces at 68-, 89-, 100-percent blade height of the DFVLR rotor. Here an adequate knowledge of the relatively large variation of τ is very important for results to be close to the experimental data.

6.4 Transonic Flow Along General S_1 Stream Filament

In a general S_1 stream filament the radial coordinate of the central S_1 surface and thickness of the filament vary in the flow direction and circumferential direction (see fig. 6.16). In transonic flow, there are abrupt changes in r and τ in the shock region. The method for solving transonic flow along an S_1 stream filament of revolution given in reference 41, has been extended in reference 86 to that along an arbitrarily twisted S_1 stream filament.

In a full-three-dimensional calculation, the shape of a general S_1 stream surface is obtained by joining corresponding stream lines on a number of S_2 stream surfaces. In reference 87, general x^1 and x^2 coordinates are placed on the central S_1 surface of an S_1 stream filament. The third coordinate x^3 is chosen in the radial direction (fig. 6.17). Then

$$\left. \begin{aligned} \epsilon_1 &= \frac{\partial r}{\partial x^1} r + \frac{\partial z}{\partial x^1} z + r \frac{\partial \phi}{\partial x^1} \phi \\ \epsilon_2 &= \frac{\partial r}{\partial x^2} r + \frac{\partial z}{\partial x^2} z + r \frac{\partial \phi}{\partial x^2} \phi \\ \epsilon_3 &= \frac{\partial r}{\partial \psi_1} r \end{aligned} \right\} \quad (6.8)$$

where

$$\frac{\partial r}{\partial \Psi_1} = r_r \quad (6.9)$$

The stream function principal equation in conservative form is

$$\frac{\partial}{\partial x_2} \left(A_1 \frac{1}{\rho} \frac{\partial \Psi}{\partial x^2} - A_2 \frac{1}{\rho} \frac{\partial \Psi}{\partial x^1} \right) - \frac{\partial}{\partial x^1} \left(A_2 \frac{1}{\rho} \frac{\partial \Psi}{\partial x^2} - A_3 \frac{1}{\rho} \frac{\partial \Psi}{\partial x^1} \right) = A_4 \quad (6.10)$$

where

$$A_1 = \sqrt{a_{11}} \left(\sqrt{a_{22}} \sin \theta_{12} \frac{1}{r} \right)$$

$$A_2 = \cos \theta_{12} / (\sin \theta_{12} r)$$

$$A_3 = \sqrt{a_{22}} \left(\sqrt{a_{11}} \sin \theta_{21} \frac{1}{r} \right)$$

$$A_4 = \frac{\sqrt{a_{11}}}{W^1} \left(\frac{\partial I}{\partial x^2} - T \frac{\partial s}{\partial x^2} \right) - 2 \sqrt{D(z, \varphi) / D(x^1, x^2)} \omega \cos(\mathbf{n}, \mathbf{r})$$

These equations are only slightly different from those on an S_1 surface of revolution. (Compare eq. (6.10) with eq. (6.1)). The procedure of solution for the transonic flow along a general S_1 stream filament is the same as that along an S_1 stream filament of revolution (ref. 41).

6.5 Transonic Flow on S_2 Stream Filament Solved by Separate Region Computation with Shock Fitting

Similar to transonic S_1 surface flow, transonic S_2 surface flow can also be solved by a separate region calculation. However, the shock on an S_2 surface is different from that on an S_1 surface. The shock usually begins at the outer casing and terminates a distance from the inner hub. Thus, the flow field is divided into three regions (ref. 39) (fig. 6.18). The first region AA_1B_1BA , is a supersonic flow region. It extends from the starting line AA_1 , which may or may not coincide with the blade leading edge, to shock line BB_1 . Supersonic flow in this region is solved by the method of characteristics. The slopes of the two families of characteristics are

$$\lambda_i = \left(\frac{dx^2}{dx^1} \right)_i = - \left(K \pm \sqrt{\Delta} \right) / 2J \quad (6.11)$$

where $i = 1, 2$ (when $i = 1(2)$ the sign is $+ (-)$).

The consistency relation along the i family of characteristics is

$$C_{1i} \frac{dW}{dx^i} + C_{2i} \frac{d\sigma}{dx^i} + C_{3i} = 0 \quad (6.12)$$

The second region $A_1A_2B_2B_1A_1$ is a transonic flow region. The flow in this region is best calculated by a Taylor series, using the following partial derivatives with respect to x^2 :

$$E_{1i} \frac{\partial W^1}{\partial x^2} + E_{2i} \frac{\partial W^2}{\partial x^2} = F_{1i} \quad (6.13)$$

$$E_{1i} \frac{\partial^2 W^1}{\partial (x^2)^2} + E_{2i} \frac{\partial^2 W^2}{\partial (x^2)^2} = F_{2i} \quad (6.14)$$

where $i = 1, 2$.

$$\frac{\partial \rho}{\partial x^2} = \frac{\rho}{(\gamma - 1)h} \left(\frac{\partial I}{\partial x^2} + \omega^2 r \frac{\partial r}{\partial x^2} - G \right) \quad (6.15)$$

$$\frac{\partial^2 \rho}{\partial (x^2)^2} = \frac{r}{\rho} \left(\frac{\partial \rho}{\partial x^2} \right)^2 + \frac{\rho}{(\gamma - 1)h} \left[\frac{\partial^2 I}{\partial (x^2)^2} + \omega^2 \frac{\partial}{\partial x^2} \left(r \frac{\partial r}{\partial x^2} \right) - \frac{\partial G}{\partial x^2} \right] \quad (6.16)$$

The coefficients $C_{1i}, C_{2i}, C_{3i}, E_{1i}, E_{2i}, F_{1i}, F_{2i}$ and G are given in reference 39.

The third region $BB_2A_2A_3C_1CB$ is a subsonic flow region, the flow of which is solved by the SOR method.

This method has been used in reference 39 to obtain the transonic S_2 flow in the CAS rotor and the rotor reported in reference 86. The computation was done on a UNIVAC 1100; CPU time was about 3 min. For the high pressure (1.94) rotor of reference 86 meridional projection of the characteristic

network on S_2 and the mesh used for the subsonic region are shown in figure 6.19. Figure 6.20 shows meridional projection of the streamlines. The abrupt change of the streamline across the shock is clearly seen. The Mach number variation in the three flow regions is seen in figure 6.21.

The variation of flow along the mid-channel S_2 surface can be seen more clearly by following the flow along three streamlines, namely, the one along the hub, the one at midspan and the one along the casing. Corresponding to the abrupt change across the shock (fig. 6.20) the decrease in S_1 stream filament thickness is large (fig. 6.22) whereas the change in the relative flow angle (fig. 6.23) is small. Across the shock, the drop in relative Mach number (fig. 6.24) and absolute Mach number (fig. 6.26) and the increase in absolute flow angle (fig. 6.25), tangential velocity, (fig. 6.27) and pressure ratio (fig. 6.28) is relatively large. It is noticed from these figures that there is quite a large overturning of the air and overshooting of the tangential velocity below mid-span and near the trailing edge of the blade.

6.6 Shock Embedding Elliptic Solution for Inverse Problem of Transonic S_2 Flow

One of the findings in reference 3 has been generally accepted since it was published. That finding states that in the case of an inverse problem where the tangential velocity component is prescribed by the designer, the partial differential equation governing fluid flow remains elliptic as long as the meridional velocity component is lower than the speed of sound, even when the flow relative to the rotating blade is higher than the speed of sound. Indeed a great number of transonic turbomachines have been designed on that basis. However, if in the design of transonic machines, the design parameter selected, for instance $V_{\theta}r$, is prescribed in the same manner as in the subsonic machines (fig. 5.5), flow discontinuity at the passage shock is not obtained in the solution. This kind of calculation is referred to as Level I calculation. If the values of $V_{\theta}r$, s , and r prescribed in the design calculation are smooth, but have steep gradients at the passage shock, then the solution obtained indicates a passage shock. This is

referred to as Level II calculation. Level III calculation has the following characteristics: (a) prescribed values have proper discontinuity across the shock provided by transonic S_1 calculations, (b) shock relations are embedded in the S_2 calculation, (c) S_2 solution obtained shows a clear shock discontinuity, and (d) one of the x^2 -coordinate lines coincides with the shock line (fig. 6.29).

Embedding Shock Relations

In the calculations of the direct problem of stream surfaces, usually the plane shock relations are used. This is equivalent to assuming that the shock surface is perpendicular to the stream surface. The error involved appears to be somewhat different for S_1 and S_2 flows and its magnitude depends on particular configuration. In reference 88, this assumption is not made and fully three-dimensional relations are used across the shock. First, two stations, a very short distance apart, are placed along the shock line one immediately upstream and the other immediately downstream. The dynamic equation in the direction tangent to the S_2 surface and also to the shock surface is

$$W_{ts}^{(+)} = W_{ts}^{(-)} \quad (6.17)$$

The dynamic equation in the direction normal to the shock surface yields

$$\gamma \left(\frac{2}{\gamma - 1} + M^{(+)^2} \right) M_r^{(-)^4} + \left[\frac{2\gamma}{\gamma - 1} (M^{(+)^2} - M^{(-)^2}) - \frac{\gamma - 1}{2} (M^{(+)^2} + M^{(-)^2}) - 2 \right] M_n^{(-)^2} - \left(M^{(+)^2} + \frac{2}{\gamma - 1} \right) = 0 \quad (6.18)$$

The dynamic equation in the direction tangent to the shock, but not tangent to the S_2 surface yields

$$\frac{S^{(+)} - S^{(-)}}{R} = \frac{\gamma}{\gamma - 1} \ln \left[\frac{2}{(\gamma + 1)M_n^{(-)2}} + \frac{\gamma - 1}{\gamma + 1} \right] + \frac{1}{\gamma - 1} \ln \left[\frac{2\gamma}{\gamma + 1} M_n^{(-)2} - \frac{\gamma - 1}{\gamma + 1} \right] \quad (6.19)$$

The energy equation is simply

$$I^{(+)} = I^{(-)} \quad (6.20)$$

The continuity is simply

$$\Psi^{(+)} = \Psi^{(-)} \quad (6.21)$$

and the condition of continuity of the stream surface S_2 is given by the φ coordinate of S_2

$$\varphi^{(+)} = \varphi^{(-)} \quad (6.22)$$

The computer program of reference 64 was modified by working equations derived from the preceding basic equations. The modified program was used to carry out the three levels of calculation for the DFVLR rotor (ref. 89), for which Laser Two Focus measured internal flow data is available (ref. 90). In addition, the experimental Mach number contour plots at several spanwise positions given in reference 34 for the peak efficiency operating condition at design speed, the meridional projection of the Mach number contours on the $S_{2,m}$ surface are constructed and shown in figure 6.32(a). The increase of

$V_{\theta r}$ and s from inlet to outlet, determined from the measured values given in references 34, is used in the calculation.

Figures 6.30 and 6.31 show input values of r , $V_{\theta r}$, and s used in the Level II and III calculations. From the results obtained in the three levels of calculations, it is immediately seen from figures 6.32 and 6.33 that the streamlines and Mach number contours obtained in the Level I calculation are quite different from Level II and III calculations as well as from the measured result. Mach number contours obtained in the Level III calculation agrees best with the measured data.

It is also seen that the difference between the results obtained in Level II and III calculations are not large. The differences in the S_1 surface shape and S_1 filament thickness, needed for S_1 calculations, are shown in figures 6.33 and 6.34, respectively.

The relative flow angle obtained in the calculation is compared to that of the mean camber line and the measured value (ref. 90) in figure 6.35. The agreement with measured value is quite good. The calculated pressure rise is shown in figure 6.36.

6.7 Direct-Problem Solution of Transonic Flow Along S_2 Stream Filament

In the case of a direct problem of transonic flow along the S_2 stream filament, it is desirable to put the nonorthogonal curvilinear coordinates, x^1 and x^2 on the mid- S_2 surface of the filaments, and the x^3 -coordinate perpendicular to the surface (refs. 91 and 92) (fig. 6.37). Then $W^3 = 0$ If $dx^3 = 1$, then $\sqrt{g_{33}} = r_n = r B \cos(n, \varphi)$ and

$$\left. \begin{aligned}
g_{11} &= \left(\frac{\partial z}{\partial x^1} \right)^2 + \left(\frac{\partial r}{\partial x^1} \right)^2 + r^2 \left(\frac{\partial \varphi}{\partial x^1} \right)^2 \\
g_{22} &= \left(\frac{\partial z}{\partial x^2} \right)^2 + \left(\frac{\partial r}{\partial x^2} \right)^2 + r^2 \left(\frac{\partial \varphi}{\partial x^2} \right)^2 \\
g_{12} &= \sqrt{g_{11} g_{22}} \cos \theta_{12} \\
g &= \pi / \theta_{12} g_{11} g_{22} \sin^2 \theta_{12}
\end{aligned} \right\} \quad (6.23)$$

The continuity equation, the dynamic equation and stream function velocity, and the principal equations are, respectively (ref. 91).

$$\frac{\partial}{\partial x^1} \left(\rho \tau_n \sqrt{g_{22}} \sin \theta_{12} W^1 \right) + \frac{\partial}{\partial x^2} \left(\rho \tau_n \sqrt{g_{11}} \sin \theta_{12} W^2 \right) = 0 \quad (6.24)$$

$$\begin{aligned}
\frac{\partial}{\partial x^2} \left[(W^1 + W^2 \cos \theta_{12}) \sqrt{g_{11}} \right] - \frac{\partial}{\partial x^1} \left[(W^2 + W^1 \cos \theta_{12}) \sqrt{g_{22}} \right] \\
= 2 \sqrt{g_{11}} \sqrt{g_{22}} \omega^3 \sin \theta_{12} + \frac{\sqrt{g_{11}}}{W^1} \left(\frac{\partial I}{\partial x^2} - T \frac{\partial s}{\partial x^2} \right)
\end{aligned} \quad (6.25)$$

where $\omega^3 = \omega \cos(n, z) / \tau_n$,

$$\tau_n \rho \sqrt{g_{11}} \sin \theta_{12} W^2 = - \frac{\partial \Psi}{\partial x^1}; \quad \tau_n \rho \sqrt{g_{22}} \sin \theta_{12} W^1 = \frac{\partial \Psi}{\partial x^2} \quad (6.26)$$

$$\frac{\partial}{\partial x^2} \left(C_1 \frac{1}{\rho} \frac{\partial \Psi}{\partial x^2} - C_2 \frac{1}{\rho} \frac{\partial \Psi}{\partial x^3} \right) - \frac{\partial}{\partial x^3} \left(C_2 \frac{1}{\rho} \frac{\partial \Psi}{\partial x^2} - C_3 \frac{1}{\rho} \frac{\partial \Psi}{\partial x^3} \right) = C_4 \quad (6.27)$$

where

$$C_1 = \sqrt{g_{11}} / \left(\sqrt{g_{22}} \sin \theta_{12} \tau_n \right)$$

$$C_3 = \sqrt{g_{22}} / \left(\sqrt{g_{11}} \sin \theta_{12} \tau_n \right)$$

$$C_2 = \cos \theta_{21} / (\sin \theta_{12} \tau_n)$$

$$C_4 = 2 \sqrt{g_{11}} \sqrt{g_{22}} \omega^3 \sin \theta_{12} + \frac{\sqrt{g_{11}}}{W^1} \left(\frac{\partial I}{\partial x^2} - T \frac{\partial s}{\partial x^2} \right)$$

This principal equation is similar to that on the S_1 stream surface, but it contains only two unknowns, Ψ and ρ . The traditional Ψ - ρ iteration is used in the solution.

The method of artificial compressibility is used in a manner quite similar to that in transonic S_1 flow (section 6.2). In the calculation for the 8:1 pressure ratio centrifugal compressor (fig. 6.38) of reference 93, it was found that the viscous effect is large and that only after appropriate entropy correction and use of a blockage coefficient of 0.18, about the same value used in reference 93, the calculated Mach number at the casing was brought up to a level close to the experimental value (fig. 6.39). Results of computation for a mass flow of 0.909 kg/s at tip Mach number of 1.25 are given in figures 6.40 and 6.41. The increase in $V_{\theta r}$ along the casing is shown in figure 6.40. The increase in V_{θ} across the shock is a small portion of the total increase. Figure 6.41 shows the meridional projection of

Mach number contours on $S_{2,m}$. It is seen that flow in an inducer of a centrifugal compressor is quite similar to that in a rotor of a transonic axial-flow compressor.

CHAPTER 7

THREE-DIMENSIONAL FLOW IN TRANSONIC TURBOMACHINES

The determination of three-dimensional flow in transonic turbomachines through the use of S_1 and S_2 stream filaments proceeds in the same manner as in the case of subsonic turbomachines. Various techniques described in Chapter 6 for solution of transonic S_1 and S_2 flow are selected for use in the three-dimensional solution. Because the blading has a stronger influence than the hub and casing walls on the passage shock, the position and shape of the shock are determined in the S_1 calculation. Together with the geometry of the S_2 stream filament and the discontinuous changes of filament thickness r , angular momentum $V_{\theta}r$, and entropy s , the position and shape of the shock are carried over to the S_2 calculation in the next cycle. This procedure not only was proven to be practical in the S_1/S_2 iteration process, but also provides a possibility to modify the geometry of the blade and meridional passage for minimizing the loss caused by passage shock. So the three-dimensional blade design procedure suggested in this Chapter is even more desirable in the case of transonic turbomachines.

7.1 Quasi-Three-Dimensional Flow Field in the DFVLR Rotor

Quasi-three-dimensional solution refers to the solution obtained by using a number of S_1 stream filaments of revolution and a mid-channel S_2 filament. In reference 95, this approximate method was applied to compute the flow field in the DFVLR rotor (ref. 89) operating at the design point, of which measured flow field (ref. 90) is available for comparison. The design stagnation pressure ratio is 1.51 and the inlet relative Mach number at the blade tip is about 1.37. The $V_{\theta}r$ distribution at the outlet at design point is determined from experimental data and is used as the fixed boundary value of the direct problem.

For $S_{2,m}$ solution a grid system of 61 stations along x^1 and 11 stations along x^2 is selected on the meridional plane. Seven S_1 surfaces located at 0, 10, 30, 50, 70, 90, and 100 percent, respectively, of the blade height at the inlet station are used in the calculation. The grid system selected on the S_1 surface has 61 stations along x^1 coordinate and 15 stations along x^2 coordinate. The methods of references 42 and 64 are used for S_1 and S_2 calculations, respectively. In order to see how high of a convergence level can be obtained for this moderately high transonic flow, nine cycles of calculation were carried out and the convergence level obtained (relative change of flow variable less than 1 percent) is as good as that previously obtained for subsonic flow. The significant advantage of the transonic three-dimensional calculation method is that the computation can be carried out at low cost in a reasonable time period on a modern microcomputer, which is readily available to all design engineers. For instance, the computing time for the transonic S_1 and S_2 solution is about 30 sec each on a 7-MIP Sun 4 machine. Thus, the total time required is less than 1 hr. This time decreases in proportion to the number of CPU's in a multiprocessor. If, say, eight S_1 flows can be done at the same time on an 8-CPU computer, the total time required will be reduced by a factor of eight. Therefore, this relatively inexpensive, approximate three-dimensional code is quite suitable for design investigation and trade-off studies. The final choice of design configuration may then be checked and refined by a full-three-dimensional analysis code or even by a viscous code, which has recently been made available.

Convergence of Iterative Three-Dimensional Solution

The key issue for the success of the present method of solving the three-dimensional transonic flow by iterative calculation between an $S_{2,m}$ surface calculation and a number of S_1 surface calculations is the convergence problem. In the case of a high subsonic flow through a compressor stator (ref. 31) it was found that when the entropy values of the two surfaces at the same intersecting point are kept the same, a convergent solution with

$$\left| \frac{r_{s_2(n)} - r_{s_2(n-1)}}{r_{s_2(n-1)}} \right| < 0.3 \text{ percent} \quad \left| \frac{\tau_{s_2(n)} - \tau_{s_2(n-1)}}{\tau_{s_2(n-1)}} \right| < 0.8 \text{ percent}$$

and

$$\left| \frac{M_{s_2} - M_{s_1}}{M_{s_1}} \right| < 2 \text{ percent}$$

was obtained after only four cycles of iteration. For transonic flow it is expected that the convergence of solution would be more difficult to obtain than that of the passage shock. However, it is believed that, in the present calculation procedure, that the shock discontinuity is determined in the S_1 solution and that the abrupt changes in entropy τ and $V_\theta r$ across the shock obtained in the S_1 solution are taken as the input values to the $S_{2,m}$ solution will help achieve convergence of the three-dimensional iterative solution.

In the example cited above, the criterion $|\Delta r/r|_{\max}$ and $|\Delta \tau/\tau|_{\max}$ are used to judge convergence, whereas $|(M_{S_1} - M_{S_2})/M_{S_1}|_{\max}$ is used to judge consistency. Between convergence and consistency, the former is more essential. If convergence is not achieved, good consistency is impossible. On the other hand, even in the case of a high degree of convergence, there may be an irreducible inconsistency of the Mach number. It is believed that consistency of entropy and mass flow coefficient in the S_1 and S_2 calculations is especially important for consistency between the S_1 and S_2 solutions.

Using a proper value of relaxation factor is very important for convergence. During the calculation for flow in transonic rotor, the thickness value of the S_1 stream filament near the casing, fluctuated and

diverged when a relaxation factor was not used (see fig. 7.1). This kind of divergence is something like that in the iterative calculation of the following algebraic equation.

$$x^{(n)} = f(x^{(n-1)})$$

when $f'(x) < -1$. Hence, in order to obtain and speed up convergence, a small relaxation factor was used.

In the numerical example to be presented in the following section, the same grid pattern in the x^1 direction is employed for both S_1 and S_2 calculations, and the entropy and mass flow coefficients are kept consistent in both calculations. It is found that using the relaxation factor of a relatively small value is very effective in obtaining quick convergence. The consistency is, at the same time, relatively good. In the case of high subsonic flow through a compressor rotor, the relative change in S_1 filament thickness is reduced to below 2 percent and the relative differences between S_1 and S_2 Mach numbers and flow angles are reduced to 0.9 percent and 0.3 degrees, respectively. In the case of transonic flow in a compressor rotor with a tip Mach number of 1.37, the relative change in S_1 filament thickness is reduced to below 1 percent and the relative difference between S_1 and S_2 Mach numbers at the same grid point is below 4 percent. These values of consistency are probably due to the fact that artificial density is employed in S_1 but not in S_2 calculations and that the conservation form of the principal equation is employed in S_1 but not in S_2 calculations.

Variation of Flow Variables During the Convergence Process

During the first few cycles of calculation there was a general tendency toward convergence. However, in the region near the casing, the values of S_1 filament thickness soon began to fluctuate. Also its magnitude tends to increase (see fig. 7.2). A small relaxation factor, less than 1, was used to make the process convergent. It was noticed in the 7th cycle that a small τ_1 input to S_1 calculation (the lower solid line in fig. 7.2) yields a large value of output from the S_2 calculation (the upper dashed line in fig. 7.2) and vice versa in the 8th cycle. The solution lies between the two. The middle value was then taken as input to the 9th cycle and the output obtained is less than 1 percent from the final value.

The difference in streamlines obtained on the $S_{2,m}$ surface in the 1st cycle and 9th cycle shown in figure 7.3 is seen to lie in the region downstream of the shock. The radius coordinate obtained in the 9th cycle in that region is considerably higher than that in the 1st cycle.

The stream-wise variation of τ for the seven S_1 surfaces assumed in the 1st cycle and obtained in the 9th cycle is shown in figure 7.4, and the value of r and τ , respectively, of the streamline at 70- and 100-percent blade height in the 7th to 9th cycles of calculation is listed, respectively, in tables I and II.

TABLE I.—THE VALUES OF THICKNESS (cm) OF THE S₁ STREAM FILAMENT AT THE BLADE TIP IN THE LAST THREE CYCLES

Station number	L.E.	21	22	23	24	25	26	27	28	29	30
7th cycle	0.754	0.756	0.760	0.767	0.771	0.775	0.769	0.759	0.747	0.735	0.723
8th cycle	0.756	0.758	0.763	0.771	0.777	0.782	0.782	0.766	0.756	0.744	0.733
9th cycle	0.755	0.757	0.761	0.769	0.774	0.779	0.772	0.763	0.751	0.739	0.728
Station number	31	32	33	34	35	36	37	38	39	T.E.	
7th cycle	0.712	0.704	0.696	0.688	0.676	0.663	0.654	0.644	0.638	0.629	
8th cycle	0.723	0.716	0.709	0.701	0.687	0.673	0.662	0.651	0.643	0.633	
9th cycle	0.717	0.710	0.703	0.694	0.681	0.668	0.658	0.647	0.641	0.631	

TABLE II.—THE VALUES OF RADIUS (m) OF THE S₁ STREAM SURFACE OF REVOLUTION AT 70-PERCENT BLADE HEIGHT IN THE LAST CYCLE

Station number	L.E.	21	22	23	24	25	26	27	28	29	30
7th cycle	.16815	.16807	.16800	.16796	.16799	.16807	.16814	.16818	.16817	.16814	.16811
8th cycle	.16816	.16809	.16802	.16799	.16803	.16823	.16823	.16825	.16825	.16825	.16818
9th cycle	.16816	.16808	.16801	.16798	.16801	.16810	.16818	.16822	.16821	.16818	.16815
Station number	31	32	33	34	35	36	37	38	39	T.E.	
7th cycle	.16810	.16810	.16812	.16815	.16818	.16819	.16820	.16820	.16819	.16818	
8th cycle	.16817	.16817	.16820	.16823	.16826	.16828	.16829	.16830	.16829	.16828	
9th cycle	.16813	.16814	.16816	.16819	.16822	.16824	.16825	.16825	.16824	.16823	

The converging process of $V_{\theta r}$ is similar to that of τ of S_1 . The variation of $V_{\theta r}$, relative to its value at the exit, along the seven streamlines in the 9th cycle of calculation is compared to that in the 1st cycle of calculation in figure 7.5.

On the other hand, the change in the angular thickness of stream filament $S_{2,m}$ is relatively simple. The stream-wise value on the seven streamlines used as input value to the 9th cycle is shown in figure 7.6(b) and is compared to those assumed in the 1st cycle (fig. 7.6(a)). The abrupt change in τ (and $V_{\theta r}$ streamline) is clearly seen in figure 7.5(b) (and 7.3(b), 7.4(b)).

Figure 7.7(a) shows the Mach number variation along the mean streamlines obtained on the seven S_1 surfaces in the 9th cycle, whereas figure 7.7(b) shows those along the streamlines on the $S_{2,m}$ surface obtained in the 9th cycle. They are very close; the maximum difference between the two being less than 4 percent. This is the same value previously obtained in the iteration for a subsonic rotor. This means that in the present solution of moderately high transonic flow, the convergence and consistency level obtained is as good as those in the subsonic case.

Three-Dimensional Flow Field

In the approximate three-dimensional solution presented herein, the three-dimensional flow field is obtained on the seven S_1 filaments of revolution extending over the whole blade passage (the $S_{2,m}$ calculation is used mainly for obtaining the geometry of the S_1 filaments). The constant Mach number contours on these S_1 surfaces can be readily obtained from the calculation. However, in order to make a comparison to test data, the contours on S_1 surfaces at 18, 45, 68, and 89 percent span are obtained through interpolation. They are shown in figures 7.8(a) to (d). They clearly show the strong effect of the passage shock. The solution of S_1 surface flow can also be used to obtain the radial variation of

flow variables at a number of stations along the flow direction. Two of them, the relative Mach number and flow angle β are shown in figure 7.9.

Although only the flow variation on the central S_2 surface is directly available in the approximate three-dimensional solution, those on the other S_2 surfaces can be constructed by the data on the corresponding streamlines on different S_1 surfaces. Constant Mach number contours on the suction and pressure surfaces are obtained in this way and are shown together with that on the central S_2 surface in figure 7.10. A second passage shock is seen on the suction surface and the central S_2 surface, extending only a short distance inward from the casing.

From data on these S_2 surfaces, stream-wise variations of flow variables on certain streamlines can be readily obtained. For instance, the variation of flow angle along three streamlines on the $S_{2,m}$ surface at 18-, 68-, and 89-percent blade height (at inlet) are shown in figure 7.11.

The variation of flow variables can also be shown on spanwise surfaces formed by x^2 and x^3 coordinates. The variations of M , β , and p on these surfaces are particularly useful for observing the influence of the passage shock and the magnitude of vorticity or secondary flow. Mach number contours on three such surfaces are shown in figure 7.12. On the 10-percent chord surface, the intersection of shock surface and this surface is seen to extend from the casing all the way inward to a point very near the hub. At the 90-percent chord surface, the flow is almost entirely subsonic.

In order to more clearly see the effect of the three-dimensional passage shock on the three-dimensional flow field, the three-dimensional passage shock is constructed in scale and is shown in figure 7.13. At the tip Mach number of 1.37 and hub tip ratio of 0.5 the passage shock extends from casing all the way inward almost to the hub.

Comparison Between Computed Flow Field with DFVLR Measured Data

The quasi-three-dimensional transonic solution obtained by the present method is compared with available DFVLR measured data in figures 7.8, 7.9 and 7.11.

The character of the flow field obtained by the present method is seen to be in good agreement with that constructed from DFVLR measured data. In the region near 18-percent span, a supersonic zone appears near the leading edge of the suction surface. In the middle of the span, a bow wave appears a short distance in front of the leading edge and the wave extends to the flow passage to form a passage shock. At about two-thirds of the span, the shock appears to be nearly attached to the leading edge. Located in the blade tip region, is a second shock downstream of the bow wave/passage shock and the shock is nearly normal to the suction surface. The position of the passage shock obtained in the calculation is slightly in front of the measured position. It seems that this difference is inherent in the solution of transonic flow by the use of the stream function/artificial density method (refs. 41, 42, and 79). Also the computed shock is more nearly normal to the suction surface, whereas the measured shock is more inclined to the suction surface.

The result calculated by a different method (ref. 34) is included in figure 7.8 for comparison. The character of flow is similar, but there is some difference in the magnitude between the two calculated results.

The relatively good agreement between the calculated and measured values of Mach number and flow angle in the radial direction (fig. 7.9) and flow angle along the stream-wise direction (fig. 7.11) indicate that flow field in the central portion of the three-dimensional passage determined in the present method is sufficiently accurate for engineering computation. It seems that a more accurate determination of the shock position, such as the separate calculation/shock fitting method (section 6.1), appropriate correction for blockage effect at higher radius (section 6.3,) and without assuming axially symmetrical S_1 stream surface may improve the solutions.

7.2 Full-Three-Dimensional Transonic Flow in Cas Rotor

Solution Obtained by Using a Number of S_1 and S_2 Stream Filaments

The method described in Chapter 5 for obtaining three-dimensional flow using a number of S_1 and S_2 stream filaments was employed in reference 96 for calculating full-three-dimensional transonic flow in the CAS rotor. A full-three-dimensional calculation was made after a quasi-three-dimensional solution was been obtained. Thus, full-three-dimensional calculation can be used as a full-three-dimensional analysis solution after the rotor is designed by the quasi-three-dimensional procedure.

The design parameters of the CAS compressor and details of testing were given in section 5.9. The meridional projection of the rotor blades, design streamlines, L2F measuring stations, and the overall performance of the rotor were given in figures 5.42 and 5.43. The radial distribution of stagnation pressure and absolute flow angle measured by optical and non-optical devices are shown in figure 5.44. Three-dimensional flow calculation has been carried out for 80 and 90 percent of design speed and compared to the L2F data available at these two speeds.

Quasi-Three-Dimensional Solution for Transonic Flow in CAS Rotor

Quasi-three-dimensional solutions of transonic rotor were obtained for 80- and 90-percent design speed. The stagnation pressure and the absolute flow angle, measured by Setra capacitance transistor and L2F velocimeter, respectively, are taken as the outlet boundary conditions. The other main input data are: flow path in meridional plane, blade geometry (coordinates given on S_1 surface or on manufacturing templates), inlet pressure and temperature, rotor speed, mass flow and mass flow coefficient.

The first step is to solve the flow along an $S_{2,m}$ surface about midway between two adjacent blades. The computer code of reference 64, with a given absolute outlet flow angle and rotor efficiency, is used for this purpose. The isentropic efficiency of the rotor is determined by the torque measurement. The radial distribution of rotor efficiency is calculated with the stagnation pressure and temperature measurements. With the absolute velocity and flow angle measured by L2F velocimeter, the angular momentum $V_{\theta}r$ is calculated. During calculation, the outlet flow angle α and radial distribution of efficiency η_s are updated successively, until $V_{\theta}r$ converges, and the calculated pressure p^0 is in agreement with the experimental values. This process takes only three to five cycles. The set of radial distribution values of p^0 , α , and $V_{\theta}r$ at the outlet station and the rotor efficiency η_s are used for three-dimensional calculation of internal flow field and are compared with the L2F measured internal flow field. Figure 7.14 shows the calculated values as compared to the measured values at the outlet station.

From this solution of $S_{2,m}$ flow, the geometry of the 11 S_1 surfaces of revolution and the variation of the S_1 stream filaments are obtained. The coordinates of the corresponding blade surface are calculated by interpolation. The computer code of reference 41 is used to calculate the S_1 transonic flow. After the solution of the flow on the 11 S_1 surfaces are obtained, a new $S_{2,m}$ surface along with the corresponding variations of thickness of the S_1 filament Number 10 in figure 7.15. The angular momentum $V_{\theta}r$ along streamline. Number 2 and Number 10 on the $S_{2,m}$ surface during iteration are shown in figure 7.16. In figure 7.17 the relative Mach numbers along the intersecting streamlines obtained on S_1 surface and on $S_{2,m}$ surface are shown. The closeness between the values shows the degree of consistency as well as convergence reached in the solution.

Table III below gives the geometry and major flow parameters on six S_1 stream filaments obtained in the solution

TABLE III.—MAJOR PARAMETERS ON SIX S_1 STREAM FILAMENTS OF REVOLUTION

S	M	β_1 , degree	β_2 , degree	Coordinates r, m			r/r_0^a			$r_{1,0}$ r_0	σ , degree
				$\bar{c} = 0$	$\bar{c} = .5$	$\bar{c} = 1$	$\bar{c} = 0$	$\bar{c} = .5$	$\bar{c} = 1$		
11	1.180	-66.2	-56.2	.3426	.3390	.3354	1.000	1.014	.943	.943	-7.98
9	1.089	-64.2	-51.2	.3133	.3102	.3078	1.092	1.021	.979	.896	-5.49
7	.993	-61.3	-45.7	.2807	.2801	.2788	1.234	1.121	1.071	.868	-1.73
5	.883	-57.4	-38.5	.2434	.2460	.2465	1.404	1.305	1.206	.859	2.61
3	.758	-51.2	-27.6	.1986	.2055	.2096	1.730	1.589	1.433	.929	8.62
1	.609	-38.7	3.8	.1370	.1499	.1628	2.638	2.461	1.929	.731	18.41

^a $r_0 = 1.141$ cm.

In the table values of r_0 , $r_{0.5}$, r_1 , and r/r_0 show clearly the quasi-three-dimensional assumption of the S_1 stream surface. Although the S_1 surface is axially-symmetric, the flow on S_1 varies in the circumferential direction.

The meridional projection of streamlines on $S_{2,m}$ is shown in figure 7.18(a).

The stream-wise variation of the S_2 filament thickness and the angular momentum $V_\theta r$ at the mean streamline on six S_1 stream surfaces is shown in figures 7.19 and 7.20, respectively. On the S_1 surface near the hub, the flow is subsonic and these curves resemble those previously obtained in the subsonic compressor (for example, fig. 5.40 and 5.39). But for the S_1 surface located in the region where a passage shock exists, the curves are greatly affected by the shock.

The circumferential variations of relative Mach number at six axial stations on five S_1 surfaces are shown in figure 7.21.

Full-Three-Dimensional Flow in CAS Rotor

As mentioned in Section 5.7 the full-three-dimensional solution can be made by going into the multi- S_2 calculation immediately after the completion of the multi- S_1 calculation in the first cycle interaction (A-B-C in fig. 7.22). But, in the present calculation, multi- S_2 calculations are carried out after the completion of the quasi-three-dimensional solution (A-B-A-B in fig. 7.22). It is found that the iterative calculation between six (in the first four cycles) to 11 (in the last two cycles) S_1 surfaces and seven S_2 surfaces reaches an acceptable level of convergence and consistency after six cycles of iteration. There are 52 (21 in the blade region) and 11 stations, respectively, along x^1 and x^2 coordinates on each S_1 surface, and 52 and 11 stations, respectively, along x^1 and x^2 coordinates on each S_2 surface. The solution of the flow on the seven S_2 surfaces employed in the iterative calculation is based on the "inverse type" solution, i.e., $V_{\theta r}$ obtained in the S_1 solution is taken as the input value to the S_2 solution. The S_2 surface adjacent to the blade surface is placed a short distance from it, and the mass flow between them is 5 percent of the total flow. The S_1 and S_2 computer codes are connected through two interpolation codes so that $V_{\theta r}$ distribution and S_2 filament thickness obtained in the solution of flow on S_1 surfaces are interpolated for input values to different S_2 surfaces. Similarly the geometry of the S_1 surfaces and the filament thickness τ obtained in the solution of flow on S_2 surfaces, are interpolated for input values to the S_1 surfaces.

Similar to the quasi-three-dimensional solution, entropy increases across the rotor at different radii are calculated according to the rotor efficiency at these radii. The variation of entropy increased along the x^1 direction is obtained by considering that (1) there is no entropy increase in the flow up to shock line, (2) entropy increases abruptly across the shock, and (3) from there on it increases linearly to the outlet value. In order to be consistent, the value of entropy used in the S_1 calculation is the same as that in the S_2 calculation at the same grid point. Because of the lack of data on how entropy varies

from blade to blade, the circumferential variation of entropy is considered neither on the S_1 surface nor on different S_2 surfaces.

Converging Process

Since the main difference between a quasi-three-dimensional and a full-three-dimensional solution is whether the radius of the S_1 surface is or is not circumferentially constant, the convergence in the geometry of S_1 surface is an indication of the convergence of the full-three-dimensional solution.

Table IV lists the changes in the radii of three S_1 surfaces during iteration. The corresponding changes in S_1 filament are listed in Table V.

TABLE IV.—CHANGES IN RADIUS (m) OF GENERAL S_1 SURFACES DURING ITERATION

S_1	S_2 Station cycle	I			IV			VII		
		21	31	41	21	31	41	21	31	41
9	1	.3111	.3102	.3083	.3125	.3102	.3077	.3127	.3098	.3070
	5	.3118	.3101	.3081	.3131	.3108	.3082	.3137	.3108	.3080
	6	.3118	.3101	.2781	.3131	.3108	.3082	.3137	.3108	.3080
7	1	.2784	.2796	.2793	.2807	.2806	.2792	.2814	.2802	.2792
	5	.2791	.2794	.2790	.2811	.2804	.2794	.2823	.2806	.2793
	6	.2791	.2794	.2790	.2811	.2805	.2794	.2823	.2806	.2794
5	1	.2425	.2453	.2473	.2451	.2476	.2481	.2471	.2483	.2490
	5	.2430	.2453	.2469	.2445	.2468	.2476	.2466	.2475	.2480
	6	.2429	.2453	.2469	.2445	.2467	.2476	.2465	.2474	.2479

TABLE V.—CHANGES IN FILAMENT THICKNESS (cm) OF GENERAL S_1 SURFACES

S_1	S_2 Station cycle	I			IV			VII		
		21	31	41	21	31	41	21	31	41
9	1	1.143	1.054	.986	1.096	1.035	.987	1.087	1.050	.987
	5	1.126	1.054	.986	1.084	1.039	.977	1.061	1.037	.955
	6	1.126	1.052	.985	1.084	1.037	.977	1.062	1.036	.955
7	1	1.189	1.131	1.063	1.174	1.087	1.033	1.127	1.059	.989
	5	1.201	1.136	1.075	1.199	1.120	1.062	1.166	1.103	1.034
	6	1.202	1.138	1.075	1.200	1.121	1.062	1.167	1.104	1.035
5	1	1.388	1.328	1.229	1.388	1.294	1.201	1.373	1.277	1.160
	5	1.366	1.298	1.213	1.401	1.295	1.204	1.374	1.279	1.158
	6	1.367	1.299	1.213	1.402	1.296	1.204	1.375	1.279	1.159

$r_o = 1.41$ cm.

Convergence in the radius of the general S_1 stream surfaces and in the thickness of the general S_1 stream filament is clearly indicated in Tables IV and V.

The Mach numbers along intersecting lines between $S_{2,m}$ surfaces and S_1 surfaces are shown in figure 7.17(b).

In figure 7.23 the Mach numbers along intersecting streamlines between S_1 surfaces and S_2 surfaces in this solution are shown. A comparison between figures 7.17(a) and 7.17(b) and figure 7.23 itself indicates that much better convergence and consistency are achieved in the full-three-dimensional solution than that achieved in the quasi-three-dimensional solution.

Geometry of S_1 and S_2 Stream Filaments

Data in tables VI and VII show that the radius of the S_1 surface increases in the circumferential direction at the blade leading edge, and the difference decreases toward the blade trailing edge. On the other hand, the filament thickness at the leading edge is larger near the pressure surface at large radius and larger near the suction surface at small radius. The difference decreases toward the trailing edge.

This configuration of the S_1 stream filaments is a combined result of the flow vorticity and the passage shock. In subsonic flow the relative circumferential difference in the radius is found to be about 0.2 percent, but in transonic flow the maximum value is about 1.3 percent, an order of magnitude higher. The geometry of the S_2 stream filaments is given in table VIII.

TABLE VI.—COORDINATE r (m) OF S_1 STREAM SURFACES

S_1, S_2 station	Number = 7					Number = 4				
	I	II	III	IV	V	I	II	III	IV	V
17	.2792	.2802	.2806	.2811	.2815	.2201	.2205	.2214	.2222	.2229
21	.2792	.2800	.2811	.2820	.2825	.2229	.2230	.2239	.2248	.2259
25	.2792	.2800	.2806	.2812	.2819	.2243	.2248	.2256	.2263	.2268
33	.2795	.2802	.2803	.2804	.2802	.2271	.2278	.2284	.2287	.2290
41	.2789	.2793	.2793	.2793	.2794	.2294	.2299	.2301	.2303	.2307
45	.2784	.2785	.2785	.2785	.2787	.2304	.2305	.2306	.2305	.2308

TABLE VII.—THICKNESS OF S_1 STREAM FILAMENTS (τ/r_o)

S_1, S_2 station	Number 11 (Filament of Revolution)					Number 7 (General Filament)				
	I	II	III	IV	V	I	II	III	IV	V
16	1.026	1.017	1.008	1.001	.995	1.251	1.262	1.253	1.246	1.239
21	1.054	1.043	1.021	1.007	.996	1.202	1.209	1.200	1.187	1.167
31	1.028	.986	.970	1.957	.957	1.138	1.130	1.121	1.114	1.104
41	.954	.946	.954	.957	.968	1.075	1.067	1.062	1.058	1.052
46	.929	.928	.929	.929	.928	1.042	1.039	1.038	1.037	1.035
	Number 4 (General Filament)					Number 1 (Filament of Revolution)				
	I	II	III	IV	V	I	II	III	IV	V
16	1.643	1.653	1.653	1.652	1.647	3.497	3.488	3.542	3.592	3.695
21	1.502	1.533	1.546	1.557	1.543	2.876	2.872	2.955	3.053	3.172
31	1.418	1.431	1.430	1.429	1.121	2.613	2.603	2.662	2.709	2.738
41	1.317	1.316	1.316	1.306	1.297	1.962	2.055	2.099	2.133	2.191
46	1.255	1.256	1.255	1.254	1.251	1.692	1.703	1.711	1.720	1.741

$r_o = 1.41$ cm.

Figures 7.24 and 7.25 show, respectively, the 10 S_1 stream filaments formed by the 11 S_1 stream surfaces and the intersecting lines of the 11 S_1 stream surfaces with three span-wise surfaces. It is found during calculation that the twist of the S_1 surface in the radial direction is relatively large at the blade leading edge and relatively small at blade trailing edge. For instance, the radii of S_1 surface Number 5

at the blade leading edge are, respectively. 0.2429 m at the pressure surface and 0.2465 m at the suction surface, a difference of 0 to 0.0036 m or 1.48 percent, but at the trailing edge they are, respectively, 0.2469 and 0.2479, a difference of only 0.001 m or 0.4 percent.

The geometry of S_1 stream surfaces is one of the most important three-dimensional flow variables. The blade section is now operating inside this filament. The flow characteristics are greatly influenced by the variation of filament thickness in stream-wise as well as in circumferential direction.

Three-Dimensional Flow Field

The three-dimensional geometry of the S_1 stream filaments, given in tables VI and VII, and the blade sections lying in the filament determine the flow along these filaments and consequently the flow over the whole channels (see fig. 5.27). The meridional projection of the streamlines obtained on the $S_{2,m}$ surface S_2 filament thickness and $V_{\theta}r$ along the mean streamline on six S_1 stream surfaces are given in figures 7.18(b), 7.19(b) and 7.20(b), respectively. The difference between the solution obtained in the present full-three-dimensional solution and the previous quasi-three-dimensional solution is quite apparent. The major geometry and inlet and outlet flow conditions of the six S_1 stream filaments are listed in table VI in which a and b denote the two corners at the upstream station, e and f at mid-point of chord length and c and d at the downstream station. r_c/r_a , r_d/r_b and r_c/r_a , r_d/r_b are the contraction in r and filament thickness r , respectively, on the two sides.

The flow determined on the six S_1 filaments is shown in figure 7.26 in terms of constant Mach number contours. They are drawn for flow fields including four stations upstream and three stations downstream of the blade. The inlet Mach number varies from 0.6 at the hub to 1.25 at the tip. The supersonic region begins to appear on surface (3). On surface (7) a bow wave appears and extends to the suction

surface as a passage shock. On the tip surface (11) the passage shock hits the suction surface at about 50-percent chord point.

TABLE VIII.—GEOMETRY OF S₂ STREAM FILAMENTS

S ₁	S ₂ station	r, m					φ, rad					r/r ₁					
		I	III	V	VII	I	III	V	VII	I	III	V	VII	I	III	V	VII
9	16	.3131	.3125	.3130	.3131	.224	.146	.069	.012	1.006	1.004	1.003	1.009	1.006	1.004	1.003	1.009
	21	.3118	.3124	.3135	.3137	.080	.020	-.043	-.111	1.078	.975	.995	1.032	1.078	.975	.995	1.032
	31	.3101	.3106	.3110	.3108	.018	-.058	-.129	-.198	.879	.922	.889	.910	.879	.922	.889	.910
	41	.3081	.3083	.3081	.3080	-.115	-.066	-.260	-.333	1.022	.965	.998	.998	1.022	.965	.998	.998
	46	.3065	.3066	.3066	.3066					1.000	1.000	1.000	1.000	1.000	1.000	1.000	1.000
7	16	.2784	.2789	.2798	.2802	.224	.155	.088	.012	1.001	1.001	.999	1.000	1.001	1.001	.999	1.000
	21	.2791	.2800	.2820	.2823	.075	.011	-.053	-.120	1.259	.959	1.005	1.016	1.259	.959	1.005	1.016
	31	.2794	.2801	.2807	.2806	-.020	-.095	-.160	-.236	.955	.922	.890	.870	.955	.922	.890	.870
	41	.2790	.2795	.2794	.2794	-.021	-.282	-.354	-.427	.998	.983	.999	1.062	.998	.983	.999	1.062
	46	.2784	.2786	.2787	.2787					1.000	1.000	1.001	1.000	1.000	1.001	1.001	1.000
5	16	.2400	.2404	.2416	.2422	.255	.154	.085	.011	1.000	1.001	.999	.999	1.000	1.001	.999	.999
	21	.2429	.2434	.2455	.2465	.074	.010	-.056	-.124	1.324	.990	.980	1.054	1.324	.990	.980	1.054
	32	.2453	.2461	.2472	.2474	-.035	-.108	-.190	-.252	.962	.913	.864	.824	.962	.913	.864	.824
	41	.2469	.2474	.2477	.2479	-.265	-.338	-.410	-.483	.946	.964	1.004	1.145	.946	.964	1.004	1.145
	46	.2475	.2477	.2478	.2479					1.000	1.001	1.001	1.000	1.000	1.001	1.001	1.000
3	16	.1933	.1934	.1946	.1935	.225	.154	.083	.010	.999	.998	.996	.999	.999	.998	.996	.999
	21	.1993	.1991	.2009	.2021	.072	.006	-.059	-.127	1.293	.980	.904	.957	1.293	.980	.904	.957
	32	.2050	.2054	.2066	.2071	-.042	-.114	-.187	-.259	.958	.890	.828	.775	.958	.890	.828	.775
	41	.2097	.2102	.2108	.2113	-.305	-.377	-.450	-.522	.948	.960	.996	1.160	.948	.960	.996	1.160
	46	.2119	.2121	.2123	.2125					1.000	.999	.999	.999	1.000	.999	.999	.999

The geometry of the S_2 stream filaments is given in table VIII. Similar to the S_1 stream filaments, the three-dimensional geometry of the S_2 stream filaments and the meridional wall shape determine the flow along these filaments and consequently the flow over the whole channel (see fig. 5.29). figure 7.27 shows the constant Mach number contours on the S_2 filaments. Notice that, whereas in the quasi-three-dimensional solution only flow on one S_2 surface (the $S_{2,m}$ surface), which took part in the iteration, is directly obtained in the solution, in full-three-dimensional solution the flow on all S_2 surfaces, which took part in the iteration, are directly obtained in the solution. The circumferentially uniform flow at the inlet station becomes nonuniform near the blade leading edge, where tip Mach number varies from 1.18 on S_2 (I) to 1.21 on S_2 (VII). It becomes uniform again at three stations downstream of the blade. From the pressure surface of one blade toward the suction surface of the adjacent blade, the intersection line of the shock and the surface becomes longer and moves downstream. The flow condition on S_2 (I) and (VII) should be particularly useful in the investigation of boundary layer flow along the blade surfaces.

Using data obtained from these two families of stream surfaces a three-dimensional view of the shock can easily be constructed (fig. 7.28). The passage shock is seen to extend from the casing part way (about two-thirds) down to the hub. The shock is nearly normal to the suction surface and more inclined at lower radius.

Using data obtained on the S_1 and S_2 surfaces, constant Mach number contours can also be constructed on a number of a third family of surfaces, formed by the x^2 and x^3 coordinates, nearly normal to S_1 and S_2 surfaces at stations 1 (L.E.), 5, 9, 11, and 21 (T.E) (fig. 7.28). In the stream-wise direction the shock intersection line becomes shorter, and the circumferential gradient in Mach number becomes smaller. Between station 11 and 21 appears a reverse circumferential Mach number

gradient in the lower part of the passage. Consequently there is also a reverse circumferential gradient in pressure, which will affect the boundary layer along the hub wall.

Constant σ contours are obtained on five such surfaces and are shown in figure 7.30. At station $J=0$ (one station upstream of the blade) there is a significant difference circumferentially in the upper half of the flow channel. At the pressure surface side σ is $+2^\circ$, whereas on the suction surface side, σ is -2° to -6° . This difference in σ means that the air is moving outward on the left and moving inward on the right. At station 2 the air on the upper left is now moving inward with -8° to -10° . Thus there is a twist of S_1 surface between station 0 and station 2. It is nearly uniform circumferentially at station 6. At station 10 a sharp change of 2° appears in the flow direction over most part of the channel. At station 21 the value σ is again nearly uniform in the circumferential direction.

The stream-wise variations of filament thickness and angular momentum $V_{\theta r}$ of S_2 stream filaments (I), (IV), and (VII) are shown, respectively, in figures 7.31 and 7.32. As for the filament thickness τ , the variation in the subsonic hub region is similar to that of $(P-t)/P$, except that there is a high peak value at the leading edge on the $S_2(I)$. In the supersonic upper region the variation of $S_2(I)$ and $S_2(VII)$ are quite different from $(P-t)/P$. On $S_2(IV)$ there is still some resemblance, but it has two peaks around the leading edge, indicating the effects of bow wave and passage shock.

The variation of $V_{\theta r}$ is somewhat similar. In the hub region it is only slightly modified from the usual shape in subsonic flow. But in the upper part there is quite a peak at leading edge near the pressure surface and an overshoot at the trailing edge near the suction surface. In the tip region there is either a two-step rise or fluctuation in the $V_{\theta r}$ variation.

Difference Between Three-Dimensional and Quasi-Three-Dimensional Solution

The difference between three-dimensional and quasi-three-dimensional solution is entirely due to the difference in the geometry of the S_1 stream filament. Tables III and VIII show the major difference between the S_1 stream filaments involved in the two calculations.

First, there is some difference in the geometry of $S_{2,m}$ in the radial coordinate and in the contraction of the filaments thickness. Figure 7.19 shows the difference in the streamwise variation of the $S_{2,m}$ filament thickness.

A rather complicated variation in the full-three-dimensional flow is much simplified in the quasi-three-dimensional flow. The streamwise variations of the important flow variable $V_{\theta r}$ on the $S_{2,m}$ surface are compared in figure 7.20. A higher overshoot exists in the quasi-three-dimensional solution. The streamwise variations of Mach number along the intersecting streamline of the S_1 and $S_{2,m}$ surfaces, obtained in the solution on the two surfaces, are compared in figure 7.17. The full-three-dimensional solution has reached a higher level of consistency and convergence than the quasi-three-dimensional solution. The former, in general, gives a slightly higher peak Mach number than the latter. This difference is also noticeable in the comparison of the constant Mach number contour maps on the $S_{2,m}$ surface shown in figure 7.34.

Circumferential variations of Mach number at six stations on five S_1 surfaces obtained in full-three-dimensional and quasi-three-dimensional solution are compared in figure 7.21. In addition to the factors influencing the solution mentioned above, the circumferential variation in the S_1 geometry in the full-three-dimensional solution also influences the result. It can be seen from tables V, VI, and VIII that for S_1 surfaces above $S_1(7)$, the filament thickness and its contraction on the side near the pressure surface

is significantly different from those on the side near the suction surface. The combined effect on the velocity distribution is that, on S_1 surfaces above $S_1(7)$, the Mach number of the full-three-dimensional solution is higher in the region from mid-channel to suction surface and lower in the region from mid-channel to pressure surface, than that of the quasi-three-dimensional solution.

Comparison with L2F Measurement

Efforts were made at IETP to obtain internal flow on S_1 surface (4), and (7) to (10) by the use of a Laser-2-Focus (L2F) velocimeter developed by DFVLR. Measured values are shown in figure 7.21. In general the measured values are a little higher than the calculated values. Constant Mach number contours, constructed from the L2F measured data, are shown in figure 7.33. The trend is similar, but again the measured Mach number is a little higher than the calculated value.

7.3 Some Remarks

The general theory of three-dimensional flow in subsonic and supersonic turbomachinery based on the iterative solution between S_1 and S_2 stream filaments has been successfully extended to a transonic flow regime. In this extension, some of the recently developed simple and quick methods for solving transonic flow along S_1 and S_2 stream filaments are utilized. For the CAS transonic rotor, three-dimensional solution is obtained after six cycles of iteration by using the quasi-three-dimensional solution as the starting value. It has a higher level of convergence and consistency than the quasi-three-dimensional solution. The difference between three-dimensional and quasi-three-dimensional solution is: The former gives a higher peak Mach number than the latter. This difference is mainly due to the neglect of the circumferential variation of the S_1 filament thickness in the quasi-three-dimensional solution. A comparison between the theoretical solution and the L2F measurement shows that the

character of the transonic flow including the three-dimensional shock structure is in fair agreement, and the calculated velocity is a little lower than that measured by L2F over most of the flow region, except at the 20-percent chord station in the upper half region near the suction surface, where the measured velocity is a little lower.

A practical three-dimensional computer aided design and analysis (three-dimensional-CADA) system has been constructed by the use of the general S_1 code and the general S_2 code. The recommended procedure of three-dimensional-CADA calculation follows.

- (1) Prescribed the through-flow design requirements on the $S_{2,m}$ surface and obtain the $S_{2,m}$ solution
- (2) Design the blade section on a number of general S_1 stream filaments
- (3) Stack the blade sections
- (4) Obtain the three-dimensional analysis for the blade just designed
- (5) Modify step 1 or step 2 and repeat steps 3 and 4 until the results obtained meet the design requirements

It is believed that the configuration of the three-dimensional geometry of the S_1 stream filaments, obtained during the iterative calculation between the S_1 and S_2 flow, to a large extent, determines the performance of the blade section lying in the stream filament. With this information available better design of the blade section and, consequently, of the whole blade can be realized. Another advantage of the presented method is that the computer storage required is very small and the amount of CPU time is also small so it is feasible to carry out all of the computations on a microcomputer.

References

1. Wu, Chung-Hua and Wolfenstein, L.: "Application of Radial-Equilibrium-Condition to Axial-Flow Compressor and Turbine Design," NACA TR 955, 1950.
2. Wu, Chung-Hua: "A General Through-Flow Theory of Fluid Flow with Subsonic or Supersonic Velocity in Turbomachines Having Arbitrary Hub and Casing Shapes," NACA TN 2302, 1951.
3. Wu, Chung-Hua: "A General Theory of Three-Dimensional Flow in Subsonic and Supersonic Turbomachines of Axial, Radial, and Mixed-Flow Types," ASME Paper Number 50-A-79, ASME Transactions, November 1952, or NACA TN 2604, 1952.
4. Wu, Chung-Hua and Brown, C.A.: "Method of Analysis for Compressible Flow Past Arbitrary Turbomachine Blades on General Surface of Revolution," NACA TN 2407, 1951.
5. Wu, Chung-Hua and Brown, C.A.: "A Method of Designing Turbomachine Blades with a Desirable Thickness Distribution for Compressible Flow along an Arbitrary Stream Filament of Revolution," NACA TN 2455, 1951.
6. Wu, Chung-Hua and Brown, C.A.: "An Approximate Method of Determining the Subsonic Flow in an Arbitrary Stream Filament of Revolution Cut by Arbitrary Turbomachine Blades," NACA TN 2702, 1952.
7. Wu, Chung-Hua and Curtis, A. et al.: "Analysis of Flow in a Subsonic Mixed Flow Impeller," NACA TN 2749, 1952.
8. Prian, V.D., Kramer, J., and Wu, C.H.: "Theoretical Analysis of Incompressible Flow Through a Radial-Inlet Centrifugal Impeller at Various Weight Flows. I. Solution by a Matrix Method and Comparison with An Approximate Method," NACA TN 3448, 1955.
9. Wu, Chung-Hua and Costilow, Eleanor, L.: "A Method of Solving the Direct and Inverse Problem of Supersonic Flow Along Arbitrary Stream Filaments of Revolution in Turbomachines," NACA TN 2492, 1951.

10. Wu, Chung-Hua: "Matrix and Relaxation Solutions that Determine Subsonic Through-Flow in an Axial-Flow Gas Turbine," NACA TN 2750, 1952.
11. Wu, Chung-Hua: "Subsonic Flow of Air Through a Single-Stage and a Seven Stage Compressor: NACA TN 2961, 1953.
12. Marsh, H.: "A Digital Computer Program for the Through-Flow Fluid Mechanics in an Arbitrary Turbomachine Using a Matrix Method," R&M Number 3509, 1968.
13. Katsanis, T.: "Computer Program for Calculating Velocities and Streamlines on a Blade-to-Blade Stream Surface of a Turbomachine," NASA TN D-4525, 1968.
14. Katsanis, T. and McNally, W.D.: "Fortran Program for Calculating Velocities and Streamlines in a Magnified Region on a Blade-to-Blade Stream Surface of a Tandem Turbomachine," NASA TN D-5044, 1969.
15. Senoo, Y. and Nakase, Y.: "A Blade Theory of an Impeller with an Arbitrary Surface of Revolution," ASME Journal of Engineering For Power, vol. 93, 1971, pp. 454-460.
16. Davis, W.R.: "Axial Flow Compressor Analysis Using a Matrix Method," Carleton University, Report Number MW/A 73-1, 1973.
17. Smith, D.J.L.: "Computer Solutions of Wu's Equations for the Compressible Flow through Turbomachines," in NASA SP-304, 1973.
18. Katsanis, T., and McNally, W.D.: "Fortran Program for Calculating Velocity and Streamlines on the Hub-Shroud Mid-Channel Flow Surface of an Axial- or Mixed-Flow Turbomachine," NASA TN D-7343, 1973.
19. Adler, D. and Krimerman, Y.: "The Numerical Calculation of the Meridional Flow Field in Turbomachines Using the Finite Elements Method," Israel Journal of Technology, vol. 12, 1974, pp. 268-274.
20. Hirsch, Ch., and Warzee, G.: "A Finite Element Method for Through Flow Calculation in Turbomachines," Journal of Fluids Engineering, vol. 98, 1976, p. 403.

21. Bianiaris, S.: "The Calculation of Quasi-Three-Dimensional Flow in the Axial Gas Turbine," ASME Journal of Engineering for Power, pp. 283-294, 1975.
22. Adler, D. and Krimerman, Y.: "Calculation of the Blade-to-Blade Compressible Flow Field in Turbo Impellers Using Finite Element Method," Journal of Mechanical Engineering Science, vol. 19, 1978, pp. 108-112.
23. Senoo, Y. and Nakase, Y.: "An Analysis of Flow Through a Mixed-Flow Impeller," Journal of Engineering for Power, vol. 94, 1972, pp. 43-40.
24. Bosman C. and El-Shaaraw, M.A.I.: "Quasi-Three-Dimensional Numerical Solution of Flow in Turbomachines," Journal of Fluids Engineering, vol. 99, 1977, pp. 132-140.
25. Hirsch, Ch. and Qarzee, G.: "An Integrated Quasi-Three-Dimensional Finite Element Calculation Program for Turbomachinery Flows," Journal of Engineering for Power, vol. 101, 1979, pp. 141-148.
26. Krimerman, Y. and Adler, D.: "The Complete Three-Dimensional Calculation of the Compressible Flow Field in Turbo-Impellers," Journal of Mechanical Engineering Science, vol. 20, 1978, pp. 149-158.
27. Wu, Chung-Hau: Formulas and Tables of Coefficients for Numerical Differentiation with Function Values Given at Unequally Spaced Points and Application to the Solution of Partial Differential Equations, Science Press, 1959.
28. Wu, Chung-Hua: "Basic Aerothermodynamic Equations Governing Fluid Flow in Turbomachines Expressed in Terms of Non-Orthogonal Curvilinear Coordinates," Research Notes, Institute of Mechanics, C.A.S., 1963.

29. Wu, Chung-Hua: "Three-Dimensional Turbomachine Flow Equations Expressed with Respect to Non-orthogonal Curvilinear Coordinates and Methods of Solution," Lecture Notes, China University of Science and Technology, 1975 or "Proceedings of the 3rd International Symposium on Air-Breathing Engines," 1976, pp. 233–252, or Engineering Thermophysics in China, vol. 1, no. 2, 1980, Rumford Publishing Company, USA.
30. Luu, T.S., Viney, B. and Corniglion, J.: "Conception optimale de l'alimentation latérale d'une turbomachine," AAAF 18^e Colloque Aérodynamique Appliquée, Poitiers 1981.
31. Zhu, G.X., and Wu, C.H.: "Three-Dimensional Subsonic Flow Through a Stator by Use of a Central S_2 Stream Surface and Several S_1 Surfaces of Revolution," Journal of Engineering Thermophysics, vol. 4, no. 2, pp. 134-142, 1983. (in Chinese).
32. Wang, Qinghuan, Wu, Wenquan, Zhu, Genxing, Li, Weihong and Wu, Chung-hua: "Solution of Three-Dimensional Compressible Flow in an Axial-Flow Compressor Stator by the Use of S_1 and S_2 Relative Surface," Journal of Engineering Thermophysics, vol. 4, pp. 336-346, 1983, (in Chinese).
33. Wu, Chung-Hua, Wang, Jianan, Fang, Zongyi, and Wang, Qinghuan: "L2F Velocity Measurement and Calculation of Three-Dimensional Flow in an Axial Compressor Rotor," Proceedings of 7th ISABE, 1985.
34. McDonald, R.W.: "The Computation of Transonic Flow Through Two-Dimensional Gas Turbine Cascades," ASME Paper 71-GT-89, 1971.
35. Gopalakrishnan, S., and Bozzola, R.: "A Numerical Technique for the Calculation of Transonic Flows in Turbomachinery Cascades," ASME Paper No. 71-GT-42, 1971.
36. Denton, J.D.: "A Time Marching Method for Two- and Three-Dimensional Blade-to-Blade Flows," Aeronautical Research Council, 35567, 1974.
37. Wu, C.H., Wu, W., Hua, Y., and Wang, B.: "Transonic Cascade Flow with Given Shock Shape Solved by Separate Supersonic and Subsonic Computations," Computational Methods in Turbomachinery, I Mech E, Paper No. C19/84, pp. 133–140, 1984.

38. Wu, Wenquan, Wu, Chunghua, and Yu, Dabang: "Transonic Cascade Flow Solved by Separate Supersonic and Subsonic Computation with Shock Fitting," *Jrl. of Engineering for Gas Turbines and Power*, Apr, 1985.
39. Qin, Lisen and Wu, Chung-Hua: "Transonic Flow along S_2 Stream Surface Solved by Separate Supersonic and Subsonic Calculations," ISABE Paper 85-7058, Proceedings of 7th International Symposium for Air-Breathing Engines, pp. 502-509, 1985.
40. Habashi, W.G., Hafez, M.M.: "Finite Element Stream Function Solution for Transonic Turbomachinery Flows," AIAA 82-1268.
41. Zhao, Xiaolu: "Solution of Transonic Flow along S_1 Stream Surface Employing Non-Orthogonal Curvilinear Coordinates and Corresponding Non-Orthogonal Velocity Components," *Journal of Engineering Thermophysics*, Aug. 1984, pp. 244-249 (in Chinese), or C64/84, *Computation Methods in Turbomachinery, I Mech E*, pp. 183-189.
42. Wang, Zhengming: "Solution of Transonic S_1 Surface Flow by Successively Reversing the Direction of Integration of the Stream Function Equation," *Jrl. of Engineering Thermophysics*, Aug. 1984. (in Chinese), or *Engineering for Power*, Apr. 1985.
43. Wu, Chung-Hua: "Fundamental Aerothermodynamic Equations for Stationary and Moving Coordinate Systems: Action of Viscous Forces and Physical Significance of Viscous Terms," *Journal of Mechanical Engineering*, vol. 13, no. 4, December 1965, pp. 43-67 (in Chinese) or *Engineering Thermophysics in China*, vol. 1, no. 1, 1980, Rumford Publishing Company, USA.
44. Wu, Chung-Hua: Discussion to Paper "A Practical Solution of a Three-Dimensional Flow Problem of Axial-Flow Turbomachinery," *ASME Transactions*, July 1953, pp. 802-803.
45. Vevra, M.H., *Aero-Thermodynamics and Flow in Turbomachines*, 1960.
46. Sirotkin, Ia, A.: "Formulation of Straight Problem of Vortex Flow of Compressed Fluid in Turbomachines," *Inzhenernyi Zhurnal, Journal of Engineering*, vol. 3, no. 2, pp. 271-279, 1963.

47. Johnson, I.A., and Bullock, R.O.: "Aerodynamic Design of Axial-Flow Compressor," NACA, SP-36, 1965.
48. Chen, Hongji, and Wu, Chung-Hua: "Accurate Solution of Inverse Problem of Transonic Flow on S_2 Surface by Means of Elliptic Algorithm." Proceedings of 7th ISABE, pp. 465-473, 1985.
49. Rahnke, C.J. and Carmody, R.H.: "The Combined Transonic Axial and Centrifugal Stage Compressor," SAE Paper 268D, 1961.
50. Serovy, G.K.: "Recent Progress in Aerodynamic Design of Axial-Flow Compressor in the United States," Journal of Engineering for Power, July, 1966.
51. Miller, M.L. and Chapman, D.C.: "Single-Stage Experimental Evaluation of Boundary Layer Blowing Technique for High Lift Stator Blades," I—Compressor Design, NASA CR-54564, 1969.
52. Fujii, S., and Matsuki, M.: "Several Topics of Axial-Flow Compressor Research at The National Aerospace Laboratory (Japan)" Gas Turbine Papers presented at Tokyo Joint International Gas Turbine Conference and Products Show, 1971.
53. Senoo, Y. and Nakase, Y.: "An Analysis of Flow Through a Mixed-Flow Impeller," Journal of Engineering for Power, vol. 94, 1972, pp. 40-43.
54. Wu, Chung-Hua and Brown, C.A.: "A Theory of Direct and Inverse Problems of Compressible Flow Past Cascade of Arbitrary Airfoils, Journal of Aeronautical Sciences, March, 1952.
55. Liu, Kao-Lien, Hsieh, Ming-Lun and Wu, Chung-Hau: "Aerothermodynamic Analysis and Design of Turbomachines," Chinese Journal of Mechanical Engineering, March, . 11, No. 1, pp. 1-28, 1963.
56. Cai, R.: "The Analytical Solution for MSLM for 2D Cascade," Journal of Mechanical Engineering, (in Chinese), vol. 14, no. 1, 1966, pp. 17-49.
57. Cai, R.: "A Method of Designing Axial Flow Turbomachine Cascades Along an Arbitrary Stream Filament of Revolution," Journal of Mechanical Engineering, (in Chinese), vol. 15, no. 1, 1979, pp. 24-36.

58. Wang, Z. and Cai, R.: "MSLM with Higher-Order Derivatives and the Computer Code," Journal of Engineering Thermophysics, (in Chinese), November, 1983, pp. 347-350.
59. Zhao, X.: "A Method for Solving Inverse Problem of Three-Dimensional Turbomachine Flow—the Mean Stream Surface Method, and the Annular Constraint Condition," M.S. Thesis, Institute of Engineering Thermophysics, 1981 (in Chinese).
60. Sun, C.: "A New Method for Series Expansion from $S_{2,m}$ Surface," M.S. Thesis, Institute of Engineering Thermophysics, 1983 (in Chinese).
61. Zhao, X., Sun, C. and Wu, Chung-Hua: "A Simple Method for Solving Three-Dimensional Inverse Problems of Turbomachine Flow and the Annular Constraint Condition," Journal of Engineering for Gas Turbines and Power, vol. 107, 1985, pp. 293-300.
62. Academia Sinica and Shengyang Aeroengine Company: "Theory, Methods and Application of Three-Dimensional Flow Design of Transonic Axial-Flow Compressor," Journal of Engineering Thermophysics, vol. 1, no. 1, 1980, pp. 44-54 (in Chinese).
63. Wu, W. and Liu, C.: "Flow-Field Matrix Solution for Direct Problem of Flow Along S_1 Relative Stream Surface Employing Non-orthogonal Velocity Components," Journal of Engineering Thermophysics, vol. 1, no. 1, 1980, pp. 18-27 (in Chinese) or Engineering Thermophysics in China, vol. 1, no. 3, pp. 307-322, Rumford Publishing Company, USA.
64. Zhu, R.: "Flow-Field Line Relaxation Solution for S_2 Relative Stream Employing Non-Orthogonal Curvilinear Coordinates and Corresponding Non-Orthogonal Velocity Components," Journal of Engineering Thermophysics, vol. 2, no. 3, 1980.
65. W.W. and Jian, H.: "A Development in Calculation of Flow Past Cascade on Arbitrary Surface of Revolution," C83/84. Computational Methods in Turbomachinery, I Mech. E, pp. 265-270, 1984.
66. Wu, Chung-Hua and Wang, Baoguo: "Matrix Solution of Compressible Flow on S_1 Surface Through a Turbomachine Blade Row with Splitter Vanes or Tandem Blades," ASME Journal of Engineering for Gas Turbines and Power, vol. 106, April, 1984, pp. 449-454.

67. Wang, Z.: "Inverse Design Calculations for Transonic Cascades," ASME Paper 85-GT-6, 1985.
68. Cai, Ruixian: "Constraint on Design Parameters and Twist of S_1 Surfaces in Turbomachines," Scientia Sinica (Series A), Apr. 1983.
69. Liu, C.E., and Wu, W.Q.: "Computer Program of Supersonic Flow Past Inlet of Cascade Section on an Arbitrary Stream Filament of Revolution and Determining Unique Inlet Flow Angle," Journal of Engineering Thermophysics, vol. 1, no. 3, 1980.
70. Moeckel, W.E.: "Approximate Method for Predicting Form and Location of Detached Shock Waves Ahead of Plane or Axially Symmetric Bodies," NACA TN 1921, 1949.
71. Love, E.S.: "A Reexamination of the Use of Simple Concepts for Predicating the Shape and Location of Detached Shock Waves," NACA TN 4170, Dec. 1957.
72. York, R.E., and Woodard, H.S.: "Flow in the Entrance Region of Supersonic Compressor Cascades," ASME Journal of Engineering for Power, Apr. 1976, pp. 247-257.
73. Starken, H.: "Research of The Flow in a Plane Supersonic Diffuser Cascade," (in English) DLR FB 71-99 DFVLR Institut fur Luftstrahlantriebe.
74. Ruan, Z.K.: "Experimental Determination of Shape and Location of Bow Shock Wave Ahead of a Plane Cascade," Journal of Engineering Thermophysics, vol. 4, no. 4, pp. 338-341, 1983.
75. Hua, Yao-nan: "Computation of the Detached Shock and the Entrance Flow Field in a Supersonic or Transonic Cascade," ASME 85-GT-7.
76. Holst, T., Ballhaus, W.: "Fast Conservative Schemes for Full Potential Equation Applied to Transonic Flows," AIAA J. 1979, 17, pp. 145-152.
77. Hafez, M.M., South, J., and Murman, E.M.: "Artificial Compressibility Methods for Numerical Solution of Transonic Full Potential Equation," AIAA Journal, vol. 17, no. 8, 1979.
78. Hafez, M., Lovell, D.: "Numerical Solution of Transonic Stream Function Equation, AIAA 81-1017.

79. Hua, Y., Wu, W.: "Numerical Solution of Transonic Stream Function Equation on S_1 Stream Surface in Cascade," ASME 86-GT-110, 1986.
80. Roach, R., Sankar, N.: "The Strongly Implicit Procedure Applied to the Flow Fluid of Transonic Turbine Cascade," AIAA 81-0211, 1981.
81. Stone, L.: "Iterative Solution of Implicit Approximations of Multi-Dimensional Partial Differential Equations," SIAM J. of Numerical Analysis, 1968, vol. 3, 530-558.
82. Dunavant, J. and Erwin, J.: "Investigation of a Related Series of Turbine-Blade Profiles in Cascade," NACA TN 3892, 1955.
83. Dodge, P.: "Transonic Relaxation Methods," ASME Paper 76-GT-63, 1976.
84. Lu, W.Q., Chen, X.M.: "The Time-Dependent Numerical Solution of Transonic Flow on S_1 Surface of Revolution Employing Non-Orthogonal Curvilinear Coordinates and Non-Orthogonal Velocity Components," J. of Engineering Thermophysics (in Chinese), 1983, 4, pp. 119-126.
85. Wang, B., Hua, Y., Huang, X., Wu, C.H.: "Transonic Flow Along Arbitrary Stream Filament of Revolution Solved by Separate Computations with Shock Fitting," ASME Paper 86-GT-30, 1986.
86. Zhao Xiaolu, Qin Lisen: "Stream Function Solution of Transonic General S_1 Flow in Turbomachines, J. of Eng. Thermophysics, vol. 8, no. 4, pp. 340-342 (in Chinese), 1987.
87. Monsarrat, N.T. et al.: Design Report. Single-Stage Evaluation of Highly-Loaded High Mach-Number Compressor Stages, NASA CR-72562, 1969.
88. Chen Hongji and Wu Chunghua: "Shock Embedding Discontinuous Solution of Elliptic Equation for Inverse problem of Transonic S_2 Flow," ASME Paper No. 87-GT-115, Journal of Turbomachinery, vol. 110, pp. 347-353, 1988.
89. Strinning, P.E., Dunker, R.J.: "Aerodynamic and Blade Design of a Transonic Axial-Compressor Stage," Forschungsberichte Verbrennungs-Kraftmaschinen, Heft 178, 1975.

90. Dunker, R.J., Strinning, P.E.: "Flow Velocity Measurements Inside of a Transonic Axial Compressor Rotor by Means of an Optical Technique and Compared with Blade to Blade Calculations," 3rd ISABE Proceedings, DGLR-Fachbuch No. 6, March, 1976.
91. Zhao Xiaolu: "Stream Function Solution of Transonic Flow Along S_2 Streamsurface of Axial Turbomachines," ASME Paper 85-GT-2, 1985.
92. Zhao Xiaolu: "Transonic Stream Function Solution on S_2 Streamsurface for a High Pressure Ratio Centrifugal Compressor," Journal of Engineering Thermophysics, vol. 9, no. 1 (in chinese), 1988.
93. Asborne, C., Runstadler, P.W., Stacy, W.D.: "Aerodynamic and Mechanical Design of an 8:1 Pressure Ratio Centrifugal Compressor," NASA CR-134782, 1975.
94. Hayami, H., Senoo, R., Veki, H.: "Flow in the Inducer of a Centrifugal Compressor Measured with a Laser Velocimeter," ASME 84-GT-74, 1984.
95. Wang Zhengming, Chen Hongji, Hua Yaonan, and Wu Chung-Hua: "Solution of Transonic Flow in an Axial Compressor Rotor by Quasi-3D Iteration Between S_1 and S_2 Stream Surface," Chinese Journal of Engineering Thermophysics, vol. 1, no. 2, pp. 153-166, 1989.
96. Zhao Xiaolu, Qin Lisen and Wu Chung-Hua: "A Quasi-3D Computation for the CAS Transonic Compressor Rotor and Comparison with L2F Velocity Measurements," Chinese Journal of Engineering Thermophysics, vol. 1, no. 1, 1989, pp. 29-37.
97. Zhao Xiaolu, Qin Lisen and Wu Chung-Hua: "A Full-3D Iterative Solution on $S_1 - S_2$ Stream Surfaces in the CAS Transonic Compressor Rotor," Chinese Journal of Engineering Thermophysics, vol. 1, no. 4, 1989, pp. 391-400.
98. Qin Lisen, Zhao Xiaolu and Wu Chung-Hua: "Analysis of Full-3D S_1-S_2 Iterative Solution for Flow in the CAS Transonic Compressor Rotor and Comparison with Quasi-3D Iterative Solution and L2F Measurement," Chinese Journal of Engineering Thermophysics, vol. 2, no. 1, 1990, pp. 29-38.

99. Wu Chunghua, Wang Zhengming, Chen Hongji: "Three-Dimensional Rotational Flow in Transonic Turbomachines, Part I—Solution Obtained by Using a Number of S_1 Stream Filaments of Revolution and a Central S_2 Stream Filament," ASME Paper 90-GT-12, J. of Turbomachinery, vol. 114, no. 1, pp. 38-49.
100. Wu Chunghua, Zhao Xiaolu, Qin Lisen: "3D Rotational Flow in Transonic Turbomachines, Part II—Full Three-Dimensional Flow in CAS Rotor Obtained by Using a Number of S_1 and S_2 Stream Filaments," ASME Paper 90-GT-13, J. of Turbomachinery, vol. 114, no. 1, pp. 50-60.

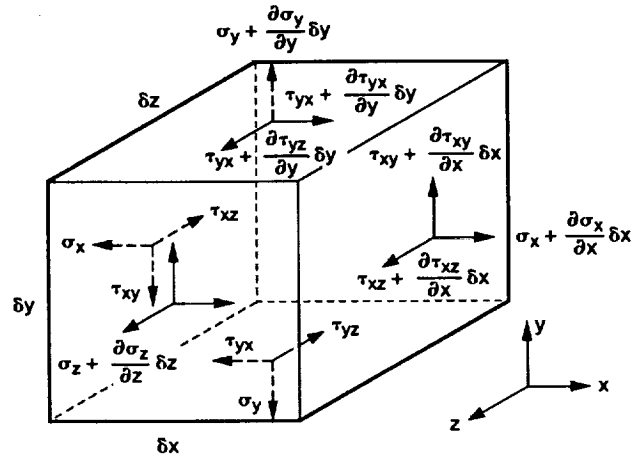


Figure 2.1.—Stress tensor.

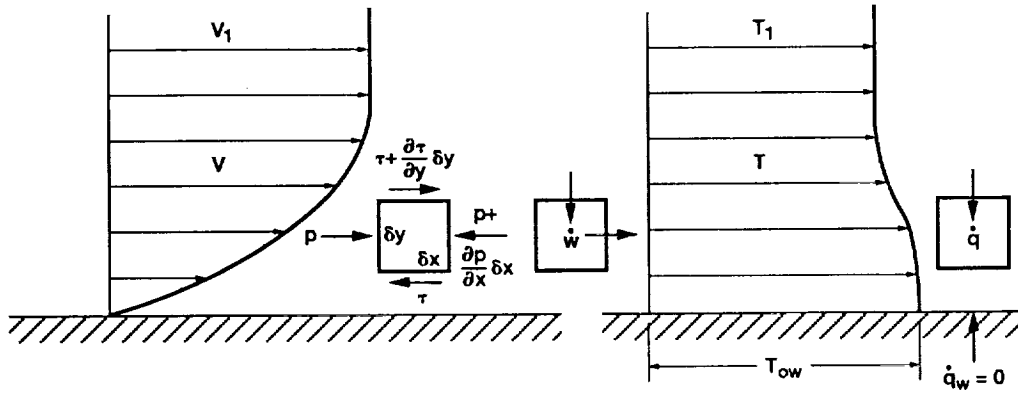
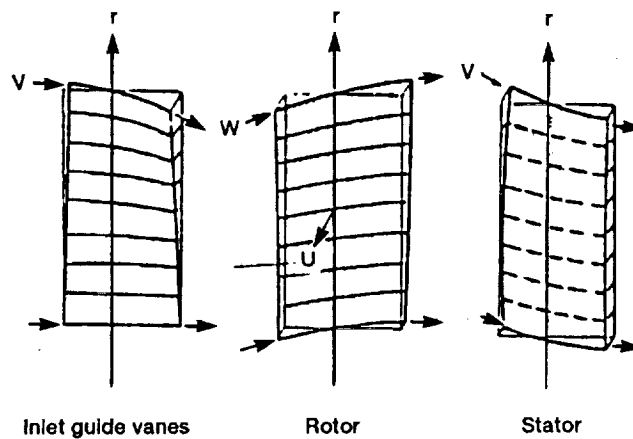


Figure 2.2.—Velocity and temperature profile and fluid element in a laminar boundary layer.



Inlet guide vanes Rotor Stator

Figure 2.3—Relative stream surface in inlet guide vanes, rotor and stator.

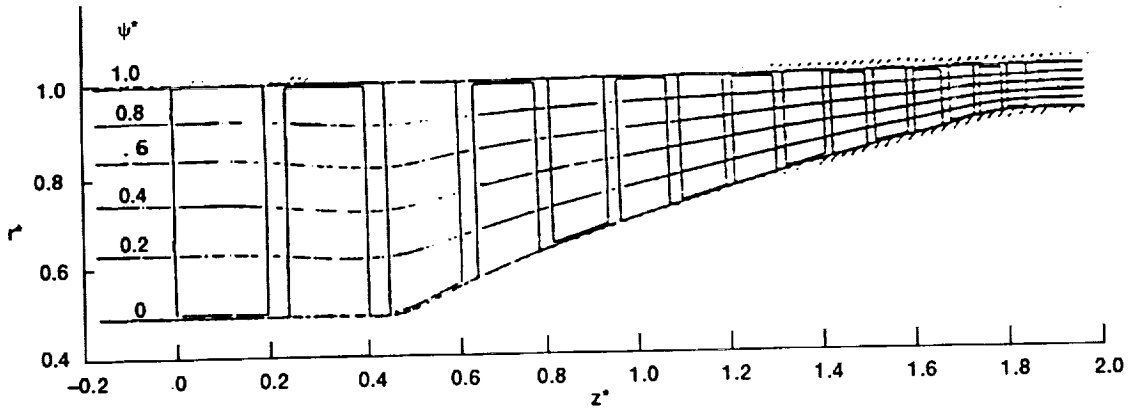


Figure 2.4—Projection of streamlines in meridional plane.

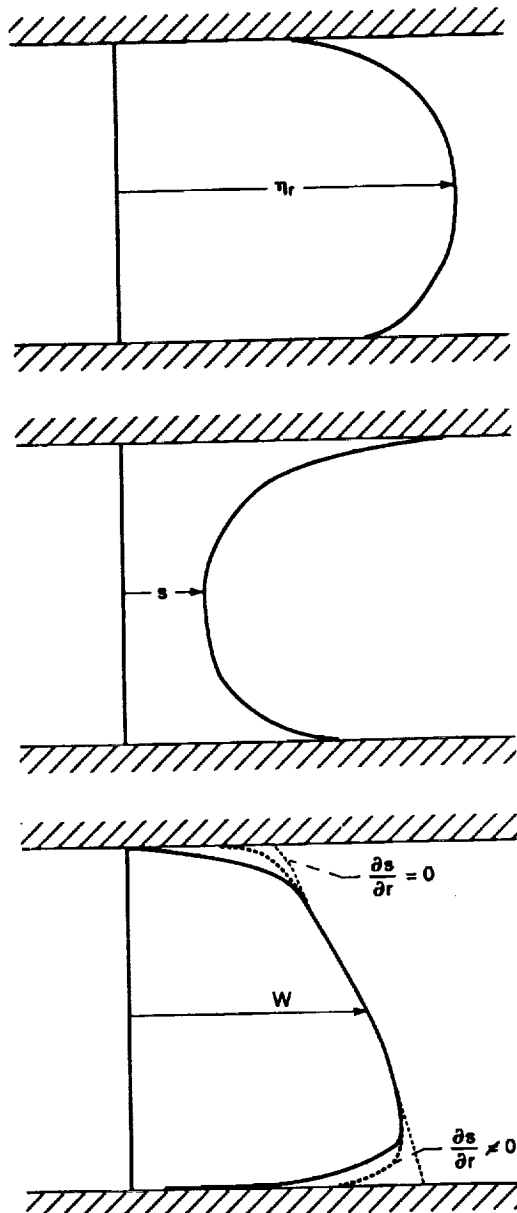


Figure 2.5.—Radial variation of rotor efficiency, entropy increase and velocity.

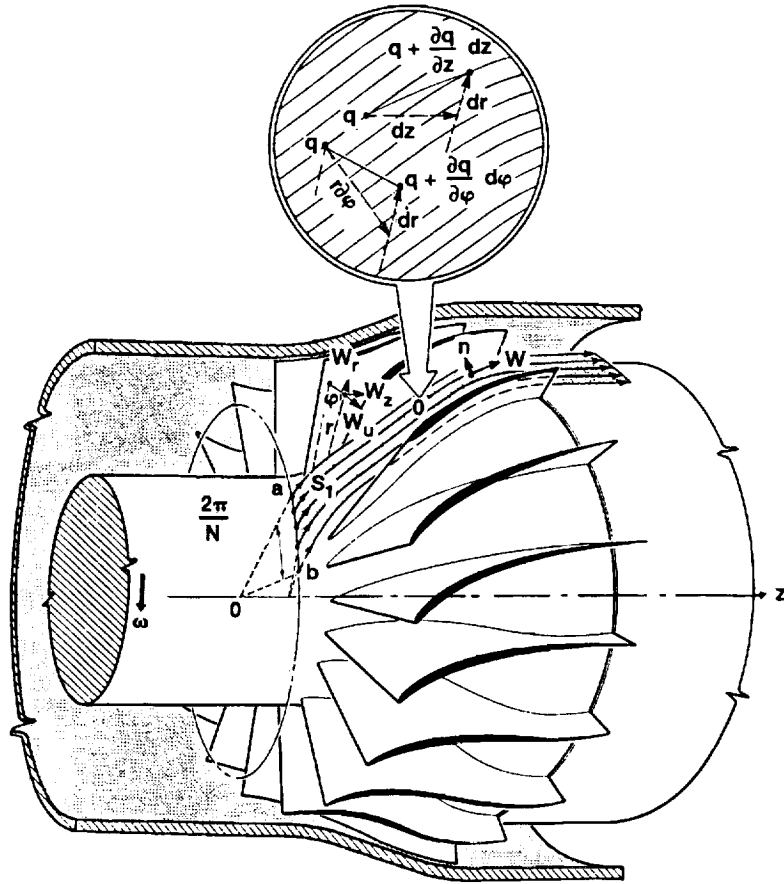


Figure 3.1—Relative stream surface S_1 .

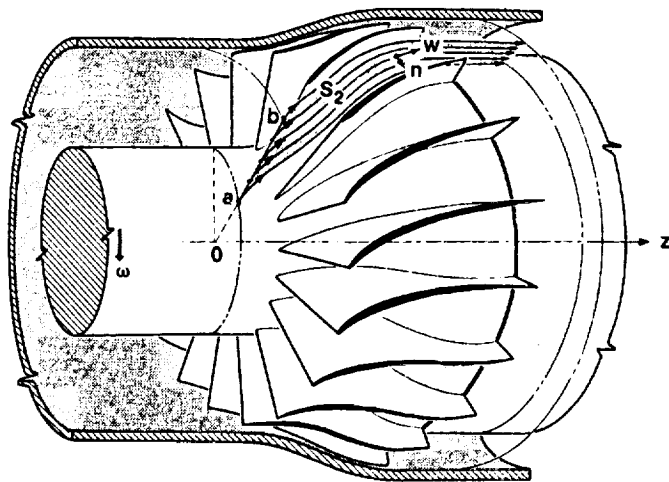


Figure 3.2—Relative stream surface S_2 .

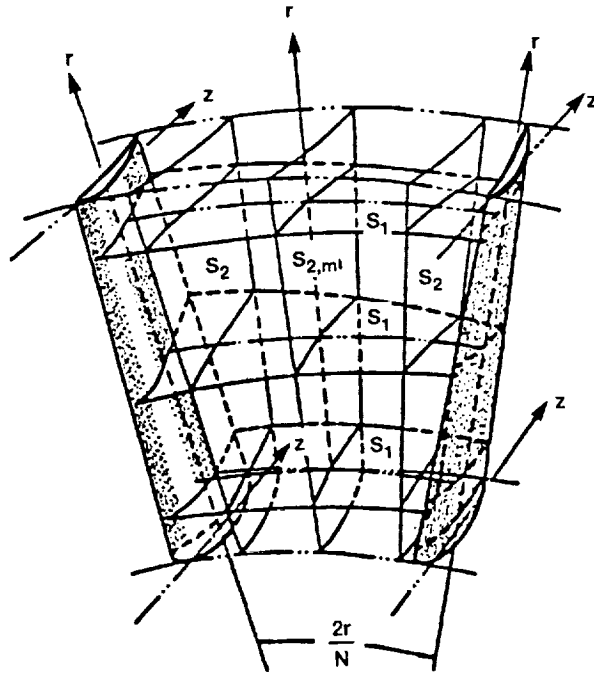


Figure 3.3.—Intersecting S_1 and S_2 surfaces in blade passage.

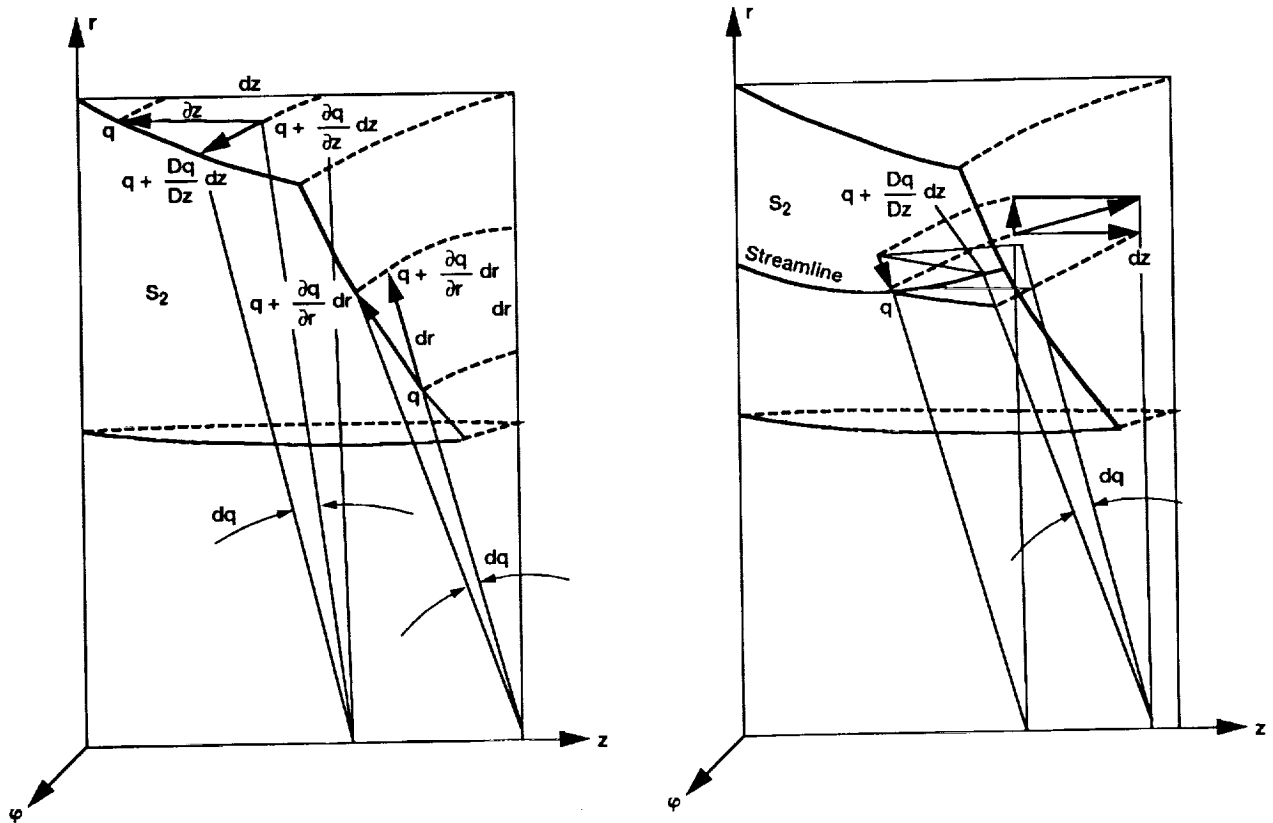


Figure 3.4.—Partial derivative and total derivative following motion on S_2 .

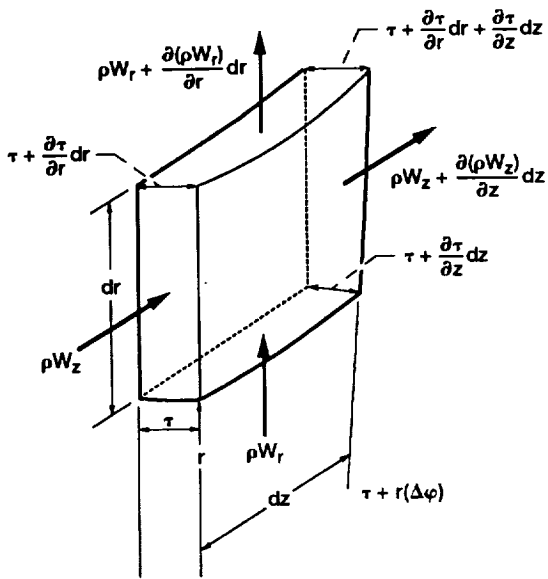


Figure 3.5.—Element of S_2 stream filament.

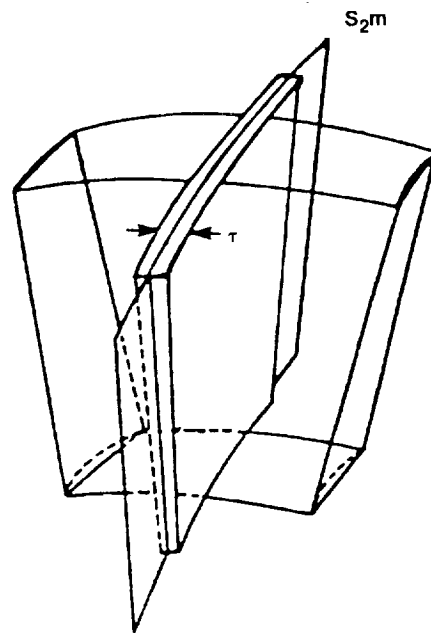


Figure 3.6— S_2 stream surface and S_2 stream filament.

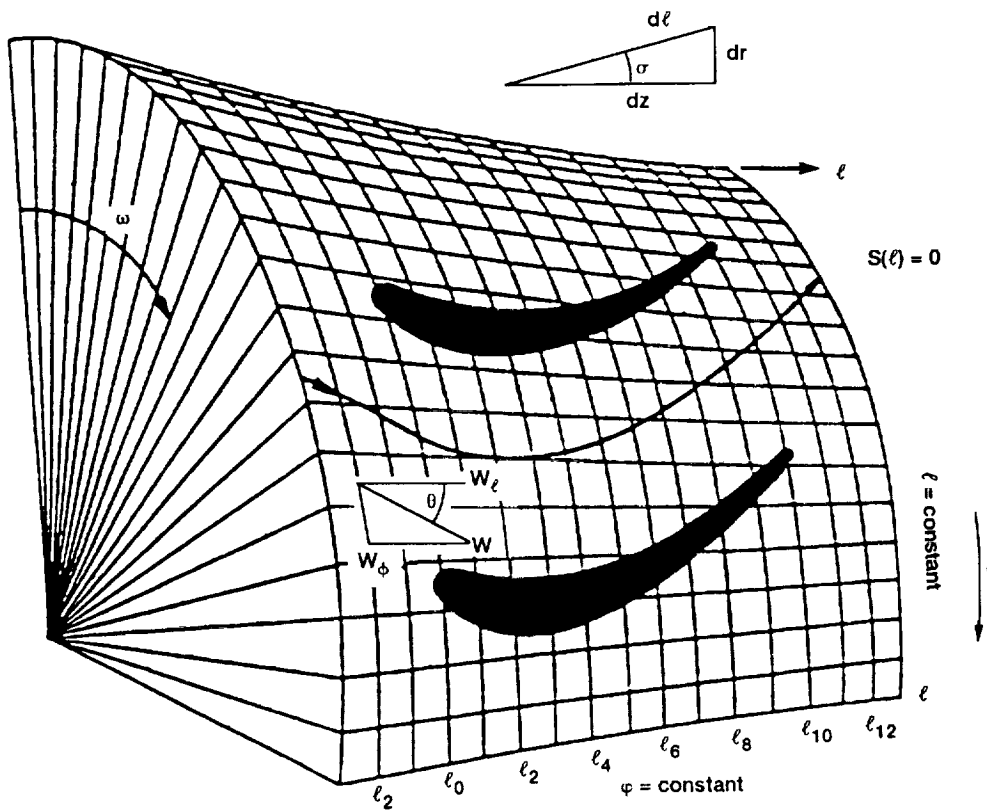


Figure 3.7.—Orthogonal curvilinear coordinates ℓ , ϕ , on S_1 surface of revolution.

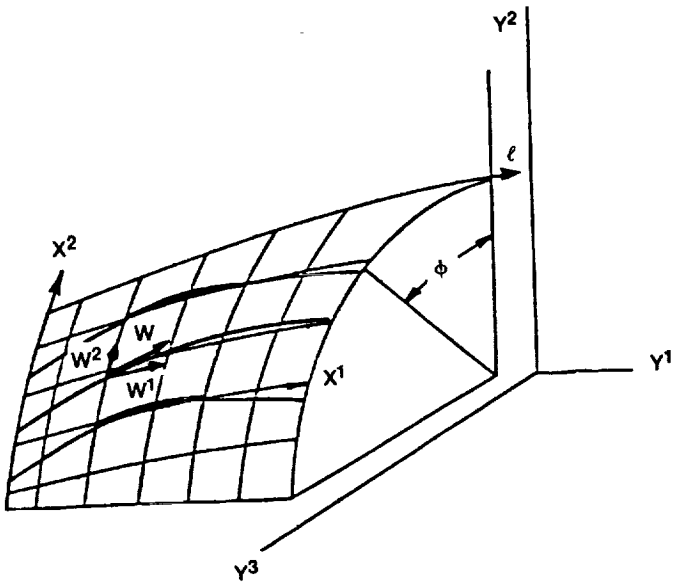


Figure 4.1.—Non-orthogonal curvilinear coordinates employed in the investigation of S_1 flow.

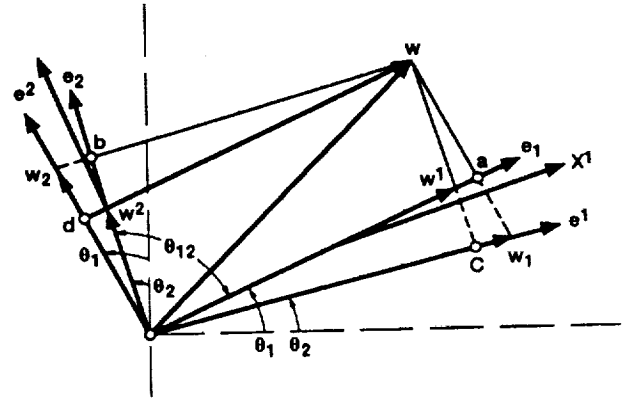


Figure 4.2.—General coordinates x^1 and x^2 , base vectors e_1 and e_2 , reciprocal vectors e^1 and e^2 and contravariant and covariant components of vector W .

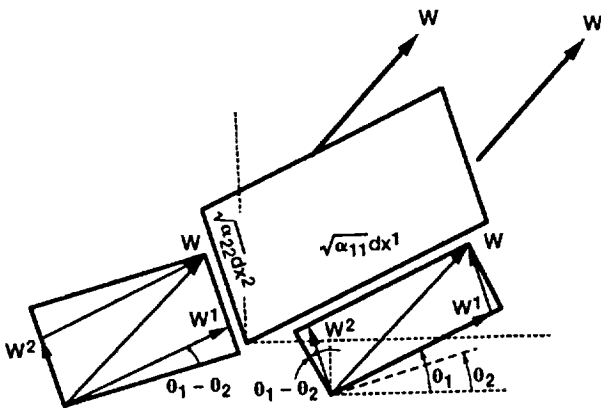


Figure 4.3.—Element of S_1 stream filament.

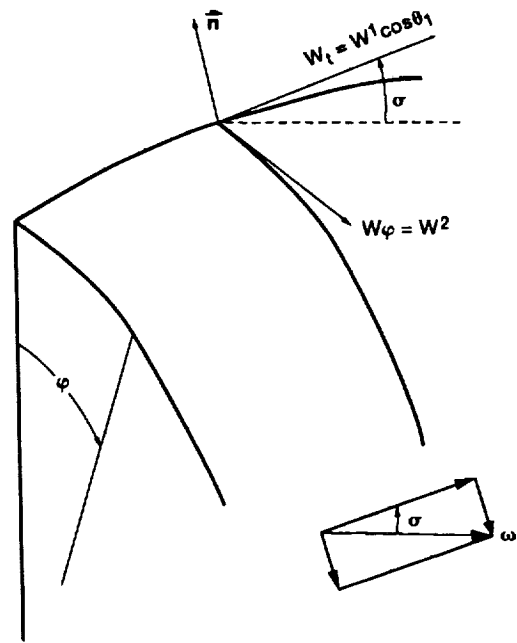


Figure 4.4.—Unit vector and vorticity normal to S_1 surface.

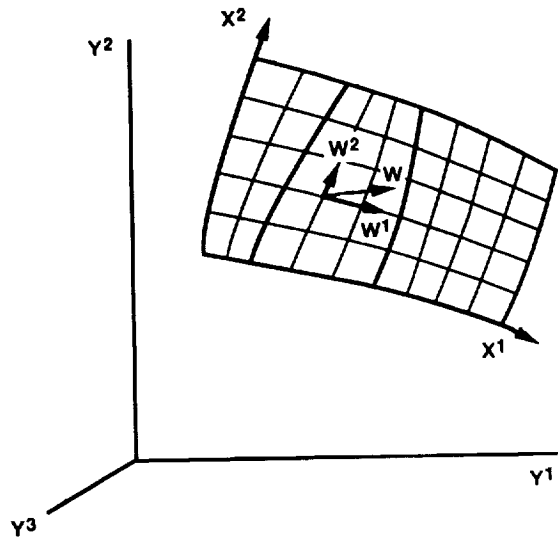


Figure 4.5.—Non-orthogonal curvilinear coordinates used for S_2 flow.

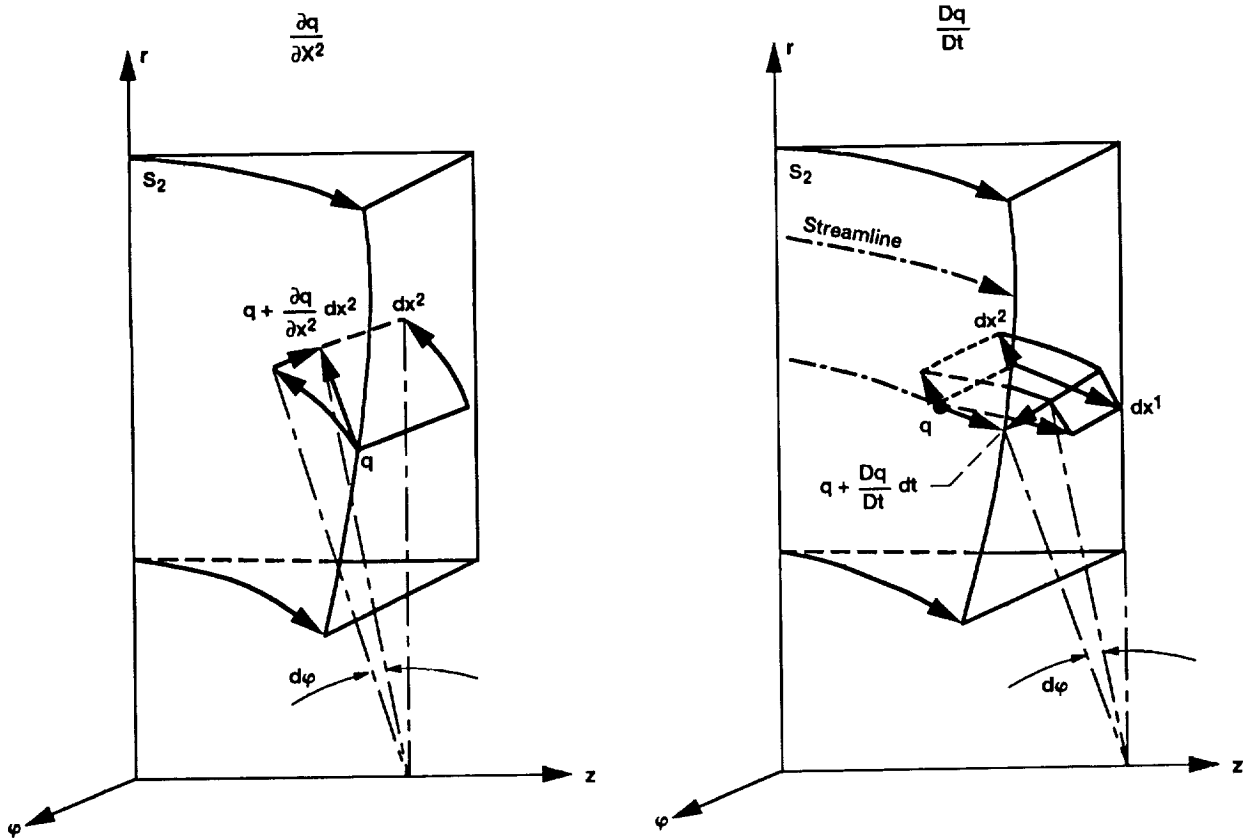


Figure 4.6.—Partial derivative and total derivative following fluid flow on S_2 surface.

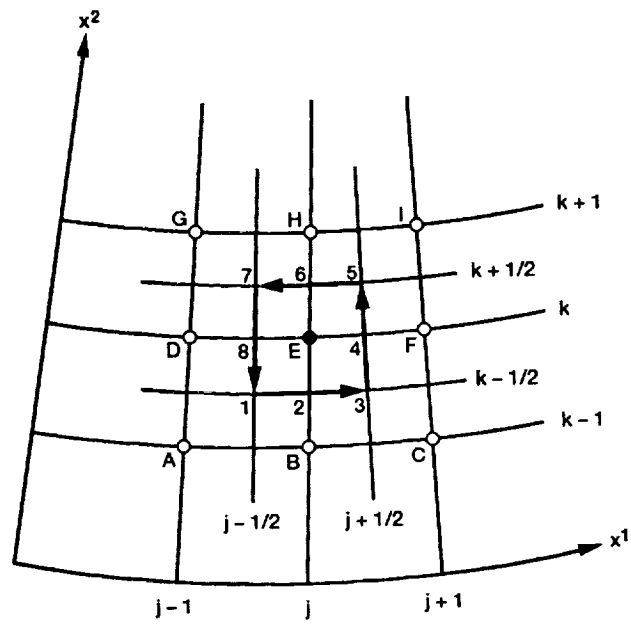


Figure 4.7.—Line integration around grid point E.

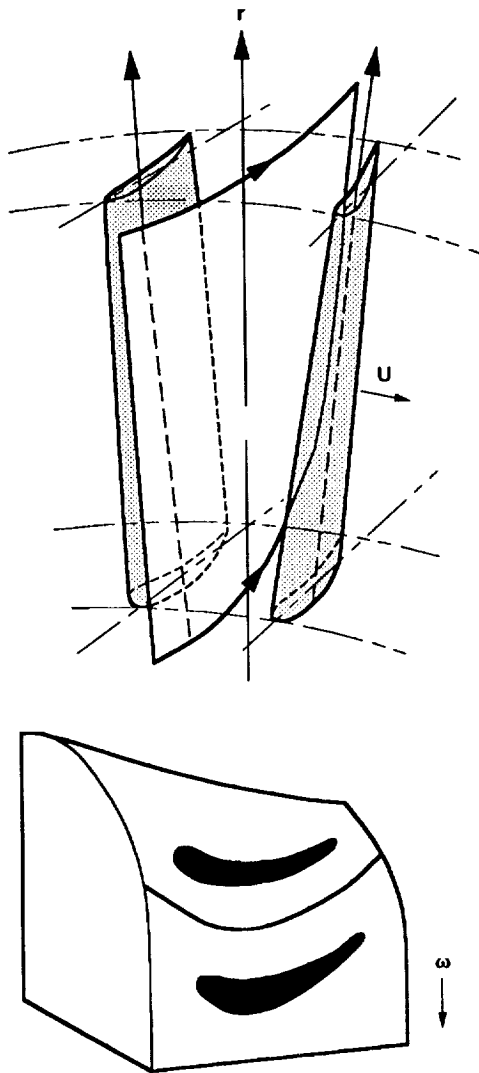


Figure 5.1.—Mean stream surface and mean streamline.

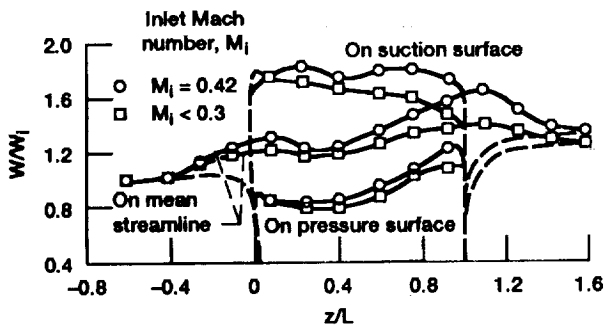


Figure 5.2.—Variations of velocity on blade surface and mean streamline.

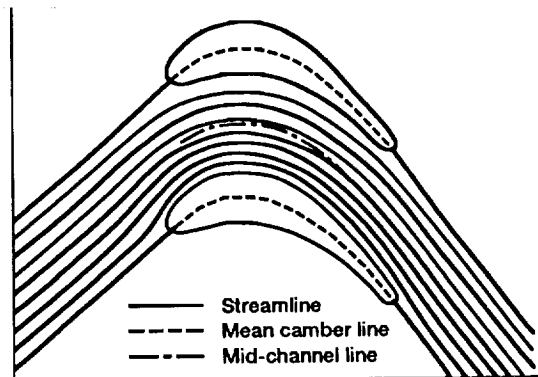


Figure 5.3.—Streamline distribution in turbine cascade.

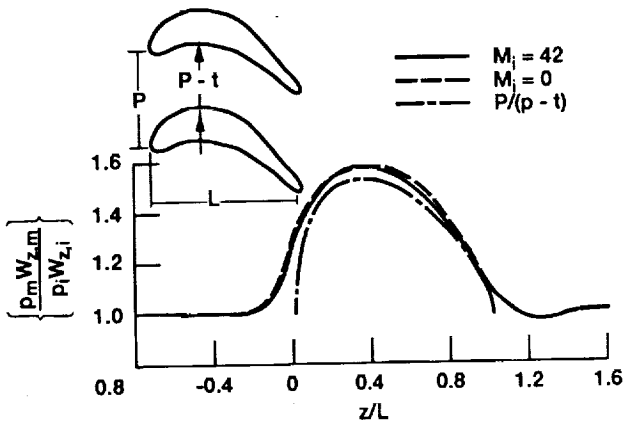


Figure 5.4.—Variation of specific mass flow and passage width ratio.

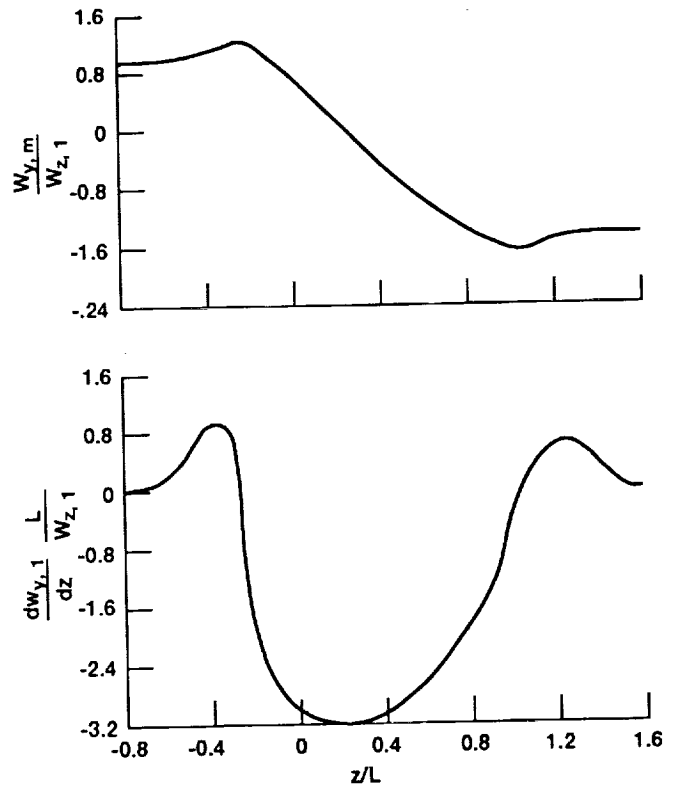


Figure 5.5.—Variation of tangential velocity and its derivative with respect to \$z\$ along mean streamline.

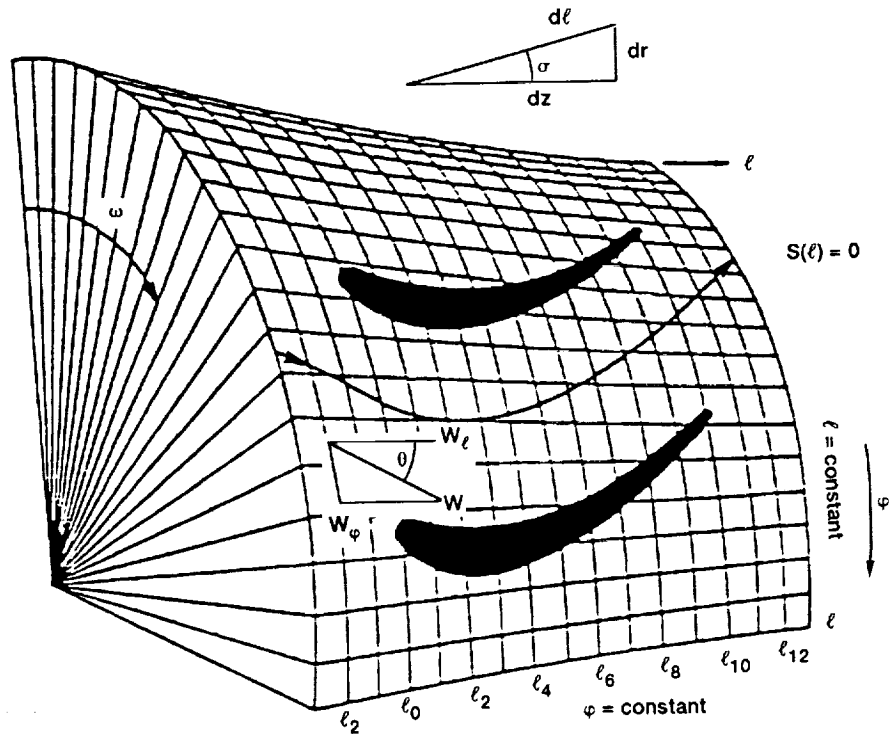


Figure 5.6.—Mean streamline in the flow passage.

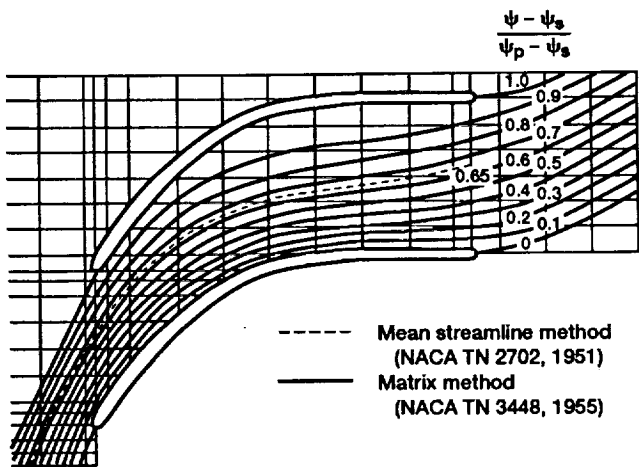


Figure 5.7.—Streamline in a radial-flow impeller.

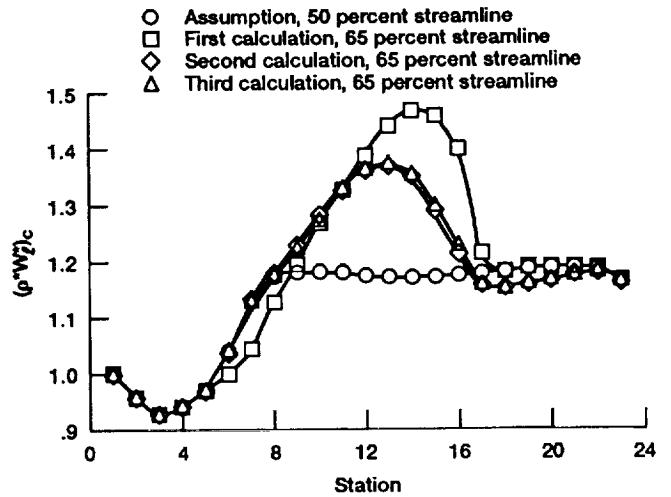


Figure 5.8.—Variation of meridional velocity on mean streamline.

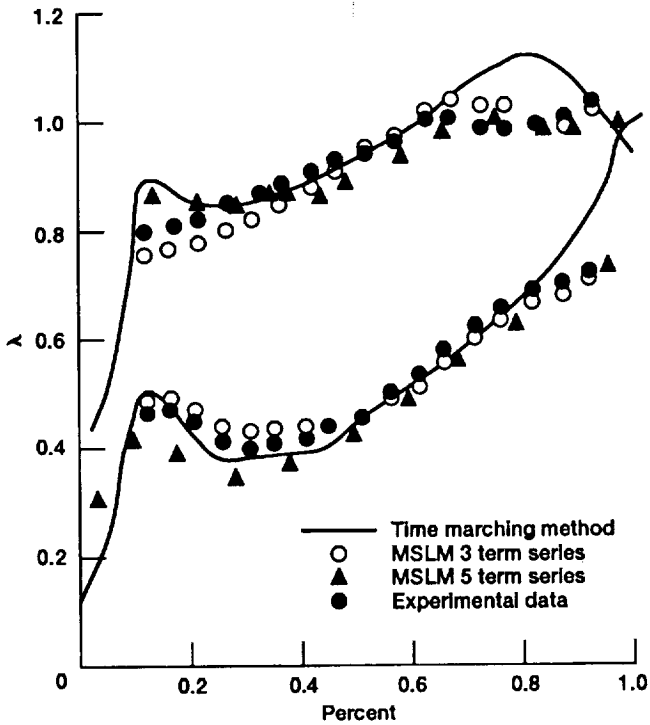


Figure 5.9.—Comparison of velocity distribution around a transonic turbine blade.

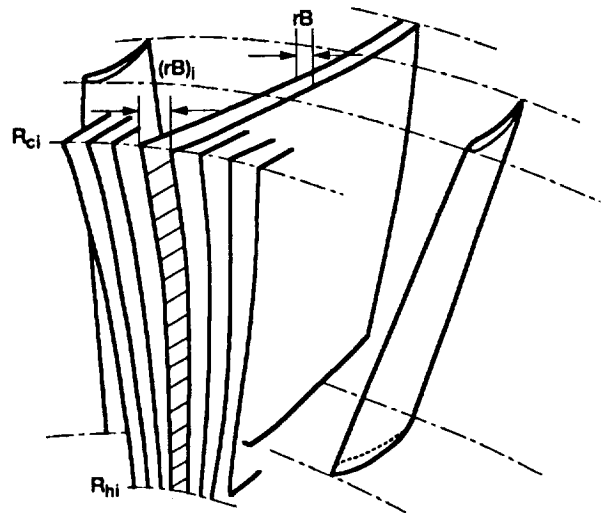


Figure 5.10.—Family of S_2 surface and intersection with inlet plane Z_i .

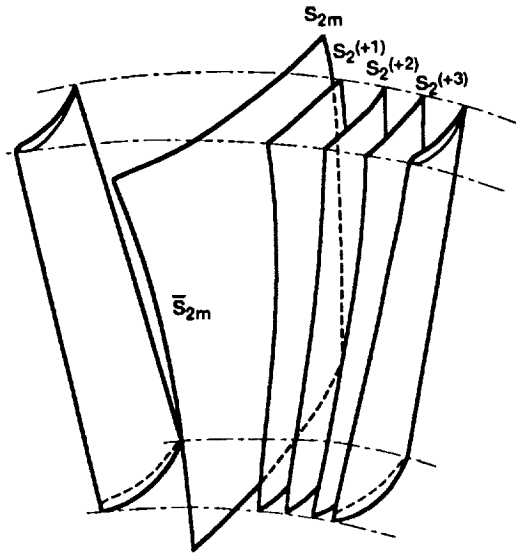


Figure 5.11.—Family of S_2 surface formed progressively from S_2 .

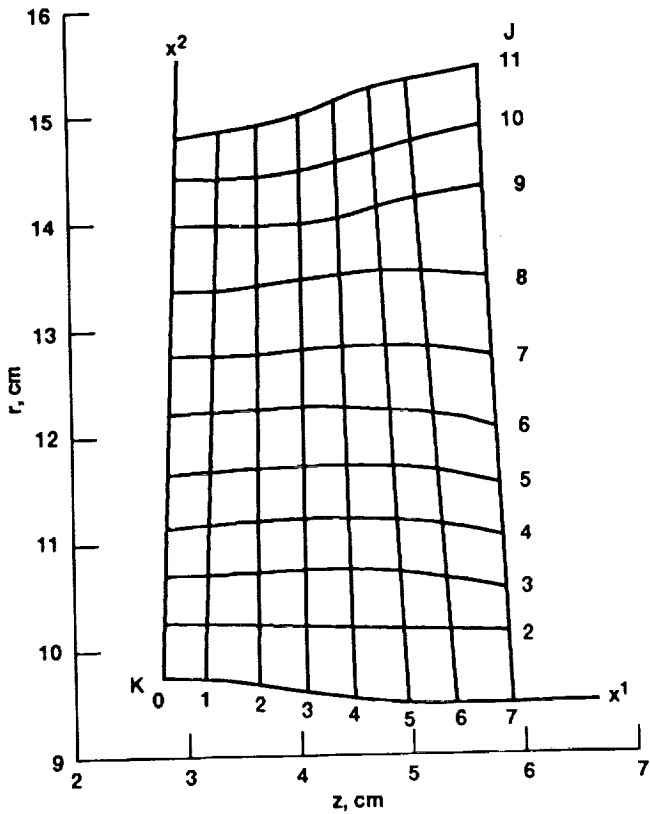


Figure 5.12.—Projection of $S_{2,m}$ streamlines on meridional plane (CAS compressor).

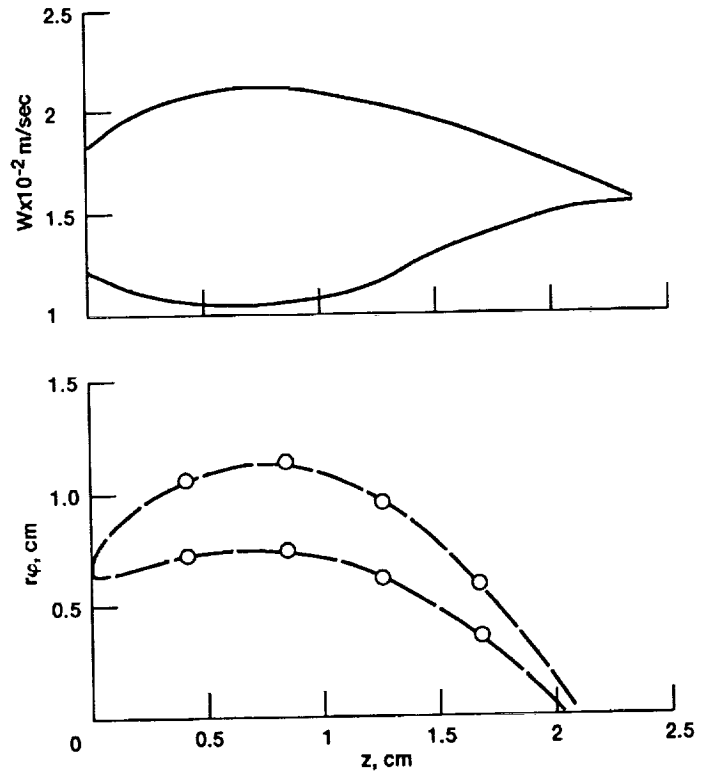


Figure 5.13.—Blade shape and velocity distribution on $J = 3 S_1$ surface.

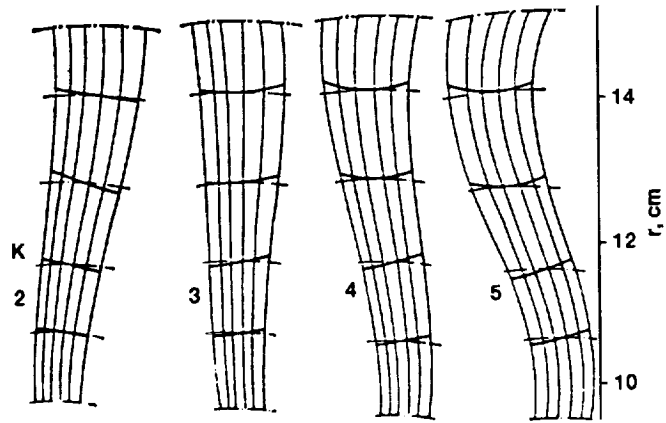


Figure 5.14.—Intersection of S_1, S_2 surfaces with the through flow cross sections of turbine rotor.

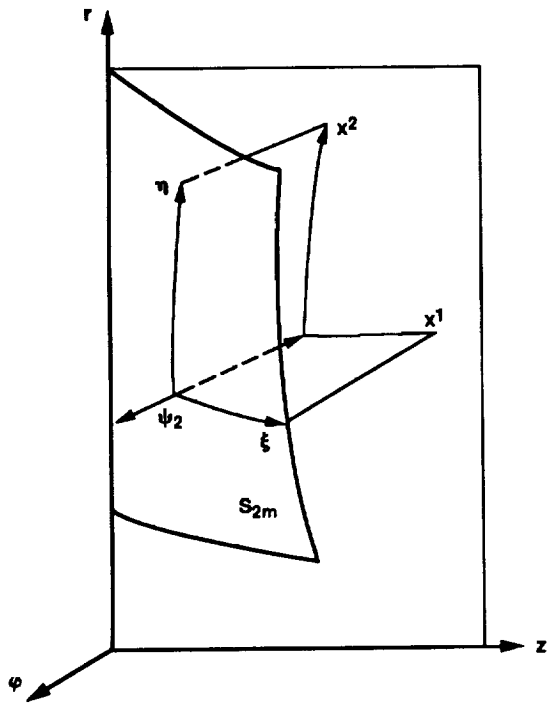


Figure 5.15.—Transformation of coordinates.

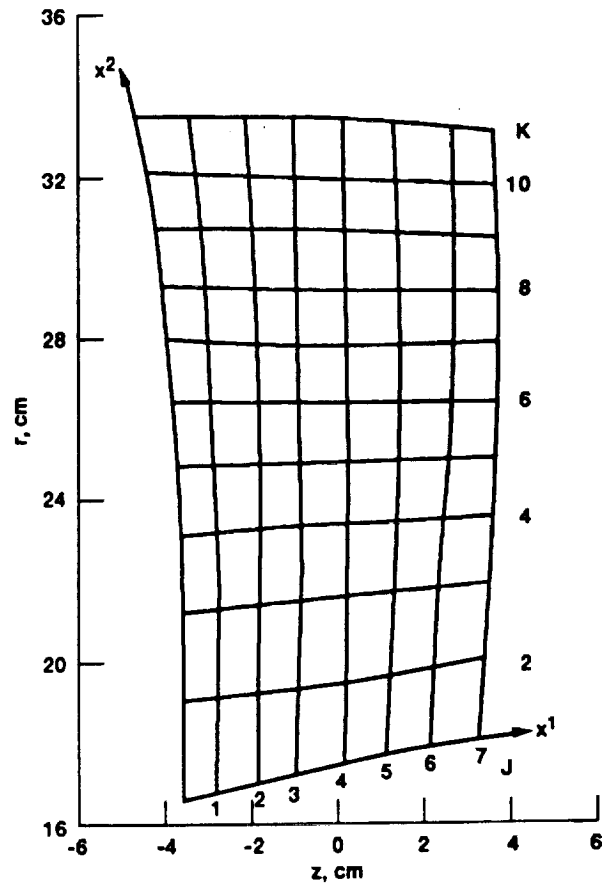


Figure 5.16.—Projection of $S_{2,m}$ streamlines on meridional plane (CAS compressor).

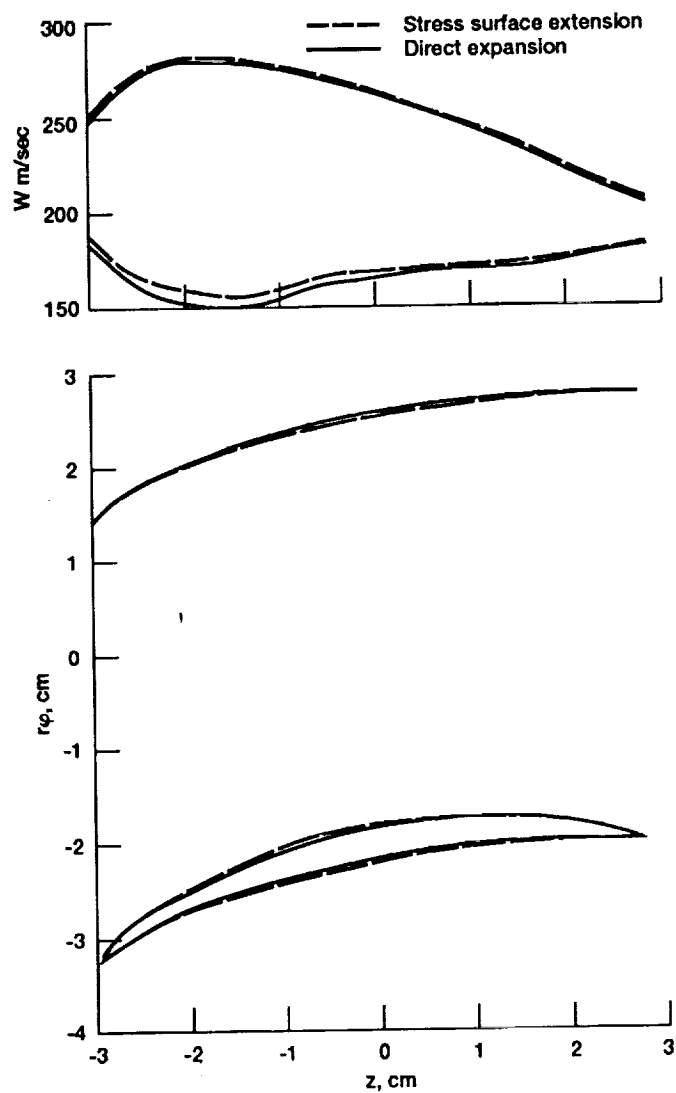


Figure 5.17.—Blade shape and velocity distribution on k-7 coordinate surface.

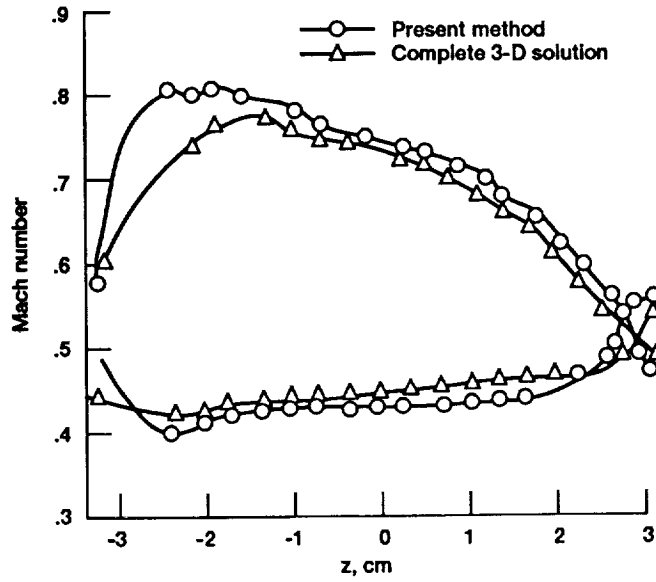


Figure 5.18.—Comparison of mach number distribution on k-9 S₁ surface.

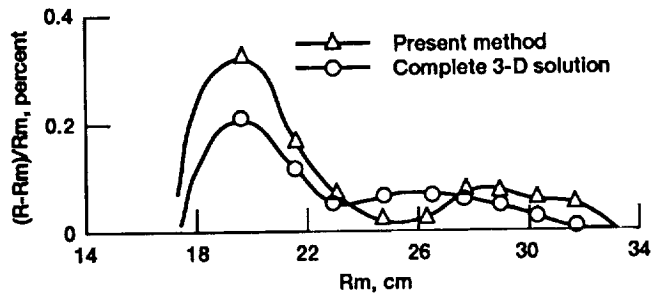


Figure 5.19.—Relative twist on J-3 suction surface.

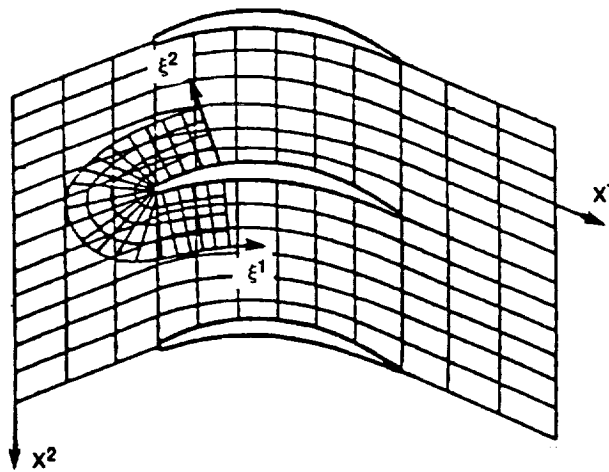


Figure 5.20.—Body-fitting quasi-orthogonal C-grid around the blade leading edge.

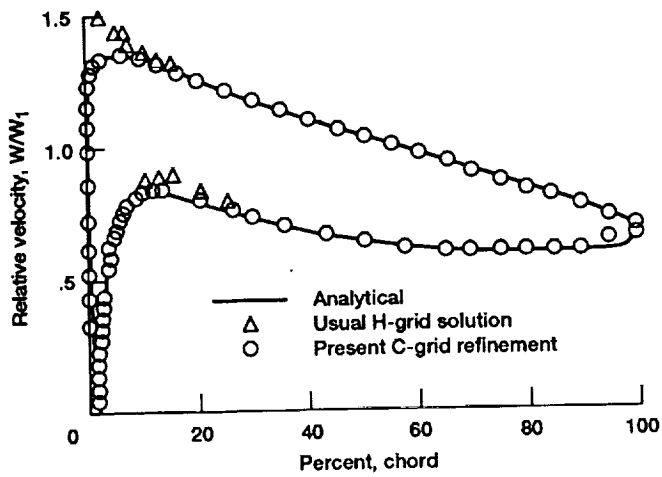


Figure 5.21.—Improvement in velocity distribution around leading blade edge.

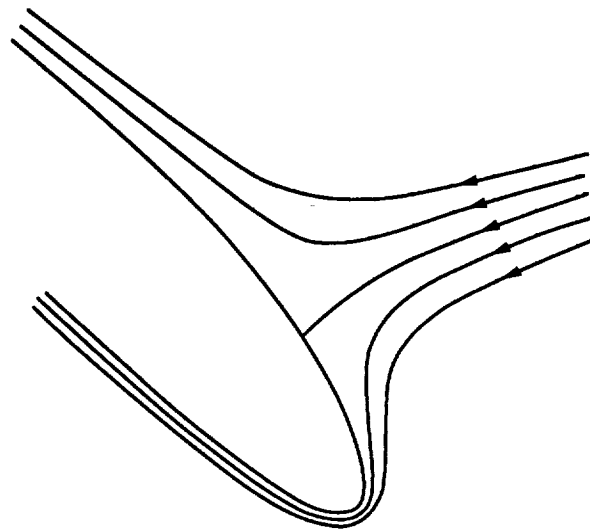


Figure 5.22.—Stagnation point determined for a large negative incidence.

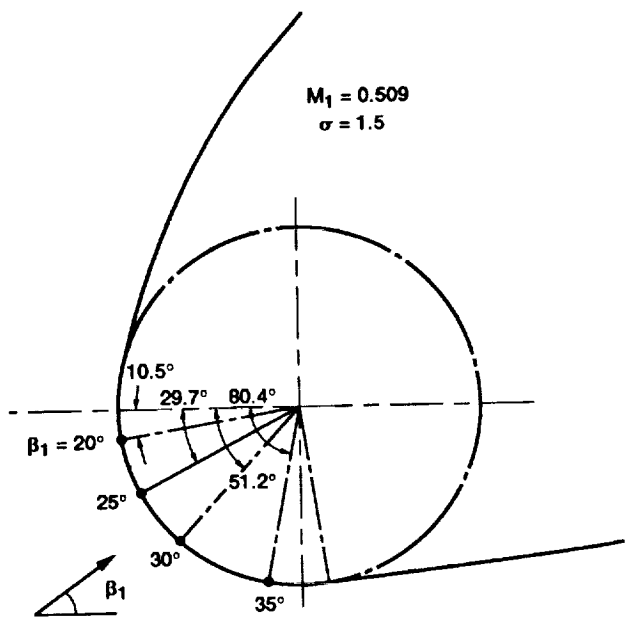


Figure 5.23.—Variation of stagnation point location with inlet angle.

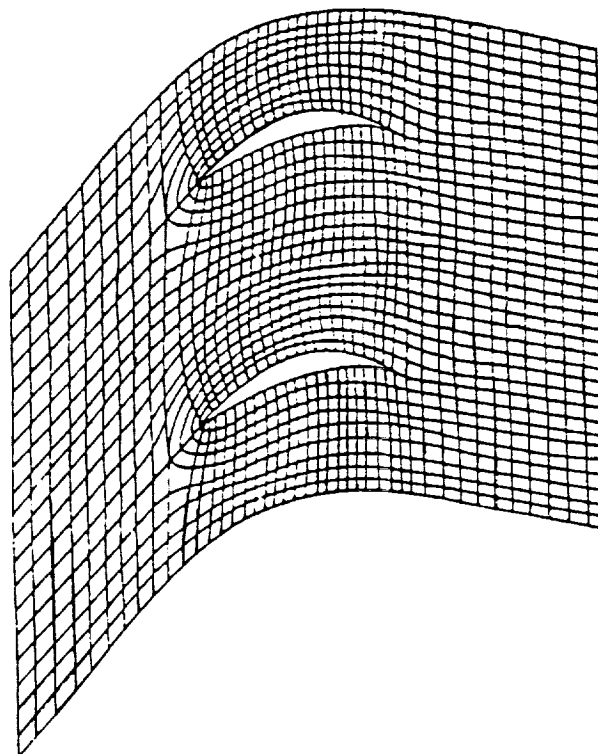


Figure 5.24—H-C grid system.

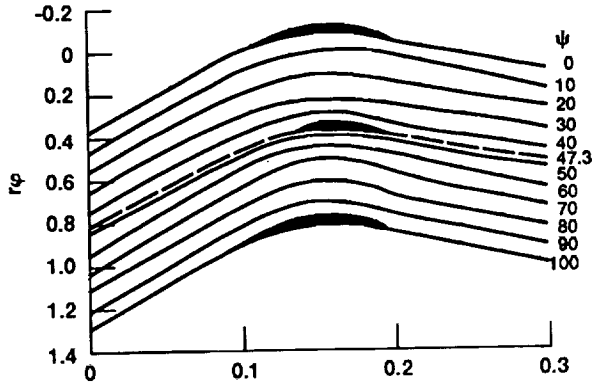


Figure 5.25.—Distribution of streamline in a cascade having splitter vanes.

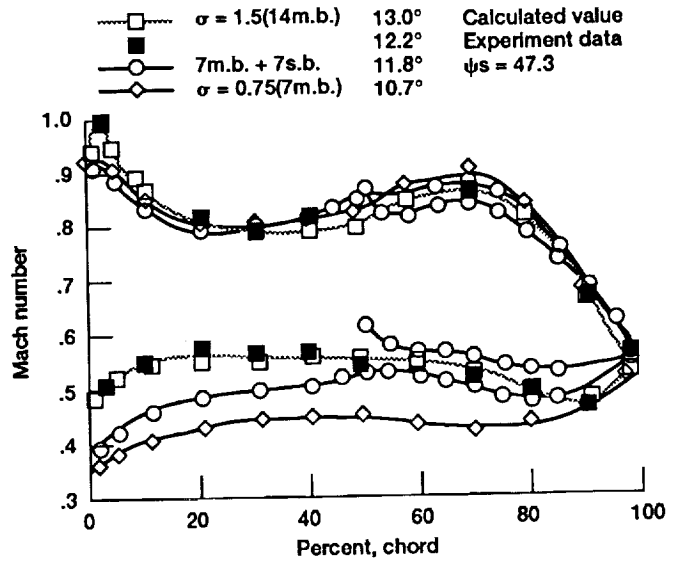


Figure 5.26.—Mach number distribution around blades of three cascades.

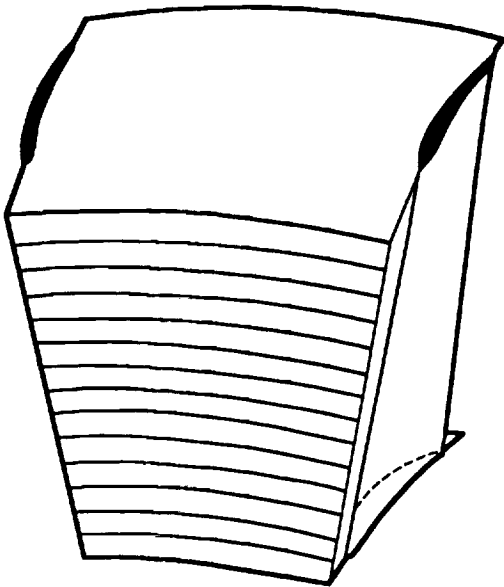


Figure 5.27.— S_1 stream filaments.

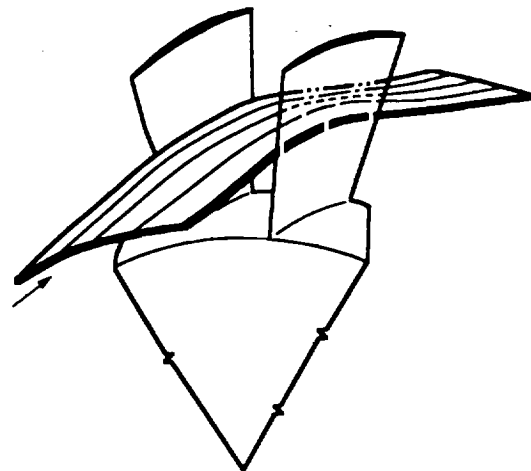


Figure 5.28.—Three-dimensional variation of an S_1 stream filament.

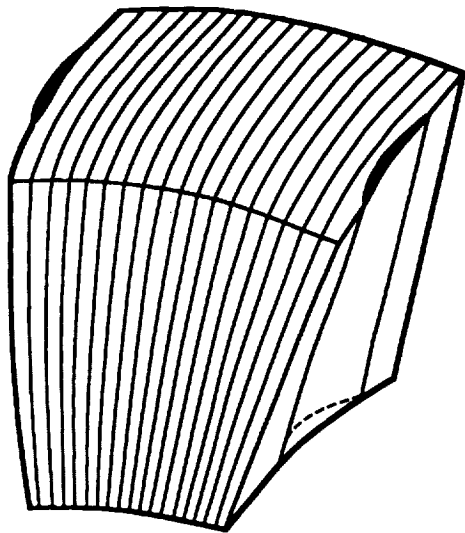


Figure 5.29.— S_2 stream filaments.

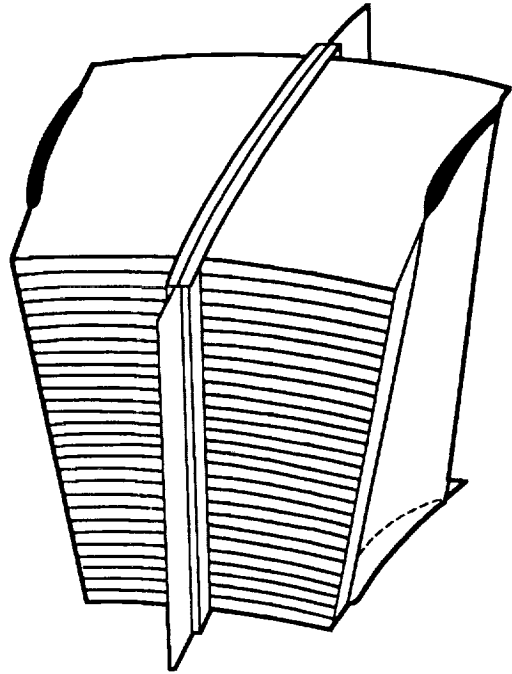


Figure 5.30.— S_1 filaments and a mid-channel S_2 employed in quasi-3D solution.

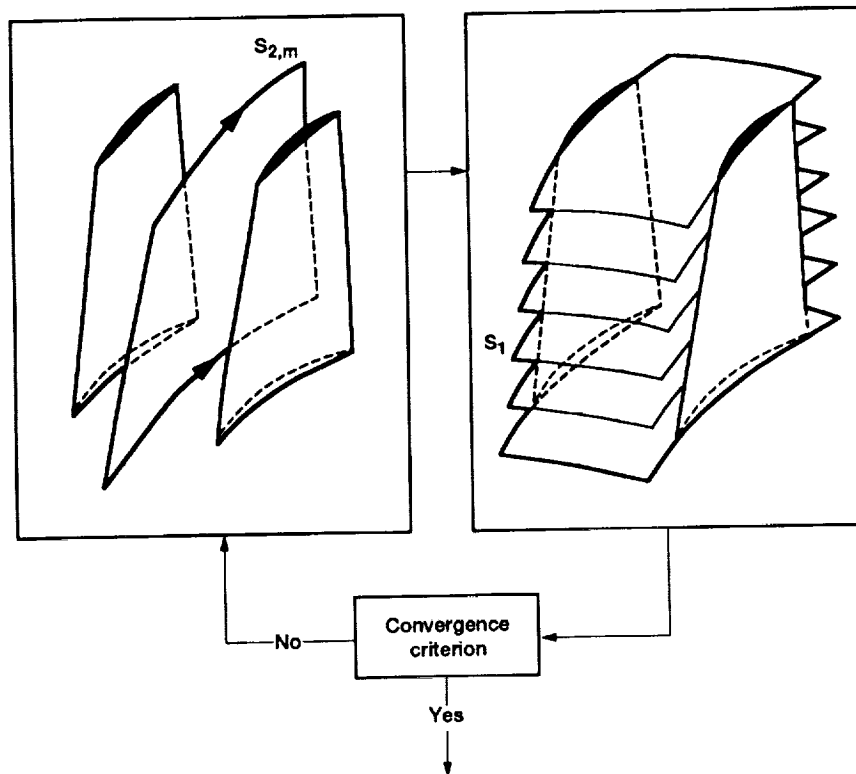


Figure 5.31.—Calculation steps in quasi-3-D blade design.

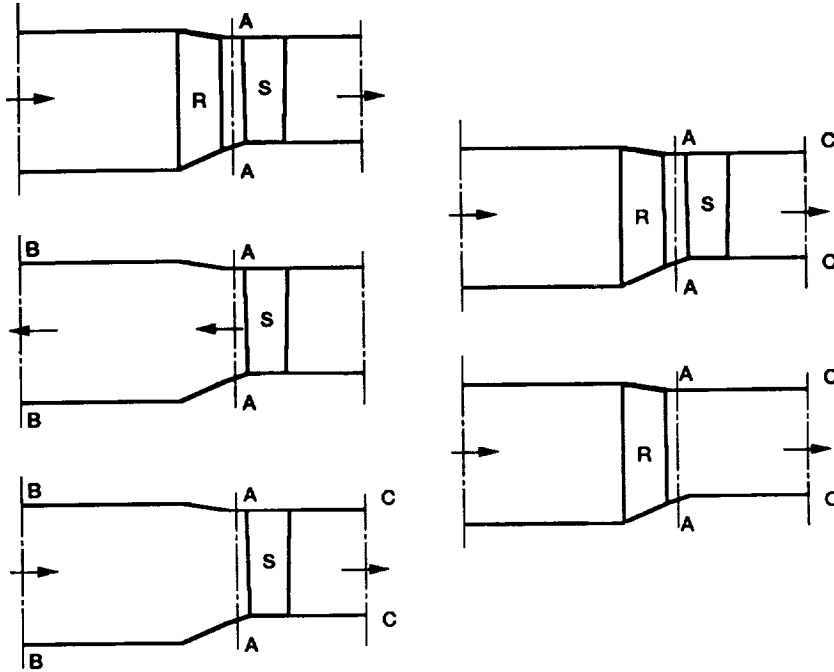


Figure 5.32.—Determination of flow condition far upstream and downstream of the embedded blade row.

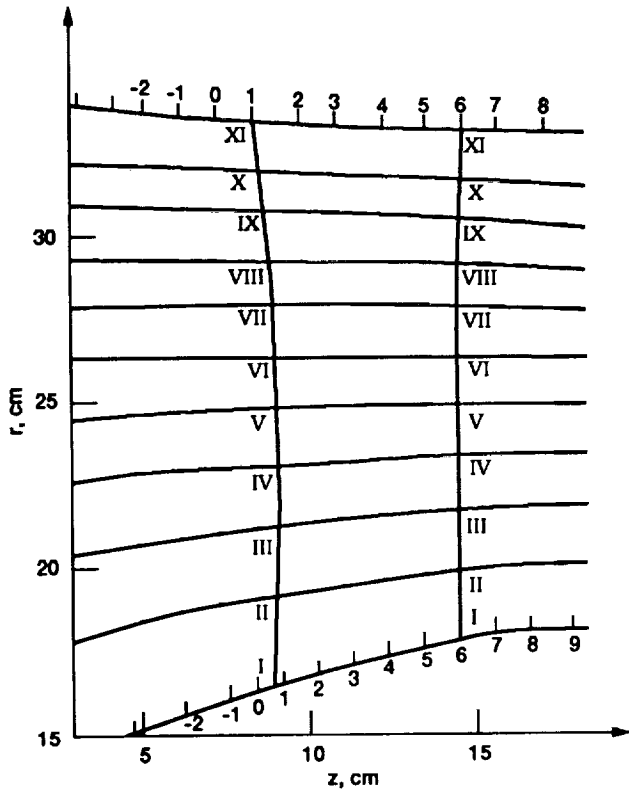


Figure 5.33.—Projection of stator blade and streamline distribution on meridional plane.

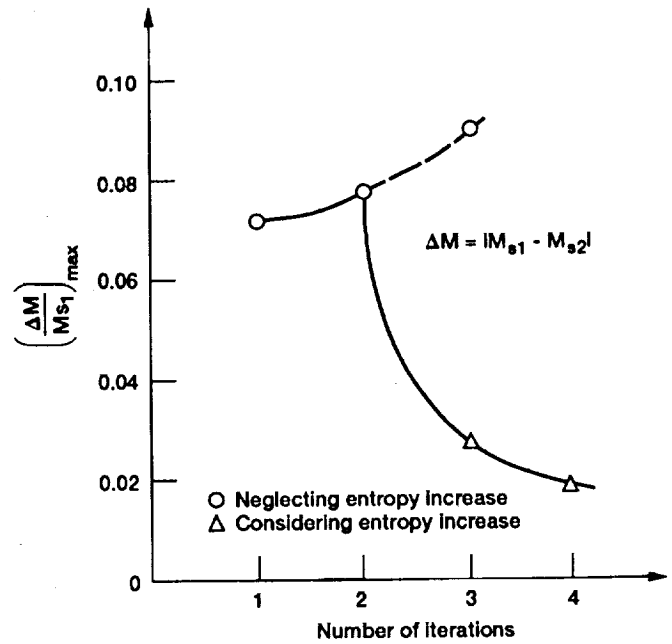


Figure 5.34.—Effect of entropy on consistency.

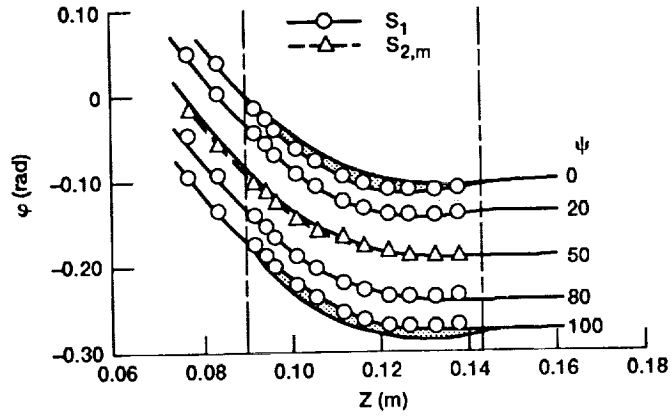


Figure 5.35.—Streamlines on S_1 and $S_{2,m}$ at blade root.

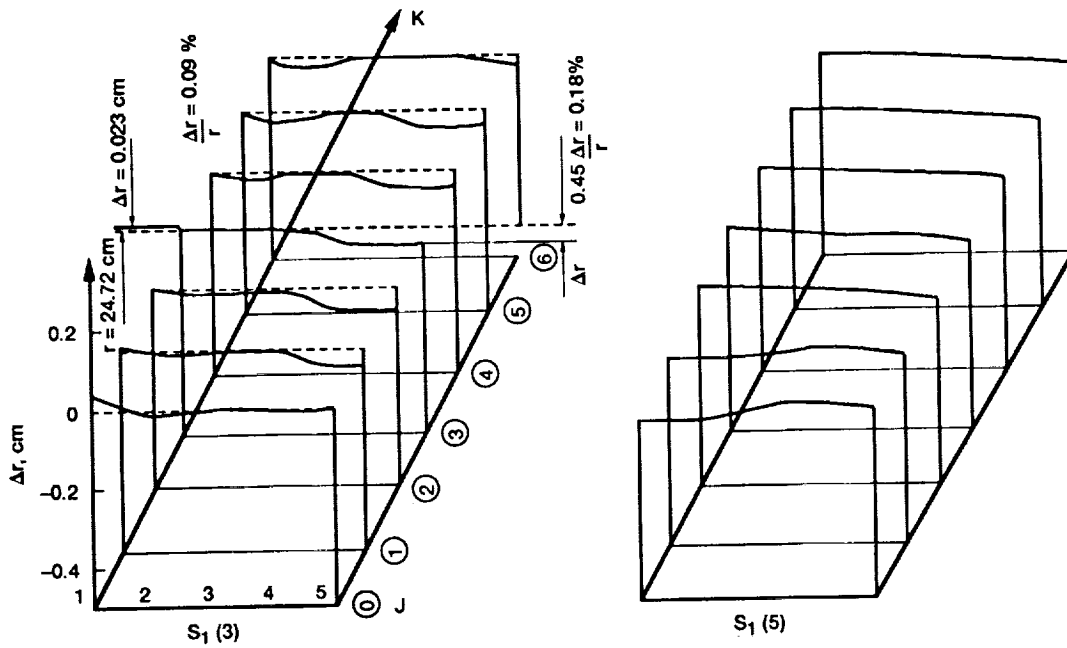


Figure 5.36.—Deviation of general S_1 surface from surface of revolution (magnified ten times).

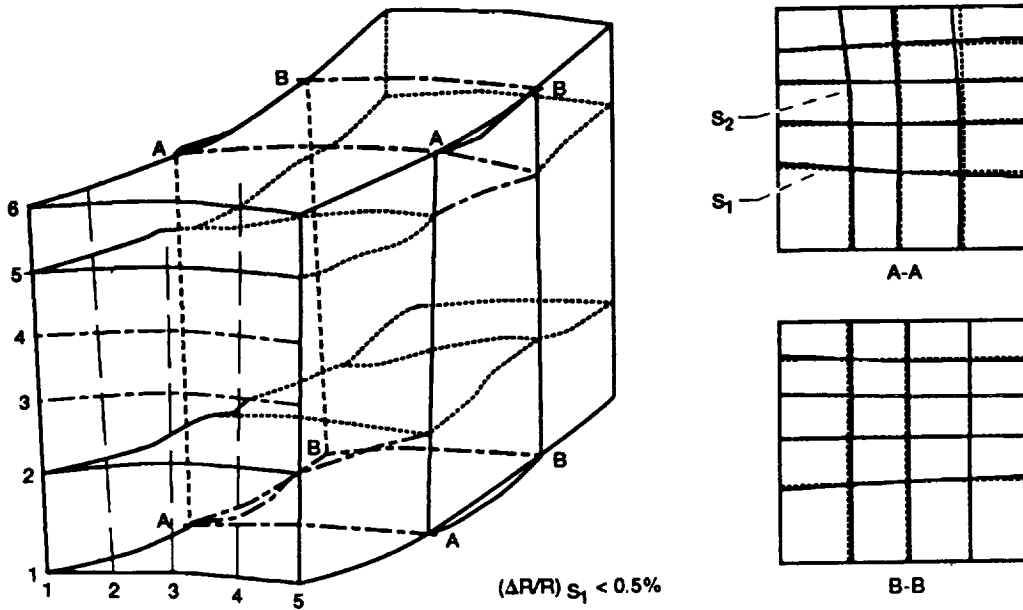


Figure 5.37.—Deviation of general S_1 surface from surface of revolution (schematic).

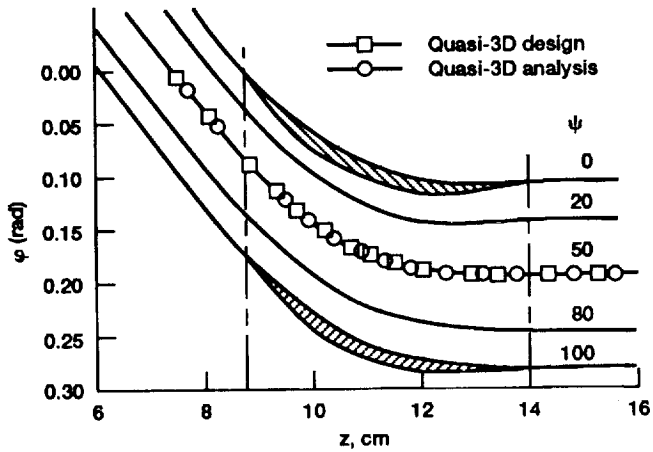


Figure 5.38.—Streamlines on S_1 stream surface (mid-span surface).

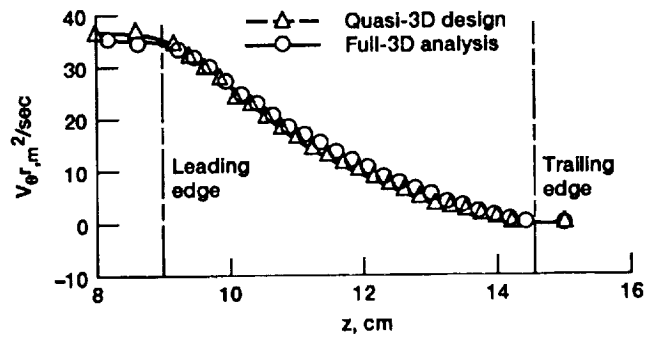


Figure 5.39.—Variation of $V_{\theta r}$ on mean streamline (mid-span surface).

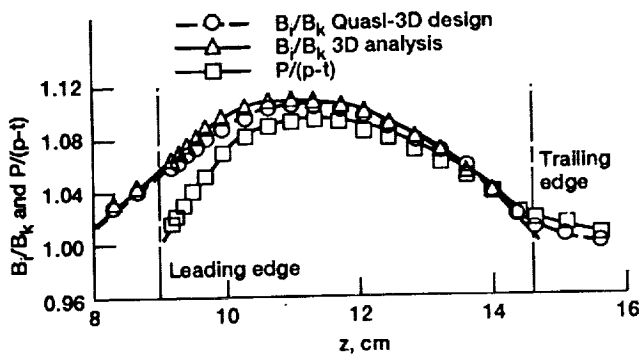


Figure 5.40.—Variation of B/B_k and $P/(p-t)$ on mean streamline (mid-span surface).

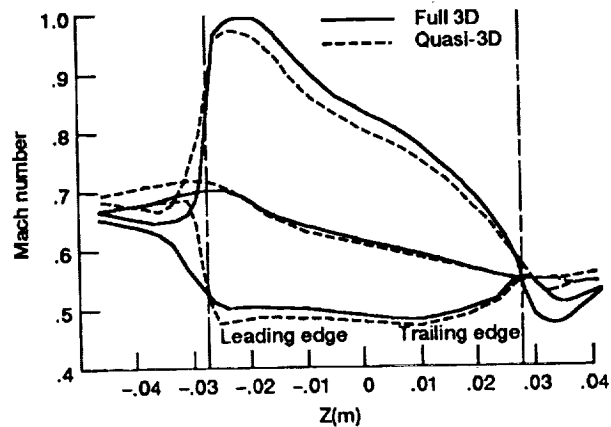


Figure 5.41.—Mach number distribution over blade surface (mid-span section).

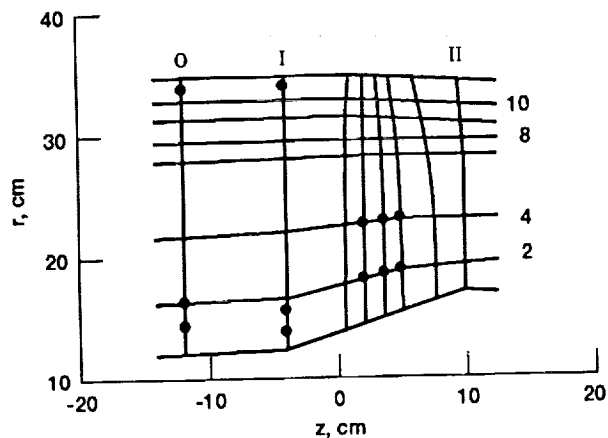


Figure 5.42.—Meridional projection of rotor blade, streamlines and L2F measuring locations.

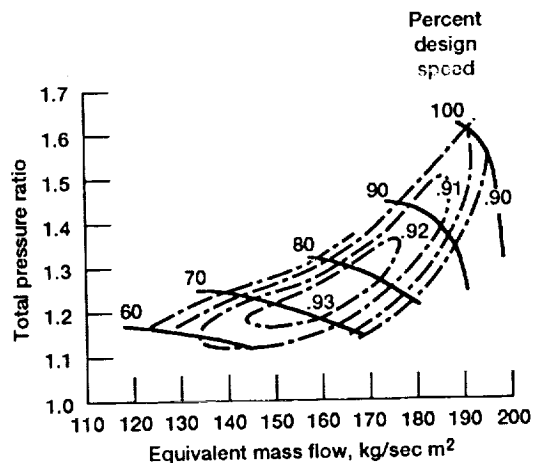


Figure 5.43.—Compressor overall performance map.

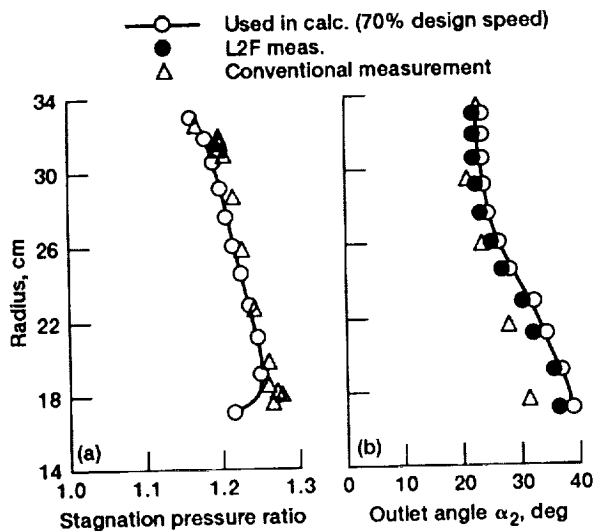


Figure 5.44.—Radial variation of stagnation pressure and outlet angle.

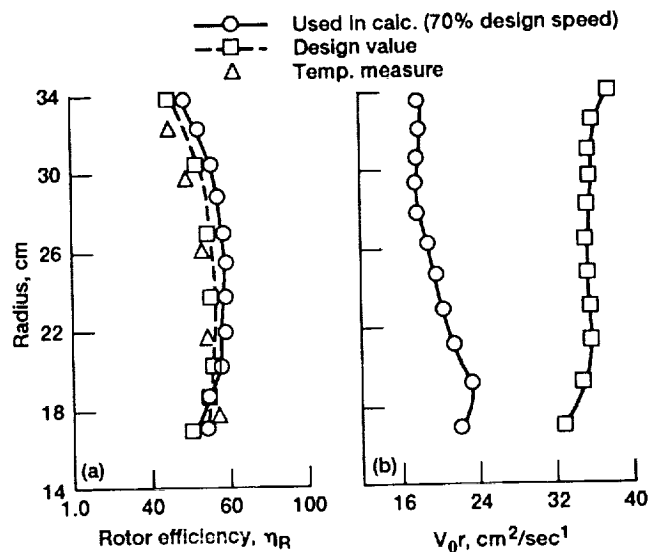


Figure 5.45.—Radial variation of rotor efficiency and outlet V_0r .

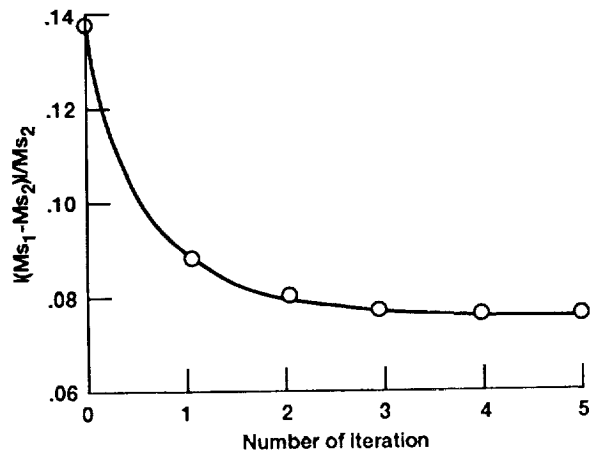


Figure 5.46.—Rate of convergence.

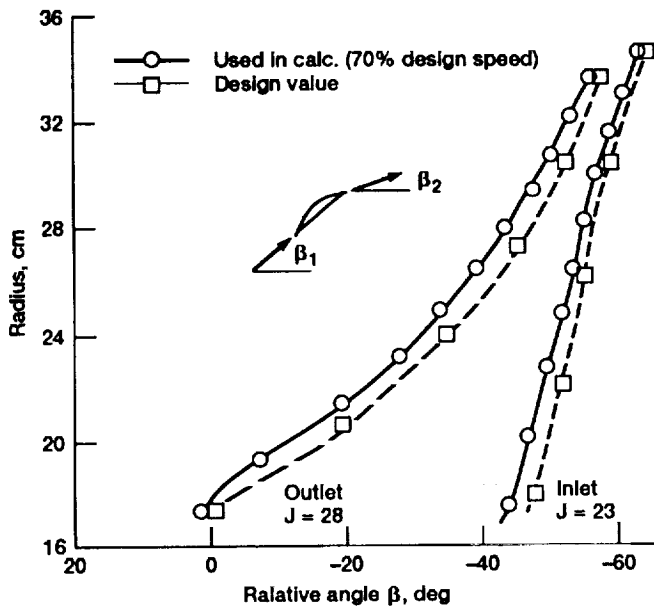


Figure 5.47.—Radial variation of β .

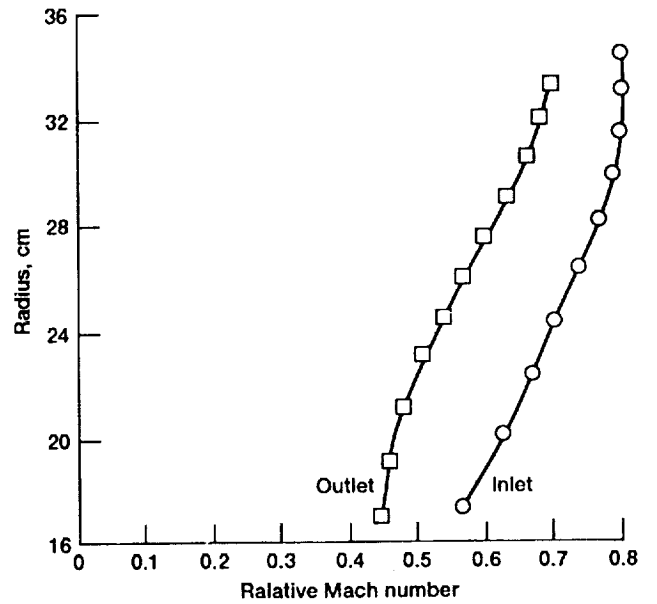


Figure 5.48.—Radial variations of relative Mach number.

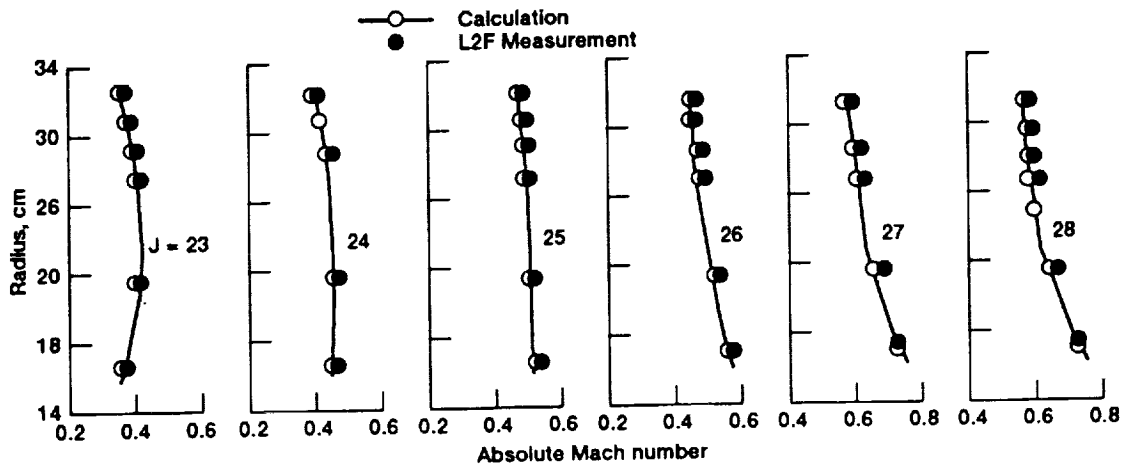


Figure 5.49.—Radial variation of absolute Mach number at Stations 23 - 28.

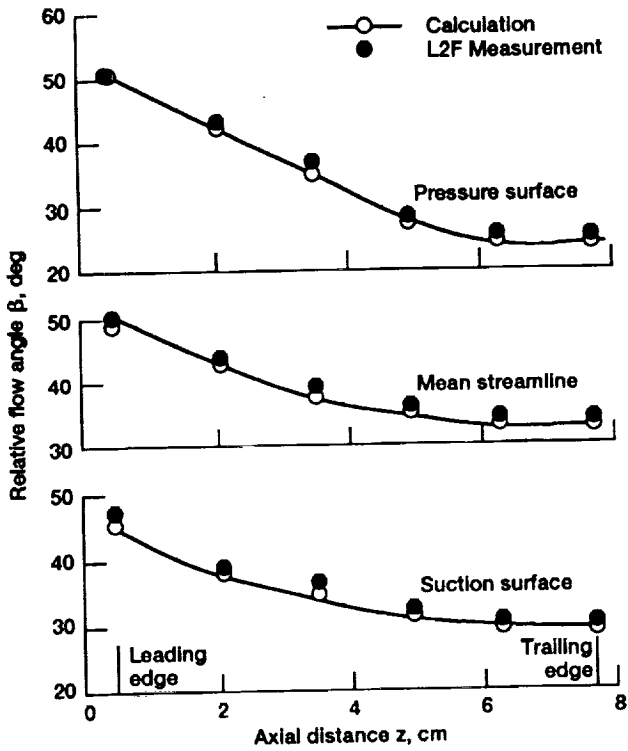


Figure 5.50.—Axial variation of relative flow angle.

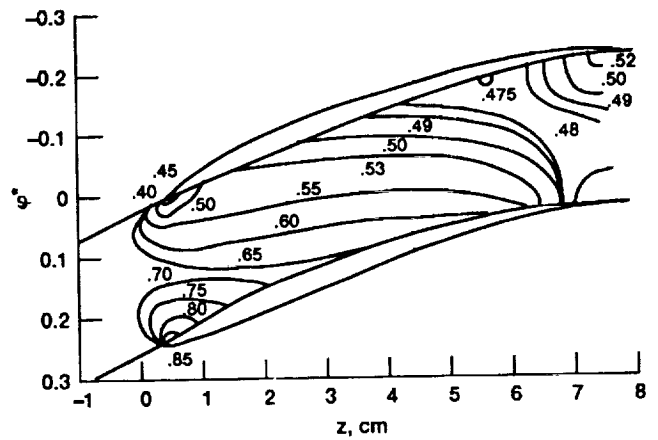


Figure 5.51.—Lines of constant relative Mach number on No. 3 S_1 surface.

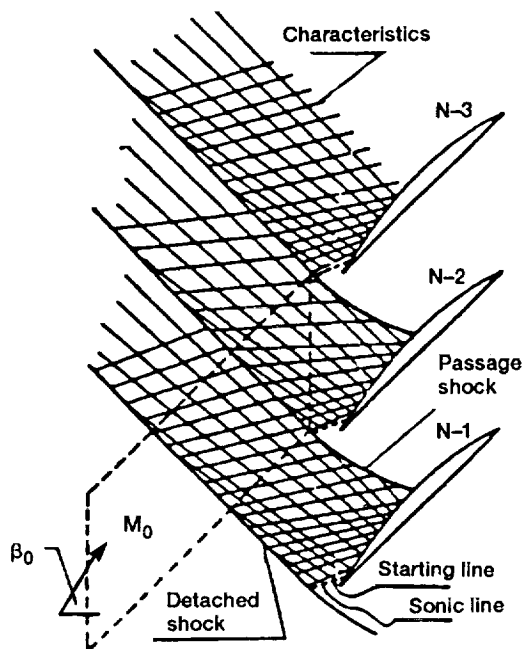


Figure 6.1—Bow wave/passage shock and characteristic net in a compressor cascade with supersonic inlet velocity.

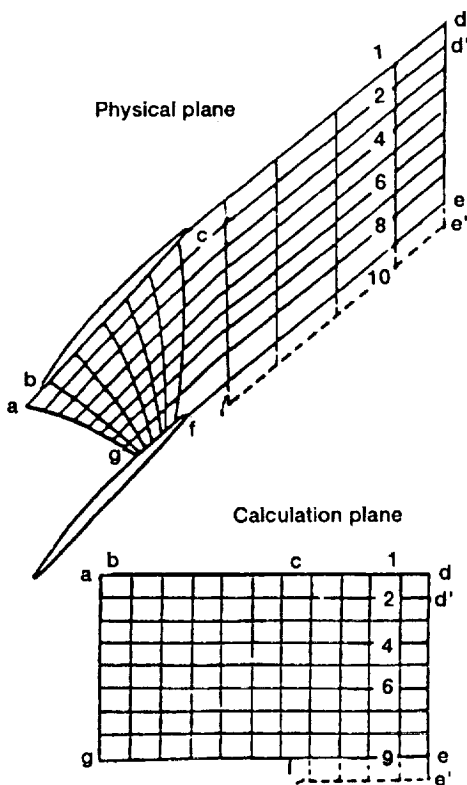


Figure 6.2—Coordinate system used downstream of passage shock.

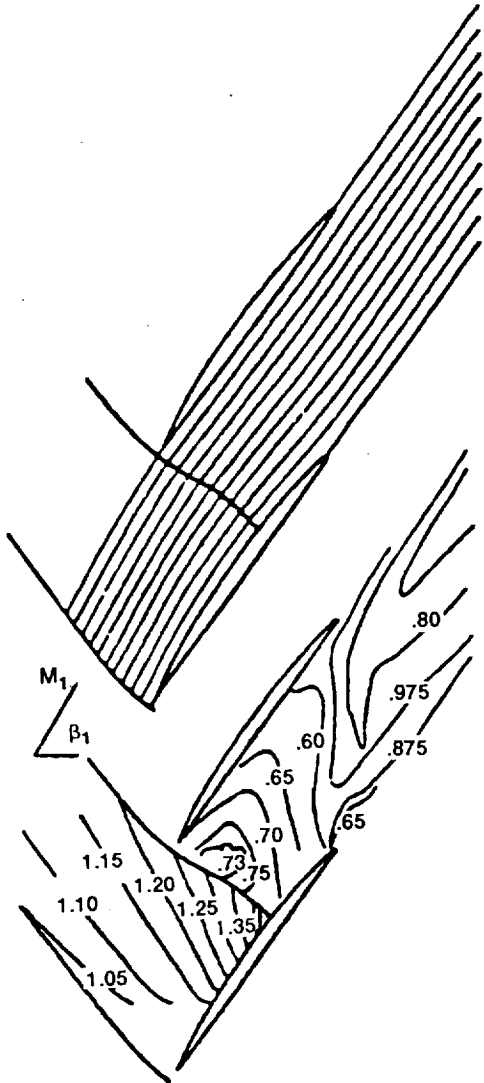


Figure 6.3—Streamline distribution and Mach contours.

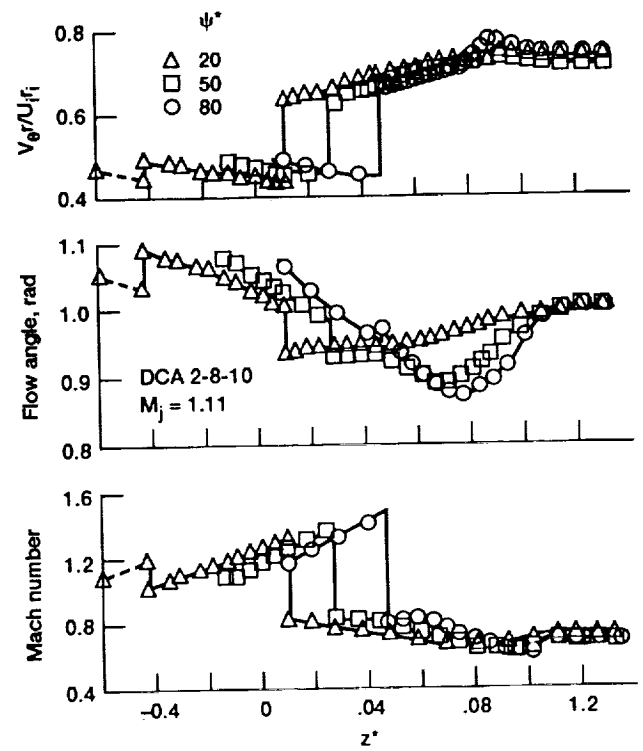


Figure 6.4.—Variations of V_{0r} , β and M along three streamlines.

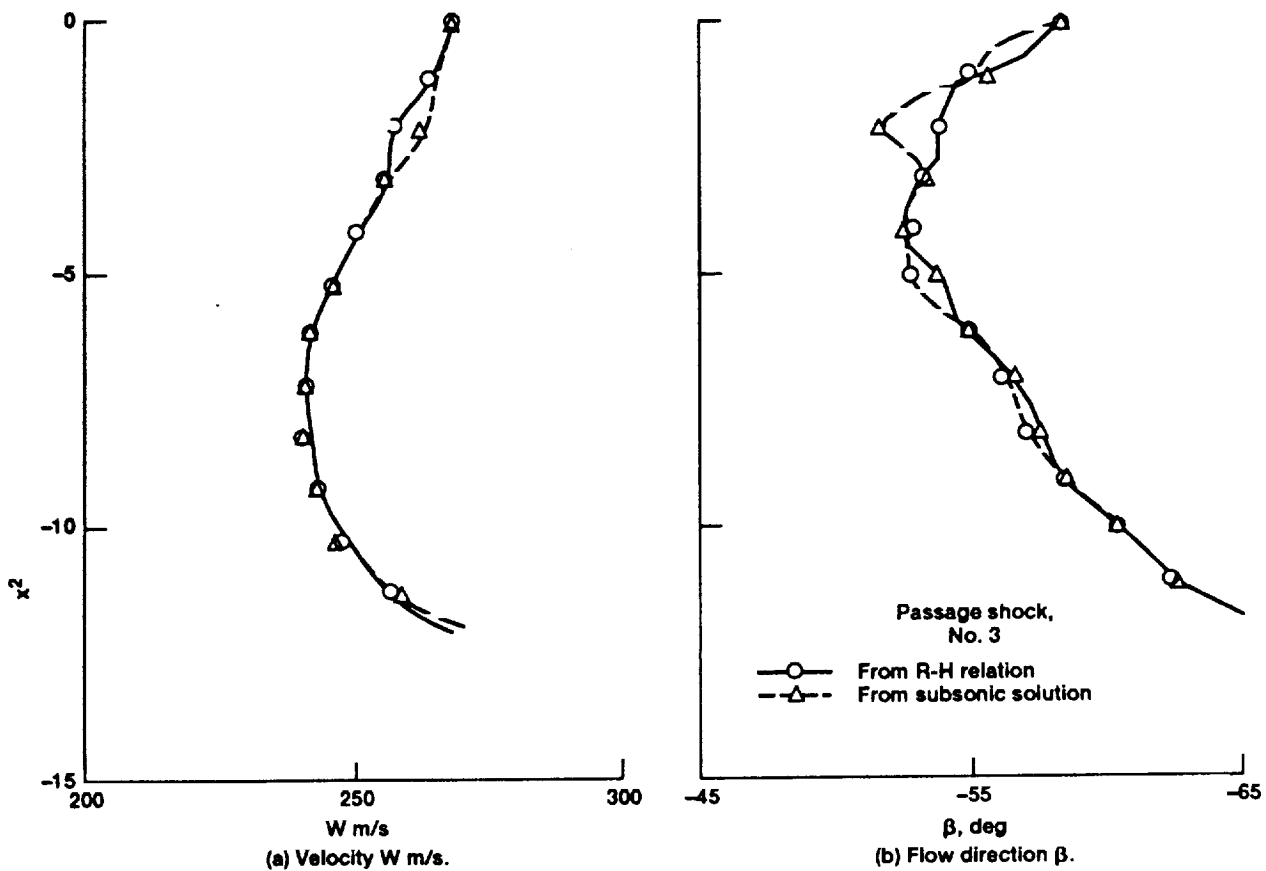


Figure 6.5.—Comparison between result calculated by R-H relations and result obtained in downstream subsonic solution.

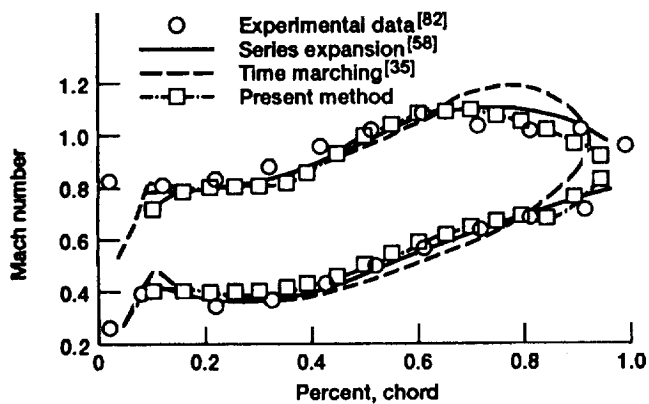


Figure 6.6.—Mach number distribution for turbine cascade.

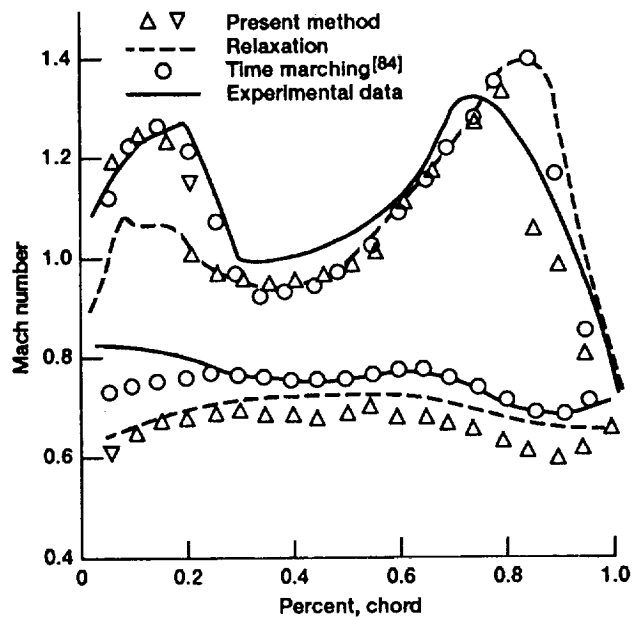


Figure 6.7.—Mach number distribution for T_1 cascade.

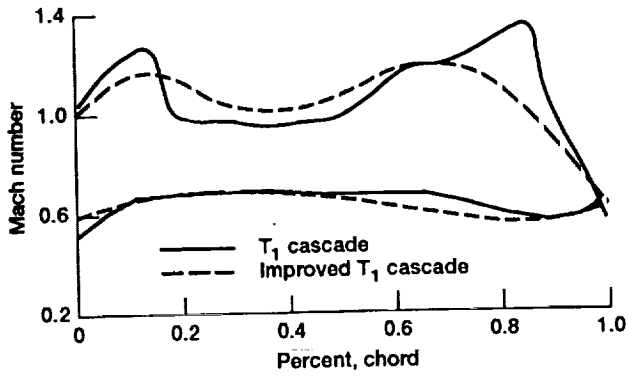


Figure 6.8.—Modification Mach number distribution for T_1 cascade.

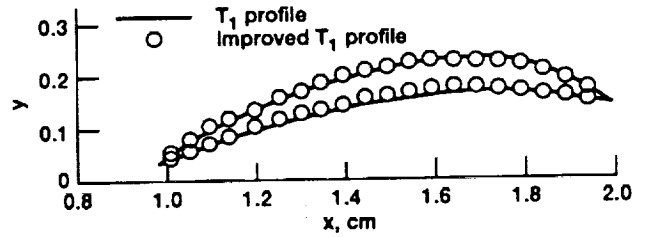


Figure 6.9.—Original and improved profile.

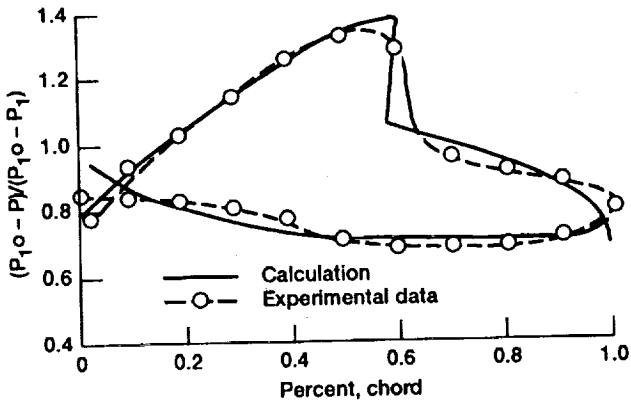


Figure 6.10.—Pressure distribution around the blade.

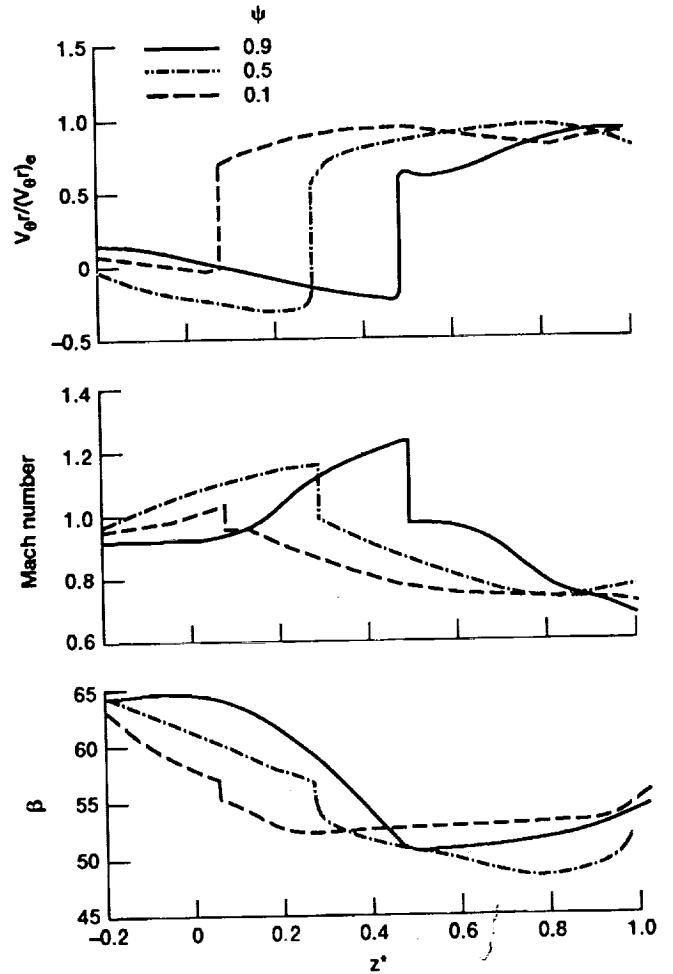


Figure 6.11.—Flow variation along three streamlines.

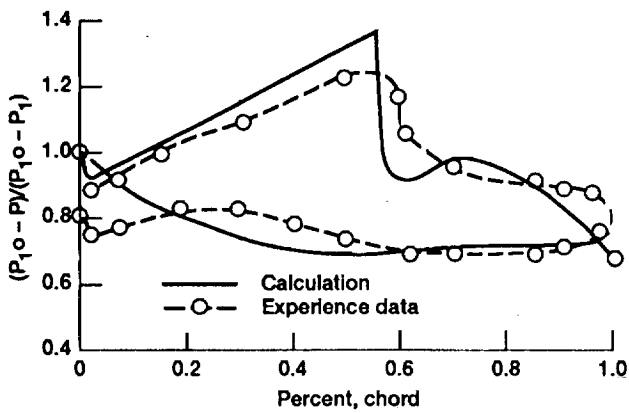


Figure 6.12.—Pressure distribution around the blade.

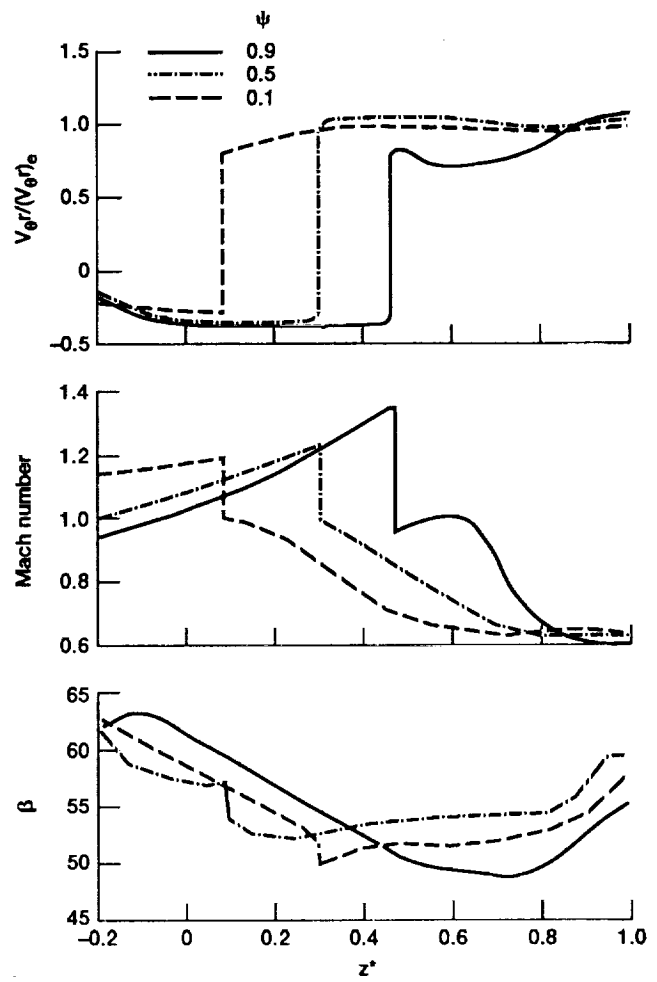


Figure 6.13.—Flow variation along three streamlines.

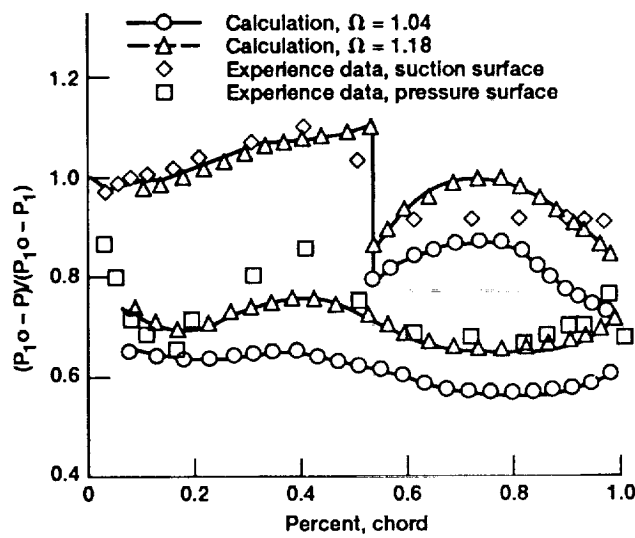


Figure 6.14.—Pressure distribution around blade.

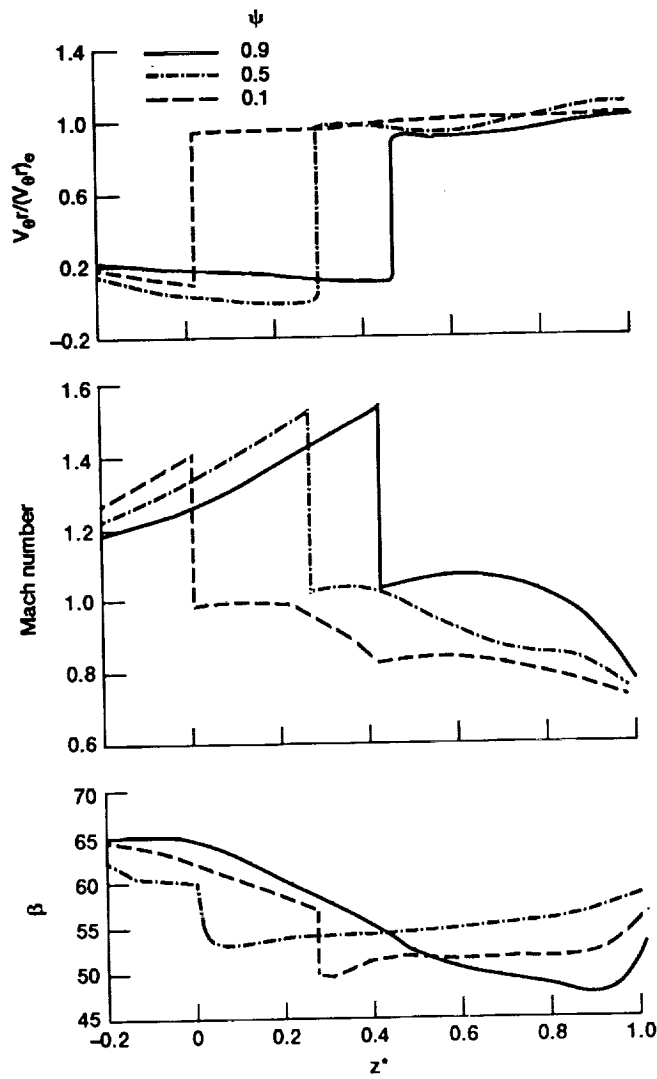


Figure 6.15.—Flow variation along three streamlines.

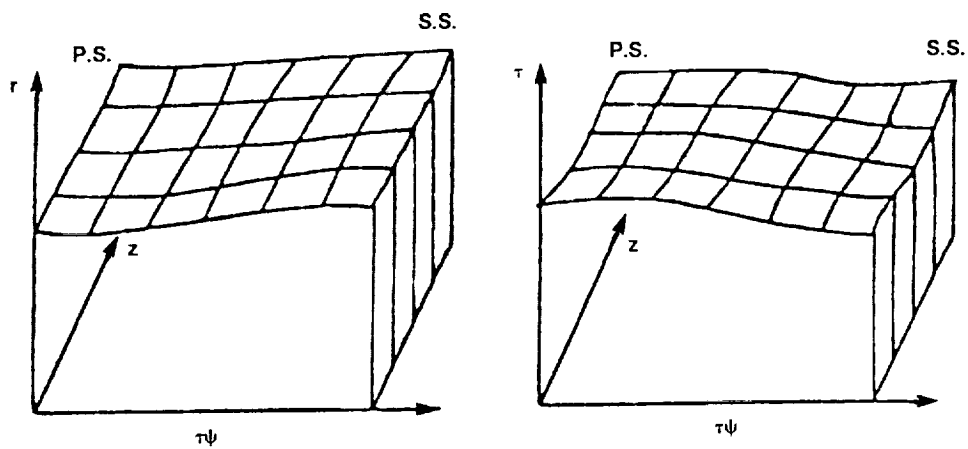


Figure 6.16.—Variation of r and ψ for a general S_1 surface.

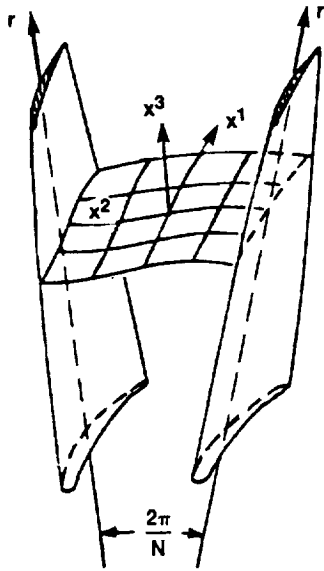


Figure 6.17.—General S_1 stream surface.

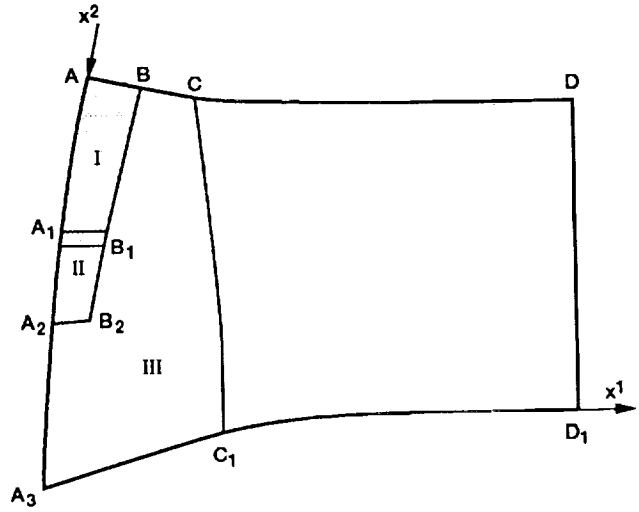


Figure 6.18.—Division of computation region.

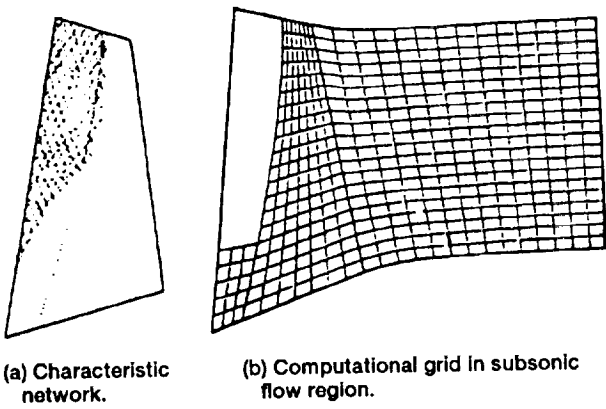


Figure 6.19.—Meridional projection of characteristic network on S_2 and mesh on meridional plane for subsonic flow region.

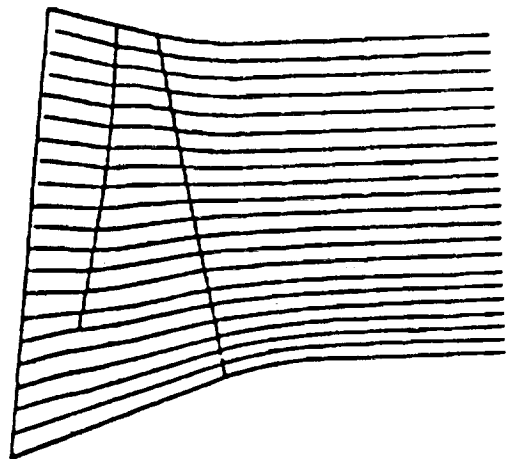


Figure 6.20.—Meridional projection of streamlines.

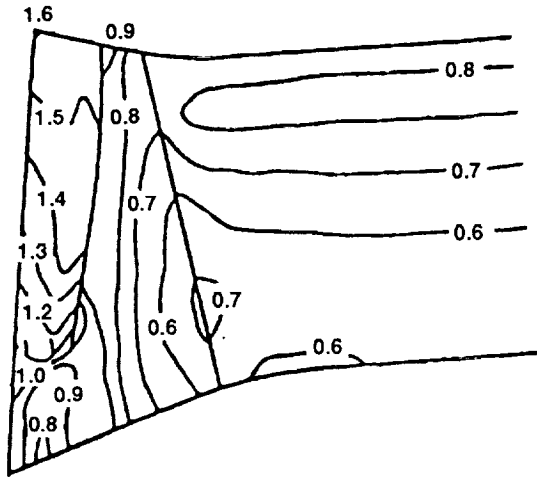


Figure 6.21.—Meridional projection of Mach number contours on $S_{2,m}$.

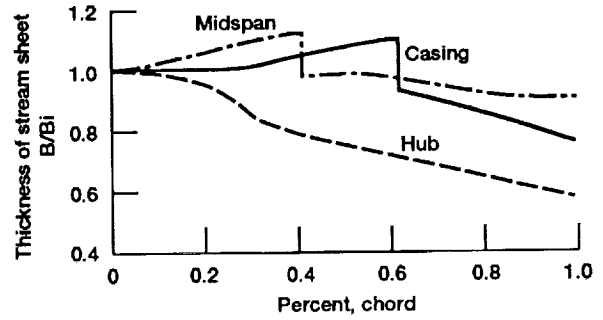


Figure 6.22.—Variation of radial thickness of S_1 stream filament.

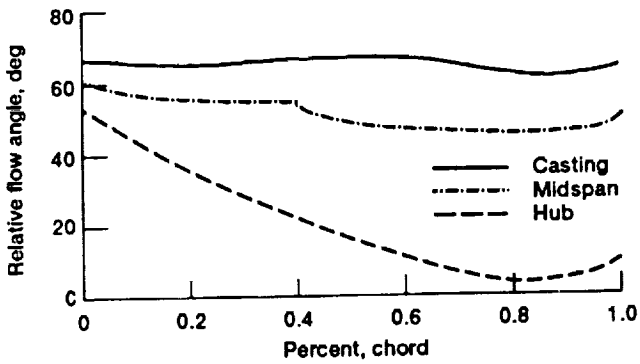


Figure 6.23.—Variation of Relative flow angle.

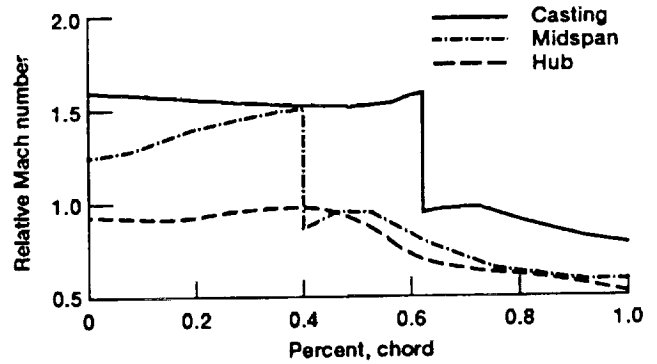


Figure 6.24.—Variation in relative Mach number.

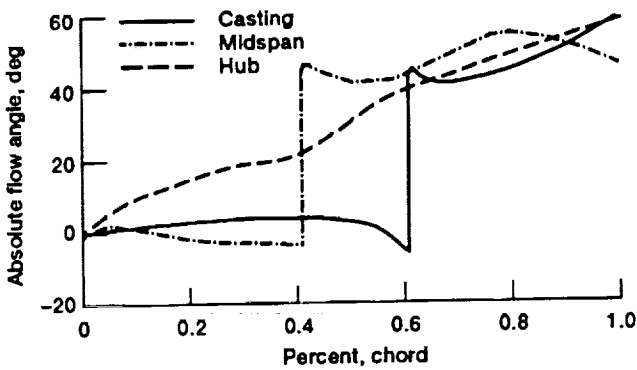


Figure 6.25.—Variation of absolute flow angle.

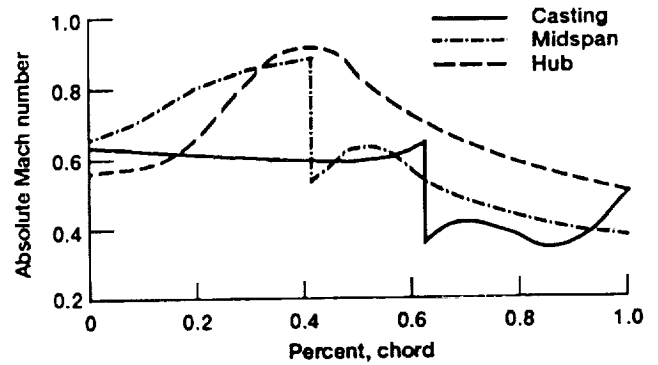


Figure 6.26.—Variation in absolute Mach number.

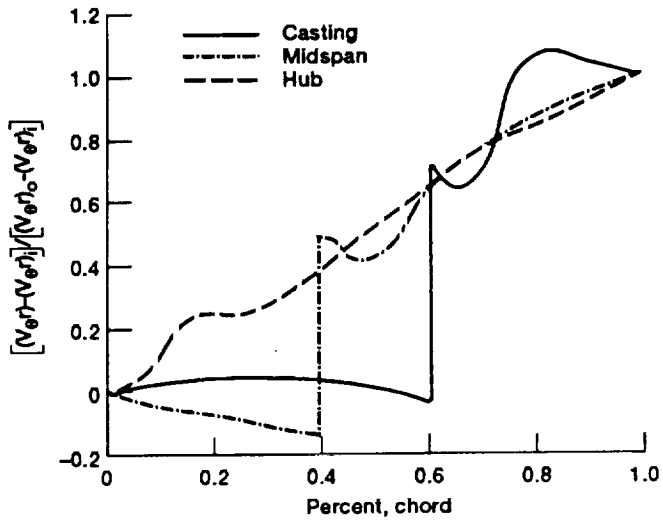


Figure 6.27.—Variation of $V_{\theta r}$.

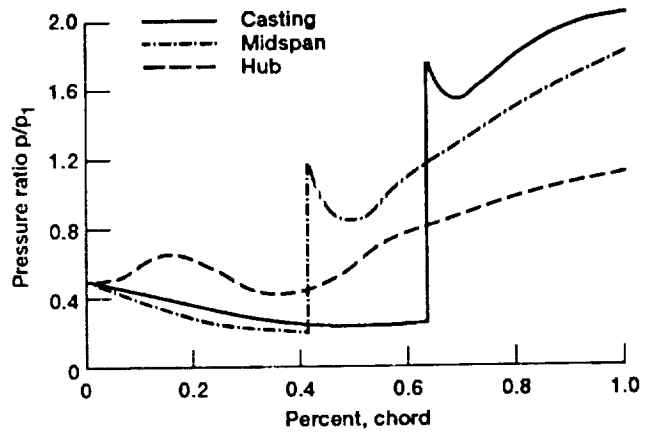
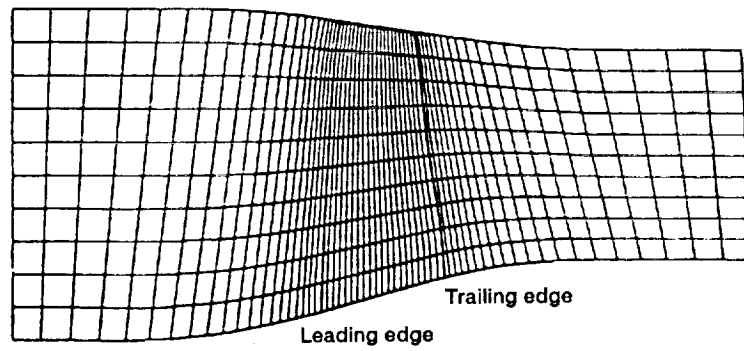
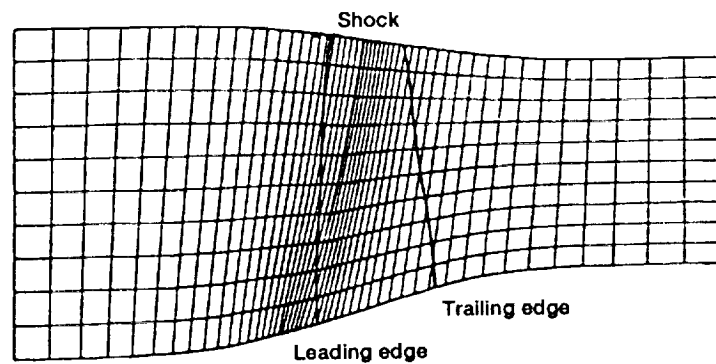


Figure 6.28.—Variation of pressure ratio.



(a) Grid used in calculations I and II, 61x11.



(b) Grid used in calculation III, 49x11.

Figure 6.29.—Grid system and project of blade and shock on meridional plane.

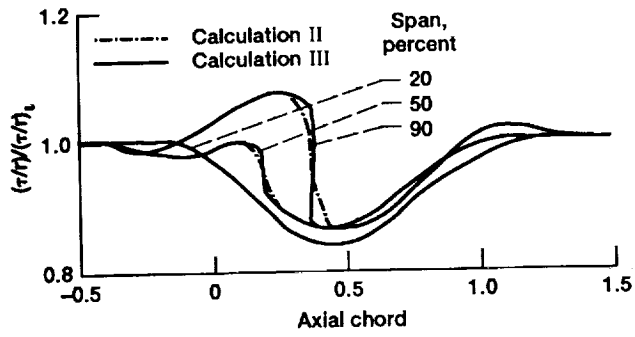


Figure 6.30.—Input value of τ on $S_{2, m}$.

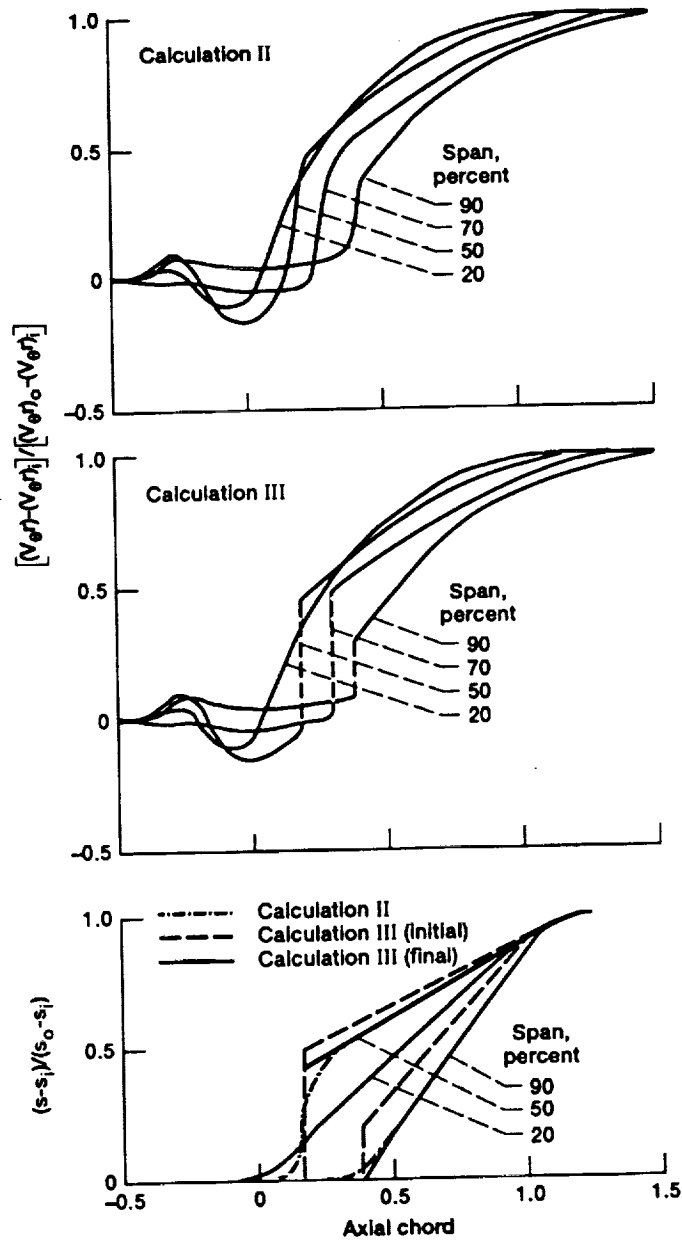


Figure 6.31.—Input value of V_{gr} and s on $S_{2, m}$.

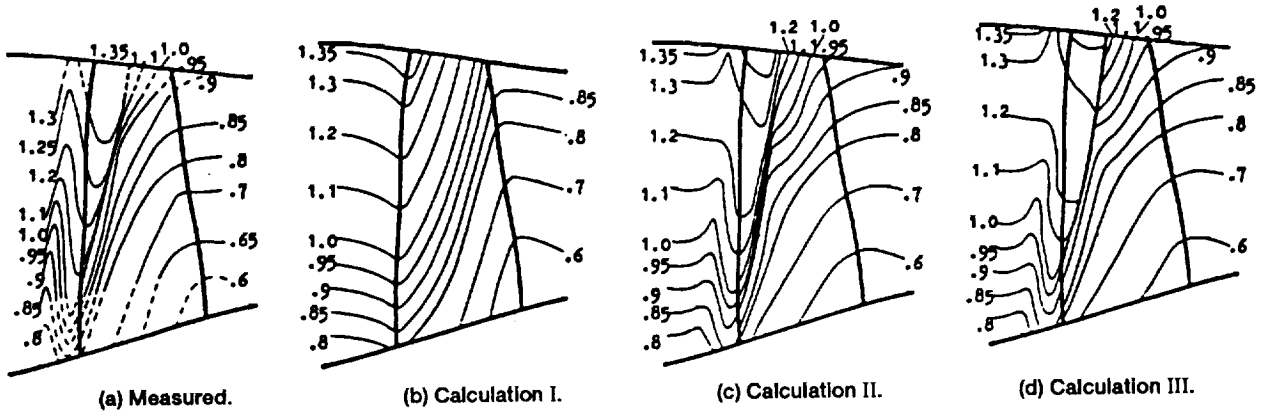


Figure 6.32.—Comparison of Mach number contours on $S_{2,mr}$

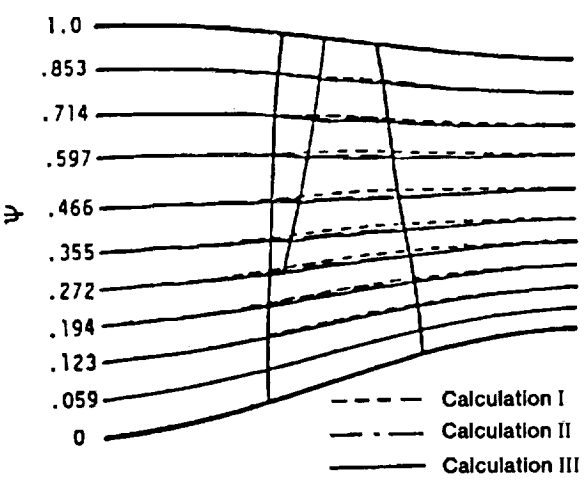


Figure 6.33.—Comparison of streamline distributions.

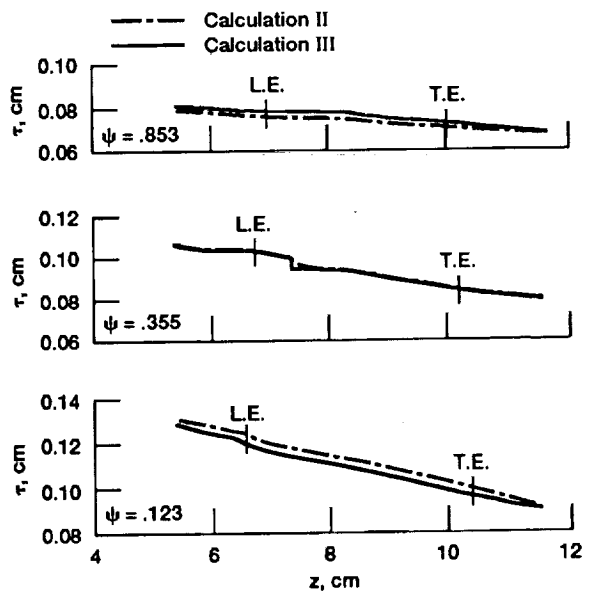


Figure 6.34.—Variation of filament thickness (1 percent mass flow).

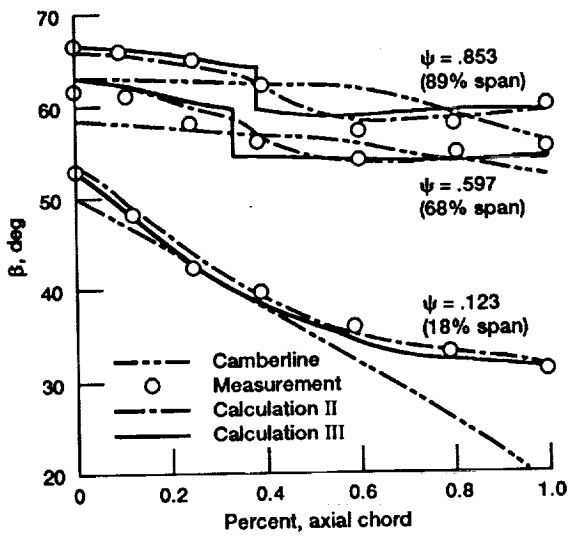


Figure 6.35.—Comparison of relative flow angle.

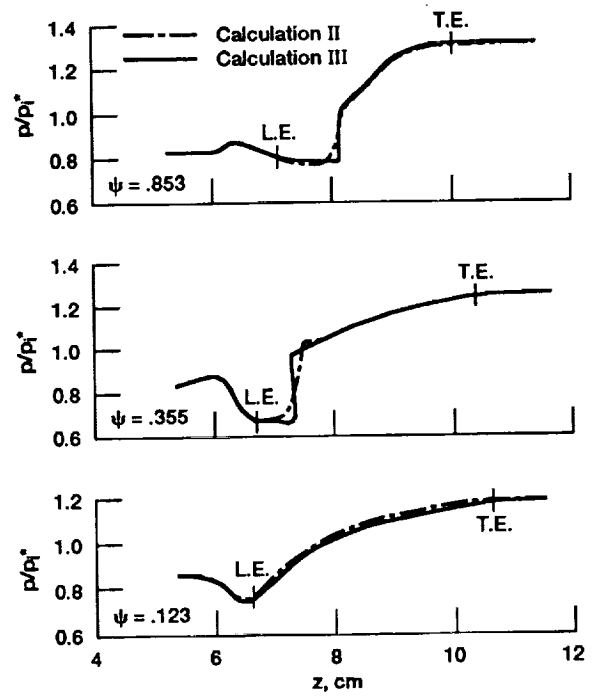


Figure 6.36.—Pressure rise on $S_{2,m}$.

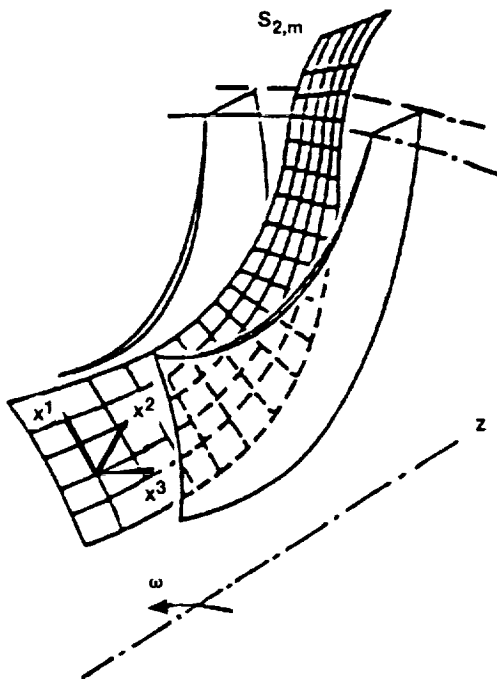


Figure 6.37.—Non-orthogonal curvilinear coordinate system used for S_2 stream surface.

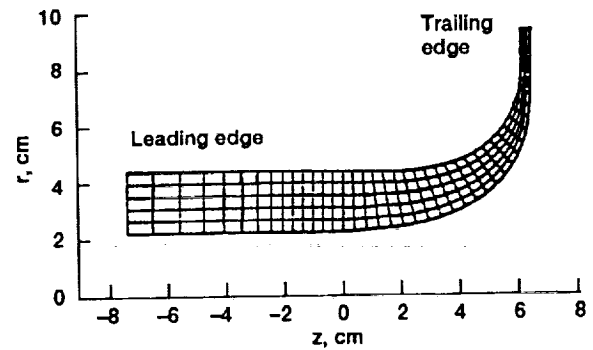


Figure 6.38.—Meridonal projection of mesh on $S_{2,m}$.

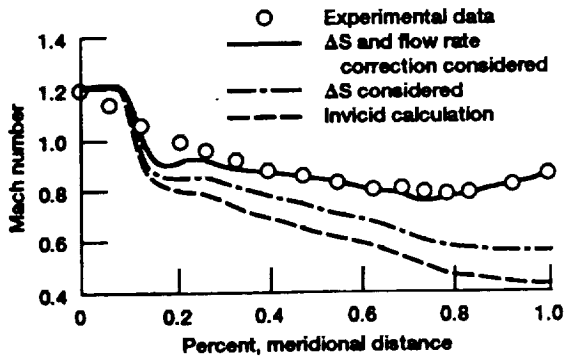


Figure 6.39.—Effect of entropy and flow rate correction.

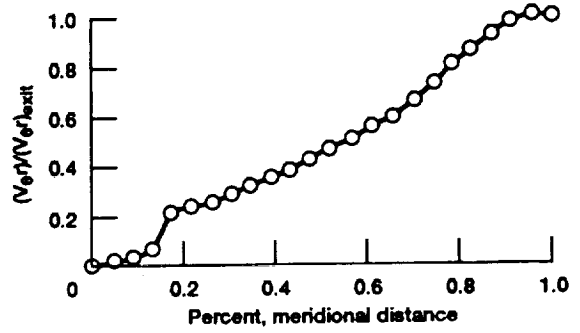


Figure 6.40.—Increase in $V_{\theta r}$ along casing.

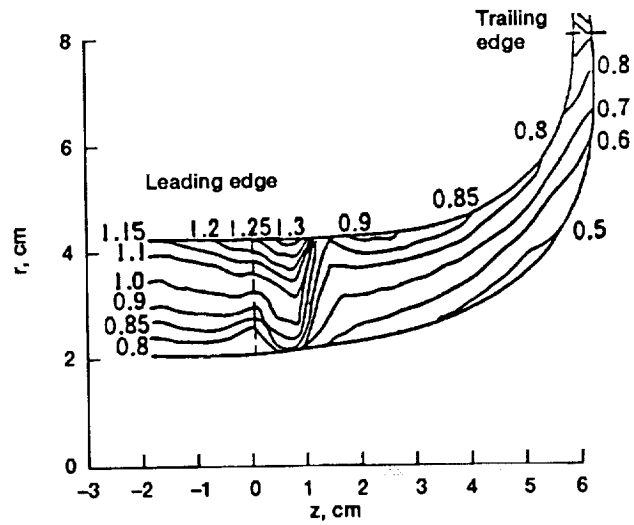


Figure 6.41—Meridional projection of Mach number contours.

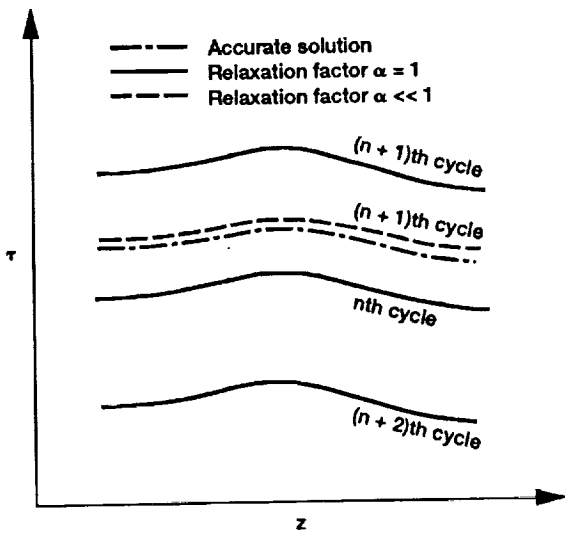


Figure 7.1.—Local fluctuation of S_1 stream filament thickness during iteration and the effect of relaxation factor (sketch).

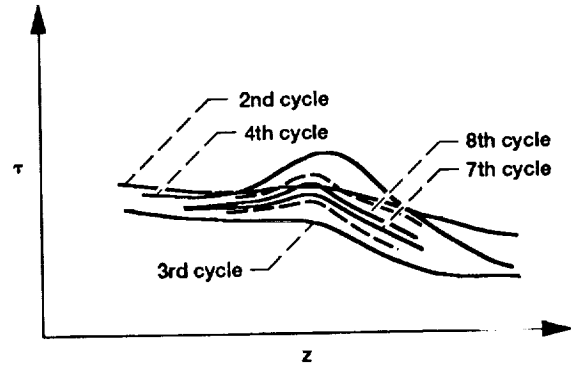
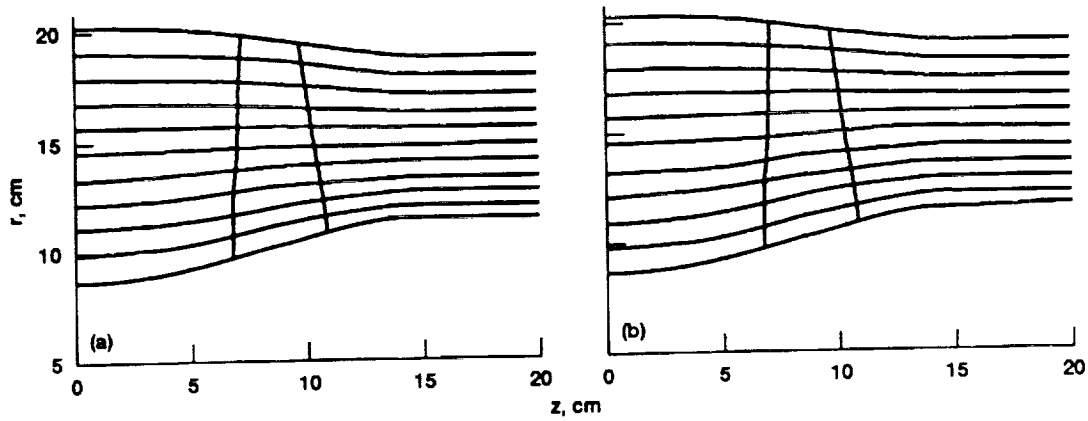
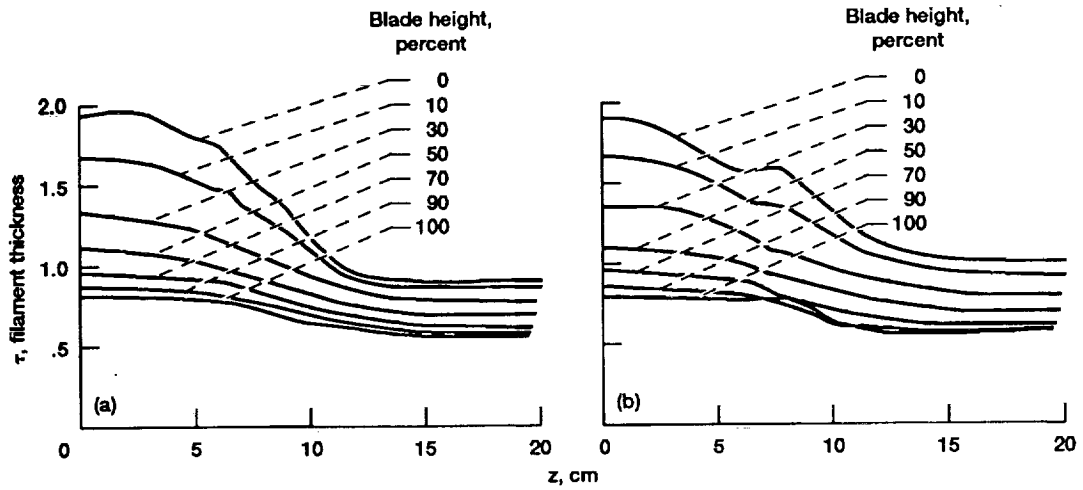


Figure 7.2.—Variation of tip S_1 filament thickness (schematic).



(a) 1st cycle.
(b) 9th cycle.

Figure 7.3.—Meridional projection of streamlines obtained on $S_{2,m}$ surface.



(a) 1st cycle.
(b) 9th cycle.

Figure 7.4.— S_1 filament thickness.

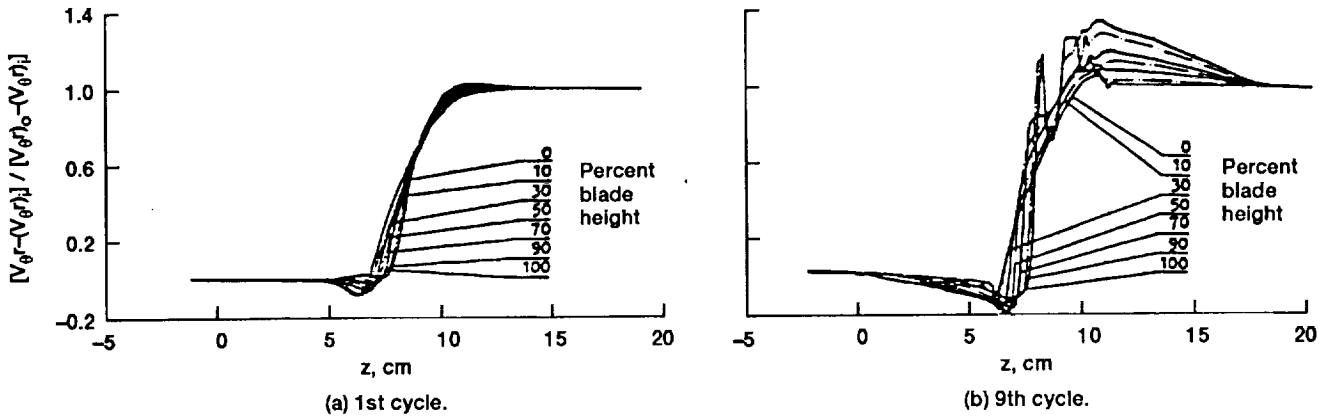


Figure 7.5.— S_2 input V_{0r} .

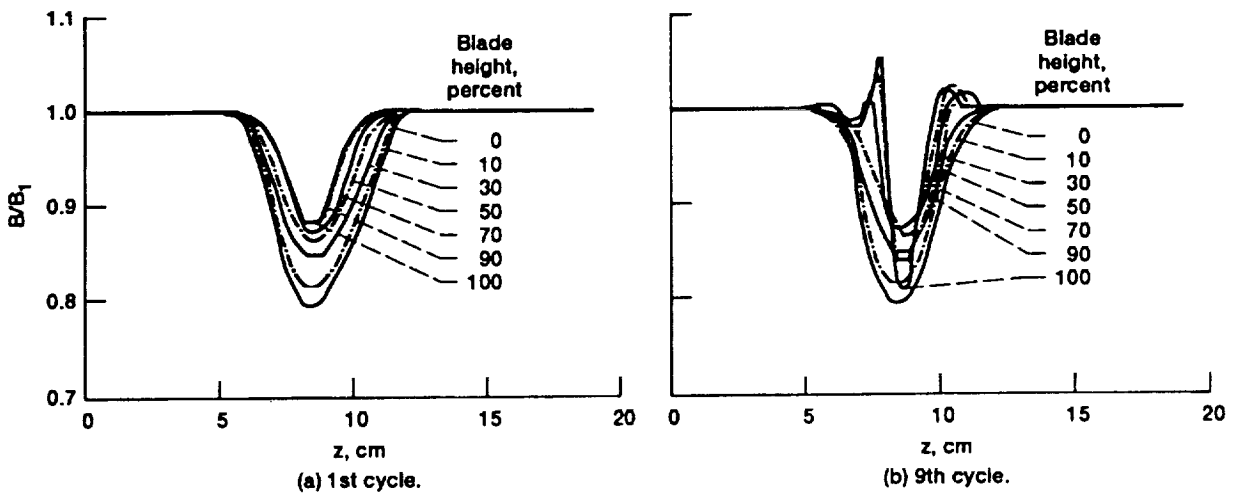


Figure 7.6.— S_2 input filament thickness.

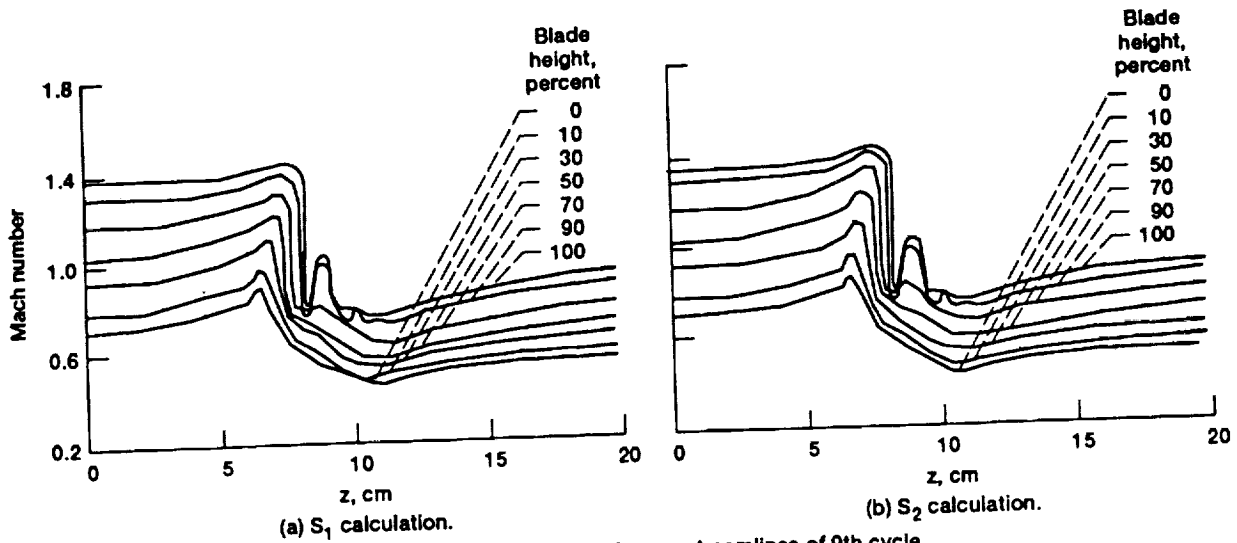


Figure 7.7.—Output Mach number on streamlines of 9th cycle.

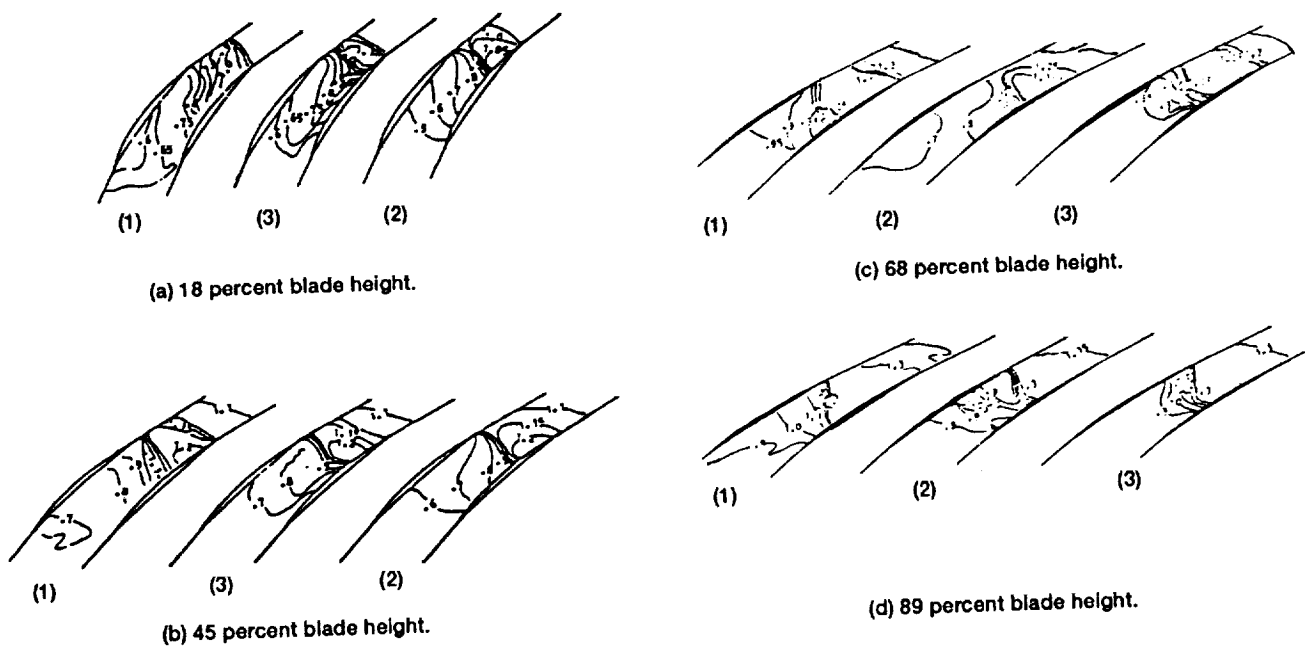
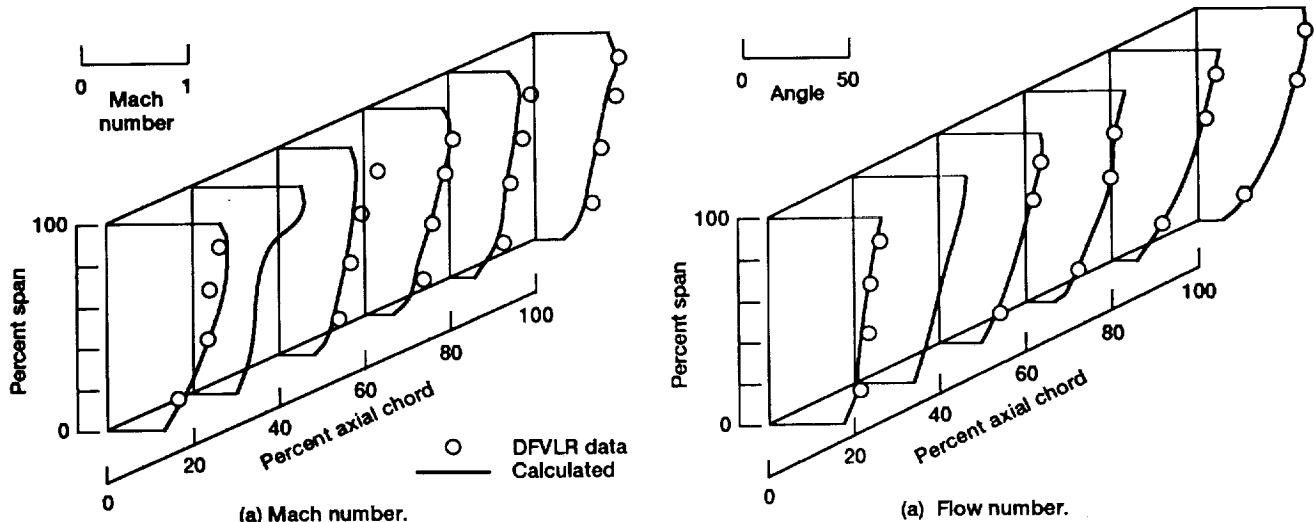


Figure 7.8.—Mach number contours on S_1 surface: (1) DFVLR measured data; (2) calculated by present method; (3) from Ref. 34.



(a) Mach number. (a) Flow number.
 Figure 7.9.—Radial variation of Mach number and flow angle at a number of stations.

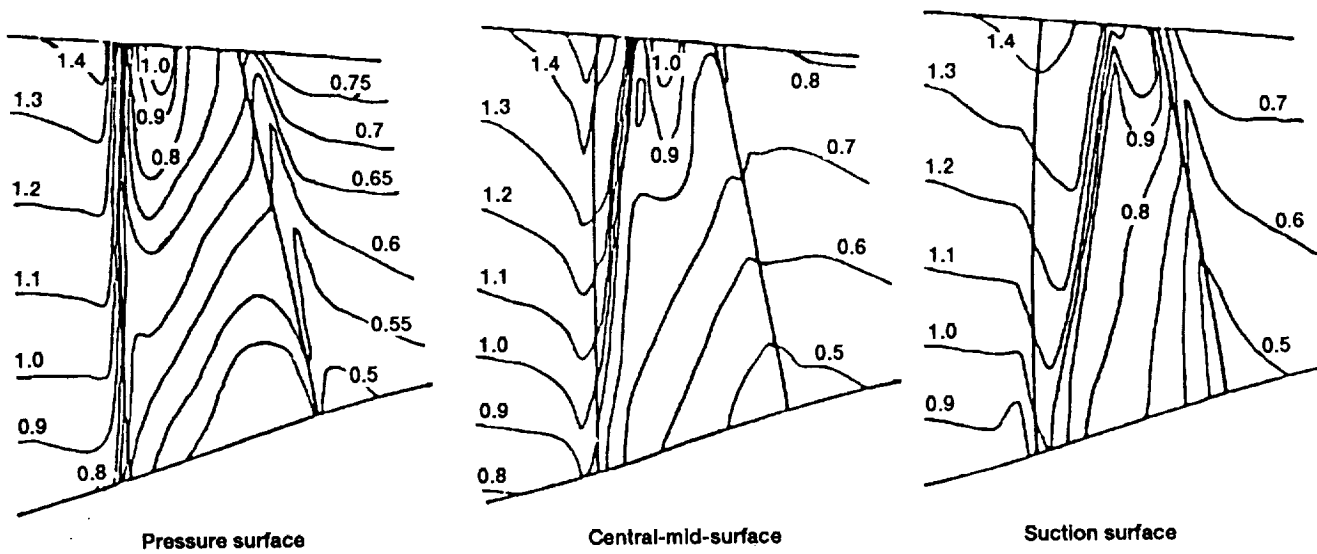


Figure 7.10—Constant Mach number contours on three S_2 surfaces.

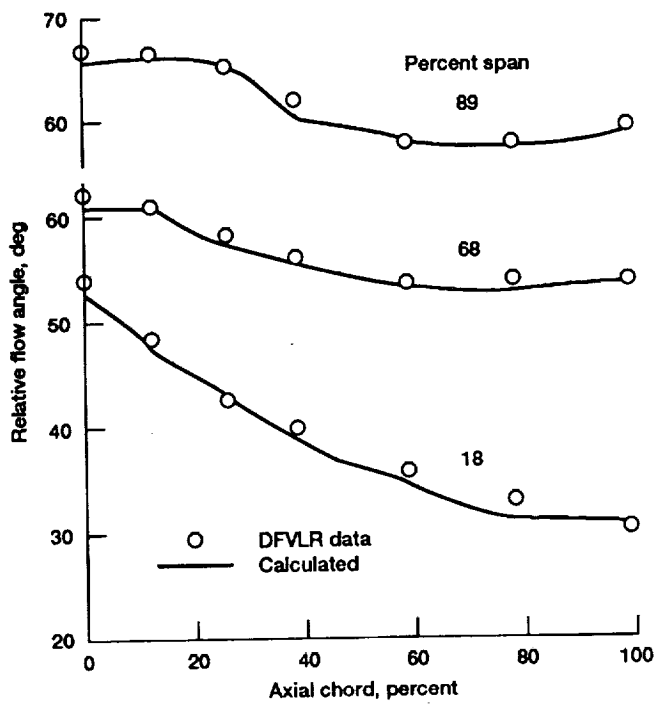


Figure 7.11—Variation of flow angle along three stream lines on $S_{2,m}$ surface.

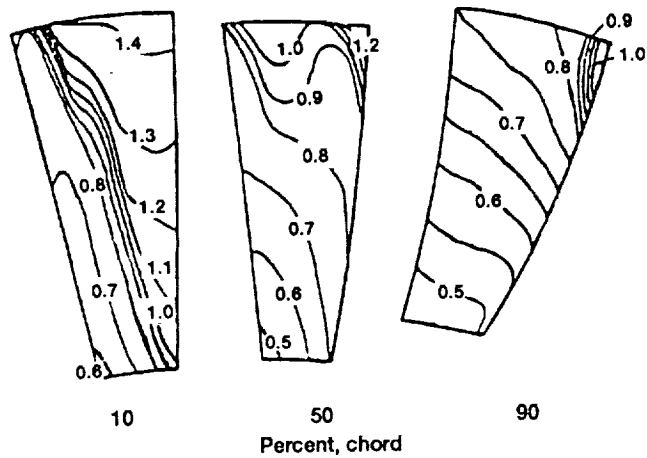


Figure 7.12.—Constant Mach number contours on span-wise surfaces formed by (x^2, x^3) coordinates.

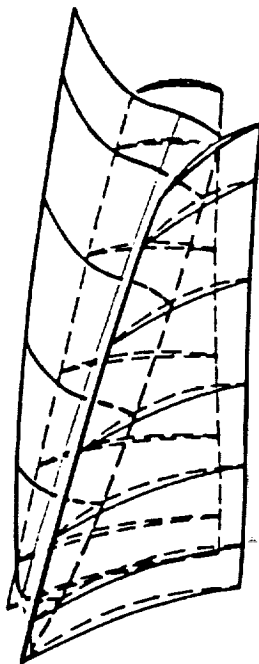


Figure 7.13.—Three-dimensional passage shock.

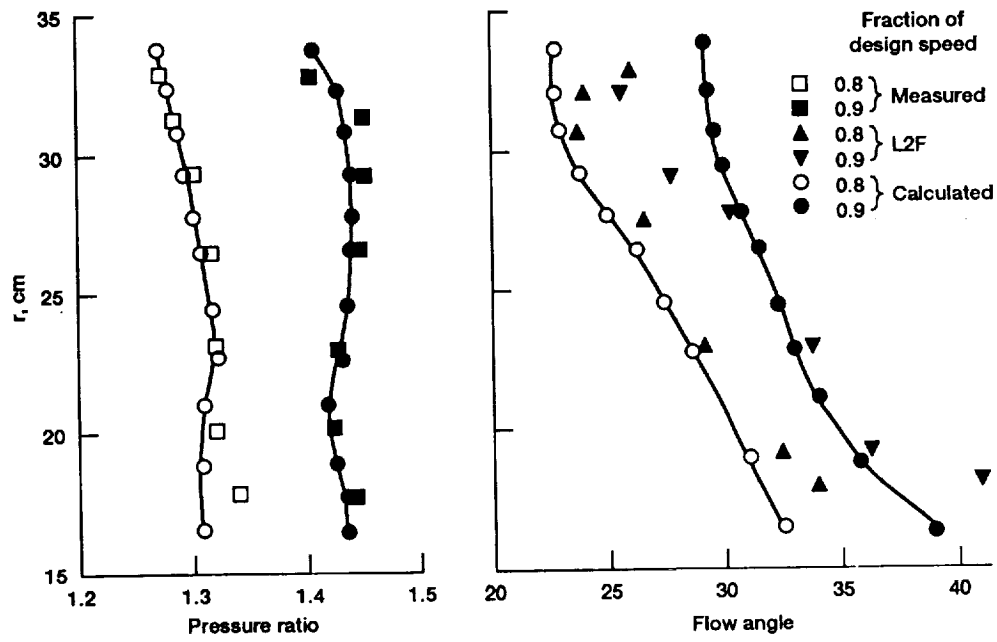


Figure 7.14—Radial distributions of pressure ratio and flow angle at rotor outlet.

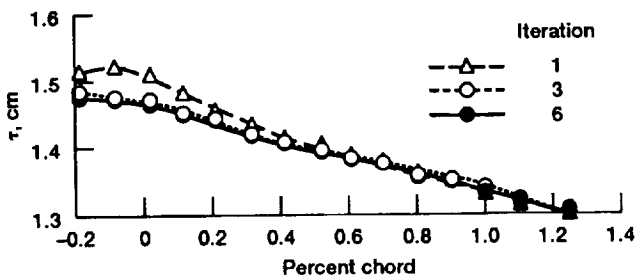


Figure 7.15—Variation of τ of S_1 filament number 10.

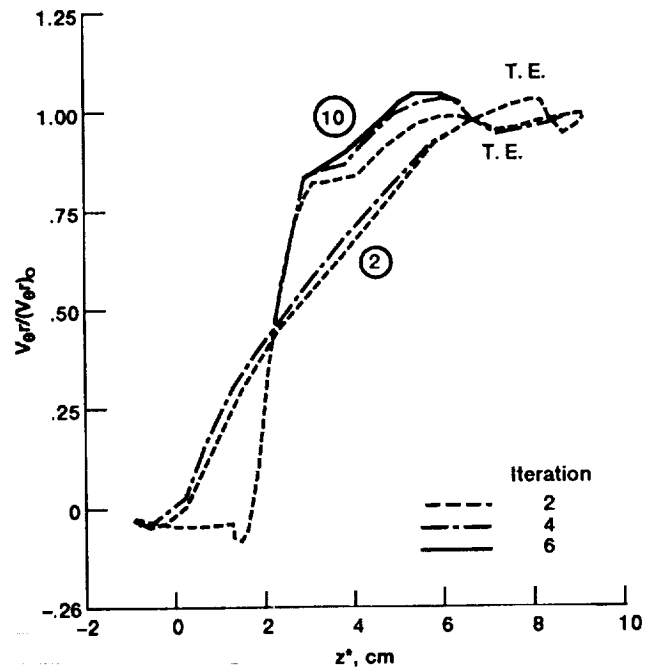


Figure 7.16.—Variation on V_{θ} of S_1 filament on $S_{2,m}$.

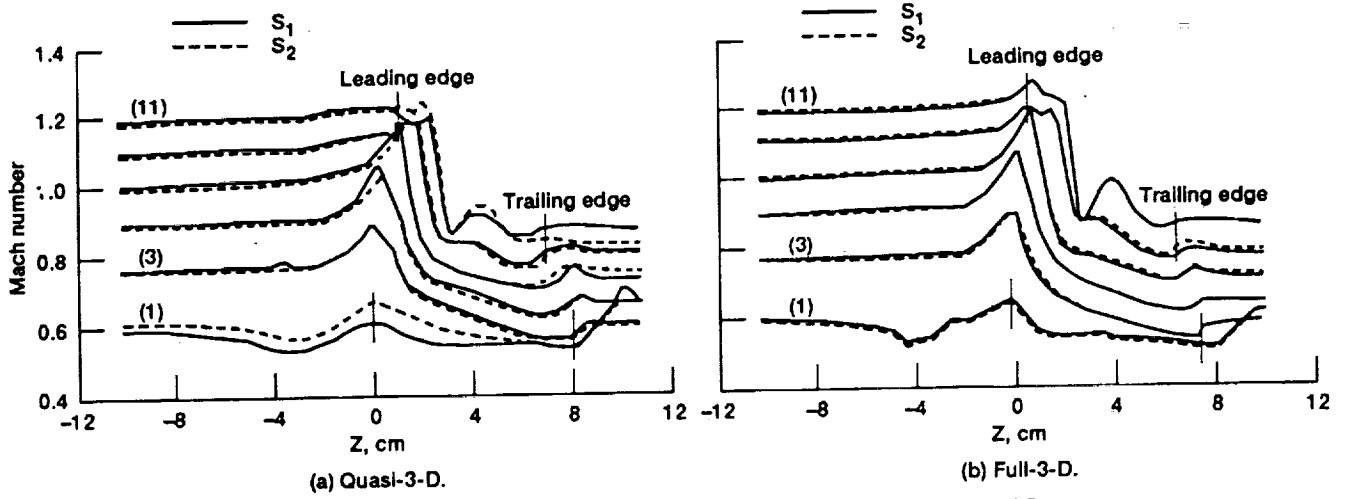


Figure 7.17—Mach number along intersecting streamlines between S_1 and S_2 .

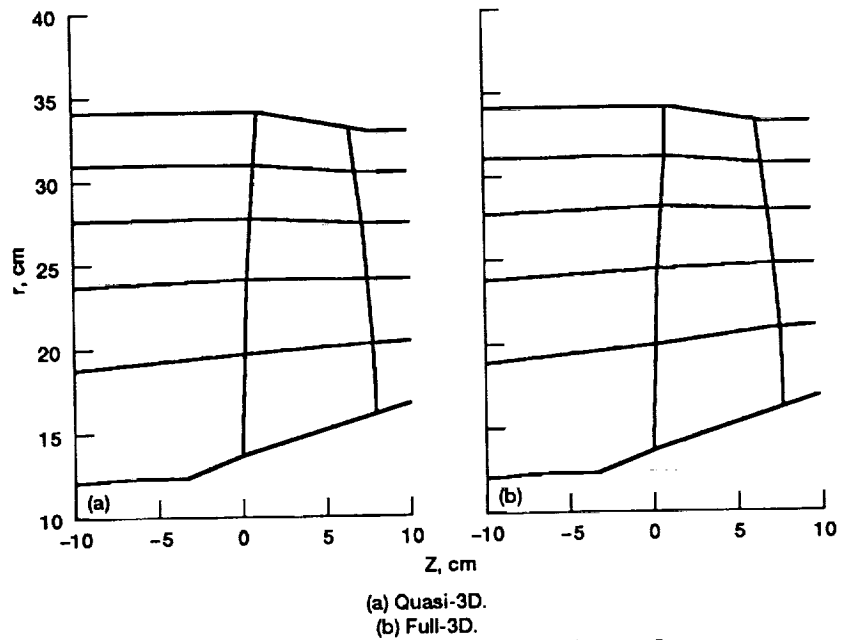


Figure 7.18.—Meridional projection of streamlines on $S_{2,m}$.

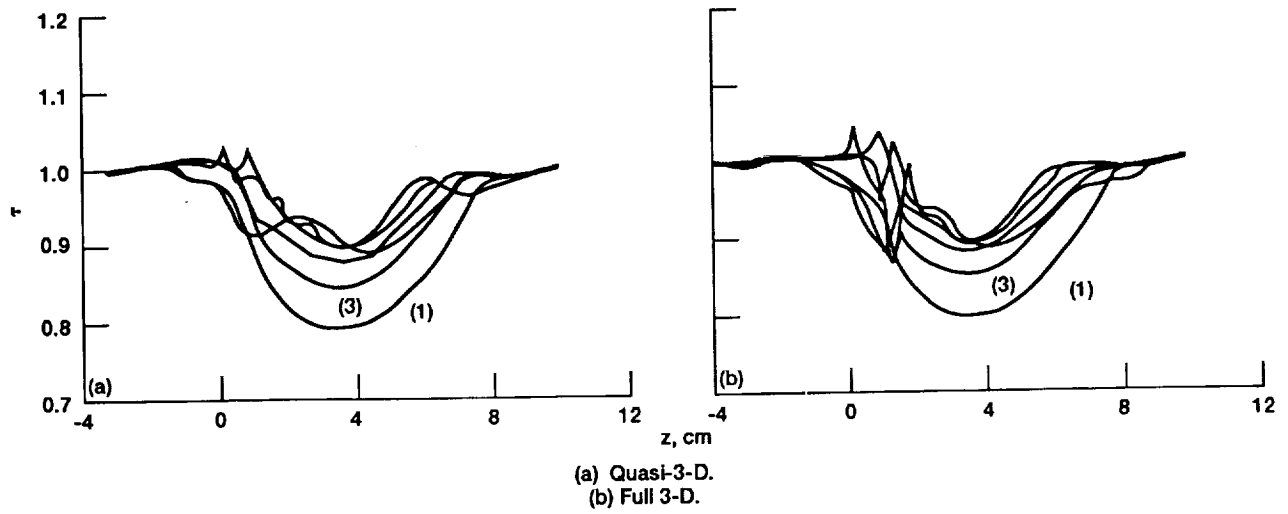


Figure 7.19.—Variation of S_2 filament thickness along mean streamlines on six S_1 surfaces.

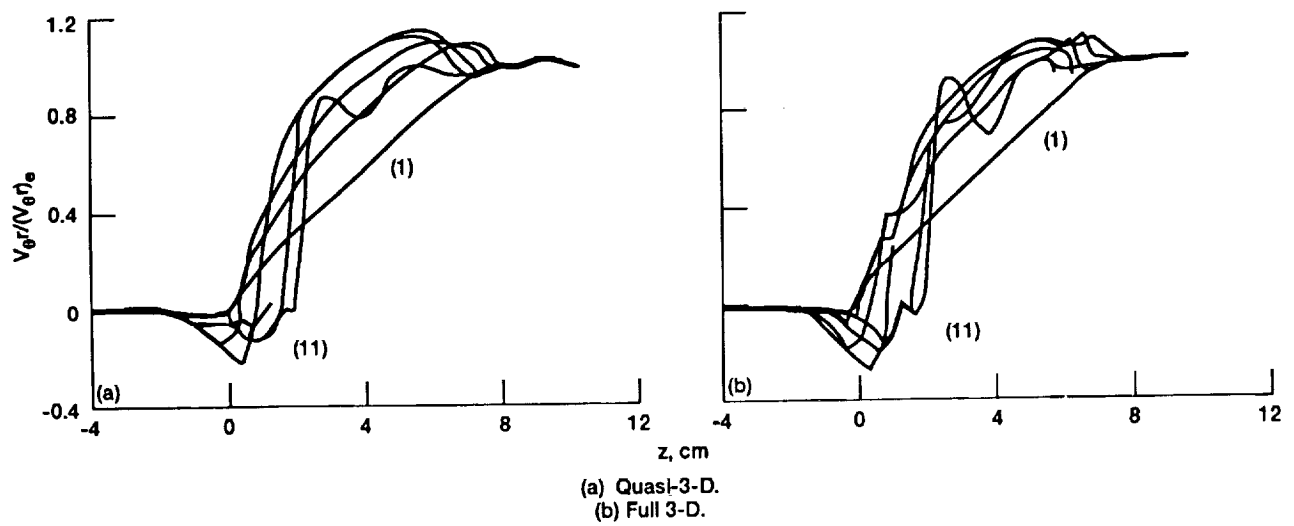


Figure 7.20.—Variation of $V_{\theta r}$ along mean streamlines on six S_1 surfaces.

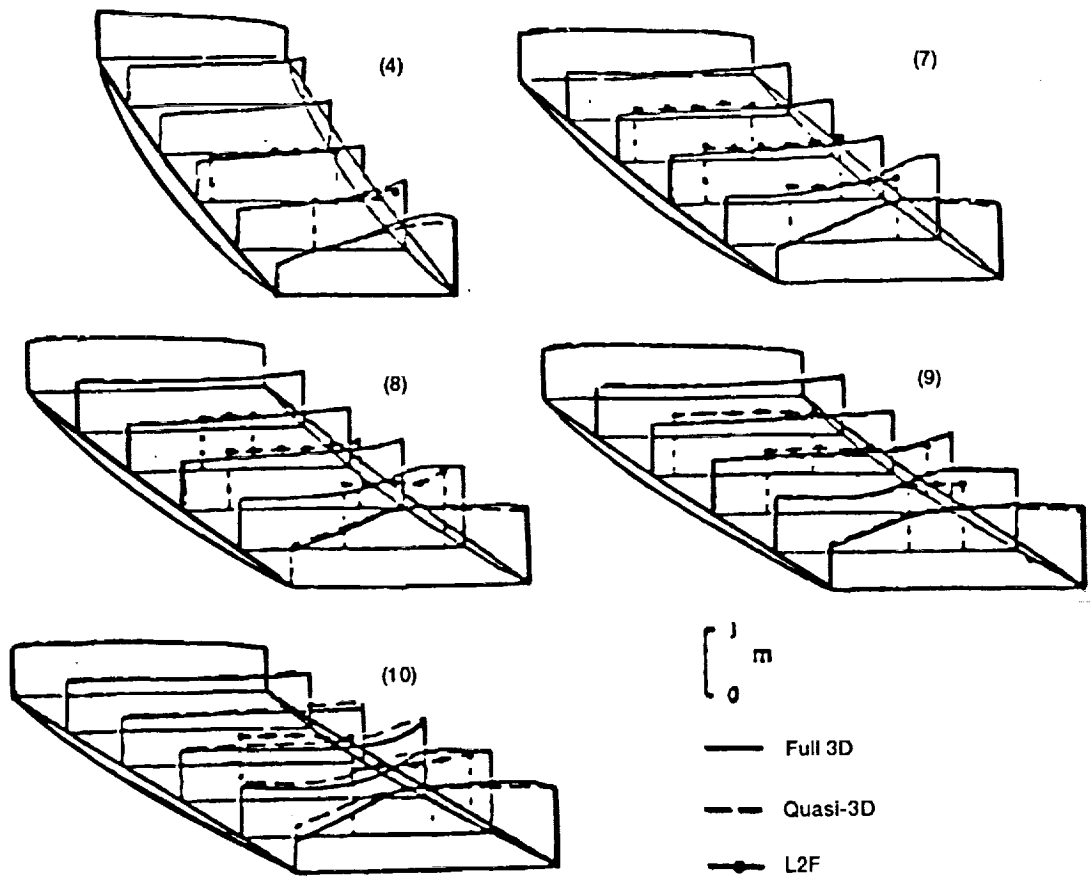


Figure 7.21.—Circumferential variations of Mach number.

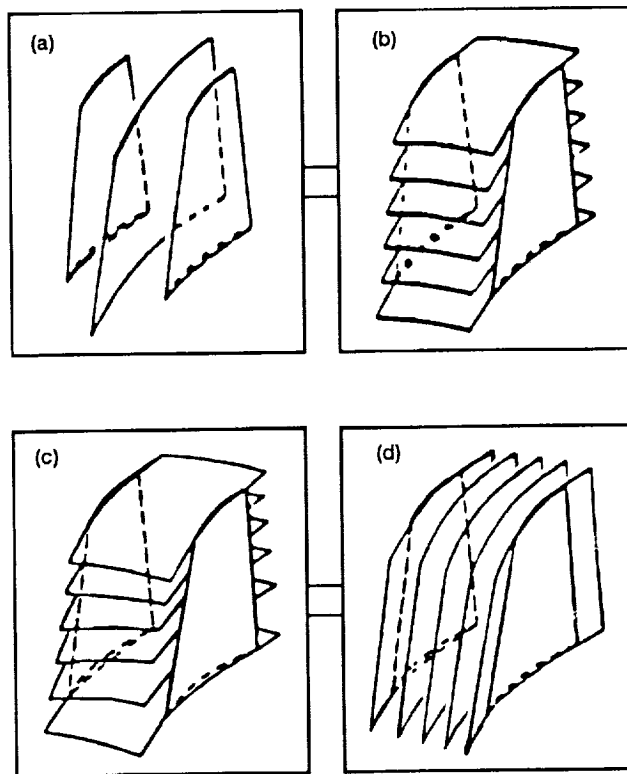


Figure 7.22.—Iterative process in 3D solution.

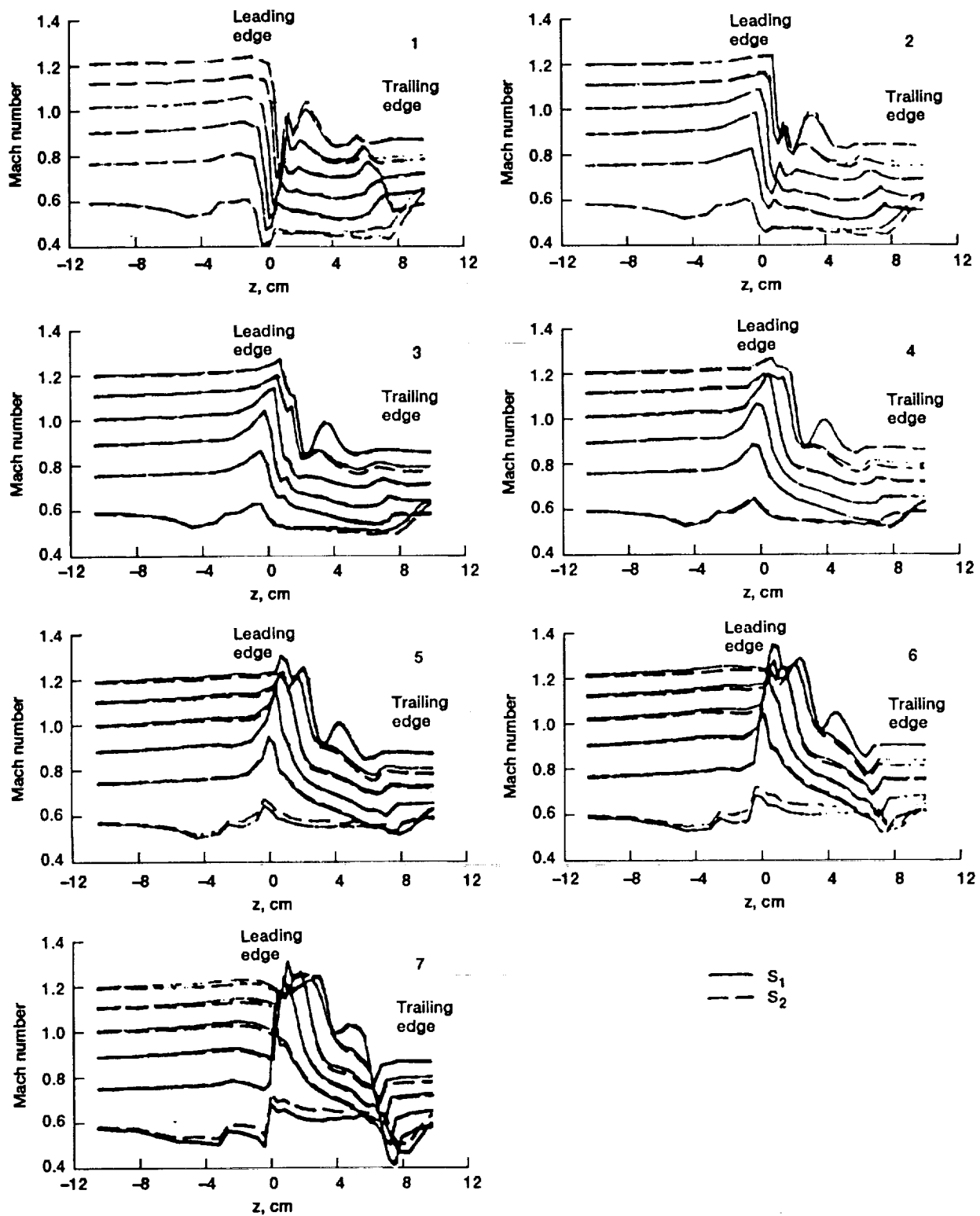


Figure 7.23.—Mach number on S_1 and S_2 surfaces.

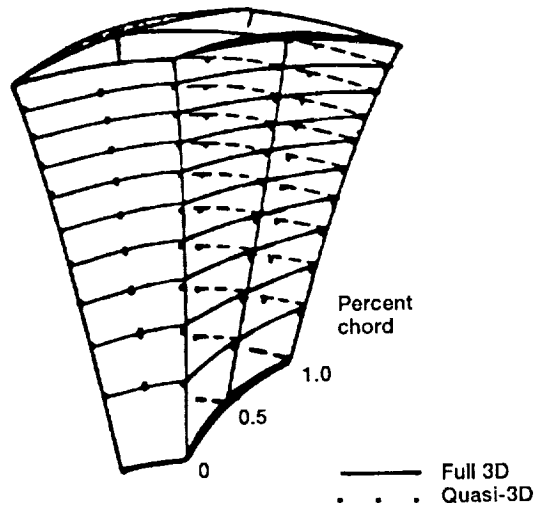


Figure 7.24.—Ten S_1 stream filaments.

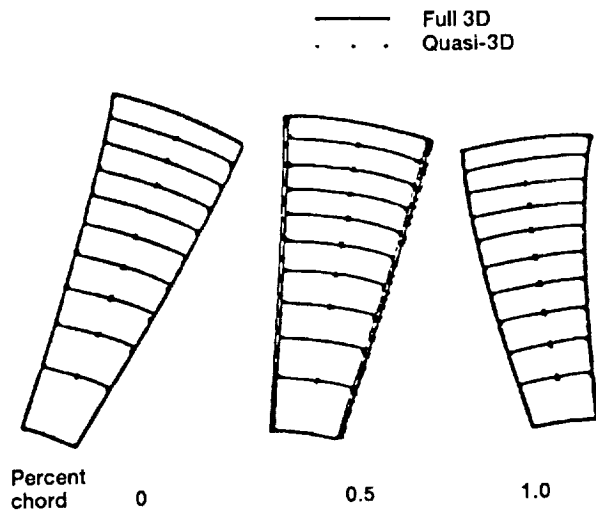


Figure 7.25.—Intersection of S_1 stream surfaces with three span-wise surfaces.

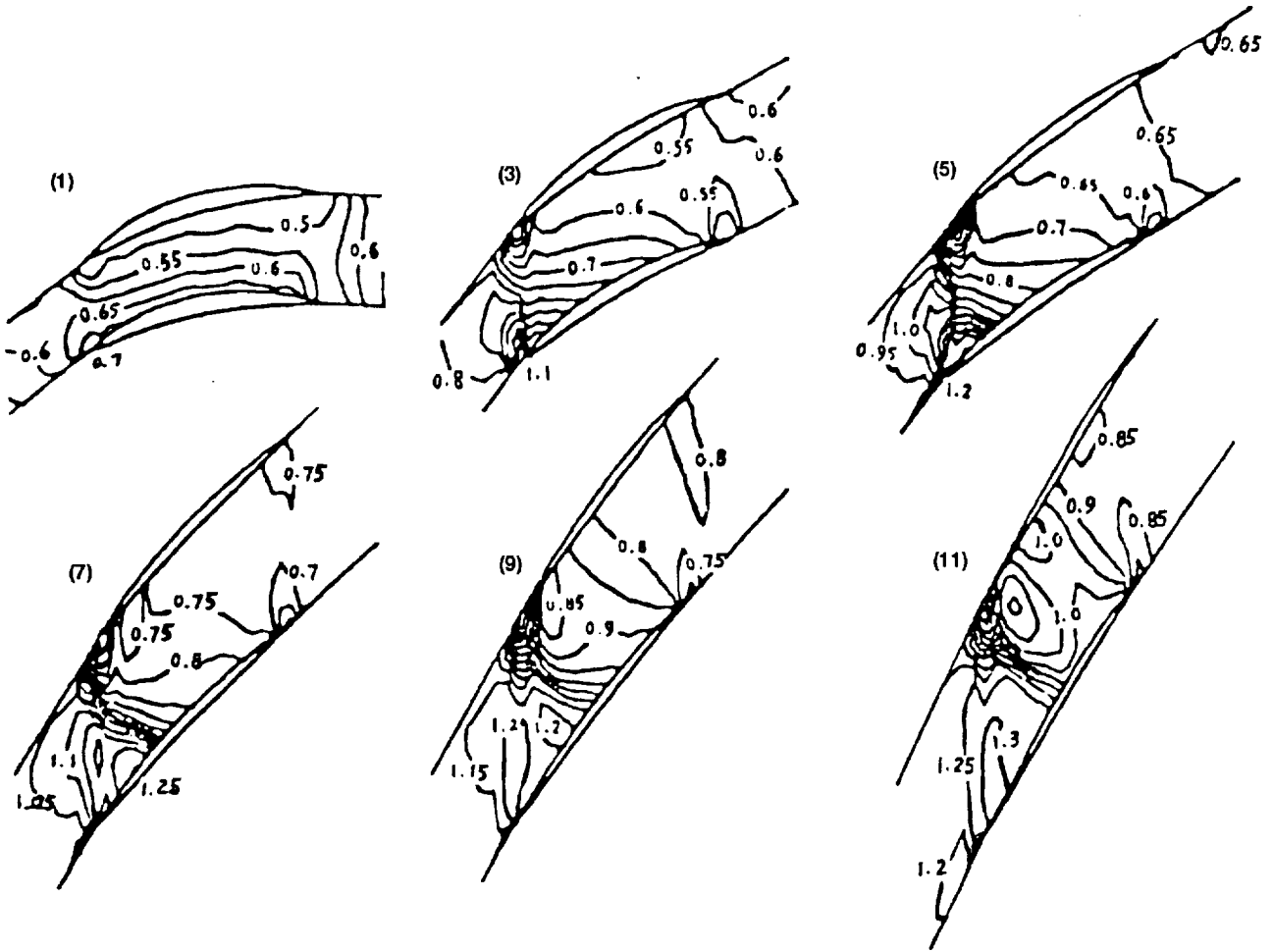


Figure 7.26.—Mach number contours in six S_1 stream filaments.

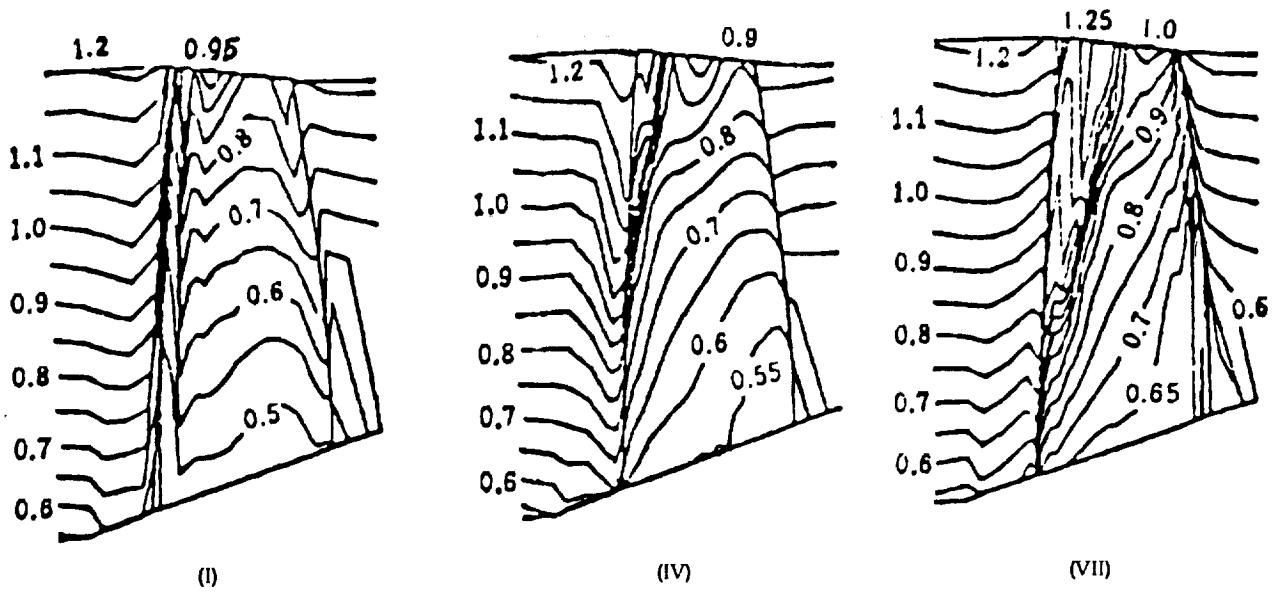


Figure 7.27.—Mach number contours in three S_2 stream filaments.

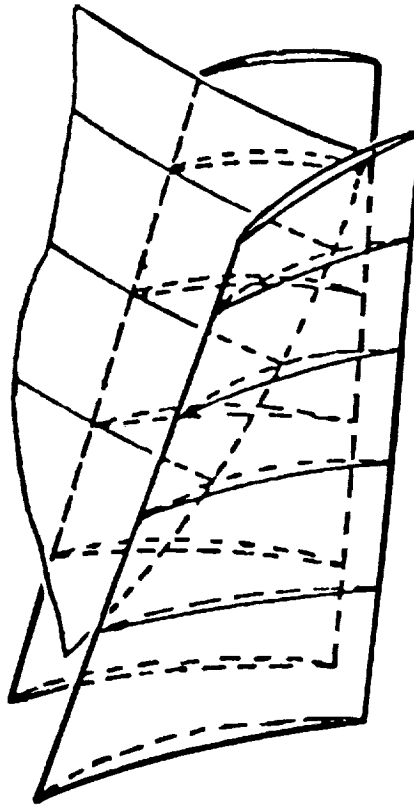


Figure 7.28.—Three-dimensional shock.

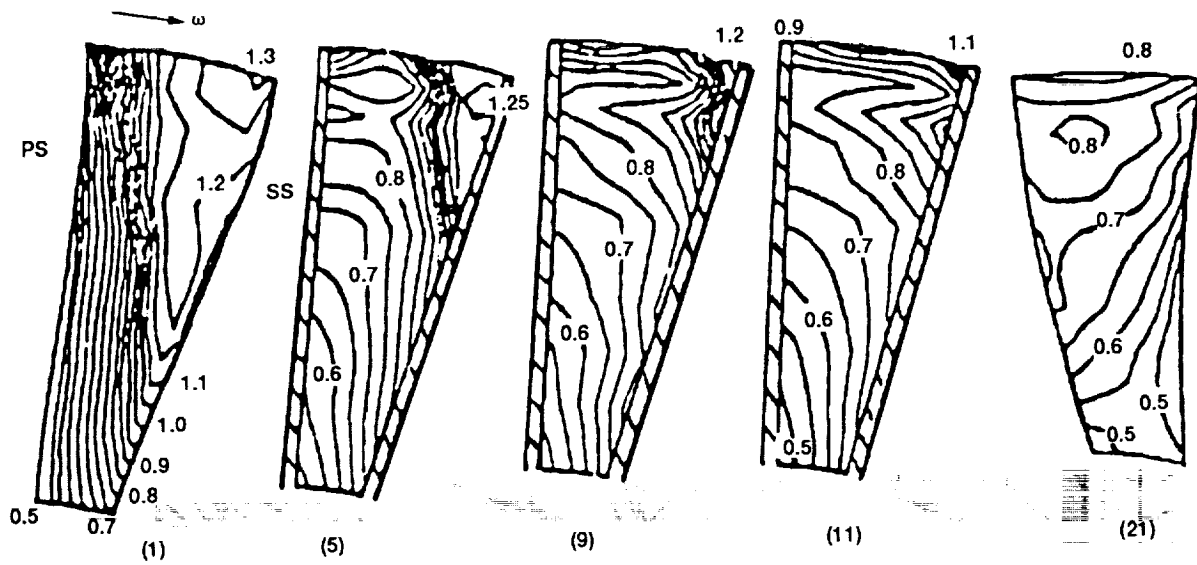


Figure 7.29.—Mach number contours on five span-wise surfaces.

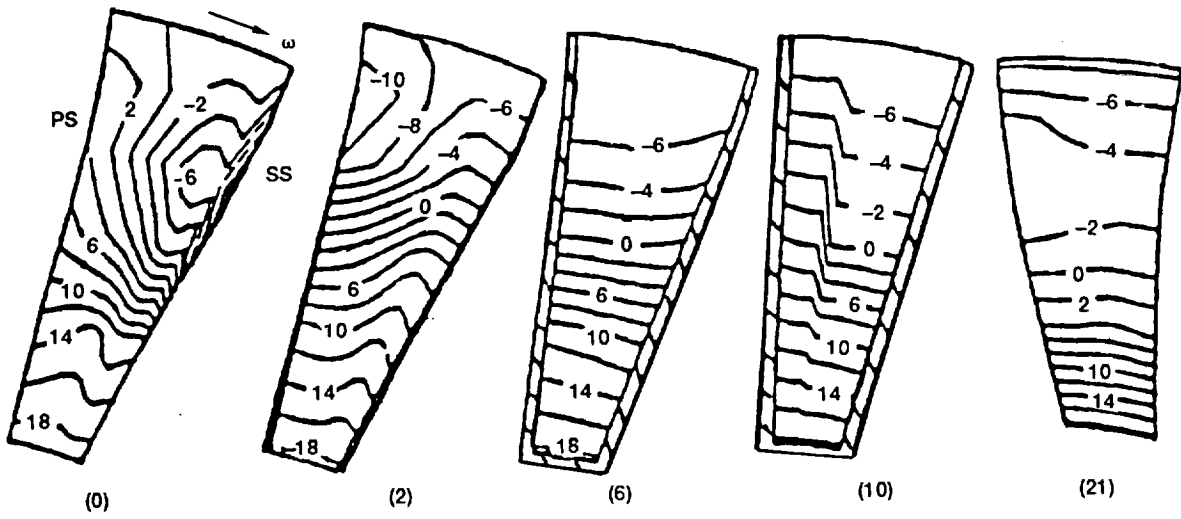


Figure 7.30.—Constant σ contours on five span-wise surfaces.

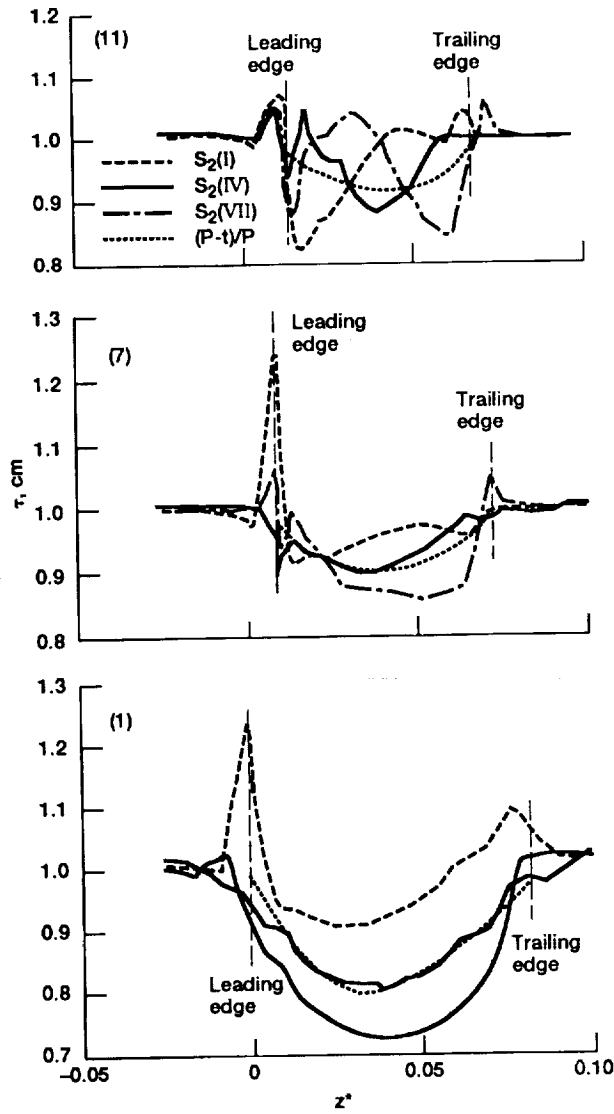


Figure 7.31.—Chordwise variations of S_2 filament thickness.

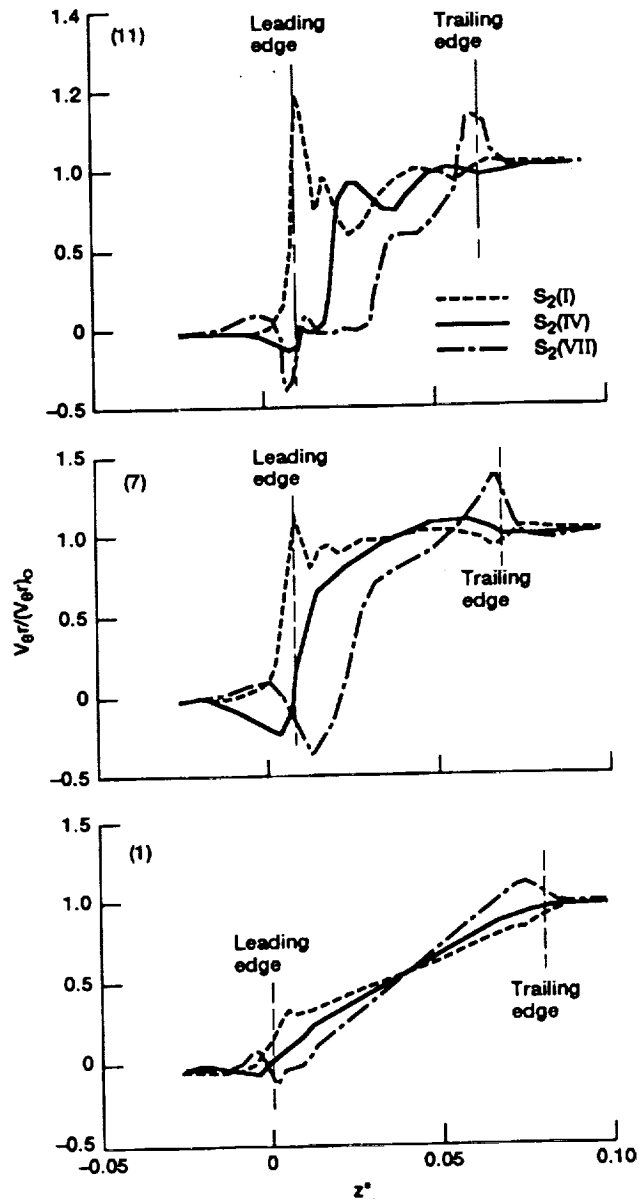


Figure 7.32.—Chordwise variations of $V_{\theta r}$ on S_2 surfaces.

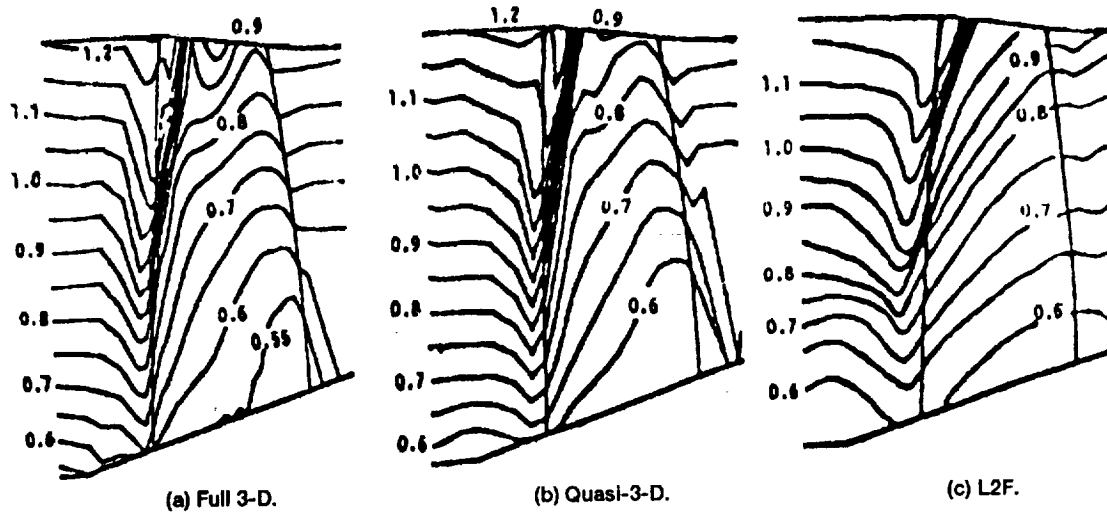


Figure 7.33.—Comparison of Mach number contours on S_{2m} .

REPORT DOCUMENTATION PAGE			Form Approved OMB No. 0704-0188	
Public reporting burden for this collection of information is estimated to average 1 hour per response, including the time for reviewing instructions, searching existing data sources, gathering and maintaining the data needed, and completing and reviewing the collection of information. Send comments regarding this burden estimate or any other aspect of this collection of information, including suggestions for reducing this burden, to Washington Headquarters Services, Directorate for Information Operations and Reports, 1215 Jefferson Davis Highway, Suite 1204, Arlington, VA 22202-4302, and to the Office of Management and Budget, Paperwork Reduction Project (0704-0188), Washington, DC 20503.				
1. AGENCY USE ONLY (Leave blank)	2. REPORT DATE May 1993	3. REPORT TYPE AND DATES COVERED Final Contractor Report		
4. TITLE AND SUBTITLE A General Theory of Two- and Three-Dimensional Rotational Flow in Subsonic and Transonic Turbomachines			5. FUNDING NUMBERS WU 505-90-21 WU 335-05-01 G NAG3-1072	
6. AUTHOR(S) Chung-Hua Wu			8. PERFORMING ORGANIZATION REPORT NUMBER E-7267	
7. PERFORMING ORGANIZATION NAME(S) AND ADDRESS(ES) Clemson University Department of Mechanical Engineering Clemson, South Carolina 29631			10. SPONSORING/MONITORING AGENCY REPORT NUMBER NASA CR-4496	
9. SPONSORING/MONITORING AGENCY NAMES(S) AND ADDRESS(ES) National Aeronautics and Space Administration Lewis Research Center Cleveland, Ohio 44135-3191			11. SUPPLEMENTARY NOTES Project Manager, Lonnie Reid, Internal Fluid Mechanics Division, (216) 433-3606.	
12a. DISTRIBUTION STATEMENT Date for general release <u>May 1993</u> Subject Category 02			12b. DISTRIBUTION CODE	
13. ABSTRACT (Maximum 200 words) This report represents a general theory applicable to axial, radial, and mixed flow turbomachines operating at subsonic and supersonic speeds with a finite number of blades of finite thickness. References reflect the evolution of computational methods used, from the inception of the theory in the 50's to the high-speed computer era of the 90's. Two kinds of relative stream surfaces, S_1 and S_2 , are introduced for the purpose of obtaining a three-dimensional flow solution through the combination of two-dimensional flow solutions. Nonorthogonal curvilinear coordinates are used for the governing equations. Methods of computing transonic flow along S_1 and S_2 stream surfaces are given for special cases as well as for fully three-dimensional transonic flows. Procedures pertaining to the direct solutions and inverse solutions are presented. Information on shock wave locations and shapes needed for computations are discussed. Experimental data from a Deutsche Forschungs- und Versuchsanstalt fur Luft- und Raumfahrt e.V. (DFVLR) rotor and from a Chinese Academy of Sciences (CAS) transonic compressor rotor are compared with the computed flow properties.				
14. SUBJECT TERMS Turbomachinery; Design; Analysis; Quasi-3D; Transonic; Subsonic			15. NUMBER OF PAGES 244	
			16. PRICE CODE	
17. SECURITY CLASSIFICATION OF REPORT Unclassified	18. SECURITY CLASSIFICATION OF THIS PAGE Unclassified	19. SECURITY CLASSIFICATION OF ABSTRACT Unclassified	20. LIMITATION OF ABSTRACT	